Aix*Marseille université
Socialement engagée

THÈSE DE DOCTORAT

Soutenue à Aix-Marseille Université
le 30 septembre 2024 par

Adrien DA ROS

Modelling of a X-ray imaging crystal spectrometer on WEST tokamak and Tungsten spectrum analysis

Modélisation d'un spectromètre X imageur à cristaux sur le tokamak WEST et analyse du spectre de Tungstène

Discipline
Physique et Sciences de la Matière

Spécialité
Énergies, Rayonnement et Plasma

École doctorale
ED352 : Physique et Sciences de la Matière

Laboratoire/Partenaires de recherche
- CEA-Cadarache - Institut de Recherche sur la Fusion par confinement Magnétique, Saint-Paul-lez-Durance, France

Composition du jury

Jean-Christophe PAIN Directeur de recherche, CEA	Rapporteur
Frank ROSMEJ Professeur, Paris Sorbonne Université	Rapporteur
Francesca BOMBARDA Research Scientist, ENEA (Italy)	Examinatrice
John RICE Senior Research Scientist, MIT (USA)	Examinateur
João Jorge SANTOS Professeur, Université de Bordeaux	Président du jury
Rémy GUIRLET Directeur de recherche, CEA-IRFM	Directeur de thèse
Rémi DUMONT Directeur de recherche, CEA-IRFM	Co-directeur de thèse
Didier VEZINET Ingénieur, Commonwealth Fusion Systems (USA)	Co-encadrant

DE LA RECHERCHE À L'INDUSTRIE cea IRFM

Affidavit

Je soussigné, Adrien Da Ros, déclare par la présente que le travail présenté dans ce manuscrit est mon propre travail, réalisé sous la direction scientifique de Rémy Guirlet, dans le respect des principes d'honnêteté, d'intégrité et de responsabilité inhérents à la mission de recherche. Les travaux de recherche et la rédaction de ce manuscrit ont été réalisés dans le respect à la fois de la charte nationale de déontologie des métiers de la recherche et de la charte d'Aix-Marseille Université relative à la lutte contre le plagiat.

Ce travail n'a pas été précédemment soumis en France ou à l'étranger dans une version identique ou similaire à un organisme examinateur.

Fait à Aix-en-Provence le 03/07/2024



Cette œuvre est mise à disposition selon les termes de la Licence Creative Commons Attribution - Pas d'Utilisation Commerciale - Pas de Modification 4.0 International.

Liste de publications et participation aux conférences

Liste des publications réalisées dans le cadre du projet de thèse :

1. A. Da Ros, D. Vezinet, G. Colledani, C. Fenzi-Bonizec, G. Moureau, G. Bertschinger, and the WEST Team. Electron and ion temperature measurement with a new x-ray imaging crystal spectrometer on WEST. Review of Scientific Instruments, 95(4) :043505, 04 2024, https://doi.org/10.1063/5.0179905

Participation aux conférences et écoles d'été au cours de la période de thèse :

1. Poster session - 2023 EPS Conference on Plasma Physics, Bordeaux (France) (https://cea.hal.science/cea-04202029/document)
2. Poster session - 2022 EPS Conference on Plasma Physics, Online (https://cea.hal.science/cea-03740636/file/paper_EPS2022_DAROS.pdf)

Abstract

The study of tokamak plasmas for thermonuclear fusion research is being carried out within a large framework of international cooperation for the future International Thermonuclear Experimental Reactor (ITER) operation. To achieve this, we need instruments capable of measuring important plasma properties such as electron and ion temperatures, two key parameters for quantifying plasma energy balance. Simultaneous measurement of T_e and T_i by the same instrument is a considerable advantage for redundancy and cross-validation of tokamak measurements. With this in mind, a diagnostic instrument for measuring photons in the soft X-ray range was recently installed and used on the W (Tungsten) Environment in Steady-state Tokamak (WEST) tokamak. This instrument, called the X-ray Imaging Crystal Spectrometer (XICS), measures the emission of certain Ar XVII, Ar XVIII and Fe XXV lines using three interchangeable crystals placed on a rotating table.

The work presented here focuses on the study of the Ar XVII spectrum in the wavelength range between 3.93 and 4.00 Å (3.1 keV < E < 3.15 keV). The first part is devoted to studying the physics of X-rays in tokamak plasmas and analysing the spectral lines of the Ar XVII spectrum. We then detail the design of the XICS diagnostic, the spectral and spatial resolutions enabled by its design, its use in experimental campaigns and the spectra obtained. This instrument enables to measure the electron and ion temperatures in WEST plasmas, $T_{e,max} \approx 5$ keV and $T_{i,max} \approx 2$ keV. A manufacturing defect in Bragg crystals is identified, causing a line-doubling of the measured lines. A simple solution was found to remedy this by hiding one half of the crystal facing the plasma.

From the spectral measurements, intrinsic properties of the plasma are characterised, such as the electron and ion temperature profiles, in space and time, in agreement with the results of other diagnostics. The identification of specific spectral lines from different tungsten ionisation stages enables a brightness calibration transfer to be carried out with a Ultra-Violet (UV) diagnostic measuring lines of the same tungsten ionisation stages. We deduce densities and concentrations of tungsten, in addition to those of argon for a typical WEST plasma discharge ($c_{Ar^{16+}} \approx 8 \times 10^{-5}$ and $c_{W^{44+}} \approx 1 \times 10^{-4}$). Prospects for future work with this instrument are also outlined, in relation to the results presented throughout this thesis.

Keywords: Tokamak, X-ray spectroscopy, Argon, Tungsten, Atomic physics, Bragg diffraction

Résumé

L'étude des plasmas de tokamak pour la recherche sur la fusion thermo-nucléaire se fait dans un cadre vaste de coopération internationale en vue de l'exploitation d'ITER. Pour cela, nous avons besoin d'instruments capables de mesurer les propriétés importantes des plasmas et notamment la température des électrons et des ions, deux paramètres de premier ordre pour quantifier le bilan énergétique du plasma. La mesure simultannée, par le même instrument, de T_e et T_i est un atout considérable pour la redondance et la validation croisée des mesures sur tokamak. Dans cette optique, un diagnostic de mesure des photons dans la gamme des rayons X-mous a été récemment installé et utilisé sur le tokamak WEST. Cet instrument, appelé XICS, mesure l'émission de certaines raies d'Ar XVII, d'Ar XVIII et de Fe XXV grâce à trois cristaux interchangeables placés sur une table de rotation.

Le travail présenté ici se focalise sur l'étude du spectre d'Ar XVII dans la gamme de longueurs d'ondes entre 3.93 et 4.00 Å (3.1 keV < E < 3.15 keV). Une première partie est dédiée à l'étude de la physique du rayonnement X issu des plasmas de tokamak et à l'analyse des raies spectrales du spectre d'Ar XVII. Puis nous détaillons la conception du diagnostic XICS, les résolutions spectrales et spatiales permises par sa conception, son utilisation en campagnes expérimentales et les spectres obtenus. Cet instrument de mesure nous permet de mesurer les températures électroniques et ioniques dans les plasmas de WEST, $T_{e,max} \approx 5$ keV et $T_{i,max} \approx 2$ keV. Un défaut de fabrication des cristaux de Bragg est idenfifié provoquant un dédoublement des raies mesurées. Une solution simple est apportée pour y remédier en cachant une moitié du cristal utilisé face au plasma.

À partir des mesures de spectres, des propriétés intrinsèques des plasma sont caractérisées, comme des profils spatiaux et temporels de températures électronique et ionique en accord avec les résultats d'autres diagnostics. L'identification de certaines raies spectrales issues de différents états d'ionisation du tungstène permet de réaliser un transfert d'étalonnage avec un diagnostic UV mesurant des raies des même états d'ionisation du tungstène et de déduire des densités et concentrations de tungstène, en plus de ceux d'argon pour une décharge plasma typique de WEST ($c_{\mathrm{Ar}^{16+}} \approx 8 \times 10^{-5}$ et $c_{\mathrm{W}^{44+}} \approx 1 \times 10^{-4}$). Des perspectives quant à de futurs travaux à effectuer avec cet instrument sont également exposées, en lien avec les résultats montrés tout au long de cette thèse.

Mots clés: Tokamak, Spectroscopie X, Argon, Tungstène, Physique atomique, Diffraction de Bragg

Résumé étendu

La recherche d'une source de production d'électricité à faible émission de carbone et moins polluante pour répondre aux besoins de l'ensemble de notre société représente l'un des défis les plus cruciaux du 21ème siècle. La consommation de combustibles fossiles comme le charbon, le pétrole et le gaz n'a jamais été aussi élevée qu'aujourd'hui, alors même que la population mondiale ne cesse d'augmenter, tout comme les besoins en électricité à l'échelle planétaire. Les rapports alarmants du Groupe d'experts Intergouvernemental sur l'Évolution du Climat (GIEC) mettent en lumière les effets nocifs de cette augmentation de la consommation d'énergies fossiles sur notre planète. Les progrès de la recherche en matière de fusion thermo-nucléaire ont incité, il y a quarante ans, plusieurs pays industrialisés à s'unir pour lancer le programme ITER, visant à développer une nouvelle source d'énergie propre et durable basée sur les réactions de fusion nucléaire. ITER est l'un des projets énergétiques les plus ambitieux au monde et les avancées scientifiques réalisées ouvriront la voie aux centrales à fusion de demain.

Le principe de la fusion thermonucléaire est intimement lié à celui de la fission thermonucléaire, toutes deux fondées sur une modification de la composition nucléaire en agissant sur les nucléons (protons et neutrons). La fusion peut se produire entre des atomes légers grâce à leur faible énergie de liaison moyenne par nucléon, créant ainsi des éléments plus lourds et plus stables, tout en libérant de l'énergie. La réaction de fusion la plus prometteuse pour la recherche est basée sur le deutérium (D) et le tritium (T), qui sont des isotopes de H, car cette réaction est exogène et sa réactivité, plus élevée que les autres réactions (D-D, D-He, etc), est atteignable à des températures plus basses et reproductibles en plasmas de laboratoire. Pour que les réactions de fusion puissent se maintenir sans ajout externe d'énergie, un plasma doit atteindre l'ignition, c'est-à-dire que les pertes radiatives sont compensées par l'énergie apportée par les produits de la fusion. La puissance perdue par le plasma doit être au moins compensée par la puissance produite par les réactions de fusion. Celles-ci peuvent être obtenues par exemple par des tirs lasers à hautes puissances sur une cible qui se comprime, augmente sa température et déclenche des réactions de fusion (Fusion par confinement inertiel (FCI)), ou bien en confinant le plasma par des champs magnétiques (Fusion par confinement magnétique (FCM)) dans des dispositifs que l'on appelle tokamak ou stellarator suivant la configuration magnétique choisie. Ce mémoire de thèse porte sur les tokamaks.

Les éléments principaux d'un tokamak sont une enceinte de section sphérique ou torique, d'un solénoïde central aligné sur l'axe de symétrie du tokamak, de bobines de champ magnétique toroïdal et poloïdal et de systèmes de chauffage additionnels. Les derniers composants essentiels d'un tokamak sont les systèmes de chauffage

auxiliaires. Ils transfèrent de l'énergie directement aux électrons et aux ions en ciblant les fréquences de rotation des particules chargées autour des lignes de champ magnétique. WEST a d'autres éléments essentiels et originaux comme un système de génération de courant et des composants face au plasma conçus pour recevoir des flux extrêmement élevés de puissance et de particules. C'est la combinaison des deux qui permet de maintenir des plasmas pendant des durées de plusieurs minutes. Notre étude est basée sur les expériences réalisées sur le tokamak WEST dont les principaux objectifs sont de tester des composants face au plasma (Composants face au plasma (CFP)) similaires à ceux qui seront employés sur ITER et de travailler sur de longues décharges plasmas en régime permanent. Autour du tokamak WEST, quelques diagnostics permettent de mesurer la température des électrons et des ions mais ici, nous nous intéresserons à un spectromètre de rayons X mous visant à mesurer des photons dans le domaine spectral [3.94, 4.00]Å, émis par les espèces d'ions argon (Ar, Z=[15+, 16+]).

Les différentes particules constituant les plasmas (atomes, ions, électrons, photons et autres) peuvent interagir de plusieurs manières entre eux. Des collisions peuvent se produire entre des particules chargées conduisant à des processus d'excitation et d'ionisation. Les phénomènes de collision dans un plasma sont très importants car ils permettent de transférer l'énergie entre les particules. Les collisions électron-ion sont les plus fréquentes et ces transferts d'énergie conduisent les ions à atteindre soit des états d'excitation plus élevés, soit des états d'ionisation différents, entraînant des émissions de photons en général. Pour les plasmas de tokamak, on fait appel à un modèle d'équilibre nommé Collisionnel-Radiatif pour prendre en compte les changements d'états entre les états d'ionisation et d'excitation des ions. Les photons émis lors de ces phénomènes proviennent de la transition d'un électron entre deux niveaux d'énergies différents pour un ion et leur énergie est égale à la différence d'énergie entre ces deux niveaux. L'ensemble des photons d'une même transition produit alors ce qu'on appelle une raie spectrale. Réciproquement, à chacune des raies spectrales mesurée dans le domaine spectral donné ci-dessus peut être associée la transition qui en est responsable, sous la forme du niveau initial et du niveau final. Chaque transition (et donc chaque raie spectrale) a sa propre dépendance en fonction de la température électronique et d'autres paramètres. On peut donc extraire cette quantité de certains rapports d'intensité de raies, en l'occurrence, entre la raie de résonance w de l'Ar^{16+} et des raies satellites diélectroniques de l'Ar^{15+} (les raies k et $n = 3$). Par ailleurs, l'effet Doppler gouverne deux caractéristiques des raies spectrales: i/ toute raie a une largeur non nulle qui dépend de la température des ions émetteurs et ii/ un décalage par rapport a son énergie (ou, de façon équivalente, sa longueur d'onde) théorique causé par la vitesse d'ensemble des ions émetteurs dans la direction d'observation.

Afin d'extraire le plus d'information possible d'un spectre en énergie, ou en longueur d'onde, nous avons besoin d'un spectromètre présentant certaines caractéristiques spécifiques. L'écart en longueur d'onde entre les deux raies aux deux extrémités du spectre d'Ar XVII est très petit, soit $\sim 5 \times 10^{-12}$ m, et l'espacement entre les raies les plus proches est encore plus petit, de l'ordre de $\sim 10^{-13}$ m. La largeur des raies est

également faible et de grandes différences d'intensité sont attendues entre les raies provenant des ions auxquels nous nous intéressons ici, à savoir Ar^{15+} et Ar^{16+}. Le spectromètre doit donc être capable de séparer ces raies très rapprochées dans une gamme étroite d'énergie, tout en mesurant un grand nombre de photons. Les plasmas de tokamak étant fortement inhomogènes, plusieurs lignes de visée sont nécessaires pour diagnostiquer de façon détaillée les grandeurs physiques mentionnées ci-dessus. Enfin, tous les composants de l'instrument doivent pouvoir fonctionner de manière fiable au fil du temps dans un environnement de tokamak. Tous ces critères ont été pris en compte lors de la conception du diagnostic.

Nous décrivons dans le deuxième chapitre tous les composants du spectromètre sur lequel cette thèse est basée, un spectromètre X à cristaux imageurs (XICS). L'élément le plus important d'un spectromètre est l'élément de dispersion en longueurs d'onde car son choix détermine non seulement la gamme d'énergie des photons mesurés, mais aussi la résolution spectrale du diagnostic. Il doit également être adapté à la mesure de l'émission d'impuretés à faible concentration dans un plasma. Pour ce faire, nous utilisons des cristaux de Bragg. La réflexion de Bragg est le moyen le plus courant de sélectionner les énergies de rayons X autour de 1 keV, où elles sont très efficaces. En effet, l'utilisation d'un cristal peut permettre d'atteindre une résolution en longueurs d'onde de $\Delta\lambda/\lambda \approx 10^{-4}$, ce qui convient parfaitement à un très petit espacement des raies spectrales. Un cristal de Bragg diffracte les photons incidents comme des miroirs mono-énergétique et mono-angulaire. Trois cristaux de Bragg différents sont montés sur le spectromètre afin de mesurer trois spectres différents provenant de trois espèces ioniques différentes (Ar XVII, Ar XVIII et Fe XXV). L'approximation du miroir n'est toutefois pas suffisamment rigoureuse car la diffraction de rayons X est faite par l'ensemble du volume du cristal. Pour déterminer cet effet, nous avons calculé la courbe de balancement d'un cristal proche de ceux utilisés sur le spectromètre. Une courbe de balancement est une distribution en intensité d'un faisceau de longueur d'onde en fonction de son angle d'incidence par rapport à un élement de diffraction. Elle nous enseigne que le rendement des photons diffractés est inférieur à un et que la diffraction induit un élargissement en énergie des raies spectrales. Nous avons ensuite détaillé la configuration dans laquelle est installé le XICS et permettant de focaliser tous les photons de même énergie sur toute la largeur du détecteur et de créer une image symétrique du plasma sur sa hauteur. La focalisation des longueurs d'onde est modélisée en calculant dans notre configuration spécifique la position exacte de leur mesure sur la largeur du détecteur et ce pour un cristal fabriqué en un bloc ou en deux moitiés. En effet, les cristaux utilisés sont fabriqués en deux moitiés identiques et cela entraîne un dédoublement des raies du spectre. Grâce à la réalisation d'un diagnostic synthétique, nous avons pu également mettre en évidence les résolutions spectrale et spatiale de l'instrument de l'ordre de $\Delta\lambda/\lambda \sim 10^{-4} - 10^{-5}$ et du centimètre respectivement. Les procédures d'installation et d'utilisation du diagnostic sont décrites, en commençant par la procédure d'alignement des composants en lumière visible et les injections de gaz d'argon nécessaires aux mesures. Aucun étalonnage ni spectral ni en brillance n'a été réalisé à la mise en service de l'instrument, ce qui ne permet pas d'avoir une connaissance complète de la fonction d'instrument avant

cette thèse.

La procédure de modélisation des spectres repose sur un traitement en deux dimensions des images mesurées. Tout d'abord, une étape de conversion des axes des images est mise en place afin de rectifier les raies spectrales en échelle de longueurs d'onde et d'angle vertical des lignes de visées du diagnostic par rapport au plan méridien du tokamak. Ensuite, un filtrage automatique de la valeur de chaque pixel pour chaque image est fait en fonction du rapport signal/bruit. Une fois ces opérations réalisées, une fonction multi-gaussienne est utilisée afin de modéliser toutes les raies spectrales d'un même spectre. Des conditions initiales en terme de longueurs d'ondes théoriques sont ajoutées à l'algorithme de traitement pour améliorer les résultats. Le choix de modéliser le fond Bremsstrahlung séparément du spectre discret est aussi détaillé car on montre que les régions spectrales du spectre d'Ar XVII présentent des raies non identifiées. Une fois la modélisation du fond Bremstrahlung effectuée, celui-ci est soustrait du spectre et permet une meilleure modélisation des raies d'argon et de tungstène. Enfin, nous présentons une méthode d'inversion tomographique qui est appliquée aux raies spectrales. Cette méthode permet de reconstruire le profil d'émissivité d'une raie le long de la ligne de visée. L'utilisation de l'équilibre magnétique du plasma est alors nécessaire afin de construire une matrice géométrique correspondant au mieux aux lignes de visée du diagnostic. Cependant, une discussion est faite sur la précision de ce calcul d'équilibre magnétique et de l'erreur induite sur les profils d'émissivité radiale. Nous montrons qu'un écart de l'ordre du centimètre sépare la position de l'axe magnétique de celle de l'axe de symétrie des profils intégrés d'intensité de raies. Ceci est vérifié par la reconstruction de profils intégrés sur les lignes de visée à partir des émissivités, où un décalage non systématique est mesuré.

Le troisième chapitre de cette thèse traite des différents résultats que l'on peut déduire du spectre d'Ar XVII. A la différence de spectres similaires montrés dans la littérature, les premiers spectres d'Ar XVII mesurés pendant la première campagne instrumentale du diagnostic présentaient un dédoublement des raies systématique. Comme nous devons extraire l'amplitude, la largeur et la position des raies sur le détecteur pour calculer les température électronique et ionique, ainsi que la vitesse de rotation toroïdale, il est très compliqué de traiter les raies doublées car nous ne comprenons pas encore entièrement ce phénomène. Ce dédoublement de raies peut être décrit à l'aide de deux paramètres, un rapport de coups R et un décalage spectral $\delta\lambda_{LD}$ entre les lignes doublées. Trois causes principales sont identifiées : la fabrication des cristaux en deux moitiés, un non-parallélisme entre la surface optique (externe) du cristal et le réseau cristallin dû au processus de fabrication et les déformations internes de la maille dues aux variations thermiques auxquelles les cristaux sont exposés. Ces hypothèses doivent être étudiées car, en fin de compte, ces causes probables de déformation des cristaux peuvent affecter la courbe de balancement réelle, induire un décalage des raies spectrales et donc fausser les quantités physiques extraites. Le rapport de coups R entre les deux composantes des raies dédoublées rend les calculs de température électronique très difficiles et le décalage spectral $\delta\lambda_{LD}$ s'ajoute au décalage Doppler. Les estimations de la vitesse de rotation toroïdale du plasma peuvent en être alors faussées. Un cristal asymétrique présente un défaut de

coupe caractérisé par un angle α entre la surface optique et les plans réticulaires. Ce défaut incline l'ensemble de la maille et la direction du vecteur réciproque du réseau. Cela conduit à la création d'une première composante du décalage angulaire $\Delta\theta_1^{\alpha}$. Une autre composante provenant des variations de température ambiante est ajoutée: la modification de l'espacement inter-réticulaire d_{hkl} par expansion thermique ($\Delta\theta_3^T$).

Des considérations géométriques simples permettent de montrer que le défaut de coupe modifie la position du foyer méridional, en changeant la valeur de l'angle de Bragg de référence du cristal. Il affecte ainsi la position idéale du détecteur, caractérisée par la distance cristal-détecteur $l_m(\alpha) = r_c.sin(\theta_B + \alpha)$. Chaque demi-cristal possède son propre défaut de coupe et pour le modéliser, nous considérons donc le double de la valeur indiquée pour l'ensemble du cristal. Ce problème de défaut de coupe induit une nouvelle distance cristal-détecteur $l_m(\alpha) = 2,2139$ m, soit une différence de $1,418$ mm avec celle du design initial. Cela signifie qu'une raie spectrale se retrouve décalée de huit pixels sur le détecteur, soit $\Delta\lambda \simeq 1.5$ mÅ, ce qui est cohérent avec les observations expérimentales. Il est démontré que ce défaut de coupe affecte directement la valeur du paramètre d'asymétrie dont dépend la courbe de balancement et affecte à la fois sa largeur à mi-hauteur et sa réflectivité intégrée. En revanche, la limite maximale du défaut de coupe qui est rapportée par le constructeur ne devrait pas modifier de manière significative la courbe de balancement pour les longueurs d'onde étudiées. Pour un défaut de coupe d'un angle $\alpha = \pm 1,5' = \pm 0,025°$, des variations très faibles de moins de 2% sont attendues pour les paramètres de la courbe de balancement.

En s'intéressant ensuite aux déformations d'ordre thermique des cristaux, une étude citée en bibliographie a estimé l'effet de la température sur la diffraction spectrale d'un cristal utilisé sur le XICS du tokamak Alcator C-Mod. La température affecte le réseau cristallin et provoque un décalage spectral. Dans cette étude, les auteurs ont constaté qu'une différence de température d'environ 12 °C provoque un décalage spectral de l'ordre d'un pixel sur toutes les raies spectrales observées sur leur détecteur. En exposant les équations reliant l'espacement inter-réticulaire avec une variation de température, une variation $\Delta T = 10$ °C de la température du cristal peut modifier l'espacement inter-réticulaire d'environ $0,328 \times 10^{-3}$ Å, ce qui équivaut à une modification de la direction de diffraction d'environ $0,182 \times 10^{-3}$ radians. Nous montrons par le tracé de plusieurs courbes de balancement, pour des déformations thermiques correspondant à un intervalle de variation de 20°C, que des décalages spectraux de $\pm 5 \times 10^{-4}$ Å sont attendus. Dans notre cas, cette erreur est du même ordre de grandeur que la résolution spectrale du spectromètre, mais quatre fois plus petite que l'espacement entre les raies les plus proches mesurées ($\Delta\lambda$(q, r) = $2,1 \times 10^{-3}$ Å). Les variations de température des cristaux sur WEST restent cependant faibles grâce à un système actif de refroidissement par eau placé sous la boîte à cristaux. Malgré cette contre-mesure, la diffusion de la température à travers les supports successifs des cristaux peut ne pas être optimale. En outre, les sources de variation de température comprennent non seulement les conditions météorologiques ambiantes (et les cycles hiver-été), mais aussi l'exposition au rayonnement du plasma qui, sur WEST, peut durer plusieurs minutes.

À ce stade, nous avons estimé que la composante $\Delta\theta_1^{\alpha}$ est une des deux principales causes du décalage spectral observé, avec la fabrication des cristaux en deux parties. Nous savons également qu'un chauffage différentiel des deux moitiés de cristal pourrait rendre ce décalage spectral non constant dans le temps. Enfin, la fabrication des cristaux en deux moitiés double également les spectres dû à la non-tangence de leur sommet sur la sphère de Rowland. Afin de modéliser la dépendance spectrale du dédoublement des raies, nous utilisons la relation géométrique qui régit la position du faisceau de rayons X diffracté sur le détecteur, selon la géométrie du XICS, en ajoutant les effets du défaut de coupe et des variations thermiques. Nous sélectionnons une vingtaine de décharges plasma de la campagne expérimentale de WEST durant laquelle les deux demi-cristaux étaient face au plasma et dont sont extraits des données expérimentales pour les paramètres de décalage spectral et de rapport de comptage. Cette étude nous permet de déduire le jeu des paramètres qui décrit le mieux les cristaux utilisés et le spectre dédoublé. Afin de quantifier la variation de $\delta\lambda_{LD}$ sur l'ensemble du domaine spectral avec le cristal d'Ar XVII ([3.93, 4.01] Å), nous avons choisi de modéliser indépendamment trois zones spectrales correspondant à cinq raies spectrales d'argon. Chaque zone spectrale d'intérêt est ainsi modélisée par une fonction multi-gaussienne prenant en compte les paramètres de dédoublement de raie $\delta\lambda_{LD}$ et R qui affectent respectivement le décalage Doppler et l'intensité de la raie considérée. A partir des données, on peut voir que les dépendances en longueurs d'onde des deux paramètres ne sont pas identiques. Afin de décrire le décalage spectral de $\delta\lambda_{LD}$, les relations géométriques qui régissent la position du faisceau de rayons X diffracté sur le détecteur par chaque moitié de cristal nous permettent de modéliser la dépendance de ce paramètre sur toute la gamme spectrale et de confronter ces résultats aux données expérimentales. Il est montré que notre modèle donne une description très précise du paramètre de décalage spectral et des valeurs optimales de défaut de coupe et de variations thermiques, $\alpha = 0.978'$ et $\Delta T = 0\,°C$ respectivement. Le nombre considérable de points expérimentaux permet d'effectuer une comparaison statistique entre le modèle et les données et de conclure sur les principales causes du dédoublement de raies. La fabrication des cristaux en deux moitiés et leur défaut de coupe en sont les principales causes. En revanche, rien ne nous permet aujourd'hui d'expliquer le rapport de coups R. La piste privilégiée mène à des défauts cristallins non-homogènes entre les deux moitiés de cristal. De plus, nous introduisons un résultat intéressant concernant des variations pour ce paramètre R en fonction de la température électronique pour laquelle les spectres ont été mesurés. Nous montrons que le rapport de coups dépend de la température électronique et que plus elle est forte, plus le paramètre R tend vers 0. Une solution simple est enfin apportée pour supprimer ce dédoublement des raies, en cachant un des deux demi-cristaux faisant face au plasma. Cette solution permet de retrouver la fonction instrumentale optimale du diagnostic, au détriment de la surface de diffraction des cristaux et de la sensibilité du diagnostic.

Un exemple de spectre sans dédoublement de raies est ensuite montré, où les raies peuvent être modélisées et dont les intensités, largeurs et longueurs d'onde sont extraites pour calculer respectivement les températures électroniques, ioniques et la

vitesse de rotation toroïdale. Nous commençons par montrer les profils de vitesse de rotation pour un plasma ohmique, uniquement soumis à un chauffage résisitif dû au courant induit par le solénoïde central, dont la température électronique n'excède généralement pas 2 keV. L'estimation des décalages des raies se fait par le calcul de leur position sur l'échelle des longueurs d'onde. Au cours de la transformation des axes des images 2D, les raies spectrales sont redressées afin de traiter les spectres en deux dimensions. En fonction de leur position sur la largeur du détecteur, la position d'une raie donne le décalage Doppler par rapport à la colonne de pixels correspondant à sa longueur d'onde de repos. A partir de deux profils de vitesse de rotation pour deux raies d'argon, les vitesses de rotation apparentes apparaissent très élevées au centre du plasma, $|V_p| \geq 100$ km/s, ce qui est plus important que prévu pour les plasmas de WEST dans lesquels il n'existe aucune source significative de quantité de mouvement injectée comme par exemple avec du chauffage Neutral Beam Injection (NBI) (ou faisceau d'injection de neutres). Les valeurs relatives de la vitesse de rotation ne sont pas fiables en raison de l'incertitude qui subsiste quant à l'emplacement exact de la caméra par rapport au cristal, c'est-à-dire sans étalonnage spectral. Plusieurs méthodes pourraient être mises en œuvre pour réduire cette incertitude, notamment avec un étalonnage spectral absolu ou une métrologie par laser sur la caméra. En tenant compte de ce défaut, nous devrions nous attendre à des profils de décalage Doppler similaires pour toutes les raies d'argon, mais une différence d'environ 22 km/s est observée entre les deux profils étudiés. Cette différence pourrait être due à des phénomènes de transport physique affectant différemment les états d'ionisation de l'argon dans le plasma. Une autre source de cette différence pourrait être l'angle différent par rapport à la direction toroïdale de la ligne de visée (Line Of Sight (LOS)) associée aux deux extrémités du spectre. Enfin, des imprécisions dans la cartographie des longueurs d'onde sur la caméra, dues à des incertitudes sur la position de la caméra, pourraient également contribuer à cette divergence. Les profils de vitesse de rotation restent alors inutilisables à l'heure actuelle sans moyen d'étalonnage spectral ou de métrologie.

La température ionique est extraite de l'élargissement Doppler des mesures intégrées sur une ligne de visée, en fonction du carré de la largeur de la raie $\propto \Delta\lambda_D^2$. Grâce à des travaux cités en bibliographie, nous avons convenu qu'utiliser la largeur du duo de raies $j+z$ donne moins d'incertitudes sur l'estimation de T_i par rapport à la raie de résonance de l'argon He-like, qui est pourtant la plus intense du spectre. Cependant, elle possède des raies satellites très rapprochées en longueurs d'onde, pouvant se mêler à elle et simuler un élargissement supplémentaire de la raie de résonance pendant sa modélisation. Nous montrons deux profils de température ionique extraits de la raie de résonance et du duo de raies $j+z$ où le premier est systématiquement plus élevé que le second de l'ordre de 100 eV tout le long du profil. La comparaison de nos profils expérimentaux de température ionique est possible avec un calcul effectué avec la base de données WEST et en utilisant les flux de neutrons issus de la fusion D-D pour calculer T_i à l'aide des simulations du code Minute Embedded Tokamak Integrated Simulator (METIS). Les deux estimations de T_i donnent alors des valeurs semblables lors des phases ohmiques du plasma étudié mais une différence de

l'ordre de 300 eV pendant la phase de chauffage . Des efforts supplémentaires doivent être menés afin de réduire les incertitudes des deux calculs pour converger vers une estimation de T_i plus fiable encore.

L'émissivité d'une raie est fonction de la densité de l'ion émetteur n_Z et des électrons n_e, de l'abondance fractionnelle de l'état d'ionisation de l'ion $f_{Z,\zeta}$ et du coefficient d'émission de photons de la raie considérée. Les deux derniers termes dépendent de la température des électrons du plasma. Nous avons vu que la température des électrons peut être extraite des rapports de raies spectrales provenant d'états d'ionisation voisins. Le rapport de raies le plus sensible au changement de température électronique est entre la raie satellite diélectronique k et la raie de résonance w. Le deuxième rapport le plus sensible est celui entre les raies satellites diélectroniques $n = 3$ et la raie w. En utilisant les fichiers de coefficients d'émission de photons pour les états d'ionisation Ar^{15+} et Ar^{16+}, les sensibilités théoriques à la température pour les deux rapports de raies $R^{th}_{k/w}$ et $R^{th}_{(n=3)/w}$ sont calculées et comparées aux rapports de raies expérimentaux de XICS. Le rapport de raies $R^{exp}_{k/w}$ donne systématiquement une estimation différente de la température électronique par rapport au second. Deux explications sont possibles. Soit l'intensité de la raie de résonance est surestimée, soit les données atomiques que nous utilisons pour calculer les rapports théoriques des raies, à partir desquels nous déduisons la température, ne sont pas optimales. Cette dernière explication est difficile à démontrer, car elle nécessiterait de tester plusieurs codes de physique atomique et de comparer leurs résultats avec les données expérimentales - un sujet d'étude à part entière. La deuxième impliquerait la contribution des électrons supra-thermiques, des électrons de hautes énergies au sommet de la fonction de distribution électronique maxwellienne, qui augmentent l'intensité de la raie de résonance dans le cas de plasmas à faible densité électronique et/ou de plasmas chauffés par des ondes radio-fréquence (). Or pour l'exemple présenté, aucun de ces cas ne correspond. D'autres études pourront être menées sur ce sujet, en tenant compte d'une caractérisation complète de la fonction de distribution en énergie des électrons dans ce type de décharges ohmiques. Nous comparons ensuite les températures électroniques issues des deux rapports de raies du XICS avec celles déduites des mesures du radiomètre Electron Cyclotron Emission (ECE). Le rapport $R^{exp}_{(k)/w}$ donne une estimation de la température plus proche des mesures ECE pour le centre du plasma. Cependant, un phénomène de saturation de l'estimation faite avec ce rapport est rapportée lorsque la température dépasse 2 keV. Pour analyser cela plus en détail, nous prenons le cas d'une deuxième décharge plasma où la température électronique s'élève jusqu'à 3.8 keV selon les mesures ECE. Pour ce plasma, deux résultats peuvent être soulignés. Lors du chauffage Lower Hybrid (LH) durant lequel T_e atteint un plateau à 3.1 keV, les mesures de T_e avec le rapport de raies $R^{exp}_{(n=3)/w}$ sont déformées par une contribution des électrons supra-thermiques augmentant l'intensité mesurée de la raie de résonance et donc abaissant l'estimation de T_e. Concernant le deuxième rapport de raies, il plafonne à 1 keV pendant la phase LH et varie de manière symétrique dans le temps par rapport aux valeurs de l'ECE. En traçant les distributions des valeurs de températures entre données XICS et ECE, on constate tout d'abord deux branches pour le rapport $T_e((n = 3)/w)/T_e(ECE)$ correspondant

à l'effet des électrons supra-thermiques pendant le chauffage LH. Pour ce qui est du rapport $T_e((k)/w)/T_e(ECE)$, on remarque que $T_e((k)/w)$ sature nettement pour des valeurs de températures de 1.8-1.9 keV. On soupçonne donc la présence de raies spectrales supplémentaires dans le voisinage immédiat de cette raie, et notamment provenant d'états d'ionisation du tungstène, ce qui a pour conséquence de fausser la modélisation de la raie d'Ar^{15+} k.

En plus de trois raies de W^{43+} et W^{44+} déjà identifiées grâce à la littérature, une multitude d'autres raies d'intensité plus faibles sont remarquées. L'étude des spectres et des déformations des raies d'argon mettent en évidence trois raies supplémentaires de W^{43+}, W^{44+} et de W^{45+}, déjà identifiées par le passé par des articles cités en bibliographie. En revanche, l'ajout de ces nouvelles raies dans l'algorithme de traitement ne permet pas de résoudre la modélisation de la raie d'argon k. Il est alors avancé que la région spectrale étroite autour de cette raie serait peuplée d'une voire plusieurs autres raies de faible intensité, potentiellement provenant d'ions de tungstène et/ou d'autres impuretés. Cependant, la résolution spectrale du diagnostic ne permet pas une identification formelle ni du nombre de raies impliquées ni de leur provenance. Nous sommes également limités puisqu'il est difficile sur WEST de pomper efficacement toute la concentration en argon dans l'enceinte à vide, ce qui ne permet pas de mesurer le même intervalle de longueur d'onde en l'absence de raies d'argon. Il est toutefois possible d'étudier les trois raies de tungstène W^{43+} $Ga-3$, W^{43+} $Zn-2$ et $Zn-3$ préalablement identifiées, Nous montrons, à partir de rapports de raies croisés, que le rapport des raies $Zn-3/Zn-2$ est constant sur une large gamme de température électronique, $T_e = [2.4, 3.8]$ keV, alors que ce n'est pas le cas pour le rapport $Zn-2/Ga-3$. Ce résultat est important car les raies spectrales $Zn-3$ et $Zn-2$ sont émises par le même état d'ionisation du W. Cela démontre que les Photon Emission Coefficient (PEC) des deux raies du même état d'ionisation du W^{43+} ont la même dépendance en température électronique dans cet intervalle, contrairement à des raies d'état d'ionisation voisin. Néanmoins, la dépendance en température du rapport $Zn-2/Zn-3$ est beaucoup plus faible que celle du rapport k/w de l'argon et ne peut pas être utilisée comme diagnostic de température.

L'identification et l'interprétation des raies spectrales du tungstène ne permettent pas encore d'extraire des profils de paramètres du plasma aussi utiles que les profils de température électronique par exemple. Cependant, elles peuvent être utilisées pour réaliser un transfert d'étalonnage en brillance à partir d'un autre spectromètre Vacuum Ultra-Violet (VUV) de WEST vers le diagnostic XICS. Ce spectromètre VUV est déjà calibré en brillance et est capable de mesurer des raies spectrales de W provenant des espèces ioniques W^{42+} à W^{45+} dans le domaine spectral [120, 160] Å. Une telle procédure a déjà été réalisée sur WEST mais entre deux spectromètres avec les mêmes raies spectrales mesurées. L'étude est faite sur les raies respectives du W^{44+} car elles sont très intenses et bien résolues en longueurs d'onde sur les deux spectres des deux diagnostics. Nous mettons également en équation la relation d'équivalence en brillance entre les mesures de brillance du Spectromètre à Incidence Rasante (or Grazing Incidence Spectrometer) (SIR) et celles en coups par unité de temps du XICS. Le but de la procédure est donc de déterminer un coefficient de calibration en

brillance. Pour cela, et en raison des différentes dépendances en température des PEC des raies sélectionnées, nous devons déterminer une fonction commune à chacun des PEC pour simplifier l'expression de la brillance. Pour cet état d'ionisation du tungstène, nous pouvons extraire une abondance maximale $f_{Z,max}$ et la température associée $T_{Z,max}$. On détermine ainsi une gamme de température dans laquelle l'état d'ionisation est dominant. Une valeur moyenne pour chacun des PEC est calculée de sorte que le coefficient de calibration ne soit plus qu'une fonction de la brillance des raies sélectionnées sur le SIR, de l'intensité des raies mesurées sur le XICS et des valeurs moyennées des PEC. Les géométries des diagnostics sont suffisamment différentes pour qu'il ne soit pas aisé de trouver des lignes de visée identiques aux deux spectromètres. Pour des raisons instrumentales, l'intervalle radial dans lequel cette méthode est applicable est restreint au domaine radial défini par $\rho_{tor} > 0.2$. On calcule ensuite les intersections de chaque ligne de visée avec toutes les surfaces de champ magnétique en utlisant les données de l'équilibre magnétique reconstruit. Les lignes de visée traversent une multitude de surfaces de champ et pour chacune d'entre elles, nous pouvons déterminer les valeurs de ρ_{tor} traversées pour chaque élément d'une ligne et la distance entre des surfaces voisines. La valeur minimale de ρ_{tor} pour chaque ligne de visée définit le paramètre d'impact. La comparaison des lignes de visée des deux diagnostics peut maintenant être effectuée dans cette gamme avec cette méthode. Plusieurs valeurs de brillance pour le spectromètre SIR et d'intensité pour le XICS sont relevées pour plusieurs instants d'un plasma cible, pour des paramètres d'impact similaires. Avec cette méthode, nous calculons enfin un coefficient d'étalonnage en brillance pour le spectromètre XICS.

Grâce à cet étalonnage en brillance, le diagnostic XICS permet d'obtenir les brillances de raies de différents états d'ionisation intégrées le long des lignes de visée. La brillance est proportionnelle à l'intégrale de l'émissivité d'une raie le long d'une ligne de visée, elle est donc fonction de la densité de l'ion émetteur. L'accès à ces brillances permet donc d'estimer les densités d'argon et de tungstène à partir des mesures XICS. Pour extraire l'information sur la densité d'impuretés à partir de la brillance, nous devons récupérer les mesures intégrées des température et densité électronique, ainsi que les abondances fractionnelles de l'ion émetteur et le PEC de la raie observée. Sur la base du calcul des surfaces magnétiques traversées par les lignes de visée, une interpolation est effectuée pour obtenir les profils de n_e, T_e, f_{W44+} et $PEC(\lambda)$ le long des lignes de visée des XICS. On peut calculer le triple facteur de n_e, f_{W44+} et $PEC(\lambda)$ dont dépend la brillance. Une approximation peut être faite sur la région radiale restreinte d'émission des impuretés dans le plasma où le triple facteur être considéré comme constant pour le tungstène pour $\rho_{tor} \leq 0,3$ et pour l'argon pour $\rho_{tor} \leq 0,5$. La densité moyennée par ligne de visée des impuretés $\overline{n}_Z$ peut être calculée en fonction de la brillance des raies et de l'intégrale sur les lignes de visée du triple facteur n_e, f_{W44+} et $PEC(\lambda)$. La concentration moyennée de l'impureté $\overline{c}_Z$ est ensuite obtenue en divisant $\overline{n}_Z$ par la densité moyennée électronique $\overline{n}_e$ pour la zone radiale d'émission de l'impureté. Deux décharges plasma sont étudiées pour déterminer ces densités et concentrations d'argon et de tungstène. Les valeurs déduites pour une décharge plasma typique de WEST sont: $n_{Ar^{16+}} \approx 4.2 \times 10^{15}\mathrm{m}^{-3}$, $c_{Ar^{16+}} \approx 7.8 \times 10^{-5}$,

$n_{W^{44+}} \approx 5.3 \times 10^{15}\mathrm{m}^{-3}$ and $c_{W^{44+}} \approx 9.5 \times 10^{-5}$. Nous avons vérifié que ces valeurs sont compatibles avec des publications antérieures concernant WEST. Nous portons enfin l'étude sur un plasma qui a connu une rupture soudaine après seulement 5 secondes due à une injection massive d'argon. Le rapport d'expérience mentionne un défaut de vidage d'une ligne d'injection devant servir à injecter de l'Hélium mais où se trouvait encore une très grande concentration de gaz d'argon. Cet quantité massive d'argon dans la ligne a été injecté avant le début du plasma et la concentration d'argon calculée avec les mesures du XICS s'élève jusqu'à $c_{Ar^{16+}} \approx 0.01$, entraînant inévitablement une fin prématurée du plasma à cause du fort rayonnement de l'argon dans le plasma.

Remerciements

J'aimerais commencer ces remerciements en étant tout à fait honnête en avouant je trouve difficile de mettre des mots sur cette expérience. Je ne suis pas naturellement très expansif, mais comme le dit l'adage, ce n'est pas la longueur qui importe. J'ai rédigé ces lignes à la toute fin du manuscrit, dans un moment de réflexion sur les années consacrées à cette thèse, sur les accomplissements et les défis surmontés, sur ma propre évolution et sur les rencontres enrichissantes faites en chemin. C'est donc à toutes les personnes qui ont contribué à l'élaboration de ce travail que je dédie cette section de remerciements.

Je voudrais remercier tout d'abord les membres du jury qui ont pris le temps de s'intéresser au travail que j'ai réalisé pendant ces trois ans de thèse. Merci à mes deux rapporteurs, Dr. Jean-Christophe Pain et Dr. Frank Rosmej, pour le temps qu'ils ont consacré à améliorer la qualité de mon manuscrit. J'apprécie énormément l'attention que vous m'accordez. Merci au Dr. João Santos pour avoir accepté de présider ce jury et pour son enseignement pendant toutes ces années à l'Université de Bordeaux dans le Master Noyaux, Plasma et Univers (NPU). Votre attention me touche particulièrement. Merci également au Dr. Francesca Bombarda avec qui j'ai eu le plaisir de longtemps échanger durant ma thèse et pour avoir contribué à la qualité de ce travail. C'est également un honneur de vous compter comme membre de mon jury. Mes remerciements au Dr. John Rice qui a accepté d'être présent le jour de ma défense et de juger mon travail. Cela compte également beaucoup pour moi.

Didier, Rémy, Rémi, vous faites également parti de ce jury mais je ne serais pas là aujourd'hui sans votre aide durant ces trois années. Mes travaux, mon manuscrit et mon évolution pendant ces trois années vous sont dus. Je ne pourrai jamais assez vous exprimer ma gratitude et l'affection que je peux vous porter. Merci pour tout vraiment.

Une grosse pensée pour tous mes collègues du deuxième étage, vous avez fait partie intégrante de ma vie pendant ces trois ans. On a partagé d'excellents moments ensemble et je vous remercie d'avoir si généreusement mangé les produits exotiques que j'ai pu vous apporter pour le petit-déjeuner. J'espère que vous trouverez un remplaçant pour cette si ardue tâche de vous sustenter.

Une pensée aussi pour le Dr. Pierre Forestier-Colleoni qui va prendre mon relais comme responsable du diagnostic. Merci d'avoir pris de ton temps de m'aider à la rédaction de ce manuscrit, tu n'y étais pas obligé mais j'apprécie grandement ton aide. Je te souhaite beaucoup de succès et de grands résultats avec cet instrument mais de ne pas trop t'arracher les cheveux quand même comme j'ai pu le faire.

Merci à toutes les personnes de l'institut et du Commissariat aux Énergies Atomiques et aux Énergies Alternatives (CEA) que j'ai pu rencontrer, travailler ou discuter

avec et avec qui j'ai pu faire partie de la grande famille WEST. Je ne vais pas vous citer tous mais je me souviendrai de vous tous quand je partirai sous d'autres horizons.

Une grosse dédicace à tous les copains d'Aix et tous mes colocataires que j'ai pu y avoir, Tonton Tibalt, Alex, Gaëtan, Dylan, les Ladies, Arnaud, Pierre, Babs, pour ne citer que vous. Ça a été trois superbes années passées à vos côtés, je me souviendrai toujours des Savims que l'on a partagé, des soirées à Marseille jusqu'à pas d'heures, de tout. Qu'importe où j'irai plus tard, on continuera à se voir promis.

À Lulu, Dédé, Titi, Goutz, Mané, toute l'équipe du festival Sur Mon Glaçon (SMG) et à tous les autres aussi à qui je pense fort. La vie nous a séparé aux quatre coins de France, ou même du monde par moment, mais on se retrouve toujours immanquablement chaque été et chaque hiver pour notre festival, comme si on ne s'était jamais quitté. Cette thèse, elle est aussi pour vous. Je n'ai pas pu être aussi souvent à vos côtés ces dernières années et spécialement ces derniers mois mais l'amitié, ça ne se perd pas. Merci les gars.

Et enfin, last but not least, merci à ma famille, tout le monde sans exception, pour m'avoir soutenu, encouragé, et bien d'autres choses encore depuis aussi longtemps que je m'en souvienne. Cela vaut aussi à ceux et celles qui nous ont déjà quitté et qui ont participé à faire de moi l'homme que je suis. Vous m'avez toujours fait confiance et poussé malgré mes choix de vie et je n'écrirais sûrement pas ces lignes sans vous. J'espère que vous êtes fier de ce que j'ai pu faire et encore une fois merci !

Contents

Affidavit 2

Liste de publications et participation aux conférences 3

Abstract 4

Résumé 5

Résumé étendu 6

Remerciements 17

Contents 19

List of Figures 22

List of Tables 30

List of Acronyms 31

INTRODUCTION 35

1. Fusion, tokamak and radiation 39
- 1.1. Introduction . . . 40
- 1.2. Energy mix and magnetic confinement fusion . . . 40
  - 1.2.1. Status of the energy today . . . 40
  - 1.2.2. Thermonuclear processes . . . 42
  - 1.2.3. Power balance and ignition condition . . . 46
  - 1.2.4. The tokamak concept . . . 48
  - 1.2.5. The WEST tokamak . . . 51
- 1.3. Soft X-ray emission in WEST . . . 54
  - 1.3.1. Atomic processes . . . 55
  - 1.3.2. Ionization equilibrium . . . 62
  - 1.3.3. Population equilibrium . . . 64
  - 1.3.4. Ar XVII spectral lines identification . . . 66
  - 1.3.5. Line profiles . . . 75
- 1.4. Conclusions . . . 78

2. Ar XVII spectrum measurement and modelling 79
- 2.1. Introduction . . . 81

2.2. The XICS spectrometer . . . 81
2.2.1. X-ray photons diffraction by crystals . . . 82
2.2.2. Johann configuration of X-ray spectrometer . . . 90
2.2.3. X-ray photons measurement . . . 99
2.2.4. Diagnostic resolution power . . . 103
2.2.5. Limitations of the spectrometer . . . 107
2.3. Spectrometer commissioning . . . 109
2.3.1. Alignment . . . 110
2.3.2. Argon impurity injection . . . 112
2.3.3. Discussion on calibration methods . . . 113
2.3.4. Discussion about defective detector modules . . . 115
2.4. Spectral modeling . . . 117
2.4.1. Preparation of the data . . . 117
2.4.2. 2D images processing . . . 120
2.4.3. Tomographic inversions . . . 129
2.4.4. Discussion of the effect of magnetic equilibrium reconstruction on inverted amplitudes . . . 132
2.4.5. Discussion of the modelling of the Ar dielectronic satellite group of lines $n = 3$ and $n = 4$ . . . 135
2.5. Conclusions . . . 138

3. Ar XVII spectrum analysis **139**
3.1. Introduction . . . 140
3.2. Crystallographic study of Bragg crystals . . . 140
3.2.1. Line-doubling phenomenon during the first campaign . . . 141
3.2.2. Modelling of the spectral shift parameter . . . 148
3.2.3. Discussion on the count ratio parameter . . . 154
3.2.4. Discussion on a possible effect of heating system on the count ratio parameter . . . 155
3.3. Extraction of physical quantities from the Ar XVII spectrum . . . 156
3.3.1. Toroidal rotation velocity . . . 157
3.3.2. Ion temperature . . . 159
3.3.3. Electron temperature . . . 162
3.3.4. W impurity measurement . . . 169
3.3.5. Discussion on the role of the photon emission coefficients data 174
3.4. Experimental impurity density profiles . . . 177
3.4.1. Brightness calibration of the XICS spectrometer . . . 177
3.4.2. Mid- and high-Z impurity profiles . . . 188
3.4.3. Discussion on an alternative brightness calibration . . . 194
3.5. Conclusions . . . 196

SUMMARY **197**

Appendices 201

A. Scattering on a unit cell of the crystal lattice 202

B. Fourier coefficients of the crystal polarization 206

Bibliography 209

List of Figures

1.1. *World electricity production by source between 1990-2021 (Source: International Energy Agency (IEA) Electricity Information https://www.iea.org/data-and-statistics/data-product/)* 40
1.2. *(Top) World electricity consumption from 1990 to 2021 in TWh (Source: IEA Data Services https://www.iea.org/data-and-statistics/data-product/); (Bottom) Primary energy consumption by source in 2022 in kWH per person.* 41
1.3. *Indicators of a changing global climate: (a) Northern hemisphere spring averaged snow cover; (b) Arctic averaged sea ice etendue; (c) change in global mean heat content in upper oceans; (d) global mean sea level change [1].* 43
1.4. *Low-carbon electricity production by source in France between 1990-2022 (Source: IEA Electricity Information https://www.iea.org/data-and-statistics/data-product/)* 44
1.5. *Aston curves representing the averaged binding energy per nucleon as a function of the number of nucleons in the nucleus (Source: Public domain, https://commons.wikimedia.org/w/index.php?curid=1540082)* 44
1.6. *Cross-sections of the D-D, D-T and D-He^3 fusion reactions as a function of the Deuterium energy [4].* 46
1.7. *Sketch of the main tokamak components [7].* 48
1.8. *Geometry of a torus and its toroidal coordinate system with a circular poloidal cross-section [8].* 48
1.9. *WEST poloidal cross-section sketch with the PFCs location.* 52
1.10. *Theoretical He-like argon spectrum [28].* 54
1.11. *Energy level diagram for a given ion.* 60
1.12. *Fractional abundances of the Ar ionization stages as a function of the temperature [37].* 63
1.13. *Ionization balance between some neighbouring ionization stages, being populated and depopulated by recombination α_Z and ionization processes S_Z.* 63
1.14. *Collisional-Radiative model sketch with three different ionization stages $(Z-1, Z, Z+1)$ and their energy levels (n_h, n_{gr}, n_i, n_j). The elementary processes are represented with arrays.* 67
1.15. *Energy diagram for the n=1 and n=2 states for He-like ion species.* . . . 69

1.16. *Product of the PECs with the fractional abundance for (top) the He-like Ar resonance line w and (bottom) the forbidden line z, for* $n_e = 5.0\times10^{19}\ m^{-3}$ *and* $T_e \in [0.1, 4.3]$ *keV. The various components of the PECs, electron collisional excitation (blue) and ionization (red), dielectronic recombination (green), are multiplied with the fractional abundance of the corresponding ion species.* 72
1.17. *Energy level diagram of H-like, He-like and Li-like ions with the resonance transitions* I_R *and corresponding satellite transitions* I_S *[50].* . . 74

2.1. *Sketch of the process of diffraction of an incident wave of wavelength* λ *by different diffraction cones of step difference n.* 83
2.2. *Sketch of the Bragg diffraction process on a Bragg crystal of reciprocal vector* $\vec{B}_{hkl} = \vec{B}_H$ *defining the reticular planes of spacing* d_{hkl}. 83
2.3. *Sketch of a hexagonal mesh system with the length* (a, b, c) *and angular* (ϕ, ψ, χ) *parameters* 84
2.4. *Two possible diffraction directions for the X-ray photons in a crystal of thickness* t_0 *depending on the sign of the asymmetry parameter b.* . . . 86
2.5. *Rocking-Curve of an* α*-Quartz Bragg crystal of hexagonal mesh, Miller indices (1,1,0), for the He-like Ar resonance line wavelength* $\lambda_w = 3.9491$Å *[37].* 89
2.6. *Sketches of a) the Johann configuration and b) the Johansson configuration.* 90
2.7. *Sketches of a spectrometer in the Johann configuration with a spherically bent crystal.* 92
2.8. *Map of the Johann error computed with the Ar XVII crystal parameters in Table. 2.1.* 93
2.9. *Sketch of the XICS spectrometer geometry in the Johann configuration, in the single crystal approximation.* 94
2.10. *Sketch of the XICS spectrometer geometry in the Johann configuration considering a splitted crystal, both halves located next to each other.* . . 96
2.11. *Zoom on the crystal location in Fig. 2.10: the positioning of each half-crystal summit* S_1 *and* S_2 *according to the single crystal summit S on the curvature circle of origin O'. The unit vectors are shown for all the summits.* 97
2.12. *Exploded-view drawing of the Be window.* 100
2.13. *Transmission coefficient of (black) a Be (Z=4) window of 150 µm thick and (blue) of Fe (Z=26) bars of 1 mm thick.* 101
2.14. *Cross-section of the PILATUS3 detector system* [1]. 102
2.15. *Reverse ray-tracing computations with the XICS configuration (a) from a source point source on the Rowland circle at the meridional focus and (b) from two source points located close to the magnetic axis, 1 cm apart vertically.* 103

1. See https://www.dectris.com/ for more information

2.16. *Computed position and broadening of two close spectral lines from a simulated bi-chromatic plasma volume of emission with the detector at the Ar XVII meridional focus.* 104
2.17. *Intersection of the two reverse ray-tracing computations shown in Fig. 2.15 wit the detector outline (left) and (right) zoom on a reduced area to show the line spreading.* 105
2.18. *Plasma coverage by the XICS spectrometer in (top) the poloidal cross-section using 100 lines of sight covering the central part of the WEST vacuum vessel and (bottom) in the toroidal cross-section of WEST tokamak. The two colors represent the two wavelengths measured at the extreme edges of the detector.* 106
2.19. *Poloidal cross-section of WEST tokamak with the three positions of the sagittal foci for the three XICS crystals. The blue area represents the focus of simulated rays from the detector.* 108
2.20. *Left: Toroidal cross-section of the XICS spectrometer with a common position for all the crystals in the tokamak frame and the approximated position of the detector. Right: zoom in to the location of the detector to highlight the difference to the Rowland sphere and meridional foci.* . . 108
2.21. *Computed position and broadening of two close spectral lines on (top) the computed position of the detector and (bottom) its optimal location at the Ar XVII meridional focus.* 110
2.22. *Top view picture of the XICS instrument on WEST tokamak [37].* 111
2.23. *Time variation of the* Ar^{16+} *line-averaged concentration for the WEST* #59974 *and* #60000 *plasma discharges from the same experimental day of operation.* D_2*/Ar injection is marked with a green arrow for the* #59974 *discharge.* 113
2.24. *Comparison of the Ar spectral line positions on the detector between (top) a measured 2D spectrum and (bottom) a simulated one.* 114
2.25. *2D spectra measured for the (left) WEST* #55076 *plasma discharges at t = 55.8s with a line-doubling issue, cf. Sect. 3.2, and (right) WEST* #56683 *plasma discharges at t = 37.7s.* 116
2.26. *(a) Raw image measured for the WEST* #59975 *plasma discharge at t = 2.1 s and (b) associated spectrum taken for* 800th *row of pixels.* 118
2.27. *(a) Re-scaled image for the WEST* #59975 *plasma discharge at t = 2.1 s and (b) associated spectrum taken for* $\phi = 0.001$. 118
2.28. *Vertical angle* ϕ *that defines the lines of sight with respect to the toroidal plane* $Z = 0$. 119
2.29. *Geometric coverage of the diagnostic lines of sight in the poloidal cross-section (brown) and definition of the impact parameter. The black crosses define the intersections of the line of sight with the magnetic surfaces [37].* 120
2.30. *Automated pixel selection of the 2D XICS images. The color code displays the different values attributed to each pixel in all the horizontal bands (black lines).* 121

2.31. *Pre-plasma image recorded by the detector, showing multiple dead pixel and two (partly) defective modules* . . . 123
2.32. *WEST* #59920 *plasma discharge where three spectra are extracted at three different time acquisitions. The line intensities are in counts per time unit, of 200ms of integration, and in a logarithmic scale. The residual of the spectra modelling is shown in the lower sub-figure. Two spectral intervals are grayed out as they are not taken into account.* . . . 124
2.33. *Typical spectrum for the WEST* #59975 *plasma discharge at t = 10.13 s (black) fitted on the experimental points (blue dots) reduced by the Bremsstrahlung background (blue line).* . . . 125
2.34. *Smoothing induced by the number of vertical bins on a vertical section of the measured intensity of a line. 1467, 100 and 50 vertical bins are shown here.* . . . 127
2.35. *Sketch of B-splines functions* $B^{i,d}$ *of degree 2.* . . . 128
2.36. *Different smoothing of the signal obtained with 100 bins presented in Fig. 2.34 with 10, 14 and 20 B-splines functions applied over the height of the image.* . . . 129
2.37. *(Top left): Measured image on which (top middle) the fitting algorithm is applied and (top right) the corresponding residual map; (Bottom): Three spectra extracted from the fitted image and the associated residual profiles.* . . . 130
2.38. *Top: LOS-integrated and middle: inverted (middle) line intensity of the Ar XVII w and (n=3) lines for the* #57796 *WEST pulse at t = 20.5 s for a time integration of 600 ms; Bottom: radial electron temperature* T_e *computed with both* $(n = 3)/w$ *and* k/w *line ratios [37].* . . . 133
2.39. *Line-integrated (coloured) and retrofitted profiles (black) of the He-like resonance line w intensity for three different times of the WEST* #59920 *plasma discharge.* . . . 134
2.40. *Simulated Ar spectrum in the spectral range of the* $n = 4$ *and* $n = 3$ *dielectronic satellite groups of lines, computed with the Aurora code [35] and the Atomic data and Analysis Structure (ADAS) datasets [47] [48].* . . . 135
2.41. *Left: PECs of the spectral lines that belong to the* $n = 3$ *group of dielectronic satellite lines; Right: PEC ratios without variation over a large electron temperature range.* . . . 137
2.42. *Comparison of the two models used to fit the* $n = 3$ *and* $n = 4$ *groups of dielectronic satellite lines: single-Gaussian (blue) and multi-Gaussian (red) models.* . . . 137

3.1. *1D spectrum of the Ar XVII crystal and WEST* #55297 *pulse affected by line-doubling. The spectrum is extracted at t =* 6.5 *s, for a time integration of* 600 *ms. Measured values (black squares) and fitting results (black line) are shown superimposed. The fitting error is also shown below the 1D spectrum.* . . . 140

3.2. *Line-doubling phenomenon affecting the Ar XVII spectral lines, defined with a count ratio R and a spectral shift $\delta\lambda_{LD}$.* 141
3.3. *1/ Sketch of the Bragg diffraction with a perfect crystal of inter-reticular spacing d_{khl}. Two causes of angular offsets on the direction of diffraction are shown: 2/ non-parallelism between the optical surface and the layers characterized by a miscut angle α ($\Delta\theta_1^\alpha$ in blue) and the missing atoms of atomic layers (green dashed circles) also contribute to the total angular offset ($\Delta\theta_2^\alpha$ in green); 3/ thermal deformation of the inter-reticular spacing d_{khl} ($\Delta\theta_3^T$ in red) and a deformation of the total electronic cloud ($\Delta\theta_4^T$ in orange).* 142
3.4. *Rocking-Curve (Rocking-Curve (RC)) parameters curves as a function of the miscut angle α: angular width of the RC (red squares), integrated reflectivity (black dots) and asymmetry parameter b (blue diamonds). The curves are normalized to their value at $\alpha = 0$.* 145
3.5. *The original Rocking-Curve of the He-like Ar resonance line wavelength in Fig. 2.5 affected by a miscut angle of $\alpha \pm 300$ arcmin. The miscut value used is 200 times greater than the value specified in Tab. 2.1.* 145
3.6. *The inter-reticular spacing d_{hkl} versus the thermal variations affecting the crystal mesh.* 147
3.7. *Diffraction pattern of the He-like Ar resonance line wavelength (Fig. 2.5), affected by a thermal variation of $\pm 10\,^\circ C$.* 148
3.8. *Example of a spectrum measured with the XICS during the WEST #55076 shot where three spectral areas are selected to study the line-doubling effect experimentally:* [3.945, 3.955] Å *for the resonance line w,* [3.965, 3.975] Å *for the intercombination lines x and y and* [3.992, 3.998] Å *for the forbidden line z and satellite line j.* 149
3.9. *(Top) Experimental distribution of the spectral shift $\delta\lambda_{LD}$ as a function of the wavelength, overlaid with a best-fit model, and (bottom) the experimental values of the count ratio R parameter.* 152
3.10. *1D spectrum of the Ar XVII crystal and WEST #59975 pulse without line-doubling. This spectrum corresponds to a central electron temperature of $T_{e,0} = 1.1$ keV and a central electron density of $n_{e,0} = 3.8 \times 10^{19}$ m^{-3}.* . . 154
3.11. *(a) R values computed for the WEST shots detailed in Table 3.1 and for the w spectral range. Color code shows the Ion Cyclotron Resonance Heating (ICRH) plasma discharges in blue and the Lower Hybrid Current Drive (LHCD) plasma discharges in green and red. The electron temperature T_e measured with the ECE radiometer is thus plotted versus the toroidal radial coordinate ρ_{tor} during (b) the Ohmic heating phase and (c) during LHCD or ICRH heating.* 156

3.12. *Time traces of the WEST #59975 and #59920 plasma parameters. From top to bottom: plasma current I_P and LH power P_{LH}, radiated P_{rad} and Ohmic P_{ohm} power, integrated electron density measured by the central interferometer chord n_l, volume averaged $< n_e >$ and central $n_e(\rho = 0)$ electron density and electron temperature measured by the most central ECE channel.* 157
3.13. *Top: Non-calibrated toroidal rotation velocity profiles of the Ar^{16+} w and Ar^{15+} k lines for the WEST #59975 pulse at t = 6.914 s; Bottom: relative profiles from the resonance line w data to t = 2.1s.* 158
3.14. *Doppler broadening profiles extracted from the He-like Ar resonance line w and j + z feature for the WEST #59975 pulse at t = 1.46 s.* 160
3.15. *Time traces of the WEST #59920 plasma parameters. From top to bottom: plasma current (black) I_P and central electron density (orange) $n_{e,0}$, LOS-integrated ion temperature (green circle) $T_{i,0}$ computed with the j + z feature Doppler width and the METIS simulations (green star). The electron temperature measured by the most central ECE channel $T_{e,0}(ECE)$ (cyan) is plotted to give an estimation of T_e.* 161
3.16. *Time traces for the WEST #59920 plasma of the ion temperature (blue circle) $T_{i,0}$ computed with the j + z feature Doppler width and the METIS simulations (red star). The ratio between the two (black dot) is also shown in the right y-axis.* 161
3.17. *Theoretical line ratio of various He-like and Li-like Ar lines to the He-like Ar resonance line w as a function of the electron temperature [28].* . . . 162
3.18. *Ratios of the Ar^{15+} dielectronic satellite line n = 3 (red line) and Ar^{16+} dielectronic satellite line k (blue line) to the Ar^{16+} resonance line w as a function of the ECE electron temperature and comparison to the experimental line ratios (circles) with the WEST #59975 data.* 163
3.19. *Theoretical line ratios between the excitation part of the He-like and Li-like Argon lines.* 164
3.20. *Electron temperature profiles deduced from the ECE (green line) and the XICS measurements, with the k/w (blue) and (n = 3)/w (red) line ratios for the WEST #59975 data at t = 8.126 s.* 165
3.21. *Time traces of the WEST #59975 plasma parameters. From top to bottom: plasma current (black) I_P and central electron density (orange) $n_{e,0}$, electron temperature measured by the most central ECE channel $T_{e,0}(ECE)$ (cyan) and from the two XICS LOS-integrated line ratios $T_{e,0}(k/w)$ (red) and $T_{e,0}((n = 3)/w)$ (blue), and the LOS-integrated ion temperature (green circle) $T_{i,0}$ computed with the j + z feature width and the total neutron flux interpolation (green star).* 166
3.22. *Time traces of the WEST #59920 plasma parameters. From top to bottom: plasma current (black) I_P, LH power P_{LH} (green) and central electron density (orange) $n_{e,0}$, electron temperature measured by the most central ECE channel $T_{e,0}(ECE)$ (cyan) and with the two XICS LOS-integrated line ratios $T_{e,0}(k/w)$ (red) and $T_{e,0}((n = 3)/w)$ (blue).* 167

3.23. $R^{exp}_{(k)/w}$ and $R^{exp}_{(n=3)/w}$ line ratios variations with time for the WEST #59920 plasma discharge during LH heating. The time duration of the LH heating is plotted in black line. . . . 168
3.24. Comparison of the T_e deduced from both Ar line ratios to the ECE radiometer estimations. . . . 168
3.25. Two spectra extracted for the XICS central line of sight measured with the Ar XVII crystal and during the WEST #59920 for t = 3.3 and 8.1 s. All the Ar and W spectral lines referenced as initial guesses in the algorithm are marked with black arrows. . . . 169
3.26. Spectral areas of the spectrum Fig. 3.25 selected to highlight additional spectral lines (in red) measured (left) around the He-like Ar feature x + y and (right) close to the dielectronic satellite line k. . . . 170
3.27. Comparison of the T_e deduced from both Ar line ratios to the ECE radiometer estimations after the integration of the second Zn-3 spectral line in the algorithm. . . . 171
3.28. Spectral line ratios between (top) the W^{43+} Ga-3 and the W^{44+} Zn-2 and between (bottom) the W^{44+} Zn-2 and the Zn-3 spectral lines measured with the XICS diagnostic [37]. . . . 172
3.29. Fractional abundances of the W ionization stages as a function of the temperature [37]. . . . 173
3.30. (Top) Ratios of the W^{43+} Ga-3 and W^{44+} Zn-2 line intensities and comparison with the associated fractional abundances ratio; (Bottom) Ratios of the W^{44+} Zn-2 and Zn-3 line intensities and comparison with the PEC ratio [37]. . . . 174
3.31. Comparison of the PECs of the He-like Ar resonance line w from (blue and red) two different Open Atomic data and Analysis Structure (OPEN-ADAS) files, (green) AtomDB and (yellow) the work of Marchuk used at Wendelstein 7-X (W7-X) [28]. PEC ratios between each data source are also displayed in dashed and dotted black lines in the same temperature range. . . . 175
3.32. Comparisons of (n = 3)/w and k/w line ratios as a function of the electron temperature from two different dataset sources. . . . 176
3.33. Left: Spatial coverage of the SIR diagnostic in the WEST poloidal cross-section. The fixed mode is represented in red and in yellow the area covered by the LOS in oscillating mode. Right: Spatial coverage by the XICS lines of sight already shown in Fig. 2.18. . . . 178
3.34. SIR spectrum from WEST #54178 plasma discharge with four W spectral lines marked with black arrows [32]. . . . 179
3.35. PECs for the XICS W^{44+} Zn-2 spectral line at $\lambda = 3.971$Å (blue) and the SIR spectral line at $\lambda = 132.273$Å (red), at $n_e = 4 \times 10^{19}$ m^{-3}; The ratio of the PECs is also shown in black with the secondary y-axis. Two temperature areas are coloured: in yellow the temperature range corresponding to the WEST 9920 plasma discharge used for the cross-calibration and in blue the temperature range over which the W^{44+} ionization stage is dominant. 182

3.36. *Fractional abundance of the W^{44+} ionization stage where are indicated the maximum abundance $f_{Z,max}$ and the temperature associated $T_{Z,max}$.* 183
3.37. *Intensity of the W^{44+} Zn-2 spectral line as a function of time and radial coordinate.* 184
3.38. *Intensity of the W^{44+} spectral line measured with the SIR spectrometer as a function of the radial coordinate.* 184
3.39. *Magnetic surfaces crossed by the hundred XICS LOS as a function of their length.* 185
3.40. *Top: Comparison between the SIR LOS for $\rho_{tor,min} = 0.25$ and the closest XICS LOS; Bottom: distance travelled between the various magnetic surfaces by the selected LOS.* 186
3.41. *Top: brightness measurement (in photons.cm^{-2}s^{-1} sr^{-1}) of the SIR W^{44+} spectral line for multiple time acquisitions of the WEST #59920 pulse and associated XICS LOS-integrated intensity (in counts.s^{-1}) of the Zn-2 spectral line (middle) for the radial coordinate ρ_{tor} associated (bottom).* 188
3.42. *$n_e, T_e, f_{W,44+}$ and PEC_{Zn-2} profiles along the XICS LOS corresponding to $\rho_{tor,min} = 0.0$, as a function of the coordinate along the LOS and ρ_{tor}.* . 189
3.43. *Triple factor $n_e \times f_{W,44+} \times PEC_{\lambda_{Zn-2}}$ profiles for the W^{44+} Zn-2 spectral line along the four XICS LOS presented in Fig. 3.40 as a function of the coordinate along the lines and ρ_{tor}.* 190
3.44. *Triple factor $n_e \times f_{Ar,16+} \times PEC_w$ profiles for the Ar^{16+} w spectral line along the four XICS LOS presented in Fig. 3.40 as a function of the coordinate along the lines and ρ_{tor}.* 191
3.45. *$n_e, T_e, f_{Ar,16+}$ and PEC_w profiles along the XICS LOS corresponding to $\rho_{tor,min} = 0$, as a function of the coordinate along the LOS and ρ_{tor}.* . . 192
3.46. *Temporal evolution of the line-averaged densities and concentrations of Ar^{16+} and W^{44+} for the WEST #59920 plasma discharge.* 193
3.47. *Temporal evolution of the line-averaged densities and concentrations of Ar^{16+} and W^{44+} for the WEST #59667 plasma discharge.* 194
3.48. *Sketch of the brightness calibration transfer from the Extreme Ultra-Violet (EUV) SIR spectrometer (lower branch) to the XICS spectrometer (upper branch). The performed method is represented by red arrows and the alternative with green arrows.* 195

A.1. Atomic scattering factor values for O and Si species. 203

List of Tables

1.1. *Values of the electron $\omega_{c,e}$ and Deuterium ion $\omega_{c,D}$ cyclotron frequency in MHz and the Larmor radius $\rho_{La,e}$ and $\rho_{La,D}$ associated for different values of magnetic field B_{tor}.* 50
1.2. *WEST tokamak main parameters.* 52
1.3. *Energy configuration of the He-like Ar spectral lines and their corresponding wavelengths in Å and key letters proposed by A.H. Gabriel [43].* 68
1.4. *The selection and exception rules for the discrete electronic transitions. [44]* 69
1.5. *Theoretical transition and wavelengths of the He-like $n = 2$ Ar dielectronic satellites lines. The wavelengths are in Å.* 73

2.1. *Main XICS Bragg crystals characteristics.* 85
2.2. *Technical specifications of the PILATUS3 detector.* 102
2.3. *Theoretical transitions and wavelengths of the Ar [42] and W [74] spectral lines identified in the Ar XVII spectrum.* 121
2.4. *Theoretical transitions and wavelengths from [94] of the Ar $n = 3$ and $n = 4$ spectral lines added to the modelling algorithm.* 136

3.1. *List of studied shots measured with the ArXVII crystal set of the XICS spectrometer with the main plasma parameters associated: plasma discharge number, time acquisition, duration, plasma current, toroidal magnetic field, LHCD and ICRH power and line-averaged electron density.* 150
3.2. *Theoretical transitions and wavelengths of the W spectral lines measured with the SIR and the XICS diagnostics.* 179

List of Acronyms

ADAS
Atomic data and Analysis Structure. 25, 71, 135, 175, 176

CD
Current Drive. 51

CEA
Commissariat aux Énergies Atomiques et aux Énergies Alternatives. 17

CFP
Composants face au plasma. 7

COVID
Corona virus disease. 42

CR
Collisional Radiative. 70

DR
Dielectronic Recombination. 63

EC
Electron Cyclotron. 51

ECE
Electron Cyclotron Emission. 13, 14, 26–28, 53, 129, 134, 135, 156, 157, 160, 161, 163, 165–168, 171, 188, 189, 196

EUV
Extreme Ultra-Violet. 29, 115, 177, 194, 195

FCI
Fusion par confinement inertiel. 6

FCM
Fusion par confinement magnétique. 6

FWHM
Full Width at Half Maximum. 76, 77, 102, 122

GIEC
Groupe d'experts Intergouvernemental sur l'Évolution du Climat. 6

HR-XIS
High Resolution X-ray Imaging Spectrometer. 199

IC
Ion Cyclotron. 51

ICF
Inertial Confinement Fusion). 47

ICRH
Ion Cyclotron Resonance Heating. 26, 30, 51, 52, 150, 155, 156

IEA
International Energy Agency. 22, 40, 41, 44

IPCC
Intergovernmental Panel on Climate Change. 42

IR
Infrared. 100

ITER
International Thermonuclear Experimental Reactor. 4–7, 35, 42, 51, 199

KSTAR
Korea Superconducting Tokamak Advanced Research. 115, 140, 170, 199

LH
Lower Hybrid. 13, 14, 27, 28, 51, 157, 160, 162, 166–168, 193

LHCD
Lower Hybrid Current Drive. 26, 30, 51, 52, 112, 150, 155, 156, 165, 167, 192, 193, 198

LMJ
Laser Mega-Joule. 35, 47

LOS
Line Of Sight. 12, 25, 27–29, 107, 119, 126, 129, 132, 133, 156, 159, 161, 165–167, 178, 185–192, 195

LTE
Local Thermodynamic Equilibrium. 70

MCF
Magnetic Confinement Fusion). 47

ME-SXR
Multi-Energy Soft X-Ray. 53

METIS
Minute Embedded Tokamak Integrated Simulator. 12, 27, 160, 161

MHD
Magneto Hydro Dynamics. 115

MIT
Massachusetts Institute of Technology. 199

NBI
Neutral Beam Injection. 12, 115, 158

NICE
Newton direct and Inverse Computation for Equilibrium. 132

NIF
National Ignition Facility. 35

NPU
Noyaux, Plasma et Univers. 17

OPEN-ADAS
Open Atomic data and Analysis Structure. 28, 62, 71, 163, 173, 175, 177

PEC
Photon Emission Coefficient. 14, 15, 25, 28, 60, 71, 76, 78, 135–137, 162–164, 172–177, 179–182, 188, 189, 195, 199

PPPL
Princeton Plasma Physics Laboratory. 199

RC
Rocking-Curve. 26, 145

RH
Resonance Heating. 51

RR
Radiative Recombination. 63

SCRAM
Superconfiguration Collisional Radiative Atomic Model. 71

SIR
Spectromètre à Incidence Rasante (or Grazing Incidence Spectrometer). 14, 15, 28–30, 177–179, 181–188, 194, 195

SMG
Sur Mon Glaçon. 18

SNR
Signal-to-Noise Ratio. 81, 113, 119

TFR
Tokamak of Fontenay-aux-Roses. 140

TFTR
Tokamak Fusion Test Reactor. 140

TN
Thermonuclear. 46

TS
Tore Supra. 36, 51, 140

UV
Ultra-Violet. 4, 5, 100

VOS
Volume Of Sight. 129

VUV
Vacuum Ultra-Violet. 14, 37, 115, 177, 192, 194, 195, 198

W7-X
Wendelstein 7-X. 28, 113, 175, 199

WEST
W (Tungsten) Environment in Steady-state Tokamak. 4, 5, 7, 10–12, 14–16, 18, 22, 24–30, 35, 36, 51–53, 78, 103, 106–108, 111–118, 123–125, 133–135, 137, 140, 141, 146, 147, 149, 153, 154, 156–161, 163, 165–172, 177–179, 181, 182, 184, 187, 188, 192–194, 196–199

XICS
X-ray Imaging Crystal Spectrometer. 4, 5, 8, 10, 11, 13–16, 23, 24, 26–30, 36, 37, 81, 84, 85, 94, 96, 101, 103, 106–108, 110, 111, 113–115, 117, 121, 122, 129, 131, 132, 134, 138, 140, 146, 148–150, 160, 162, 163, 165–167, 169–172, 177–179, 181–183, 185–192, 194–199

XOP
X-ray Oriented Programs. 143

INTRODUCTION

A famous French engineer and founder of the Shift Project association [2] named Jean-Marc Jancovici once declared: "I had been hearing about global warming for a long time. I was hiding behind a distant deadline. Now it is a reality." This sentence expresses the anxious climate in which the world lives today in terms of energy. Since the Industrial Revolution in the latter half of the 18th century, the world economic society based its means of production and consumption mainly on fossil fuels. The yields of industrial production lines and agriculture thus exploded. Although it has contributed greatly to the rise of the general life expectancy, quality of life and purchasing power during the last centuries, we are now reaching the limits of our society in terms of natural resources and energy consumption. Global warming has become an alarming reality, and the world needs cleaner sources of energy to counter it. One area of research in particular could solve this problem in the medium term: the thermonuclear fusion.

Thermonuclear fusion could provide a cleaner source of electricity production. Fusion is based on two hydrogen isotopes, Deuterium and Tritium (D-T reactions). The first can be easily recovered from the oceans. The second is more difficult to find naturally, as it is a radioactive element with a short half-life (around 12 years). To understand the physics of thermonuclear fusion and to produce electricity via power-plants like the fission power-plants, we need technological means to study it. It exists today two main directions to develop fusion power-plants: inertial-confinement fusion, with the Laser Mega-Joule (LMJ) (France) project and the National Ignition Facility (NIF) (USA) in particular, and magnetically-confined fusion with the so-called tokamaks. The basic principles of tokamaks will be presented to understand how the fusion is achieved and we will introduce the WEST tokamak which is used to test scenarios and components of the future ITER tokamak. Thus, we will detail the physics of soft X-rays radiation (of 1keV - 15 keV energy range) emitted from tokamak plasmas as they are carrying useful information about the plasma as its density, temperature and impurity content. One way to probe these plasma quantities is to study a specific spectrum, that of Ar XVII. Details about the processes of emission of these spectral lines will be given to understand how the ion and electron temperature of the plasma can be deduced from the measurements.

The measurements of electron and ion temperature are important since number of phenomena that happens in a plasma depend on these parameters. The D-T reactions depend mostly on the ion temperature and is an important parameter that has to be optimized to obtain long-sustained plasmas. The ratio of the electron to

2. See for more information: https://theshiftproject.org/

the ion temperatures is also a key indicator of the energy transfers between charged particles. Indeed, due to their mass ratio, electrons and ions react very differently to the various heating means available on a tokamak, and the general hope when heating one population is that it will transfer some of its kinetic energy to the other. Different heating systems can be used to heat electrons or ions directly, so it is important to be able to measure their kinetic energy at any time in a plasma.

As in astrophysics, the Doppler effect gives us information about the momentum of matter in motion relative to the observer by measuring the shift of a wavelength relative to its theoretical value. We can also extract from the Doppler effect the broadening of a spectral line due to the thermal agitation of the emitting species. These two quantities were already been measured on the Tore Supra (TS) tokamak (early version of the WEST tokamak) with a single-line of sight X-ray spectrometer. This diagnostic of high spectral resolution ($\Delta\lambda/\lambda \sim 10^{-4} - 10^{-5}$) aimed at measuring the ion and electron temperatures and the toroidal rotation velocity with ten different impurity spectra between Ar and K, for a single line of sight crossing the plasma center. Each spectral line measured with a spectrometer can be characterized by its energy, wavelength or frequency. It is characteristic of a given atomic transition and requires specific measurement means. The measurement of the Ar XVII spectrum in particular requires very high spectral resolution, i.e. the power to separate wavelengths, from the spectrometer since the spectrum is extended over less than one ten-billionth of a metre (10^{-10}m = 1Å). It has been replaced since on the WEST tokamak by a new X-ray spectrometer with multiple lines of sight that aims to measure this spectrum, called the XICS .

This thesis is dedicated to the operation, acquisition and modelling of the XICS spectrometer to compute the electron and ion temperatures and toroidal rotation velocity from Ar spectral line ratios, Doppler broadening and shifts respectively and to study the tungsten spectrum measured in the same wavelength range. The outline of this work is the following:

- Chapter 1 is dedicated to the introduction of thermonuclear fusion in the world energetic context and to present the basics of fusion, tokamaks and radiations. A theoretical approach about the soft X-ray emission in WEST tokamak will provide the essential information to understand how a X-ray spectrometer has to be designed and what it has to measure.
- Chapter 2 describes the design of the spectrometer. Details about the components are given to understand the principle of the diagnostic and to define its limitations, in terms of spatial and spectral resolutions. The entire acquisition and modelling processes are also detailed. A dedicated Section will be also devoted to the commissioning of the instrument, describing the alignment of the components in the tokamak environment, the calibration and its operation during experimental campaigns. A third part will detail the treatment of the measurement, describing the spectral fitting algorithm used to model the spectral lines.
- Chapter 3 covers the results obtained from the various analyses of the experimental spectra. Three important results are exposed: a distortion of the instrument

function due to the Bragg crystals, the analysis of the rotation and temperature profiles and a brightness calibration transfer method implemented from a VUV spectrometer measurements. The latter provides a way to compute the density and concentration profiles of the Ar and W impurities.

The work presented in this thesis provides an effective method to analyze the Ar XVII spectrum with the XICS diagnostic. We cover from the data acquisition during experimental campaigns to the computation of physical quantities of interest from the spectral lines, while detailing the many stages involved in understanding the instrument function. The electron and ion temperatures measurements appear in agreement with other measurements from various diagnostics. The use of rotation velocity profiles is made difficult by the lack of spectral calibration, adding a further unknown to the instrumental function. Measurements of tungsten lines, which make it difficult to compute the electron temperature, are, however, used to calibrate in brightness the diagnostic and extract density and concentration profiles for argon and tungsten impurities.

1. Fusion, tokamak and radiation

Sommaire

1.1. Introduction . . . 40
1.2. Energy mix and magnetic confinement fusion . . . 40
1.2.1. Status of the energy today . . . 40
1.2.2. Thermonuclear processes . . . 42
1.2.3. Power balance and ignition condition . . . 46
1.2.4. The tokamak concept . . . 48
1.2.5. The WEST tokamak . . . 51
1.3. Soft X-ray emission in WEST . . . 54
1.3.1. Atomic processes . . . 55
1.3.1.1. Collisional processes . . . 55
1.3.1.2. Rate coefficients for collisional processes . . . 58
1.3.1.3. Radiative processes . . . 60
1.3.2. Ionization equilibrium . . . 62
1.3.3. Population equilibrium . . . 64
1.3.3.1. Local Thermodynamic Equilibrium . . . 64
1.3.3.2. Coronal equilibrium . . . 65
1.3.3.3. Collisional-Radiative model . . . 66
1.3.4. Ar XVII spectral lines identification . . . 66
1.3.4.1. Definition of the energy levels . . . 67
1.3.4.2. Electromagnetic multipole transitions . . . 69
1.3.4.3. Intensity of the resonance line . . . 70
1.3.4.4. Satellite lines . . . 72
1.3.5. Line profiles . . . 75
1.4. Conclusions . . . 78

1.1. Introduction

The quest for a low-carbon and cleaner electricity production for all domains of our society is one of the most important challenges in the 2000s. So far, mankind has not found yet a "green" energy source that can sustain all sectors of our society, i.e. industry, transport, residential, agriculture, etc. Thermonuclear fusion could provide one day, at mid or long term, a safe and massive electricity production. This Chapter presents the goals for the challenges involved in the search for cleaner sources of energy and why fusion is such a promising field. The scientific principles behind the study of fusion by magnetic confinement, with the so-called tokamaks, are then presented here.

1.2. Energy mix and magnetic confinement fusion

1.2.1. Status of the energy today

Never before has the world consumed so much fossil fuel, whether coal, oil or gas, as it does today. The world population continues to grow day by day, as does the need for electricity around the globe. Coal is, from the data shown in Fig. 1.1, since the

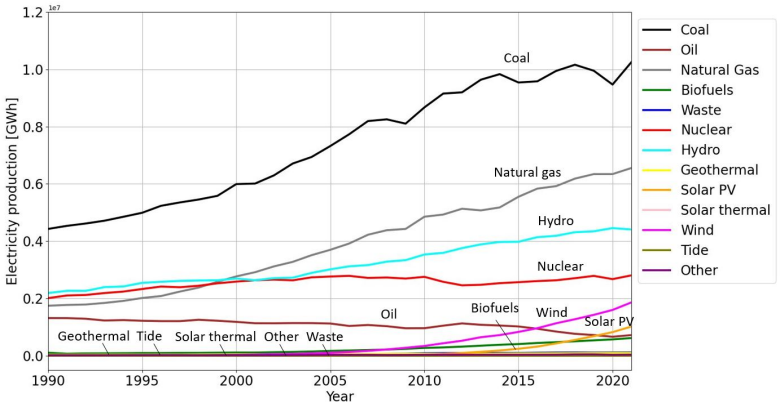

Figure 1.1. – *World electricity production by source between 1990-2021 (Source: IEA Electricity Information https://www.iea.org/data-and-statistics/data-product/)*

1990s the main source of electricity generation. We still also depend mostly on fossil fuels like natural gas while more environmentally-friendly sources are struggling to play a bigger role in the energy mix, in the exception of hydroelectric power whose global percentage is rising steadily. As the world nations develop and industrialize, and as their population move towards more comfortable lifestyles, global electricity consumption increases every year as shown in top Fig. 1.2. Faced with these growing demands, each nation has set up various energy production regimes. From bottom Fig. 1.2, we can see that France relies heavily on nuclear power and oil while in Germany, denuclearization has led to the construction of coal- and gas-fired power

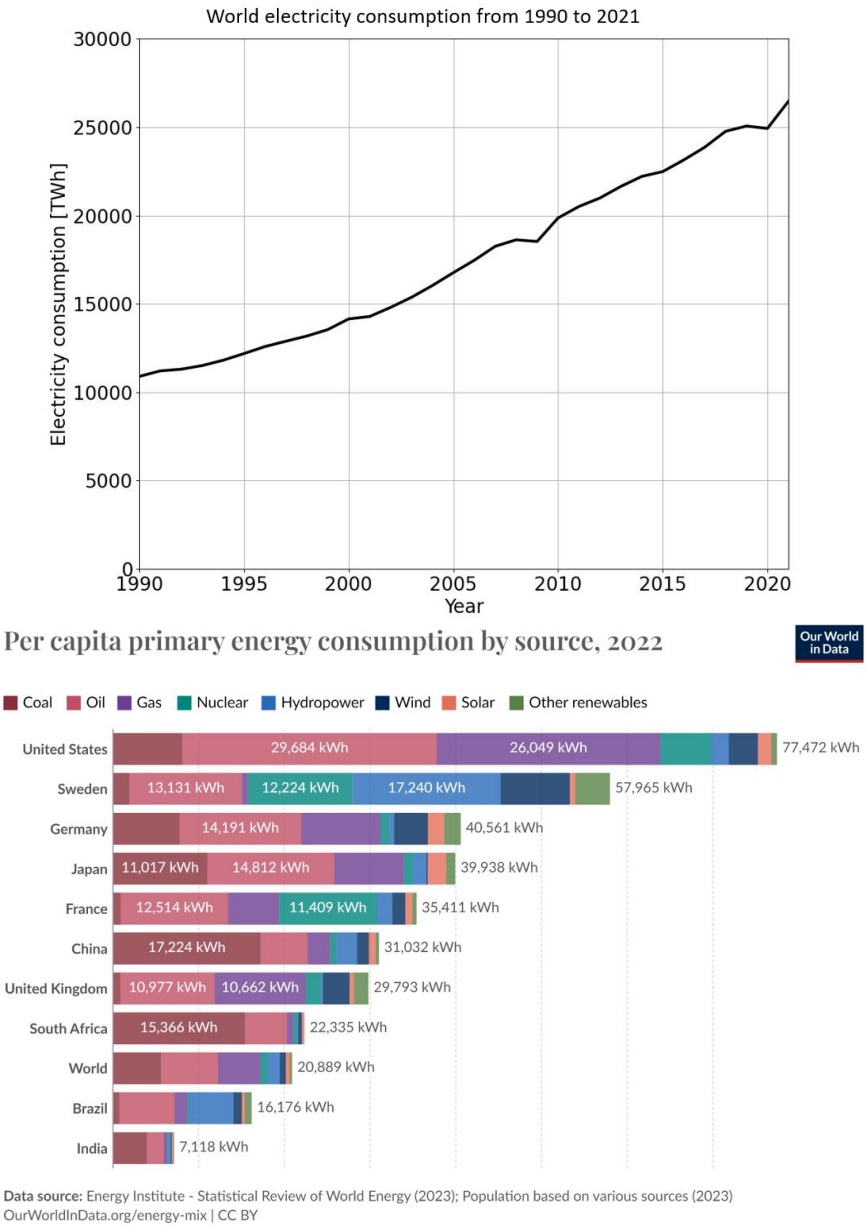

Figure 1.2. – *(Top) World electricity consumption from 1990 to 2021 in TWh (Source: IEA Data Services https://www.iea.org/data-and-statistics/data-product/); (Bottom) Primary energy consumption by source in 2022 in kWH per person.*

plants. The United States rely heavily on natural gas, and in particular in shale gas [1] (natural gas produced from organic shale formations) and oil, while Scandinavian countries rely heavily on hydroelectric power and nuclear power plants. What is more, the Intergovernmental Panel on Climate Change (IPCC) reports are more than alarming about this rise in consumption and the harmful effects it is having on our planet. Fig. 1.3 displays various indicators related to the state of water on Earth and global warming measured over a period of more than a hundred years. We can see that rising temperatures are having a snowball effect, reducing snow and glacier content at the poles, leading to rising global sea levels and warming, with a detrimental effect on ecosystems. But fossil fuel resources are limited, and a race against time is underway to reduce our dependence. Innovations in renewable energies over the last few decades have improved the efficiency of wind, hydro and solar power generation.

However, these are not means of production that are as continuous over time as nuclear fission power plants, or at least as efficient. As we can see in France between 1990 and 2022 in Fig. 1.4, the absolute low-carbon electricity production has not increased significantly in recent decades. Nuclear power has been on the decline in recent years, partly due to the Corona virus disease (COVID) crisis, recent maintenance work on active reactors as well as the closure of some of them, such as Fessenheim. In parallel, wind and solar power have been on the rise since 2005, but account for only a few per cent of nuclear power. In 2022, these low-carbon electricity production sources will not account for 4×10^5 GWh in France, wiping out almost twenty years of progress in this field especially because of our dependence in nuclear power-plant. Here again, we are dependent on what research and industry have to offer as viable alternatives, while making every effort to reduce energy consumption as recommended by the IPCC (Intergovernmental panel on climate change).

Forty years ago, several industrialized nations joined forces to launch a program aimed at developing a new, cleaner and more sustainable energy source based on nuclear fusion reactions. The ITER program [2] was born at the superpower summit in Geneva in November 1985. Further negotiations culminated in the ITER Agreement, officially signed on November 21, 2006 by the ministers of the seven ITER Members at the Élysée Palace in Paris. ITER is one of the world's most ambitious energy projects, and the results of its scientific program will pave the way for the fusion power plants of tomorrow.

1.2.2. Thermonuclear processes

The principle of thermonuclear fusion is closely related to that of thermonuclear fission. Both deal with the modification of the nuclear composition, made up of nucleons (protons and neutrons). Of the four fundamental interactions that govern the Universe, the strong interaction holds the atom nucleus together. This interaction can be characterized here by the binding energy between nucleons. The Aston curve shown in Fig. 1.5 represents the averaged binding energy per nucleon as a function

1. See for more information: US Energy Information Administration https://www.eia.gov/dnav/

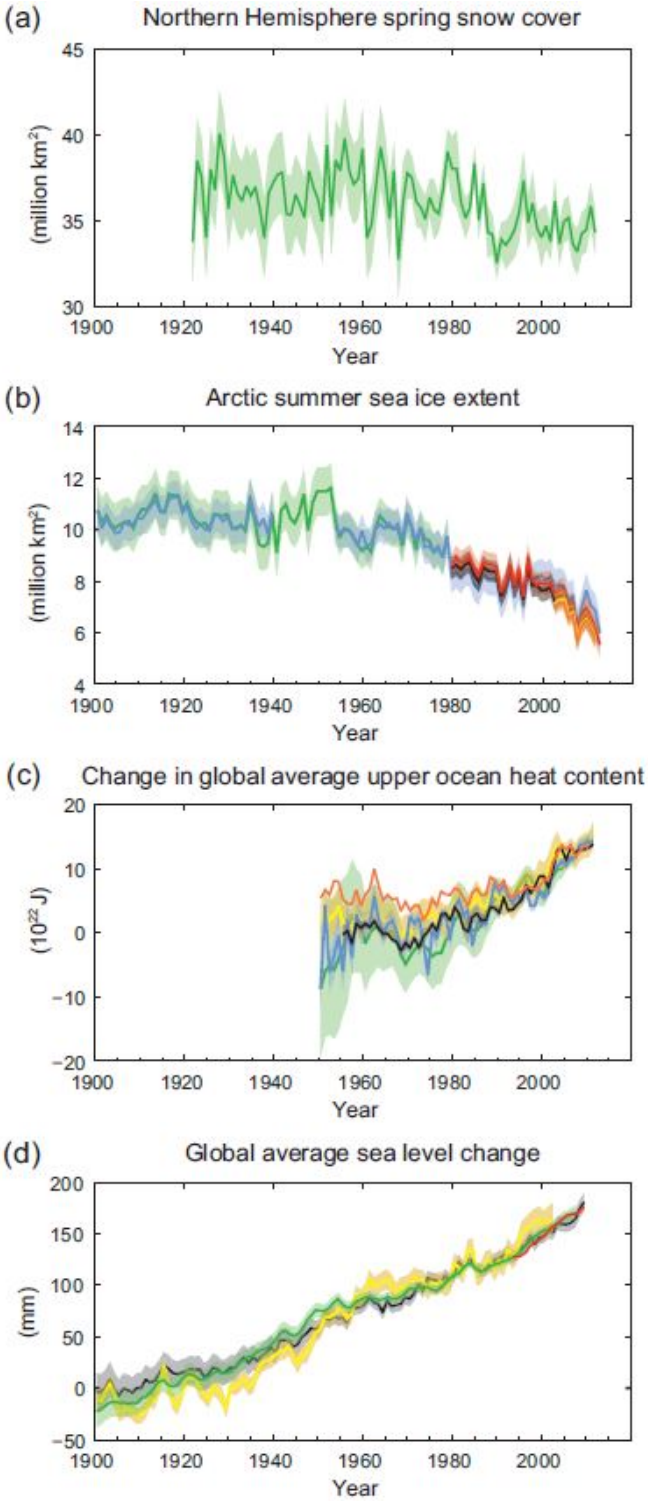

Figure 1.3. – *Indicators of a changing global climate: (a) Northern hemisphere spring averaged snow cover; (b) Arctic averaged sea ice etendue; (c) change in global mean heat content in upper oceans; (d) global mean sea level change [1].*

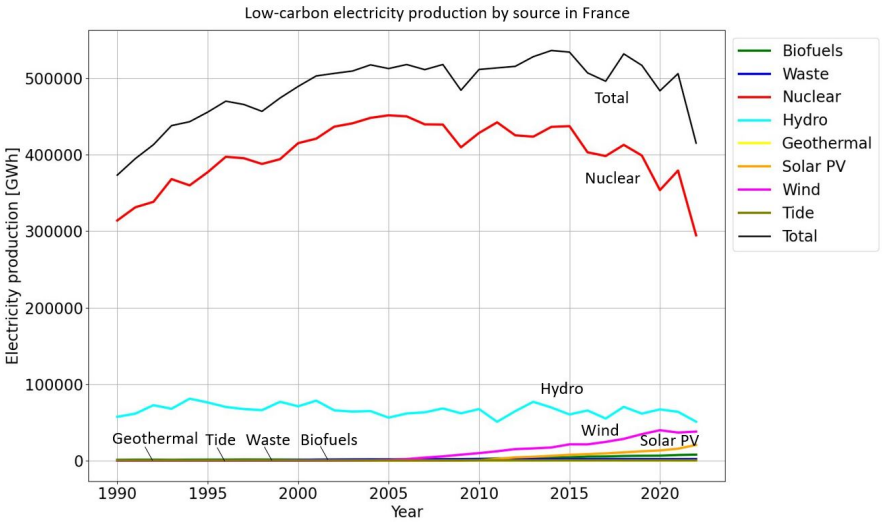

Figure 1.4. – *Low-carbon electricity production by source in France between 1990-2022 (Source: IEA Electricity Information https://www.iea.org/data-and-statistics/data-product/)*

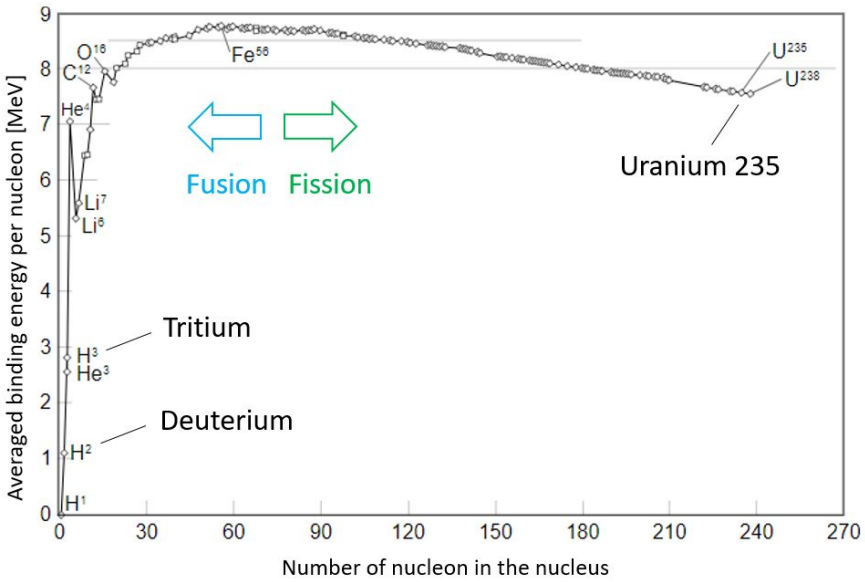

Figure 1.5. – *Aston curves representing the averaged binding energy per nucleon as a function of the number of nucleons in the nucleus (Source: Public domain, https://commons.wikimedia.org/w/index.php?curid=1540082)*

of the number of nucleons in the atomic nucleus. For light elements, the averaged binding energy per nucleon increases up to $Z = 30$, which means that they can react together to create heavier and more stable elements and release energy. This is called a fusion reaction and is interesting for the energy it releases. For heavier elements than Fe, the curve decreases with increasing mass. It means that they can release

energy if they split, this is a fission reaction.

The fission nuclear plants are based on these fission reactions, exploiting the fission of U atoms ($A = 235, Z = 92$). The fission reaction is as follows:

$$^{235}_{92}U +^{1}_{0} n \rightarrow^{236}_{92} U \rightarrow^{92}_{36} Kr +^{141}_{56} Ba + 3^{1}_{0} n \tag{1.1}$$

where the fission products are Kr and Ba with three neutrons of high energies resulting a chain of fission reactions. According to Fig. 1.5, the binding energy of the ^{236}U is 7.55 MeV per nucleon. For each fission reaction, about 200 MeV [3] is carried by the products of the reaction of which 168 MeV by the fission products themselves (Kr and Ba) and only 5 MeV for the neutrons. A part of these neutrons react with the reactor wall components to vaporise high pressure water to generate electricity by mechanical transfer and others participate to the next fission reactions.

In contrast, fusion reactions for energy production occur between very light elements. Fusion reactions occur naturally in the core of stars which contains mostly very light elements such as H and He. These elements are burnt throughout the life of the stars, releasing the products of the fusion reactions into the outer layers. Matter in stars is so hot and compressed by gravity that it is in a state of plasma, which is the fourth state of matter along with gas, liquid and solid. For a reaction to take place, two atomic nuclei must be able to come close enough to each other to collide and fuse. However, due to the presence of positively-charged protons in the nucleus, a Coulomb repulsion potential keeps them apart above a minimum distance r_m for which the potential is maximum: $V(r, max) = e^2/4\pi\epsilon_0 r_m$. One must then give enough energy to the nucleus to overpass the barrier and to fuse. Nuclei with kinetic energy lower than this threshold are still able to overcome this potential barrier and fuse thanks to a quantum phenomenon called tunneling. It corresponds to the probability of an atom to pass the potential barrier and finally the atom act as if the potential barrier was statistically lower. High temperatures are of course still necessary for fusion reactions to occur, but we will see that in practice, the required values are within reach.

The most promising fusion reaction for research is based on Deuterium (D) and Tritium (T) which are isotopes of H:

$$^{2}_{1}D +^{3}_{1} T \rightarrow^{4}_{2} He +^{1}_{0} n \tag{1.2}$$

This reaction produces an alpha particle ($^{4}_{2}He$) of energy E = 3.5 MeV and a neutron of high energy E = 14.1 MeV, which is much larger than that of a fission neutron of 5 MeV. It is the most promising because comparing the D-T cross-section as shown in Fig. 1.6 with those for D-D and D-^{3}He reactions, these fusion reactions occur at much lower energies, $T_D(\sigma_{D-T,max}) \approx 100$ keV. A reaction cross-section defines the probability of a fusion reaction, the larger the cross-section and the greater the probability of fusion. The temperature needed to achieve D-T fusion reactions is lower than for D-D or D-He^3 reactions, and combined with the high kinetic energies of the neutrons produced by the reactions and the higher reaction rate among the three, this is the preferred reaction for research today.

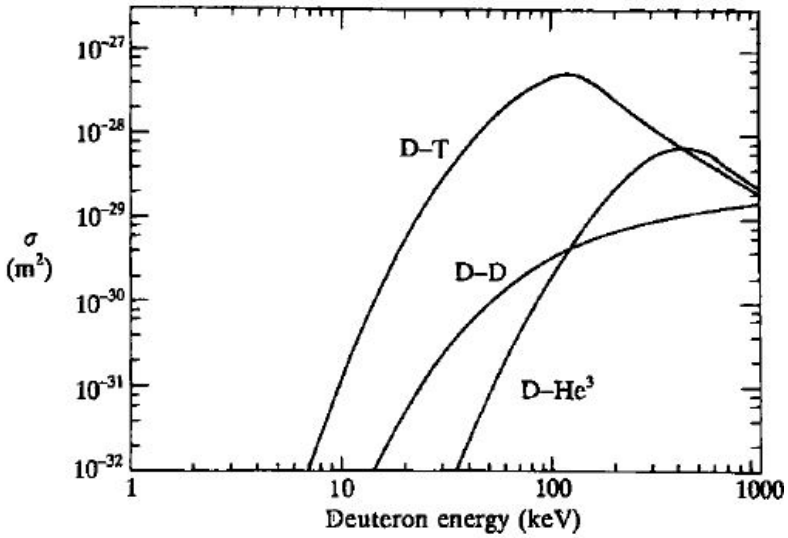

Figure 1.6. – *Cross-sections of the D-D, D-T and D-He^3 fusion reactions as a function of the Deuterium energy [4].*

1.2.3. Power balance and ignition condition

Once the fusion reactions occur, we need to do the energy balance to study the sustainability of the plasma. The Thermonuclear (TN) power of fusion per volume unit P_{TN} in a pure D-T plasma is written as:

$$P_{TN} = n_D \times n_T \times <\sigma v> \times E_{rel} = n_D(n-n_D) \times <\sigma v> \times E_{rel} \qquad [\mathrm{J\,s^{-1}\,m^{-3}}] \qquad (1.3)$$

where n_D, n_T and n are the Deuterium, Tritium and total ion densities, $<\sigma v>$ is the reaction rate of the reaction (see Sect. 1.3.1.2) and E_{rel} is the energy released per reaction. This power is carried by the fusion products defined in Eq. 1.2, by alpha-particles and neutrons. The part taken by the neutrons is qualified as loss power since when they do not participate to the fusion reactions, they leave the plasma since they are not electrically charged and have a mean free path (defined as the inverse of the cross-section of interaction) higher than the tokamak sizes. The alpha-particles on the contrary participate to the plasma heating through collisions. For a 50-50% D-T plasma, the heating contribution from these particles per volume unit can be written as:

$$p_\alpha = \frac{n^2}{4} <\sigma v> \times E_\alpha \qquad [\mathrm{J\,s^{-1}\,m^{-3}}] \qquad (1.4)$$

and thus the total power is:

$$P_\alpha = \int p_\alpha dV = \frac{V}{4} \times E_\alpha \times \overline{n^2 <\sigma v>} \qquad [\mathrm{W}] \qquad (1.5)$$

where V is the plasma volume, $E_\alpha = 3.5$ MeV and $\overline{x}$ defines a volume averaging. In parallel, the notion of power loss is important because if P_{TN} is low, additional, or

external, heating has to be added to sustain the fusion reactions. The rate of energy loss P_{loss} is characterized by the confinement time τ of the total energy W available in the plasma:

$$P_{loss} = \frac{W}{\tau} \qquad [\mathrm{J\,s^{-1}}] \tag{1.6}$$

where $W = 3V\overline{nT}$ is the volume-averaged energy available in the plasma (with T the temperature of the particles) found by expressing the plasma energy per volume unit of $w = 3n_eT/2 + 3n_iT/2$ with $n_e = n_i$. A power balance can be established between the power loss and the power supplied by the alpha-particles:

$$P_\alpha + P_H = P_{loss} \tag{1.7}$$

where the additional heating power P_H must be efficient enough to compensate the losses. In the case where $P_\alpha = P_{loss}$, a self-sustained plasma is achieved and the ignition is reached. The requirement for ignition can be retrieved from the power balance expression:

$$P_\alpha \geq P_{loss} \Rightarrow n\tau \geq \frac{12 \times T}{E_\alpha < \sigma v >} \tag{1.8}$$

where we have assumed that the plasma is homogeneous to remove the volume averaging. The relation becomes only dependent on the temperature of the plasma with T and the reaction rate $< \sigma v >$. From [4], the demonstration of the optimal numerical value for the ignition condition can be retrieved to find the Lawson criterion:

$$nT\tau \geq 5 \times 10^{24} \qquad [\mathrm{eV\,m^{-3}\,s^{-1}}] \tag{1.9}$$

Fusion can be achieved through Inertial Confinement Fusion) (ICF) by firing high-power lasers at a target that compresses, rising in temperature and initiating fusion reactions, as for the LMJ project [5]. Another way of achieving this is to study the plasmas created in what is known as a tokamak where the plasma is confined with magnetic fields (Magnetic Confinement Fusion) (MCF)).

Since gravity cannot be used for confining the plasma in laboratory conditions, another solution was investigated early based on magnetic confinement. This relies on the fact that the trajectory of a charged particle is constrained by the presence of a magnetic field to follow helical trajectories. Several concepts were first investigated. Magnetic mirrors for example rely on the fact that if the magnetic field increases along the particle trajectory, the particle will, at some critical magnetic field value, see its parallel velocity change of sign. It can then go back-and-forth between two locations of maximum magnetic field. But this solution had limits pertaining to the loss of particles that add a small perpendicular velocity.

Hence, another way involved to use magnetic fields to enclose the plasma in what are known as tokamaks. The first attempt to master the fusion reactions with such a method was performed by Tamm and Sakharov in 1950 [6] with a preliminary theoretical substantiation of the magnetic thermonuclear reactor. Russian scientists followed their theoretical ideas to create a toroidal confining magnetic field and

leading to the plasma confinement in a toroidal experiment. The concept of toroidal chamber with magnetic coils, or tokamak in Russian, was born with the T1 device in the 1950s. A multitude of tokamaks around the world are in operation, with different research objectives but all aim at improving our knowledge of the physics of fusion plasmas.

1.2.4. The tokamak concept

A tokamak is composed of a vessel of spherical or toroidal section, a central solenoid in the tokamak axis of symmetry, toroidal and poloidal magnetic field coils and additional heating systems, as shown in Fig. 1.7. The shape of the vessel is described

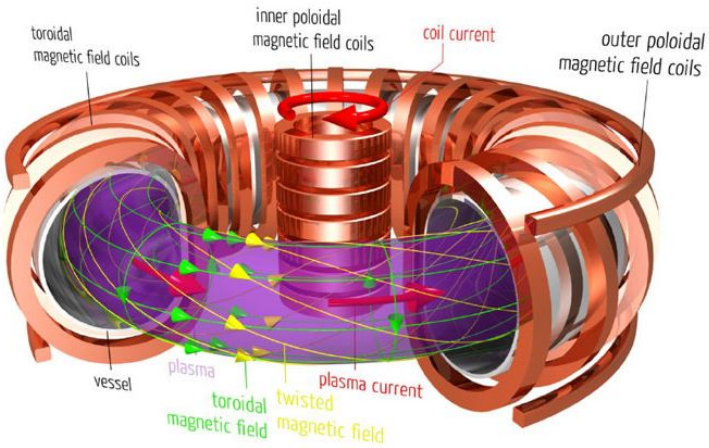

Figure 1.7. – *Sketch of the main tokamak components [7].*

by two lengths: a major radius R that characterises the radius from the axis of symmetry of the tore and a minor radius a which defines the shape of the cross-section. We should use to describe the vessel shape both Cartesian $(\vec{X},\vec{Y},\vec{Z})$ and cylindrical coordinates $(\vec{e}_r,\vec{e}_\varphi,\vec{e}_\theta)$ as shown in Fig. 1.8. The plane where the angle φ is defined

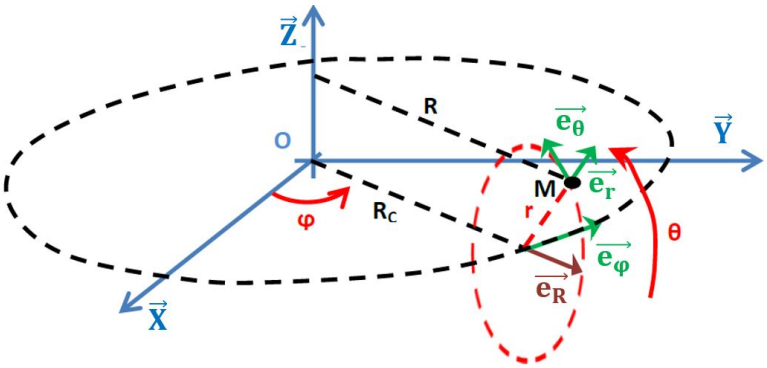

Figure 1.8. – *Geometry of a torus and its toroidal coordinate system with a circular poloidal cross-section [8].*

is called the toroidal plane and the one with the angle θ is the poloidal plane. In this example shown here of a circular poloidal cross-section, we can describe the position of any point M located on the cross-section by:

$$\vec{OM} = R\vec{e}_R + Z\vec{Z} = R_c\vec{e}_R + r\vec{e}_r \tag{1.10}$$

where R_c is the major radius of the torus and r the minor radius of the circular cross-section. The definition of the shape of the tokamak, denoted aspect ratio ϵ, is made with the ratio between the major and minor radii:

$$\epsilon = \frac{R_c}{r} \tag{1.11}$$

Thus, for any point r in the poloidal cross-section with $r = [0, a]$, we may define the normalized minor radius as $\rho = r/a$.

Once the shape of the tokamak defined, we can detail the magnetic field coils installed around the vessel. First, a central solenoid is installed at the axis of symmetry of the tokamak, see Fig. 1.7. The function of this magnet is to induce the plasma current, maintain it throughout the discharge and to create a toroidal magnetic field. It is used to adjust the plasma trajectory while supporting the magnetic field generated by the poloidal coils. Through its Ohmic effects, it also serves to heat the plasma by Joule effect. However, much of the energy is dissipated in the form of heat:

$$Q = R \times I^2 \tag{1.12}$$

where the dissipation is a function of the square of the current. As much as the plasma is heated, its resistivity decreases in parallel as $T^{-3/2}$, leading to a saturation of the maximum temperature reached by Joule effect. We will get back to the external energy sources injected to the plasma later.

The toroidal magnetic field coils are placed regularly around the tokamak vessel to ensure a magnetic field in the toroidal direction by the Ampere law. The charged particles follow helical trajectories centered on the magnetic field lines because of the Lorentz force. The Lorentz force applied to a charged particle is a function of the toroidal magnetic field $\vec{B}_{tor}$:

$$\vec{F}_L = q\left(\vec{v} \wedge \vec{B}_{tor}\right) \tag{1.13}$$

which creates an helical movement around the magnetic field lines. Their movement can be better described by setting the motion equation of a charged particle of mass m and charge q in a toroidal magnetic field $\vec{B}_{tor}$:

$$m\frac{d\vec{v}}{dt} = q(\vec{v} \wedge \vec{B}_{tor}) \tag{1.14}$$

which can be simplified taking into account an uniform magnetic field in the Z

direction:

$$\begin{cases} \frac{d}{dt}\vec{v}_x = \omega_c^2 \vec{v}_y \\ \frac{d}{dt}\vec{v}_y = -\omega_c^2 \vec{v}_x \\ \frac{d}{dt}\vec{v}_z = 0 \end{cases} \tag{1.15}$$

where

$$\omega_c = \frac{qB_{tor}}{m} \tag{1.16}$$

is the cyclotron frequency. The resolution of these equations leads thus to the Larmor radius which describes the motion of the charged particles around a magnetic field line:

$$\rho_{La} = \frac{m \times v_\perp}{q \times B_{tor}} \tag{1.17}$$

where $v_\perp$ is the orthogonal component of the velocity of the particle relative to the magnetic field. The greater the mass of the particle and the lower is its charge, the greater the Larmor radius is. The stronger the field and the smaller the Larmor radius. Table 1.1 details the values for the cyclotron frequency of electron and Deuterium ion, plus their Larmor radius for various magnetic field.

	$\omega_{c,e}$ [MHz]	$\omega_{c,D}$ [MHz]	$\rho_{La,e}$ (1 keV) [mm]	$\rho_{La,D}$ (1 keV) [mm]
B = 1T	28.01	7.62	0.107	6.463
B = 3T	84.03	22.87	0.035	2.154
B = 5T	139.90	38.12	0.021	1.293

Table 1.1. – *Values of the electron $\omega_{c,e}$ and Deuterium ion $\omega_{c,D}$ cyclotron frequency in MHz and the Larmor radius $\rho_{La,e}$ and $\rho_{La,D}$ associated for different values of magnetic field B_{tor}.*

But this toroidal magnetic field alone cannot confine efficiently the plasma in the vessel for few reasons. First, the curvature of the magnetic field lines induces a centrifuge force $F_c = mv^2/R$ on the charged particles which depends on the major radius of the vessel. Adding this new component to the motion equation Eq. 1.14, it leads to a drift velocity expressed as:

$$\vec{v}_{dr} = \frac{\vec{v}_\parallel \wedge \vec{B}_{tor}}{R \times \omega_c \times B_{tor}} \tag{1.18}$$

where $v_\parallel$ is the parallel component of the velocity of the particle relative to the magnetic field. This drift appears stronger with the mass of the particle involved and in the opposite direction depending on the particle charge. In addition, if there is an electric field orthogonal to the toroidal magnetic field, which is a function of the tokamak dimensions as R^{-1}, the so-called $E \times B$ drift is applied on the particle. The electric field has the effect to separate the particles with opposite charge in the plasma. This leads to the induction of a force pushing the charged particle outside of the plasma. Let us consider the equation of motion of the charged particles in a toroidal magnetic

field $\vec{B}_{tor}$:

$$m\frac{d}{dt}\vec{v} = q(\vec{E} + \vec{v} \wedge \vec{B}_{tor}) \tag{1.19}$$

This is equivalent to write for each component of the velocity:

$$\begin{cases} \frac{d}{dt}\vec{v}_x = \frac{q}{m} v_y \times B_{tor} \\ \frac{d}{dt}\vec{v}_y = \frac{q}{m}(E - v_x \times B_{tor}) \\ \frac{d}{dt}\vec{v}_z = 0 \end{cases} \tag{1.20}$$

The resolution of these equations leads to the $E \times B$ drift velocity:

$$\vec{v}_{dr,EB} = \frac{\vec{E} \wedge \vec{B}_{tor}}{\vec{B}_{tor}^2} \tag{1.21}$$

The $\vec{B}_{tor}$ magnetic field being in the toroidal direction and the $\vec{E}$ electric field along the $\vec{Z}$ axis of symmetry of the torus, the drift pushes the charged particles outside and inside respectively for electrons and ions. Additional poloidal magnetic field $\vec{B}_{pol}$ coils are thus added around the tokamak in the toroidal plane to push inwards the charged particles and counter these drifts.

The last essential components of a tokamak are the auxiliary heating systems. There are several types but we are going to focus on electromagnetic waves heating. Resonance mechanisms between particles and electromagnetic (EM) waves transfer energy to the particles. By modifying the polarization and/or the injection angle of the waves with respect to the magnetic field, we preferentially heat (Resonance Heating (RH)) or generate plasma current (Current Drive (CD)). Ions and electrons can be heated directly by injecting radio-frequency waves in the Ion Cyclotron (IC) range into the plasma. The same applies to the electrons, with highly localized injections into the plasma at the Electron Cyclotron (EC) frequency. There is also a range of intermediate frequencies known as LH to heat electrons and drive currents [9]. Examples of frequencies that can be used to heat the electrons and Deuterium ions in the plasmas are found in Table 1.1. The most interested readers can find more information on the LHCD and ICRH heating systems with [10], [11] and [12].

1.2.5. The WEST tokamak

Our study is based on the experiments performed on the WEST tokamak [13]. WEST is a superconducting tokamak with a X-point divertor configuration and actively cooled tungsten (W) plasma facing components (PFCs), built as an upgrade to TS [14], [15]. Its main parameters are detailed in Table 1.2. It has been equipped with two heating and/or current drive systems, LHCD [16] and ICRH [17], to perform high performance long pulses and steady-state scenarii in order to prepare operations for ITER.

To fulfill these objectives, it is equipped with two upper and lower divertors made of W mono-blocks [18], as seen in Fig. 1.9. Located on the floor and top of the vacuum

Parameters	Value
Plasma current	1 MA
Toroidal field B_T	3.7 T
Major radius	2.5 m
Minor radius	0.5 m
Aspect ratio ϵ	5-6
Elongation	1.38
Triangularity	0.5
Plasma volume V_p	15 m^3
ICRH heating power P_{IC}	9 MW
LHCD heating power P_{LH}	7 MW
ECRH heating power P_{EC}	Planned in 2024
Flat-top duration	up to 1000 s

Table 1.2. – *WEST tokamak main parameters.*

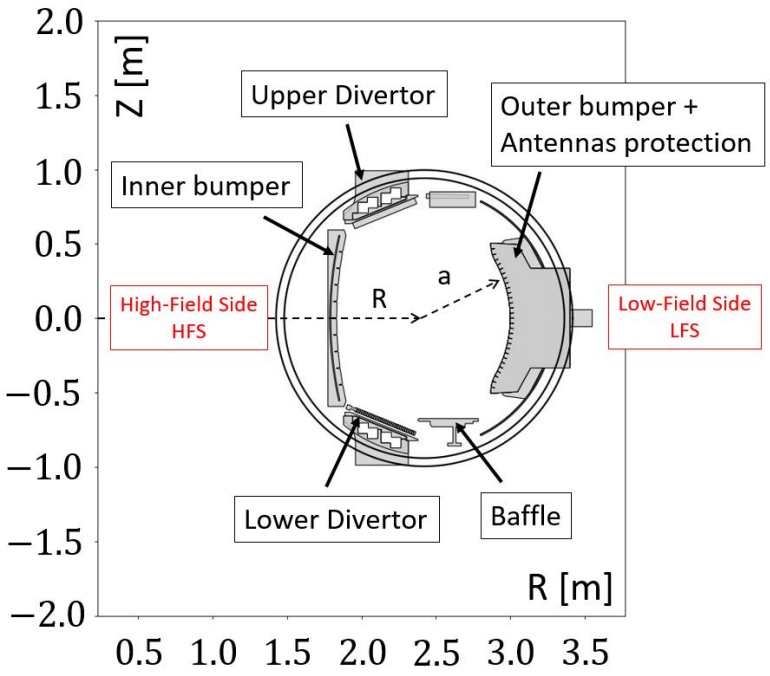

Figure 1.9. – *WEST poloidal cross-section sketch with the PFCs location.*

chamber, the divertor extracts gaseous effluents and impurities, as well as some of the heat generated by the fusion reactions. The baffle, located above the divertor, increases the particle pumping efficiency by creating a toroidal pumping throat and protects the lower divertor cooling pipes. The inner and outer bumpers, or limiters, are them used to constrain spatially the plasma during the start-up and ramp-down, to prevent it coming into contact with or discharging too much heat flux onto more sensitive components. The W divertor components appears to be a source of impurity in the

plasma, as they can be eroded and migrate into the plasma core where they absorb a non-negligible part of the power injected. The higher the concentration of tungsten in the plasma, the more it will radiate and the less energy will be available for the plasma to last. Indeed, [19] has shown that the ignition condition presented in Eq. 1.9 can be altered in the presence of a too high W concentration. The operating window for achieving ignition becomes increasingly narrow, until a certain concentration is reached, above which ignition is no longer possible.

The need to measure the W concentration in the plasma then appears necessary to study its effect on the state of the plasma, which can be characterized by measuring the temperature of the electrons and ions especially. In WEST, a few diagnostics are able to measure the electron temperature for example from different ways:

- The ECE radiometer [20] is based on the measurements of the ECE in the radio-frequency range. The intensity of the plasma radiation at the Electron Cyclotron frequency and its harmonics in the non-relativistic case is given by [21]:

$$I_{\omega_{c,e}}(r,t) = \frac{\omega_{c,e}^2 \times T_e(r,t)}{8\pi^3 c^2} \times f \tag{1.22}$$

  where T_e is the electron temperature, $\omega_{c,e}$ is the electron cyclotron frequency defined in Eq. 1.16, c is the light velocity and the function f, the optical grayness function, is a correction factor taking into account the tokamak wall reflectivity and plasma opacity.
- The Thomson Scattering instrument [22] [23] [24] [25], which is brand new installed on WEST, is based on the interaction between laser beam(s) and the plasma. The incident laser photons are scattered by the free electrons of the plasma by incoherent Thomson scattering process. From the scattered power can be extracted a spectral density function in which the information about the electron temperature can be used.
- The Multi-Energy Soft X-Ray (ME-SXR) diagnostic [26] also provides electron temperature estimations [27]. It is based on the measurements of soft X-ray photons at different energies in a region of the spectrum where emission comes only from Bremsstrahlung, i.e. no impurity lines are measured. On WEST, the energy range is chosen between 11 and 18 keV and the ratio of these X-rays radial emissivities measured at different energies is a function of the electron temperature.

Here we will be interested in another soft X-ray spectrometer aiming to measure photons with much lower energies. Historically, the measurement of soft X-ray photons in the [3.94, 4] Å spectral range, emitted from argon (Ar, Z=[15+, 16+]) ion species, is used to compute the electron and ion temperatures, as well as toroidal rotation velocity, from the components of the measured lines. An example of such radiations is shown as a modelled Ar XVII spectrum in Fig. 1.10.

1.3. Soft X-ray emission in WEST

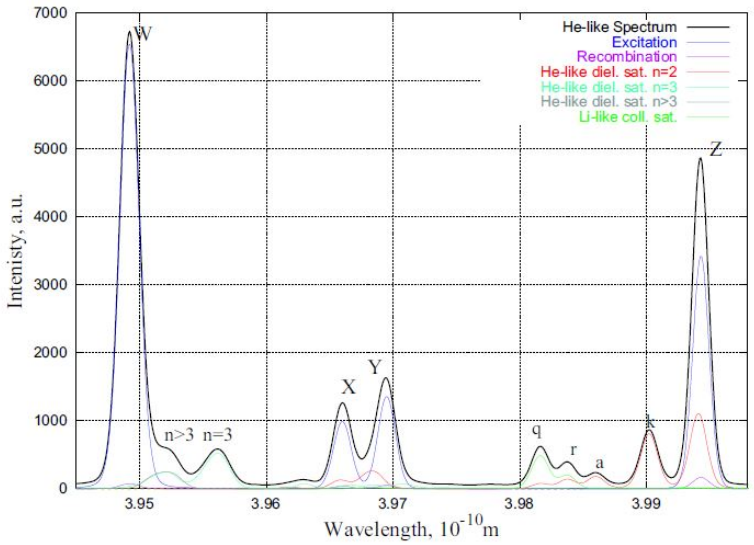

Figure 1.10. – *Theoretical He-like argon spectrum [28].*

The aim of this Section is to understand the physical phenomena at the origin of the spectral lines measured in a tokamak plasma. First, we need to investigate in Sect. 1.3.1 the various atomic processes that may lead to the emission of X-ray photons. In general, the atomic processes considered are the excitation, ionization and recombination. Then, in Sect. 1.3.2, we will describe how the different charge stages of ions are distributed in a plasma. We will see how the plasma temperature is the main dependency and rules the abundances of each charge state. Then we will outline why we can measure the emission from some ion species and not others on the spectrum shown in Fig. 1.10.

Sect. 1.3.3 will focus on the description of the distribution of bound electrons between the different energy levels in an ionization stage. Depending on the electron density of tokamak plasmas, three models can be used to describe the ionization equilibrium. The choice of the theoretical model that defines the ionization population equilibrium in a plasma constrains the various atomic processes involved, which can result in the emission of photons at well-defined energies.

Thus, the contribution of each atomic process in the measurement of the spectral lines in Fig. 1.10 is detailed and an analysis of their main components is done in Sect. 1.3.4. Through a brief reminder of how we describe the energy levels, we will see that each spectral line do not belong to the same ionization stage and originate from different atomic processes. Finally, in Sect. 1.3.5, different line shapes are introduced that can be used to model a spectral line. The various mechanisms that broaden the line shape are described and weighted for our specific case.

1.3.1. Atomic processes

In plasmas, atoms and ions can interact in two different ways with the plasma components. Collisions can happen between charged particles, either with free electrons or even with other ion species, leading to excitation and ionization processes described in Sect. 1.3.1.1. They could also interact with surrounding photons of different energies by various processes as we will see in Sect. 1.3.1.3. These interactions are very different, not only in terms of the probability of the events occurring, but also in terms of the elements involved. We will see that the coefficient rates that characterize them are expressed in different ways but always have an effect on the structure of the atoms or ions involved.

1.3.1.1. Collisional processes

Ordering of collisional processes Collision phenomena in a tokamak plasma are very important as they allow energy to be transferred between particles. We may speak of Rutherford scattering when a collision happens between two charged particles [29]. What interests us most here are the characteristic time scales of each type of collision that can occur in a plasma, i.e. between which types of particles. A collision is considered to occur when a particle enters the Debye sphere of another particle, defined by the Debye radius. It is defined as the approximate distance beyond which interactions are dominated by collective phenomena from the surrounding plasma. In tokamak plasmas, the electron and ion density is sufficiently large, see Sect. 1.3.3, to allow this kind of collision between electrons and ions. We can thus define a collision frequency between two populations of charged particles. To define them, we start with the expression of the collision frequency between two charged particle populations 1 and 2, for the population 1 of thermal velocity v_1 and mass m_1 colliding with a population 2 of mass $m_2 >> m_1$ as:

$$\nu_{12} = \frac{e_1^2 \times e_2^2 \times n_2 \times ln(\Lambda)}{(4\pi\epsilon_0)^2 \times m_1^2 \times v_1^3} \qquad [\mathrm{s}^{-1}] \tag{1.23}$$

where e is the elementary electric charge and $ln(\Lambda)$ is the Coulomb logarithm. This relation can be extended for the case of electrons, of mass m_e, colliding a population of ions of density n_i with higher mass m_i and considered at rest:

$$\nu_{e-i} = \frac{e^4 \times n_i \times ln(\Lambda)}{(4\pi\epsilon_0)^2 \times m_e^{1/2} \times (k_B T_e)^{3/2}} \tag{1.24}$$

where we have considered a Maxwellian electron velocity distribution:

$$v_{th,e} = \sqrt{\frac{k_B T_e}{m_e}} \qquad [\mathrm{m\,s}^{-1}] \tag{1.25}$$

where k_B is the Boltzmann constant ($\approx 1.381 \times 10^{-23} \mathrm{kg\,m^2\,s^{-2}\,K^{-1}}$) and T_e the electron temperature in Kelvin. The electron-electron and ion-ion collision frequencies can be written in a similar manner as:

$$\nu_{e-e} = \frac{e^4 \times n_e \times ln(\Lambda)}{(4\pi\epsilon_0)^2 \times m_e^{1/2} \times (k_B T_e)^{3/2} \times \sqrt{2}} = \nu_{e-i} \times \frac{n_e}{\sqrt{2} \times n_i} \tag{1.26}$$

$$\nu_{i-i} = \frac{e^4 \times n_i \times ln(\Lambda)}{(4\pi\epsilon_0)^2 \times m_i^{1/2} \times (k_B T_i)^{3/2} \times \sqrt{2}} = \nu_{e-i} \times \sqrt{\frac{m_e}{m_i}} \times \left(\frac{T_e}{T_i}\right)^{3/2} \tag{1.27}$$

Assuming a pure 50-50% D-T plasma where $n_e = Z_{eff} n_i$ with Z_{eff} the effective charge of the plasma defined in Sect. 2.4.2.2 set to one and $T_e = T_i$, we can order frequency collision frequencies as follows:

$$\nu_{e-i} > \nu_{e-e} >> \nu_{i-i} \tag{1.28}$$

The electron-ion collisions appear to be the most frequent collision processes in tokamak plasmas, approximately equal to 10^4 collisions per second for $T_e = 2$ keV and $n_e = 2 \times 10^{19} m^{-3}$ ([4]). The electrons are the main transport vectors of energy towards ions in particular. These energy transfers lead the ions to either reach higher states of excitation or different ionization stages, resulting in relaxations in the form of energy emission, photon emission in general. We can also define a characteristic thermal equilibration time for each species as the inverse of the collision frequency:

$$\tau_{th} = \frac{1}{\nu} \qquad [\mathrm{s}] \tag{1.29}$$

Thus, another order of thermal equilibration time can be made:

$$\tau_{e-i} < \tau_{e-e} << \tau_{i-i} \tag{1.30}$$

where $\tau_{e-i} \approx 10^{-4}$ s for the same plasma conditions expressed above and a thermal equilibration time between ions of 7 ms. This brings us to the study of various collisional processes between electrons and ions.

Electron collisional ionization and three-body recombination In this process, a free electron collides with an ion and transfers a part of its energy to a bound electron. The transferred energy is higher than the ionization limit of the bound electron, which leads to its ejection:

$$A_Z + e^- \rightleftharpoons A_{Z+1} + e^- + e^- \tag{1.31}$$

The notion of energy levels will be detailed in Sect. 1.3.4.1. The inverse process, written here with the $\rightleftharpoons$ sign, i.e. the three-body recombination, involves a collision between an ion and two electrons, resulting in the capture of one of them and a gain of kinetic energy from the still-free electron. For the electron collisional ionization

process and its inverse, the computation of the reaction rate can also be done. It can be demonstrated, from [30], that the three-body recombination depends on the square of the electron density and could be neglected in fusion plasmas because of the low densities.

Autoionization and dielectronic recombination This process involves the recombination of a free electron with an ion of charge $Z+1$ in an excited level. The energy of this free electron is just below the threshold for the excitation of a resonance transition but sufficiently high to be captured in an outer excited state. This recombination process leads to a doubly excited state of the ion A_Z^{**}, in addition of the excited core:

$$A_{Z+1} + e^- \rightleftharpoons A_Z^{**} \rightarrow A_Z^* + \frac{hc}{\lambda} \rightarrow A_Z + \frac{hc}{\lambda} \tag{1.32}$$

Two cases can therefore happen for the multiply excited state, as described by Eq. 1.32. The left side of the equation leads to the ejection of one or more electrons through the relaxation of the ion, i.e. auto-ionization. The whole system returns to its original state and no recombination process happens.

The other case in the right side of Eq. 1.32 is a stabilisation process. A radiative deexcitation of the excited electron can occur from the doubly excited state. The recombined ion emits a photon of specific energy and is left in a stable single excited state. The photon is emitted during the ion transition between two discrete energy levels, giving rise to a specific line emission which is called a dielectronic satellite line. The satellite line has a different transition from the one between the first excited state and the ground state of the recombined ion. We then speak of a parent line. These dielectronic satellite lines appear generally more or less close to the parent line, on the longer wavelength side. Finally, when the stabilizing transition happened, the single excited state cascades with one or more radiations to its ground state.

Usually, we can separate the different satellite lines with the excited orbital in which the stabilizing electron lies. For the systems where the electron is bound in highly excited orbitals ($n \geq 4$), cf. Sect. 1.3.4.1, the emission appears blended in the parent line and contributes to its overall intensity. For lower excited orbitals ($n < 4$), the emission moves further and further away from the parent line and on the longer wavelength side. We will come back later on this topic in Sect. 1.3.4.4.

Electron collisional excitation and deexcitation An incident free electron transfers by collision a part of its kinetic energy to a bound electron of an ion of charge Z, raising it to a higher internal energy level of the same charge state. The inverse process is called collisional deexcitation. Here, no radiation is emitted, the colliding electron carries away the deexcitation energy. Both interaction can be written as follows:

$$A_Z(i) + e^- \rightleftharpoons A_Z^*(j) + e^- \tag{1.33}$$

The electron collisional excitation is an important process in tokamak plasma for high temperatures, especially for the intensities of the lines of He-like ions [31].

Charge-exchange processes Collisions between light atoms or ions may infer a transfer of bound electrons between the two protagonists. Here the interaction between fast Hydrogen (H) species with an ion of charge Z, which captures the electron of the incident atom onto an excited level, as for the recombination process:

$$A_Z + H \rightleftharpoons A^*_{Z-1} + H^+ \tag{1.34}$$

The process rate is proportional to the density of neutral hydrogenic species, which is extremely low in the plasma region where our ions of interest (Ar^{15+}, Ar^{16+}, Ar^{17+} for example) are present.

1.3.1.2. Rate coefficients for collisional processes

The probability of a collisional process is characterized by its cross-section. Let us consider the reaction rate per unit of volume and time of an incident beam of particles (mass m_1 and density n_1) on a second population of particles (mass m_2 and density n_2) and of velocities $\vec{v}_1$ and $\vec{v}_2$ respectively:

$$R(v_1, v_2) = n_1 \times n_2 \times \sigma(\| \vec{v}_2 - \vec{v}_1 \|) \times \| \vec{v}_2 - \vec{v}_1 \| \times f_1(\vec{v}_1) \times f_2(\vec{v}_2) \qquad [\mathrm{s}^{-1}] \tag{1.35}$$

where $\sigma(\| \vec{v}_2 - \vec{v}_1 \|)$ is the cross-section of interaction between the two species, expressed in m^2, and $f_i(\vec{v}_i)$ is the velocity distribution of the species i. In the case of thermalized plasma, we can be assume that the velocity distribution is a Maxwellian function:

$$f_i(\vec{v}_i) = \left(\frac{m_i}{2\pi k_B T_i} \right)^{3/2} \times exp\left(\frac{-m_i \vec{v}_i^{\,2}}{2 k_B T_i} \right) \tag{1.36}$$

where $k_B T$ is the temperature of the species i in Joule. The factor in front of the Gaussian allows to normalize the distribution. In this case, after integrating Eq. 1.35 in the velocity space, the total reaction rate becomes:

$$R = n_1 n_2 \int d^3 v_1 d^3 v_2 \sigma(v) \times v \times f_1(\vec{v}_1) \times f_2(\vec{v}_2) \tag{1.37}$$

with $v = \| \vec{v}_2 - \vec{v}_1 \|$. We can then define the coefficient rate as:

$$< \sigma v > = \int_{v_1, v_2} \sigma(v) \times v \times f_1(\vec{v}_1) \times f_2(\vec{v}_2) d^3 v_1 d^3 v_2 \qquad [\mathrm{m}^3\,\mathrm{s}^{-1}] \tag{1.38}$$

so that the reaction rate becomes:

$$R = n_1 n_2 < \sigma v > \tag{1.39}$$

where $< \sigma v >$ is called the rate coefficient of the process.

In the case of an electron collision excitation, the ion target can be considered motionless as the mass ratio induces a strong velocity ratio in favor of electrons. Let us consider a population of electrons of mass m_e and defined by a temperature $k_B T_e$

colliding with an ion species. A Maxwell distribution function can be reasonably applied for the electron velocity distribution in tokamak plasmas where their probability to have a velocity between $[v_e, v_e + dv_e]$ is expressed as:

$$f(v_e)dv_e = 4\pi v_e^2 \left(\frac{m_e}{2\pi k_B T_e}\right)^{3/2} exp\left[-\frac{m_e v_e^2}{2k_B T_e}\right] \tag{1.40}$$

Taking this into account, it is possible to define the transition rate from a level i into an upper excited level j of the same ionization stage can be written as:

$$X(i \rightarrow j, T_e) = <\sigma(i \rightarrow j)v> = \int_{v=0}^{\infty} \sigma(v) \times v \times f(v)dv \tag{1.41}$$

The reaction is only possible if the energy of the free electron is $E_{kin} > E(j) - E(i)$ so the lower limit of the integral is replaced by $\Delta E_{ij} = E(j) - E(i)$. Replacing Eq. 1.40 in Eq. 1.41, and with $2E = mv^2$ and the derivative of $(\sqrt{u})' = u'/2\sqrt{u}$, the excitation rate coefficient becomes:

$$X(i \rightarrow j, T_e) = A\frac{E_H}{g(i)}\left(\frac{1}{m_e k_B T_e}\right)^{1/2} \times exp\left(-\frac{\Delta E_{ij}}{k_B T_e}\right) \times \gamma(i \rightarrow j, T_e) \tag{1.42}$$

where A is a proportionality factor, E_H is the Rydberg energy (= 13.6 eV), $g(i)$ is the statistical weight of the lower energy level or degeneracy $g(i) = (2S+1)(2L+1)$ (see Sect. 1.3.4.1 for the quantum numbers L and S) and γ is the effective collision strength which can be expressed as a function of the collision strength Ω:

$$\gamma(i \rightarrow j, T_e) = \int_0^{\infty} \Omega(i \rightarrow j, E_{kin}) \times exp\left(-\frac{E_{kin}}{k_B T_e}\right) d\left(\frac{E_{kin}}{k_B T_e}\right) \tag{1.43}$$

where E_{kin} is the energy of the incident electron. The collision strength $\Omega(i \rightarrow j, E_{kin})$ is a dimensionless parameter derived from the cross-sections:

$$\Omega(i \rightarrow j, E_{kin}) = g(i)\frac{\sigma(i \rightarrow j, v)}{\pi a_0^2}\frac{E_{kin}}{E_R} \tag{1.44}$$

where πa_0^2 is the unit of atomic cross-section (a_0 is the Bohr radius).

The deexcitation rate can also be found from the principle of detailed balance which states that, in thermodynamic equilibrium, the rates of forward and reverse processes are identical:

$$X(i \rightarrow j) = X(i \rightarrow j)\frac{g(i)}{g(j)} exp\left(\frac{\Delta E_{ij}}{k_B T_e}\right) \tag{1.45}$$

Through this formalism, all collisional rate coefficients can be found. The transition rate depends strongly on the electron temperature with the exponential term which is called the Boltzmann factor. The quantum properties of an energy level also have a non-negligible effect through their statistical weight $g(i)$. The major dependence comes from the collision strength and the kinetic energy of the free incident electron

participating to the collision.

1.3.1.3. Radiative processes

Electromagnetic emission in plasmas can happen in various forms. Fig. 1.11 shows the distinction between three types of radiation: "free-free" radiation emitted from an electron free before and after the emission, "free-bound" radiation when an electron recombines with ions and "bound-bound" emission between energy levels of an ion. The "bound-bound" transition belongs to discrete transitions between energy levels of atoms or ions for well-defined frequencies. In this Section, we will detail how each contribution are described and how they are related to the Ar XVII spectrum in Fig. 1.10.

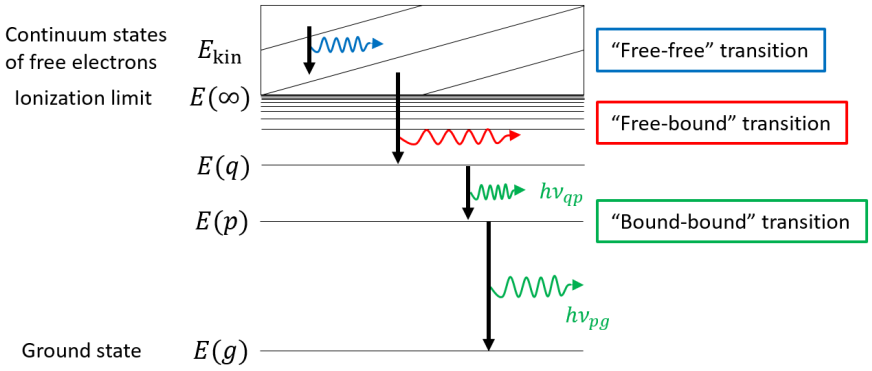

Figure 1.11. – *Energy level diagram for a given ion.*

Free-free radiation A major contribution to the overall emission in tokamak plasmas comes from "free-free" radiation or Bremsstrahlung. It takes its name from the German for braking radiation. It is an electromagnetic radiation emitted from the deceleration of an electron when it is deflected by the field of the ions. It is a "free-free" emission (the emitter is not bound to any ion or atom before and after the emission) which gives a continuous contribution to the spectrum. The expression of the PEC for Bremsstrahlung can be expressed as in [32]:

$$C_{ff}(\lambda) = A\frac{Z^2}{\lambda\sqrt{k_B T_e}} \times exp\left(\frac{-hc}{\lambda k_B T_e}\right) G_{ff}(Z, T_e, \lambda) \qquad [\text{photons.m}^3\,\text{s}^{-1}] \qquad (1.46)$$

where A is a proportionality factor, ff refers to the free-free interaction, E_H is the Rydberg energy and $G_{ff}(Z, T_e, \lambda)$ is called the Gaunt factor which is a quantum mechanical correction and depends also on the electron temperature, the wavelength and the charge Z [33]. In this equation and with the exception of the Gaunt factor, two terms depend on the wavelength of the measurement. For short wavelengths as it is the case for the Ar XVII spectral range between [3.93, 4.00] Å, the function

decreases with the exponential term stronger than λ^{-1} and dominates the shape of the Bremsstrahlung spectrum. The main contribution to the background measured in the Ar XVII spectrum comes from the Bremsstrahlung emission. The total Bremsstrahlung emissivity can thus be written as a double summation for all the ionization stages z of an impurity and for all impurities Z:

$$\epsilon_{ff} = n_e \times \sum_Z n_Z \times \sum_z f_{Z,z}(T_e) \times C_{ff}(\lambda) \tag{1.47}$$

where n_e and n_Z are respectively the electron and total impurity densities in m^{-3} and $f_{Z,z}(T_e)$ is the fractional abundance of the ion species defined as $f_{Z,z} = n_{Z,z}/n_Z$. This emissivity is expressed in photons.$\mathrm{m}^{-3}\,\mathrm{s}^{-1}$.

Free-bound radiation About the "free-bound" interaction, it refers to the radiative recombination of a free electron with an ion. For radiative recombination, an electron is captured in an excited energy level, leading to the emission of the exceeding energy as a photon:

$$A^*_{Z+1} + e^- \rightleftharpoons A_Z + \frac{hc}{\lambda} \tag{1.48}$$

The inverse process is photo-ionization: a photon is absorbed by an ion of charge Z and the ejection of a bound electron occurs if the photon energy is higher than the ion ionization limit.

Discrete emission Discrete contributions occur when ions relax from an excited energy level to a lower one via spontaneous decay. This is a radiative deexcitation and its inverse is a photoexcitation:

$$A^*_Z \rightleftharpoons A_Z + \frac{hc}{\lambda} \tag{1.49}$$

The emitted photon energy is equal to the energy difference between the initial (upper) and final (lower) levels, as described in Eq. 1.50. It is "bound-bound" interaction since the electron involved in the transition is bound to the ion before and after the radiation emission. After excitation, the atom may return to a lower excited state, or to the ground state, by emitting a photon with an energy $h\nu$ equal to the difference between the initial $E(i)$ and the final $E(j)$ energy levels:

$$h\nu = E(j) - E(i) \qquad [\mathrm{eV}] \tag{1.50}$$

This is the definition of an emission line, which are caused by a transition between well-defined energy states. The shape of these lines will be the subject of Sect. 1.3.5. We can characterize this interaction evaluating the density variation with time of the upper state (j) to a lower one (i):

$$\frac{d}{dt} n_Z(j) = -n_z(i) \times A(j \rightarrow i) \tag{1.51}$$

where $A(j \rightarrow i)$ is called the Einstein coefficient of spontaneous emission, expressed in photon.s^{-1} [34]. Deexcitation can happen in cascade from the orbital of the excited electron. We must then consider every radiative decay as a line emission that may be measured. The population density of a level j must be adapted to take into account this process:

$$\frac{d}{dt} n_Z(j) = -n_Z(j) \times A(j \rightarrow i) + n_z(i) \times X(i \rightarrow j) \tag{1.52}$$

with $X(i \rightarrow j)$ the electron collisional excitation rate expressed in Eq. 1.42.

1.3.2. Ionization equilibrium

In this Section, we will describe how the various ionization stages distribute themselves in a tokamak plasma. The quantity of interest here is the fractional abundance of all the ionization stages z of an ion of charge Z, already introduced previously as:

$$f_{Z,z} = \frac{n_{Z,z}}{\sum_z n_{Z,z}} = \frac{n_{Z,z}}{N_Z} \tag{1.53}$$

The fractional abundance of an ionization stage is the proportion of a specific ion species and represents the ratio of the density of this ion species to the total density of the element. The ionization equilibrium of a element is determined by the energy available in a plasma. This heating brings enough energy to the atoms composing the gas to ionize themselves. The higher the plasma temperature, the more the electrons in the deepest electron shells of the atoms can escape the electrostatic attraction of the nucleus. A charge-state distribution can then be computed from purely atomic physics and without transport. It relies on the assumption that there is a balance between ionization and recombination processes.

A fractional abundance of each ionization stage of a ion species can be calculated with the Aurora atomic physics package [35] and using OPEN-ADAS datasets [36] for Ar as shown in Fig. 1.12. The fractional abundance of the ionization stages of the ions Ar^{15+} and Ar^{16+} are wide (a few thousands of keV), the widest being for the He-like ions. The ionization states of an ion are also generally noted in terms of the number of electrons remaining, so that Ar^{17+} with only one electron remaining can be identified as H-like. Subsequently, Ar^{16+} will be referred to as He-like, Ar^{15+} as Li-like and so on. Note that the ionization stages can overlap for the temperature ranges studied. This indicates that they can exist at the same radial position in the plasma. The reason is that a system with many electrons has close successive ionization energies and the electron distribution is not mono-kinetic, it is assumed to be Maxwellian in tokamak plasmas.

The evolution equation of a population of charge Z is computed taking into account the various recombination and ionization between the neighbouring charge states

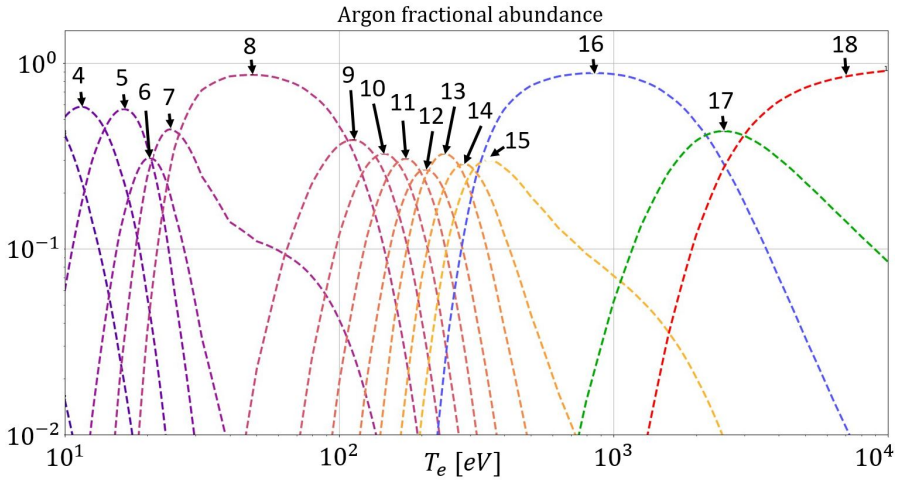

Figure 1.12. – *Fractional abundances of the Ar ionization stages as a function of the temperature [37].*

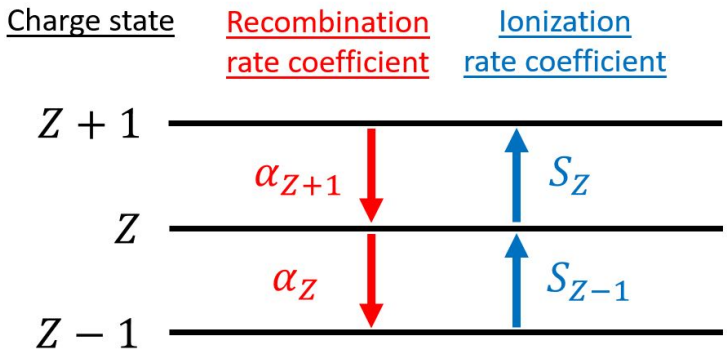

Figure 1.13. – *Ionization balance between some neighbouring ionization stages, being populated and depopulated by recombination α_Z and ionization processes S_Z.*

$Z+1$ and $Z-1$ as shown in Fig. 1.13:

$$\begin{aligned} \frac{d}{dt}n_Z &= n_e \times n_{Z-1} \times S_{Z-1} \\ &- n_e \times n_Z \times S_Z \\ &+ n_e \times n_{Z+1} \times \alpha_{Z+1} \\ &- n_e \times n_Z \times \alpha_Z \end{aligned} \tag{1.54}$$

where S_Z is the electron collisional ionization rate from an ionization stage Z to the upper one $Z+1$ and α_Z contains the contributions of the Radiative Recombination (RR) and Dielectronic Recombination (DR) rate coefficients from an ionization stage Z to the lower one $Z-1$. The resolution of this equation gives the first ionization stage, dependent on the temperature of the plasma. The task is repeated in the same way for higher ionization stages, taking into account the distribution of the previous.

To connect this subject on the modelled spectrum shown in Fig. 1.10, two ionization stages of argon are identified, Ar^{15+} and Ar^{16+}. According to the fractional abundances f_{Ar} in Fig. 1.12, one can easily deduce which ionization stages of these species populate the plasma for such temperatures. The H-like (Z=1, Ar^{17+}), He-like (Z=2, Ar^{16+}) and Li-like (Z=3, Ar^{15+}) ionization stages are the only three ionization stages that may emit spectral lines in the spectrum for this temperature range (the fully striped Ar^{18+} is also present but cannot emit). The notion of temperature dependence can be introduced here. The electron temperature dependencies of the fractional abundances of Ar^{15+} and Ar^{16+} are sufficiently different that an estimation of the plasma electron temperature can be made from intensity line ratios. Such computations will be dealt with in theory in Sect. 1.3.4.4 and in experimentally in Sect. 3.3.

1.3.3. Population equilibrium

The determination of the charge-state distribution of the ion species in a plasma is a difficult task because it requires a complex system of equations which describes the population and depopulation of all the energy levels by the collisional and radiative process between the energy levels of a same ionization stage and with the neighbouring. Three models are generally used to describe a plasma given specific density conditions. A brief description of these models is done here.

1.3.3.1. Local Thermodynamic Equilibrium

In a thermodynamic equilibrium, there is a principle of detailed balance which states that every atomic or ion process has its inverse and their probability is described by the associated rate coefficients. By the principle of detailed balance, the access to all the rate coefficients is not mandatory since one can be calculated from the other.

The computation of the population densities of all the energy levels within an ionization stage is done according to the Boltzmann law:

$$\frac{n_z(j)}{n_z(i)} = \frac{g_z(j)}{g_z(i)} exp\left(-\frac{E(i)-E(j)}{k_B T}\right) \tag{1.55}$$

where Z is the charge of the ion, i and j refer to the energy levels i and j for $j > i$ in an ion of charge Z and g_Z is called the statistical weight characterizing the number of electrons in the level considered. Here, the notion of temperature with the $k_B T$ term is important because it determines the population densities of the energy levels. The exponential in $1/x$ then shows that the higher energy levels j will be increasingly populated as the plasma temperature increases.

At high electron densities ($n_e > 10^{25} m^{-3}$), the collisional processes between free electrons and ions or atoms become more frequent than radiative decay from excited energy states in a specific ionization stage or from energy levels from higher ionization stages. The population density balance can be expressed between two energy levels i

and j with $E(j) > E(i)$ as:

$$n_e \times X_Z(i \rightarrow j) > A_Z(i \rightarrow j) \tag{1.56}$$

where n_e is the electron density, $X(i \rightarrow j)$ is the electron collisional rate coefficient and $A(i \rightarrow j)$ the Einstein coefficient of spontaneous decay. The population of the excited states j of energy $E(j)$ in an ion of charge Z in comparison with lower energy levels $E(i)$ follows the Boltzmann law defined in Eq. 1.55. It is also possible to describe the distribution over the neighbouring ionization stages in an ion by the Saha-Eggert equation [38]. The Saha equation describes the degree of ionization of any gas in a thermodynamic equilibrium as a function of temperature, density and atomic ionization energies. It is an extension of the Boltzmann factor used in Eq. 1.55 for continuum states:

$$\frac{n_{Z+1}(gr)}{n_Z(i)} = \frac{2}{n_e}\frac{g_{Z+1}(gr)}{g_Z(i)}\left(\frac{m_e k_B T}{2\pi\hbar^2}\right)^{3/2} exp\left(-\frac{E_{Z+1}(gr) - E_Z(i)}{k_B T}\right) \tag{1.57}$$

where the connection is made between the population density of an energy level i of the charge state Z and the ground state gr of the next ionization stage $Z+1$ and assuming a Maxwellian distribution of the velocity of the free electrons.

1.3.3.2. Coronal equilibrium

For low electron densities ($n_e < 10^{18} m^{-3}$), we make the approximation that the spontaneous radiative decay from an excited energy level j to a lower level i, and to the ground state by cascades, is quicker than the excitation. The spontaneous decays being much more frequent than the collisional excitation, the population of the ground state gr is dominant over all the other levels in this equilibrium. The population of any excited level i is always made from the ground state and is depopulated by radiative decays to lower levels. This leads to the following balance equation about the population of a level i for the Coronal equilibrium [39]:

$$n_Z(j) \times A_Z(j \rightarrow i) >> n_e \times n_Z(gr) \times X_Z(gr \rightarrow i) \tag{1.58}$$

where $A_Z(j \rightarrow i)$ represents the Einstein coefficient from an upper level j to all the lower energy levels i and $X_Z(gr \rightarrow i)$ is the electron collisional rate coefficient from the ground state gr to an higher level i. In this equilibrium model, and due to the low excitation process rates compared with the radiative decay rates, all the ions can be considered at their ground state gr and we still consider a Maxwellian distribution for the energy of the free electrons. The equation of the ionization population in steady-state, in the presence of three energy levels for $E(gr) < E(i) < E(j)$, can be written as follows:

$$\begin{aligned} \frac{d}{dt}n_i &= n_e \times n_{gr} \times X(gr \rightarrow i) \\ &+ n_e \times n_j \times A(j \rightarrow i) \\ &- n_e \times n_i \times A(i \rightarrow gr) \end{aligned} \tag{1.59}$$

1.3.3.3. Collisional-Radiative model

In tokamak plasmas, the electron density is considered to be neither at a high density limit nor at low density limits ($n_e \approx 10^{19} - 10^{20} m^{-3}$). It implies that there is a permanent competition for the density populations between the ionization processes between neighbouring charge states and the excitation processes within an ionization equilibrium. All these components depend on the population density of the ground states of the corresponding ions. As a result, we may express the intensity of any transition as the sum of the different contributions:

$$I^{tot} = I^{exc} + I^{recomb} + I^{ion} \tag{1.60}$$

where the terms of the equation refer respectively to the excitation, recombination and ionization processes. Here, all these processes have to be taken into account simultaneously to compute a general ionization and population equilibrium. The Collisional-Radiative model is the best suited to take these coupling effects into account. The general set of equations describing the population of a level i can be written as:

$$\begin{array}{rcll} \frac{d}{dt} n_Z(i) & = & n_e \sum_{h<i} n_Z(h) \times X_Z(h \rightarrow i) & [1] \\ & - & n_e \sum_{j>i} n_Z(i) \times X_Z(i \rightarrow j) & [2] \\ & + & \sum_{j>i} n_Z(j) \times A_Z(j \rightarrow i) & [3] \\ & - & \sum_{i>h} n_Z(i) \times A_Z(i \rightarrow h) & [4] \\ & + & n_e \sum_{h} n_{Z-1} \times S_{Z-1}(h \rightarrow i) & [5] \\ & - & n_e \sum_{gr} n_Z \times \times S_Z(i \rightarrow gr) & [6] \\ & + & n_e \sum_{gr} n_{Z+1} \times \alpha_{Z+1}(gr \rightarrow i) & [7] \\ & - & n_e \sum_{h} n_Z \times \alpha_Z(i \rightarrow h) & [8] \end{array} \tag{1.61}$$

with the electron collisional excitation rate coefficients X_Z between two levels of an ion of charge Z, the Einstein coefficient of spontaneous decay A_Z between two levels of an ion of charge Z, the collisional ionization rate coefficient S_Z between an excited level i of the ionization stage Z and the ground state of the next ionization stage (gr for $Z+1$ and h for $Z-1$) and finally α represents the combination of the radiative, dielectronic and three-body recombination rate coefficients. Fig. 1.14 represents the different processes taken into account in this model, associated to the ones numbered in Eq. 1.61.

1.3.4. Ar XVII spectral lines identification

A spectral line can be characterized by the upper and lower energy levels between which a bound electron has traveled. In Sect. 1.3.4.1, we remind some quantum physics basics to define an energy level. From the definition of these energy levels, we can identify the Ar^{16+} ionization stage of argon for example and identify the four main lines of the Ar XVII spectrum. We will define in Sect. 1.3.4.2 the association of the He-like argon spectral lines to their main denomination: resonance, intercombination and forbidden lines, and explain what it means. The definition of the intensity of the

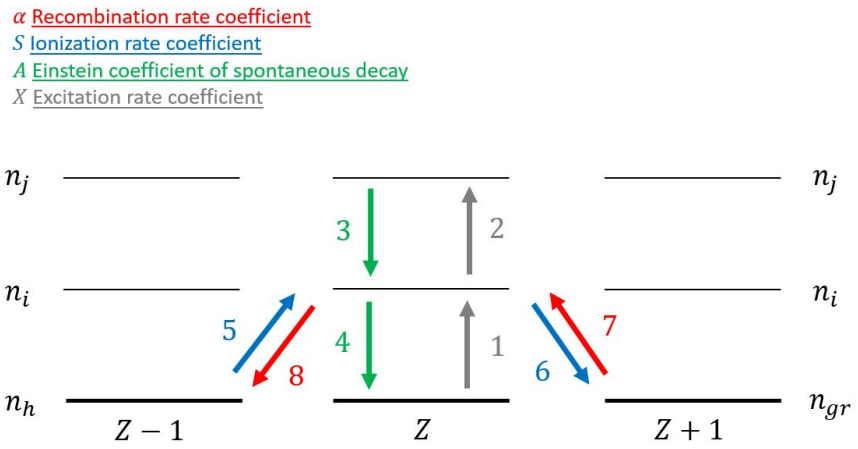

Figure 1.14. – *Collisional-Radiative model sketch with three different ionization stages* $(Z-1, Z, Z+1)$ *and their energy levels* (n_h, n_{gr}, n_i, n_j)*. The elementary processes are represented with arrays.*

resonance line is defined in Sect. 1.3.4.3, which is essential for the determination of the electron temperature and to describe in Sect. 1.3.4.4 all the other spectral lines measured as satellites of the resonance lines.

1.3.4.1. Definition of the energy levels

All the spectral lines that are modelled in Fig. 1.10 are from line emissions, described in Sect. 1.3.1.3, of the Ar ion species. In order to describe accurately the behavior of a many-electron ion, the quantum theory is used to determine the wavefunctions of the electrons. It is described by the Schrödinger equation:

$$H\psi = E\psi \tag{1.62}$$

where ψ and E are respectively the eigenfunction and the corresponding eigenvalue of the system and H the Hamiltonian. The simplest expression of H for a many-electron ion is:

$$H = \sum_i \left(\frac{-\hbar^2}{2m_e} \Delta_i - \frac{Ze^2}{4\pi\epsilon_0 r_i} \right) + \sum_i \sum_{j>i} \frac{e^2}{4\pi\epsilon_0 r_{i,j}} \tag{1.63}$$

where the first term refers to the intrinsic kinetic energy of the ith electron of mass m_e and with the reduced Planck constant $\hbar$, the second corresponds to the electrostatic attraction from the nucleus to the ith electron at a distance r_i and of total ion charge Z and the last term is the electron-electron interaction of distance $r_{i,j}$ for $Z > 1$. The eigenfunctions associated with the Hamiltonian are spatial functions and can be described by quantum numbers. The quantum state of electrons in atoms is entirely defined by those quantum numbers:

- n is the principal quantum number ($n > 0$, $n \in \mathbb{N}$) and describes the energy level of the electron in the atom. We call a shell a group of orbitals with the same

principal quantum number n.

- l is the orbital quantum number ($0 \leq l \leq n-1$, $l \in \mathbb{N}$) and represents the orbital angular momentum of the electron around the nucleus. This number defines the number of sub-shells which can contain at least $2(2l+1)$ electrons. For a system with many electrons, it is necessary to define also the total orbital momentum number $\vec{L} = \sum_i \vec{l}_i$;
- m_l is the magnetic quantum number, $-l \leq m_l \leq l$, and is associated to the projection of the orbital angular momentum on a specific axis $L_z = m_l \hbar$;
- s is the spin quantum number with $s = 1/2$ for electrons and represents the intrinsic angular momentum of the electron. For a system with many electrons, we use $\vec{S} = \sum_i \vec{s}_i$;
- m_s is the spin magnetic quantum number with $m_s = \pm 1/2$;
- J is the total angular momentum, $\vec{J} = \vec{L} + \vec{S}$, and take the values: $|L-S| \leq J \leq L+S$;

The combination of the orbitals of all the electrons is called a configuration. Two important rules must be respected when associating the electrons of an atom with their sub-shells: Pauli's exclusion principle which forbids two electrons from being placed in the same orbital with the same spin number s, and Klechkowski's rule which characterises the order in which the electrons are filled in the sub-shells.

With these numbers, and without going into theory, we can define an electronic configuration for all the electrons in an atom or ion, determined by the orbital and spin of each electron. These configurations describe each electron as moving independently in an orbital in an average field generated by the other orbitals. Let us take an example, the ground state $1s^2$ of Ar^{16+} (Z=2). The sub-shell $1s$ corresponds to $n = 1$ and $l = 0$, so it can contains only two electrons. Both electrons have the same orbital number $l_1 = l_2 = 0$ and the total orbital number $L = l_1 + l_2$ is zero. The total spin number S is also zero because they can not belong to the same sub-shell with the same spin according to the Pauli principle of exclusion, $s_1 = s_2 = \frac{1}{2}$ and $m_{s_1} = -m_{s_2} = \frac{1}{2}$. Finally we find $J = 0$. To describe each configuration, we use the spectroscopic term $^{2S+1}L_J$ representing the set of quantum numbers associated with the angular momentum (orbital and spin) for an electronic configuration with the LS (Russell-Saunders) coupling. This leads to the following for $1s^2$: $^{2S+1}L_J = {}^1S_0$, that is associated to the ground state of the He-like Ar transitions. Table 1.3 summarizes the transitions responsible

Configuration	Multiplet (^{2S+1}L)	Line (J value)	Key	λ [40] Å	λ [41] Å	λ [42] Å
$1s^2$ - 1s 2p	^1S - ^1P	0 - 1	w	3.94906	3.9493	3.94906
	^1S - ^3P	0 - 2	x	3.96586	/	3.96586
	^1S - ^3P	0 - 1	y	3.96936	3.9696	3.96936
$1s^2$ - 1s 2s	^1S - ^3S	0 - 1	z	3.99415	/	3.99415

Table 1.3. – *Energy configuration of the He-like Ar spectral lines and their corresponding wavelengths in* Å *and key letters proposed by A.H. Gabriel [43].*

for the He-like Ar spectral lines seen in Fig. 1.10 and also their theoretical wavelength.

The classification of these lines has been proposed by [43] and is still used nowadays, as we shall see for the satellite line letters in Sect. 1.3.4.4.

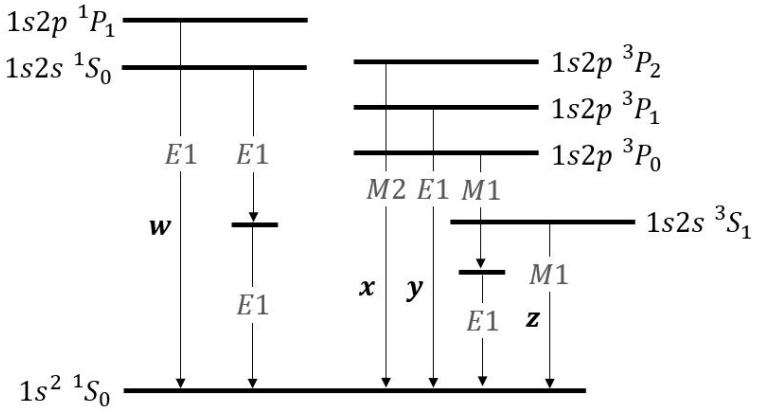

Figure 1.15. – *Energy diagram for the n=1 and n=2 states for He-like ion species.*

1.3.4.2. Electromagnetic multipole transitions

Generally, the radiative emission is governed either by an electric E_x or by a magnetic M_x multipole operator characterizing the transition, following the electric dipole approximation that is used to describe the photons. Selection rules are applied to allow or forbid specific transitions as a function of the change in the quantum numbers J, L and S and with respect to the conservation laws. The number x corresponds to the change of total angular momentum number J of the transition, E1 for an electric dipole, E2 for an electric quadrupole or E3 for an electric octupole. On Table 1.4

Allowed transitions I_x	Dipole		Quadrupole	
	Electric E1	Magnetic M1	Electric E2	Magnetic M2
Total angular momentum J	$\Delta J = 0, \pm 1$ $(0 \nleftrightarrow 0)$		$\Delta J = 0, \pm 1, \pm 2$ $(0 \nleftrightarrow 0, 0 \nleftrightarrow 1, \frac{1}{2} \nleftrightarrow \frac{1}{2})$	
Total orbital momentum L	$\Delta L = \pm 1$	$\Delta L = 0$	$\Delta L = 0, \pm 2$	$\Delta L = \pm 1$
Total spin number S	if $\Delta S = 0$ $\Delta L = 0, \pm 1$	if $\Delta S = 0$ $\Delta L = 0$	$\Delta S = 0$ $\Delta L = 0, \pm 1, \pm 2$ $(0 \nleftrightarrow 0, 0 \nleftrightarrow 1)$	

Table 1.4. – *The selection and exception rules for the discrete electronic transitions. [44]*

are summarized the selection rules for the L-S coupling scheme for the electric and magnetic multipole transitions. From the change in the quantum numbers between the energy levels for the He-like Ar spectral lines, we can deduce their electromagnetic

multipole denomination, as represented in Fig. 1.15. For the He-like Ar lines referenced in Table 1.3, we can attribute an electromagnetic multipole transition to each with the following quantum numbers changes:

- w line ($^1P_1 - ^1S_0$): $\Delta J = 1 \rightarrow$ E1 or M1, $\Delta S = 0$, $\Delta L = 1 \rightarrow$ E1
- x line ($^3P_2 - ^1S_0$): $\Delta J = 2 \rightarrow$ E2 or M2, $\Delta S = 1$, $\Delta L = 1 \rightarrow$ M2
- y line ($^3P_1 - ^1S_0$): $\Delta J = 1 \rightarrow$ E1 or M1, $\Delta S = 1$, $\Delta L = 1 \rightarrow$ E1
- z line ($^3S_1 - ^1S_0$): $\Delta J = 1 \rightarrow$ E1 or M1, $\Delta S = 1$, $\Delta L = 0 \rightarrow$ M1

where the w line is the resonance line, the x and y are the intercombination lines and z the forbidden one. The $^3P_1$ component is the upper level of the by far the strongest component y of the intercombination line and $^3P_2$ is the upper level of the weakest component x. If the conditions for the electric dipole radiative transitions are not fulfilled, the dipole transition is called forbidden. The transitions with a change of spin $\Delta S = 1$ are called inter-combination transitions. However, the forbidden lines are not literally forbidden, the transition probabilities are generally a few orders of magnitude less probable than the dipole ones and because of the change of spin S, they are called intercombination lines. We will take a closer look at this probability principle in the next Section where we will introduce the PECs.

One can also notice three other transitions. From the $1s2s\ ^1S_0$ level, a two-photons transition happens to the ground state and increases the intensity of the w line at very high densities [45]. Same density condition for the population of the metastable $1s2s\ ^3S_1$ level that can be depopulated to the triplet $^3P_{0,1,2}$. The $1s2p\ ^3P_0$ level cannot decay to the ground state since it is a magnetic dipole transition $M1$ but can decay to $1s2s\ ^3S_1$.

1.3.4.3. Intensity of the resonance line

The tokamak plasmas have to be studied in the context of the Collisional-Radiative model as introduced in Sect. 1.3.3.3. We saw that the set of equations Eq. 1.61 appears delicate to solve, compared with the population density set of equations for the Local Thermodynamic Equilibrium (LTE) and Coronal models, because all the processes have to be taken into account at the same time. We introduced in Sect. 1.3.1.2 how we can express the collisional excitation rate coefficient is computed in Eq. 1.42 and what are the main dependencies. The electron temperature appears to be the main dependency of all the processes important in this context and the intensity of the resonance line can be approximated as:

$$I_w = n_e \times n_Z \times \frac{\gamma(T_e)}{g(i)} \times \left(\frac{E_H}{k_B T_e}\right)^{1/2} \times exp\left(\frac{-E_w}{k_B T_e}\right) \tag{1.64}$$

where $g(i)$ is the statistical weight of the initial level, n_e and n_Z are respectively the density of the electrons and of the species in the plasma, $\gamma(T_e)$ is the effective collision strength defined in Eq. 1.43 and E_w is the energy of the resonance transition.

To take into account all the processes that participate to the overall intensity of the resonance line in the Collisional Radiative (CR) model, various atomic codes have been

created for this purpose. High-precision codes taking into account a wide range of excitation and deexcitation processes that can compute high-fidelity theoretical spectra, for a given species and in given plasma conditions. But none is perfect and the line intensities and/or wavelengths can be off in proportions that can still be measurable for high-resolution spectrometers. Those high-fidelity codes like Superconfiguration Collisional Radiative Atomic Model (SCRAM) [46] involve long computation times. The tokamak community is used to a more practical, although somewhat less accurate, approach. Regular use is made of codes that tabulate a Maxwellian-averaged PEC as a function of electron temperature and density. One of the most frequently used database is ADAS [2] and its open version OPEN-ADAS [3].

Computing those PECs can be done using a variety of assumptions. This approach has the advantage of de-correlating the PEC tabulation, which can imply specialists discussions and long computations, from the needs of the end-user who can simply and quickly interpolate on a set of pre-defined coefficients. As a result, care must be taken by the user to chose wisely the set of PEC files to use depending on the experimental conditions. The results of these algorithms provide PEC for all the different contributions of these processes at a given wavelength. From this, the emissivity of a transition line can be written as the following:

$$\epsilon_Z(\lambda_{ij}) = n_e \times n_Z \times f_{Z,z}(T_e) \times PEC_{Z,ij}(n_e, T_e) \qquad [\text{photons.s}^{-1}\,\text{m}^{-3}] \qquad (1.65)$$

where n_Z is the impurity density, $f_{Z,z}$ is the fractional abundance of the ionization stage z of the species Z (see Fig. 1.12 for the Ar ionization stages) and $PEC_Z(\lambda_{ij})$ is the PEC of the targeted line transition of wavelength λ_{ij}. A PEC depends on the electron temperature T_e and density n_e. We can compare the PEC datasets for the ArXVII resonance line w and forbidden line z as shown in Fig. 1.16. The source files are obtained from ADAS datasets [47] [48].

The various atomic processes plotted, the electron collisional excitation in blue, the electron collisional ionization in red and the dielectronic recombination in green, do not have the same importance in the line emission. The product of the Ar^{16+} and the electron collisional excitation process for the resonance line w is greater by a factor 14 at $T_e = 2$ keV than the recombination process for the resonance line emission. This process is therefore considered to be the dominant but it is not for the forbidden line z. Indeed, a factor 2.8 only separates the excitation and the recombination process values for an electron temperature T_e of 2 keV. We can consider that all three processes participate to the forbidden line z.

Finally, there is only a factor three of difference between the excitation components between the two line emissions. Despite the forbidden nature of the z line, its measurement remains only slightly less probable over the electron temperature ranges of tokamak plasmas. The term forbidden refers to the formal selection rules and correspond to the fact that the electric dipole term for that transition is zero, but the transition still happens through higher-order terms at a lower rate. As shown in the Ar

2. See for more information: https://www.adas.ac.uk/
3. See for more information: https://open.adas.ac.uk/

XVII spectrum in Fig. 1.10, this spectral line is well measured, even though it is very close to a satellite j line, $\Delta\lambda \approx 1 \times 10^{-3}$ Å.

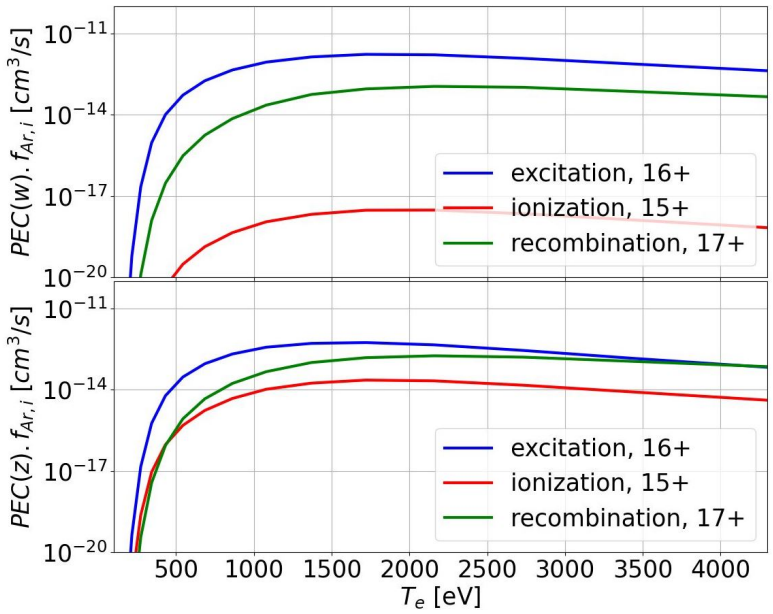

Figure 1.16. – *Product of the PECs with the fractional abundance for (top) the He-like Ar resonance line w and (bottom) the forbidden line z, for $n_e = 5.0 \times 10^{19}$ m^{-3} and $T_e \in [0.1, 4.3]$ keV. The various components of the PECs, electron collisional excitation (blue) and ionization (red), dielectronic recombination (green), are multiplied with the fractional abundance of the corresponding ion species.*

Through the description of the Collisional-Radiative model, all the collisional and radiative processes exposed earlier become important to outline the various states in which the argon species can be found in tokamak plasmas. We saw that the system of equations needed to compute the electron populations for all the ionization stages and energy levels is very complicated and a large data set must be used. These datasets are a milestone to define a line emissivity, which depends on the electron density and temperature mainly. A first introduction of the spectral lines measured has been done here, through the comparison of the PECs for two Ar^{16+} lines in Fig. 1.16. As the simulated spectrum shown at the very beginning of this Section in Fig. 1.10 shows a greater number of lines than those of He-like argon, we need to introduce them here.

1.3.4.4. Satellite lines

As described in Sect. 1.3.1.1, the dielectronic satellite lines come from the stabilisation process of dielectronic recombination. They are not well constrained within the framework of the energy level diagrams because the measured photon results from some transitions within a dielectronic recombination or inner-shell excitation by electrons or photons [49]. The dielectronic satellite lines appear generally on the

Configuration	Multiplet	Line	Key	λ [40]	λ [41]	λ [42]
$1s^2$ 2p - 1s $2p^2$	^2P - ^2P	3/2 - 3/2	a	3.98573	3.9858	3.9857
		1/2 - 3/2	b	3.98167	3.9818	3.9817
		3/2 - 1/2	c	3.98979	3.9899	3.9898
		1/2 - 3/2	d	3.98572	3.9858	3.9857
	^2P - ^4P	3/2 - 5/2	e	4.01250	4.0126	4.0125
		3/2 - 3/2	f	4.01450	4.0146	4.0145
		1/2 - 3/2	g	4.01038	4.0105	4.0104
		3/2 - 1/2	h	4.01631	4.0164	4.0163
		1/2 - 1/2	i	4.01219	4.0123	4.0122
	^2P - ^2D	3/2 - 5/2	j	3.99380	3.9939	3.9938
		1/2 - 3/2	k	3.98981	3.9899	3.9898
		3/2 - 3/2	l	3.99388	3.9939	3.9939
	^2P - ^2S	3/2 - 1/2	m	3.96561	3.9656	3.9656
		1/2 - 1/2	n	3.96159	3.9616	3.9616
$1s^2$ 2p - 1s $2s^2$	^2P - ^2S	3/2 - 1/2	o	4.07272	4.0730	4.0727
		1/2 - 1/2	p	4.06848	4.0688	4.0685
$1s^2$ 2s - 1s 2p 2s	^2S - $(^1P)^2P$	1/2 - 3/2	q	3.98130	3.9815	3.9813
		1/2 - 1/2	r	3.98340	3.9835	3.9834
	^2S - $(^3P)^2P$	1/2 - 3/2	s	3.96760	3.9677	3.9676
		1/2 - 1/2	t	3.96850	3.9686	3.9685
	^2S - ^4P	1/2 - 3/2	u	4.01480	4.0150	4.0148
		1/2 - 1/2	v	4.01590	4.0161	4.0159

Table 1.5. – *Theoretical transition and wavelengths of the He-like n = 2 Ar dielectronic satellites lines. The wavelengths are in* Å.

long wavelength side of the so-called parent line, i.e. here the Ar^{16+} resonance line w. Depending on the orbital of the captured electron, the spectral spacing between the satellite line and the parent line vary, as well as the intensity. The He-like $n = 2$ dielectronic satellite lines are resumed in Table. 1.5, where they are labelled with letters from a to v from the Gabriel notation [43]. Fig. 1.17 illustrates the energy level diagram of H-like, He-like and Li-like ions where the lines described in Table 1.5 can be found.

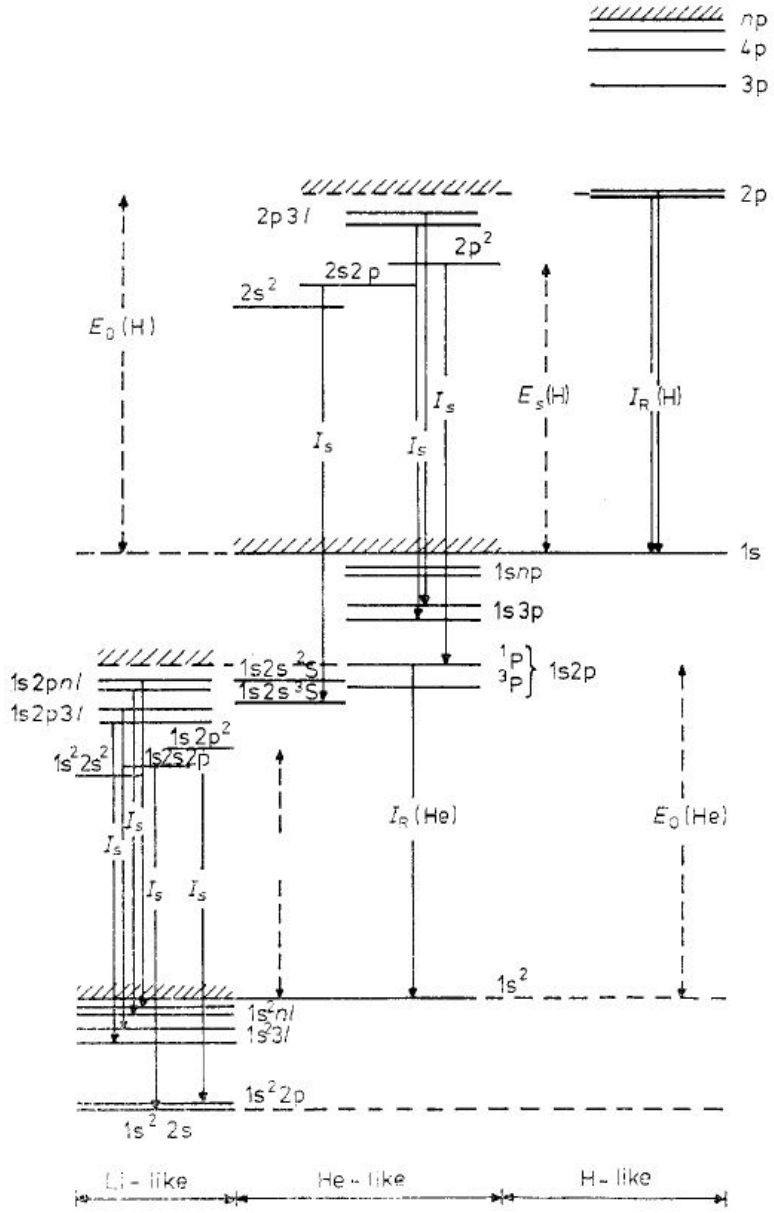

Figure 1.17. – *Energy level diagram of H-like, He-like and Li-like ions with the resonance transitions I_R and corresponding satellite transitions I_S [50].*

The population density N_S of the states at the origin of the satellite lines is deter-

mined by the competition between dielectronic capture, autoionization and radiative decay processes, as described in Sect. 1.3.1.1, as:

$$N_S \times A^{tot}(s) = n_e \times n_Z \times C^{di} \tag{1.66}$$

where n_Z and n_e are respectively the population density of the recombined ion and the electron density, $A^{tot}(s)$ represent the total decay rate coefficient of the satellite state s by auto-ionization A^a and spontaneous decay A^{rad} and C^{di} is the dielectronic capture rate coefficient, depending on the electron energy distribution which is assumed to be Maxwellian for tokamak plasmas. The intensity of the satellite line s to a any final state j can be expressed as follows:

$$I_s(j) = n_Z \times n_e \times C^{di} \times \frac{A^{rad}(s \rightarrow j)}{A^{tot}(s)} \tag{1.67}$$

where the expression of the dielectronic capture rate coefficient can be retrieved approximately from [50] as:

$$C^{di} = \left(\frac{E_H}{k_B T_e}\right)^{3/2} \times \frac{g(s)}{g(gr)} \times exp\left(\frac{-E(s)}{k_B T_e}\right) \times A^a(s) \tag{1.68}$$

where $g(s)$ and $g(gr)$ are respectively the statistical weights of the satellite line s in the recombined ion and of its ground state gr and $E(s)$ is the energy difference between the energy levels s and gr. The expression of the intensity ratio between any dielectronic satellite line S and the excitation part of the resonance line w can thus be found from the ratio between Eq. 1.67 and Eq. 1.64:

$$\frac{I(S)}{I(w)} = F_1(T_e) \times F_2(S) \tag{1.69}$$

where the first function $F_1(T_e)$ contains all the electron temperature dependency and has the form:

$$F_1(T_e) \propto \frac{1}{\gamma(T_e)} \times \left(\frac{E_H}{k_B T_e}\right)^2 \times exp\left(\frac{\Delta E_{sw}}{k_B T_e}\right) \tag{1.70}$$

The second function $F_2(S)$ is a function that characterizes the satellite transition containing all the decay rate coefficients. The temperature function $F_1(T_e)$ has a double temperature dependency but due to the low value of $\Delta E_{sw} = E(s) - E(w)$, the main dependence is from the $1/T_e$ term. As they belong to different ionization stages of argon, the ratio between the parent and the dielectronic satellite is related to the electron temperature and we will see later how we can extract this quantity.

1.3.5. Line profiles

The three more important quantities to extract from the spectral lines measured are the brightness, the width and the central wavelength, or frequency of the line. We saw in Eq. 1.65 that the emissivity of a spectral line, a local quantity expressed in

photons per unit of time and volume (in photons.s^{-1} m^{-3}), depends on the electron density n_e and temperature T_e through the fractional abundance of the charge state of the emitting ion and the PEC of the line. The line brightness is thus defined as the integration of the local emissivity along a photon path:

$$\begin{aligned} B(\lambda) &= \frac{1}{4\pi}\int \epsilon_Z(\lambda) dl \\ &= \frac{1}{4\pi}\int n_e \times n_Z \times f_Z(T_e) \times PEC_Z(\lambda, n_e, T_e) dl \qquad [\text{photons.s}^{-1}\,\text{m}^{-2}\,\text{sr}^{-1}] \end{aligned} \tag{1.71}$$

This quantity can be used to determine density profiles in space and time of the emitting ions. Such computations will be presented in Sect. 3.4.

Marchuk [28] also describes analytically the line shape of a spectral line $L(\lambda)$. The choice of the right line shape to describe the spectral lines is essential as the amplitude, the half width and the central wavelength are related to the emitter density, temperature and its velocity respectively. The most common line shapes used in soft X-ray spectroscopy are Lorentzian and Gaussian functions. These two functions are related to two broadening mechanisms: the natural and Doppler broadening.

The natural broadening is linked to the finite lifetime of the excited states at the origin of the spectral lines measured. According to the Heisenberg uncertainty principle, the uncertainty ΔE of the energy E of a level is connected to the uncertainty Δt of the time during which the measurement can be done as:

$$\Delta E \Delta t \geq \frac{\hbar}{2} \tag{1.72}$$

The finite duration an electron spends in this level is the lifetime of an excited state. It can be expressed as the inverse of the corresponding radiative rate coefficient from this level to another, as written in Eq. 1.51:

$$\tau(p) = \frac{1}{A(p \rightarrow)} \qquad [\text{s}] \tag{1.73}$$

where $A(p \rightarrow)$ is the Einstein radiative coefficient from an excited level p and expressed in s^{-1}. The higher $A(p \rightarrow)$, the less time Δt an electron spend on the level and the width of the line ΔE becomes stronger. The wavelength distribution for the natural lifetime of an excited level is described by a Lorentzian function and can be found in [30]:

$$f_L(\lambda) = \frac{A}{2\pi} \frac{\Delta\lambda}{(\lambda - \lambda_0)^2 + \frac{\Delta\lambda_L}{2}^2} \tag{1.74}$$

where A is the amplitude, λ_0 the center of the peak and $\Delta\lambda_L$ the Full Width at Half Maximum (FWHM) of the profile defined as:

$$\frac{\Delta\lambda_L}{\lambda_0} = \frac{\lambda_0}{2\pi c}\left[\frac{1}{\tau(p)} + \frac{1}{\tau(p)}\right] = \frac{\lambda_0}{2\pi c}\left[A(p \rightarrow) + A(q \rightarrow)\right] \tag{1.75}$$

The Doppler broadening comes from the Maxwellian distribution of ions in the plasma and the random motion of the particles due to their temperature T_i. Let us consider a small volume of plasma in which ions are emitting a specific photon energy in a isotropic way. Depending on the direction of propagation as a function of the direction of measurements, the Doppler effect changes the observed wavelength of the photons. This effect leads to the broadening of the spectral line. The Maxwellian distribution of the ions can be modelled from its definition in Eq. 1.36:

$$f(v)dv = \sqrt{\frac{m_i}{2\pi k_B T_i}} exp\left[\frac{-m_i v^2}{2k_B T_i}\right] dv \tag{1.76}$$

The equivalence between wavelength and velocity allows to write the wavelength distribution of the photons emitted by the ions:

$$f(\lambda)d\lambda = f(v)dv \tag{1.77}$$

$$f(\lambda) = \sqrt{\frac{m_i c^2}{2\pi k_B T_i}} \frac{1}{\lambda_0} exp\left[\frac{-m_i c^2}{2k_B T_i}\left(\frac{\lambda-\lambda_0}{\lambda_0}\right)^2\right] \tag{1.78}$$

where the Doppler shift has been introduced as:

$$\Delta\lambda_{shift} = \frac{v}{c} \times \lambda_0 \tag{1.79}$$

As we can notice, the width of the spectral line depends on the ion temperature. The Doppler width can thus be expressed as:

$$\Delta\lambda_{width} = \sqrt{\frac{2k_B T_i \times \lambda_0^2}{m_i c^2}} \tag{1.80}$$

This leads to a similar writing of the wavelength velocity distribution of the ions to a normal distribution as:

$$f(\lambda) = \frac{1}{\sqrt{\pi} \times \Delta\lambda_{width}} exp\left[-\frac{(\lambda-\lambda_0)^2}{2\Delta\lambda_{width}^2}\right] \tag{1.81}$$

Thus, the FWHM of the Gaussian line shape has the following Doppler broadening dependency:

$$FWHM_G = 2\sqrt{2ln(2)} \times \Delta\lambda_{width} \approx 2.35 \times \Delta\lambda_{width} \tag{1.82}$$

whereas the FWHM of the Lorentzian line shape is found smaller, as equal to:

$$FWHM_L = 2 \times \Delta\lambda_{width} \tag{1.83}$$

Taking into account these two mechanisms in the shape of the measured lines would lead us to use a Voigt function which is the product of convolution of a Gaussian and a Lorentzian. An approximated relation is given in the following, which does not have a

simple analytic form beyond the integral, where we write $\Delta\lambda_{width} = \Delta\lambda_D$:

$$f_V(\lambda) = \frac{a}{\pi}\sqrt{\frac{4ln(2)}{\pi}}\frac{1}{\Delta\lambda_D}\int_{-\infty}^{\infty}\frac{exp(-t^2)}{a^2+(x-t)^2}dt \tag{1.84}$$

where the wavelength variable x is defined as:

$$x = \frac{\lambda-\lambda_0}{\Delta\lambda_D}2\sqrt{ln(2)} \tag{1.85}$$

and the a parameter defines the relative importance of Gaussian over Lorentzian component:

$$a = \frac{\Delta\lambda_L}{\Delta\lambda_D}\sqrt{ln(2)} \tag{1.86}$$

Moreover, the Doppler broadening is the dominant broadening mechanism for tokamak plasmas. The lifetime of an X-ray state is small because of its dependence on the atomic number Z [51], leading to small energy level widths. The natural broadening can thus be neglected and the Ar XVII spectral lines are approximated with Gaussian functions.

1.4. Conclusions

In this chapter, we focus on the promise of thermonuclear fusion as a source of electricity generation in the medium to long term. The neutrons from D-T fusion reactions have a much higher energy than those from fission reactions, which could improve the efficiency of power stations. We have seen that tokamaks are a mean of studying plasmas and we have introduced WEST, on which this thesis is based. In order to study a plasma, it is necessary to have diagnostics that can measure any information that comes out of it, in particular the temperature of the electrons and ions that make it up. Various diagnostics exist for this purpose and here we studied what soft X-rays could provide.

The plasma emission lines are modelled by a Gaussian function whose width and position give us information about the temperature and rotation speed of the ions in the plasma (via the broadening and Doppler shift of the lines). We have also seen that not all the lines measured belong to the same ionic species, and as their presence in the plasma depends on the electron temperature, this quantity can be deduced from spectral line intensity ratios. To do so, the emissivity of a spectral line has been expressed as a function of the electron and impurity densities, the fractional abundance of the emitting ion and the PEC which represents the probability of a photon emission for a particular transition. It is through the different temperature dependences of each measured intensity, coming from different ionization stages of an impurity, that we can compute the electron temperature of the plasma.

2. Ar XVII spectrum measurement and modelling

Sommaire

2.1. Introduction . . . 81
2.2. The XICS spectrometer . . . 81
2.2.1. X-ray photons diffraction by crystals . . . 82
2.2.1.1. The Bragg equation . . . 82
2.2.1.2. Choice of the crystal . . . 84
2.2.1.3. The Rocking-Curve . . . 85
2.2.2. Johann configuration of X-ray spectrometer . . . 90
2.2.2.1. Outline of the diagnostic geometry . . . 90
2.2.2.2. Line position on the detector calculation . . . 93
2.2.3. X-ray photons measurement . . . 99
2.2.3.1. Beryllium filter . . . 100
2.2.3.2. Two-dimensional semi-conductor detector . . . 101
2.2.4. Diagnostic resolution power . . . 103
2.2.4.1. Spectral and spatial resolutions . . . 103
2.2.4.2. Doppler shift and broadening resolution . . . 105
2.2.5. Limitations of the spectrometer . . . 107
2.2.5.1. Differences caused by the different crystals . . . 107
2.2.5.2. Broadening due to the detector position . . . 109
2.3. Spectrometer commissioning . . . 109
2.3.1. Alignment . . . 110
2.3.2. Argon impurity injection . . . 112
2.3.3. Discussion on calibration methods . . . 113
2.3.4. Discussion about defective detector modules . . . 115
2.4. Spectral modeling . . . 117
2.4.1. Preparation of the data . . . 117
2.4.1.1. 2D image transformation . . . 117
2.4.1.2. Data selection and signal-to-noise . . . 119
2.4.2. 2D images processing . . . 120
2.4.2.1. Spectral constraints . . . 120
2.4.2.2. The Bremsstrahlung background . . . 122
2.4.2.3. The multi-Gaussian function . . . 125
2.4.2.4. Vertical binning with B-splines function . . . 127

2.4.3. Tomographic inversions 129
2.4.4. Discussion of the effect of magnetic equilibrium reconstruction on inverted amplitudes 132
2.4.5. Discussion of the modelling of the Ar dielectronic satellite group of lines $n = 3$ and $n = 4$ 135
2.5. Conclusions 138

2.1. Introduction

We have introduced in the last Chapter a theoretical ArXVII spectrum in Fig. 1.10 computed by [28]. From this spectrum, several plasma physical quantities can be extracted to measure the electron and ion temperature profiles, in time and space, in tokamak plasmas. Those quantities can be evaluated from the measurements of highly ionized mid-Z elements emission such as He-like and H-like Ar. The Ar emission has been introduced because its ionization stages exist over a broad range of electron temperatures in tokamak plasmas. The Ar XVII spectrum has also been extensively studied to measure these quantities [52]. In order to extract as much information as possible, we need a spectrometer with certain specific features. The entire wavelength scale is narrow, $\sim 5\times10^{-12}$ m, and the spacing between the closest lines is even smaller, of the order of $\sim 10^{-13}$ m. The width of the lines is also narrow and large differences in intensity are expected between the Ar^{15+} and Ar^{16+} lines.

The spectrometer must then be able to resolve these closely-spaced lines in a very small energy range, while measuring a large number of photons. Several lines of sight should be available to compute radial profiles of the temperature. At the same time, we need to be able to filter out all the other photons with a wide range of wavelengths coming from the plasma to obtain a spectrum with the best possible Signal-to-Noise Ratio (SNR). And equally important, all the instrument components must be able to operate reliably over time in a tokamak environment. All these criteria have been well though during the diagnostic design, as well as the time resolution and the stigmatic criterion of the measured images.

In this chapter, each component is described in Sect. 2.2.1 to show its usefulness for the measurement of this spectrum under the conditions described previously. In Sect. 2.3, the commissioning of the instrument is described and its operation during experimental campaigns. Finally, we will describe in Sect. 2.4 the fitting algorithm that has been implemented to process the Ar XVII spectrum.

2.2. The XICS spectrometer

In this Section, we describe what are the main components of the instrument, essential to measure the Ar XVII spectrum. The dispersing element is chosen to be a Bragg crystal of which the diffraction properties are described in Sect. 2.2.1. The crystal characteristics are important because they determine the final configuration of the spectrometer. In this case, the chosen configuration is the Johann one, which allows to separate the foci to obtain both spectral focusing and a spatial image on the detector. This is introduced in Sect. 2.2.2. Finally, information about the filtering and collecting elements are given in details in Sect. 2.2.3. Finally, the spatial and spectral resolutions of the spectrometer are studied in Sect. 2.2.4 via computations with the XICS synthetic diagnostic implemented.

2.2.1. X-ray photons diffraction by crystals

The most important element of a spectrometer is the dispersing element because its choice determines not only the energy range of the photons collected, but also the spectral resolution of the diagnostic. It also needs to be suitable for measuring the emission of low-concentration impurities in plasma. This is performed by using Bragg crystals here. The Bragg reflections from crystals are the most common way to select X-ray energies around 1 keV, where they are highly efficient. Indeed, crystals can achieve an energy resolution of $\Delta E/E \approx 10^{-4}$, which is highly suited for very small spectral line spacing.

2.2.1.1. The Bragg equation

To understand the physical principle of the Bragg diffracting crystals, we should begin by demonstrating the Bragg relation. To simplify how such crystals work, we will describe them as mono-chromatic and mono-angular mirrors.

If we consider two atoms in a single row scattering a wave with an angle of incidence $\theta_i = 90° - \theta_B$. There is a constructive interference between the two scattered waves if the step difference, i.e. the difference in the path travelled by the two scattered waves, is equal to an integer number of wavelength, for a scattering angle equal to the angle of incidence. Let's now consider an infinite row of atoms. Constructive interference occurs between all the waves scattered by the atoms in the row if the path difference is equal to an integer number of wavelengths, changing from constructive to destructive interference as the scattering angle increases. We then move from a scattering process to a diffraction process involving a large number of atoms in a row. Atoms scatter in all directions in space. There is a symmetry of revolution around the row of atoms, and the diffracted rays form a cone whose axis coincides with the row for all step differences for an integer number of wavelengths. This number corresponds to the order n of diffraction. For each direction of the cone, we need the same step difference to obtain the same constructive interference.

This situation is shown in Fig. 2.1. The final direction of diffraction is produced at the intersection of each diffraction cone, i.e. for each order n of diffraction, produced by the diffraction on each direction of the medium. The intensity diffracted then decreases with increasing diffraction angle. The angle of diffraction is defined by the wavelength of the incident beam but also by the inter-reticular spacing between the planes of the crystal. The empirical law to compute the diffraction angle has been determined by [53]. This is how the Bragg law can be found. Fig. 2.2 represents a two-dimensional section of a crystal where the planes are separated by a inter-reticular spacing d_{hkl}. An incident beam is focused on these planes at an angle θ_B. Considering that all planes have an infinite number of atoms, they diffract the incident beam with the same diffraction angle as the incident one. Each diffracted wave by each plane interferes with each other if a constructive interference occurs. The lower waves, i.e. those diffracted by the low-level planes, have a step difference with respect to the first-level wave, equal to the sum of the distances AB and BC, both equal to

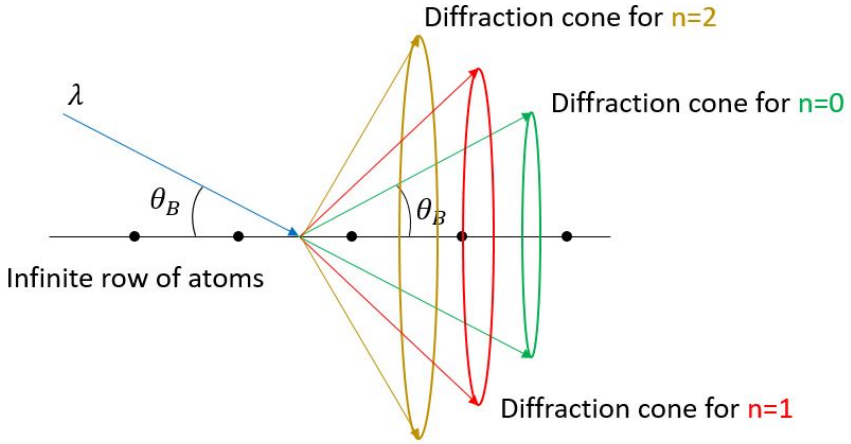

Figure 2.1. – *Sketch of the process of diffraction of an incident wave of wavelength λ by different diffraction cones of step difference n.*

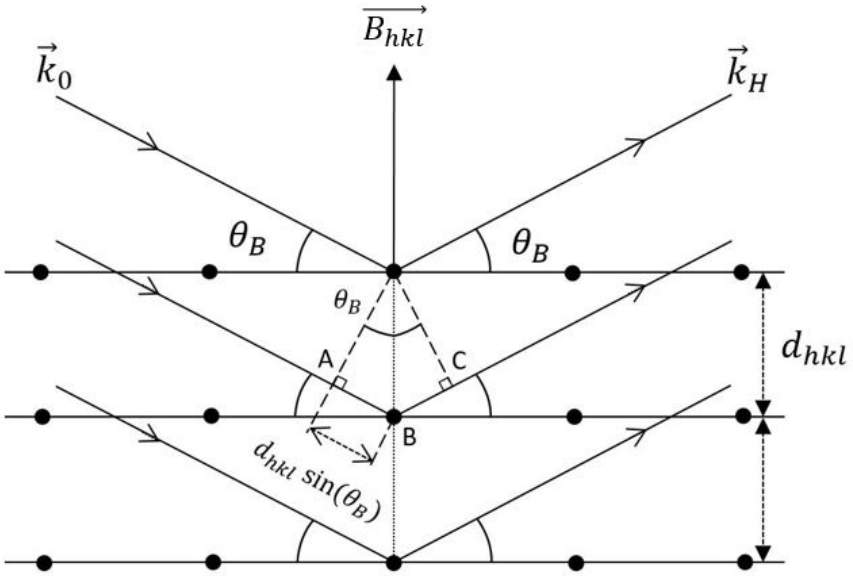

Figure 2.2. – *Sketch of the Bragg diffraction process on a Bragg crystal of reciprocal vector $\vec{B}_{hkl} = \vec{B}_H$ defining the reticular planes of spacing d_{hkl}.*

$d_{hkl} \times sin(\theta_B)$. The interference between all the diffracted waves is then constructive if the step difference is equal to an integer number n of the wavelength and the Bragg relation can be defined as follows:

$$n\lambda = 2d_{hkl}sin(\theta_B) \tag{2.1}$$

where d_{hkl} is the inter-reticular spacing of Miller indices h,k,l that describe the lattice planes, n is the order of diffraction, and θ_B is the Bragg angle of diffraction corresponding to the incident wavelength λ.

From the data extracted from [54] and [55], we detail here the procedure to connect the inter-reticular spacing of an α-Quartz crystal, made of SiO_2 molecules in a hexagonal mesh, and the mesh characteristics. The atomic distribution within the

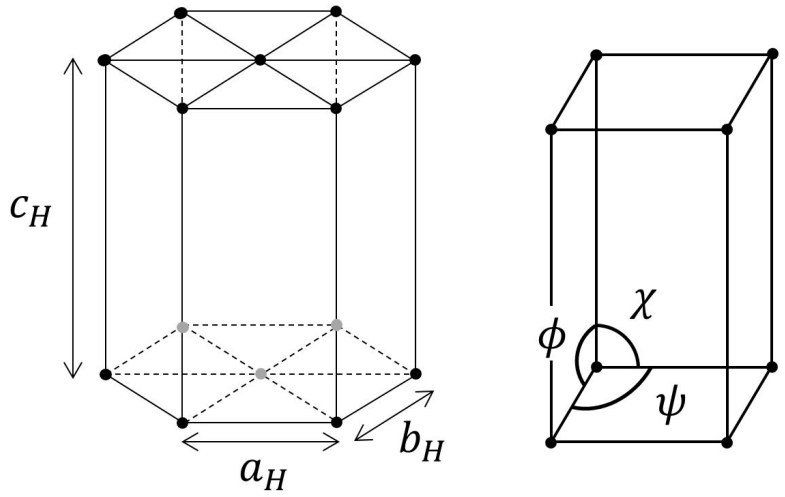

Figure 2.3. – *Sketch of a hexagonal mesh system with the length (a,b,c) and angular (ϕ,ψ,χ) parameters*

unit cell can be found in several literature sources among which [54]: $u(Si) = 0.4705$, $x(O) = 0.4152$, $y(O) = 0.2678$ and $z(O) = 0.118$. The associated positions of each atom are the combination of these parameters. Picking from [56] the Quartz lattice parameters represented in Fig. 2.3, $a_H = b_H = 4.9130 \times 10^{10}$ m, $c_H = 5.4045 \times 10^{10}$ m, the inter-reticular spacing becomes a function only dependent on the Miller indices:

$$d_{hkl} = \frac{\sqrt{3}.a_H c_H}{\sqrt{4c_H^2(h^2+hk+k^2)+3l^2a_H^2}} \quad \text{[m]} \tag{2.2}$$

2.2.1.2. Choice of the crystal

In order to maximize the throughput and thus the signal-to-noise ratio, despite the low impurity concentration, the crystals were designed as large as possible (to maximize photon collection) and the material and Miller indices were chosen to allow a good reflectivity without limiting the spectral resolution. The choice of the inter-reticular spacing d_{hkl} is dependent on the choice of the spectral range.

As shown in Table 2.1, the three crystals for the XICS diagnostic are used to observe three wavelength ranges corresponding to ionization stages of Ar and Fe. Different values for the Bragg angle of reference and the inter-reticular spacing can thus be investigated. Quartz and Germanium materials were first considered because they are easy to manufacture in large sizes and with reasonable quality of the cuts. Quartz crystals, with hexagonal mesh, are preferred and thus, testing several values for the inter-reticular spacing, the choice of the final crystal mesh was done. For the Ar

Id	Ar XVII	Ar XVIII	Fe XXV
Material	Quartz	Quartz	Germanium
Thickness [μm]	197	197	176
Mesh type	Hexagonal	Hexagonal	Cubic
Miller cut	(1,1,-2,0)	(1,0,-1,2)	(4,2,2)
Inter-reticular spacing d_{hkl} [Å]	2.457	2.281	1.155
Parallelism [arcmin]	≤ 1.5	≤ 1.5	≤ 1.0
Dimension [mm×mm]	2 × (40×100)	2 × (40×100)	2 × (53×40)
Curvature radius r_c [m]			
- from technical specification	2.716	2.716	2.716
- verified experimentally	2.745	2.745	2.745
Central wavelength λ_{ref} [Å]	3.96	3.75	1.86
Central energy E_{ref} [eV]	3131.31	3306.67	6666.66
Bragg angle of ref. $\theta_{B,ref}$ [deg]	53.709	55.282	53.636
Crystal-to-detector distance l_m [mm]	2212.520	2256.289	2210.451
Crystal-to-source point distance l_s [mm]	7391.553	6423.658	7445.055

Table 2.1. – *Main XICS Bragg crystals characteristics.*

XVII Quartz crystal of Miller indices $(h,k,l) = (1,1,0)$, the inter-reticular spacing is found to be $d_{110} \approx 2.457$ Å resulting in a Bragg angle of reference of $\theta_B \approx 53.709°$ and a wavelength of reference of $\lambda_B \approx 3.96$ Å. In order to reduce the stress on the crystals and because of the large surface area required (80 x 100 mm cf. Table 2.1), each crystal is made of two identical vertical stripes. As in Sect. 2.2.2 we expressed the line position on the detector for a single and two crystals side by side,

2.2.1.3. The Rocking-Curve

In theory, crystals must diffract a specific wavelength at a specific diffracting angle according to Eq. 2.1. However, as real beams have a finite bandwidth, small deviations from the Bragg angle of reference for any wavelength has to be included in the spectrometer design. This energy resolution can be measured with a Rocking-Curve technique [54].

The principle of this technique is the following: a monochromatic X-ray source emits photons towards a crystal to be scattered over a narrow range of angle of incidence θ_i. Whether the crystal or the source is placed on a rotating table, the angle of incidence oscillates within a narrow range of values around the Bragg angle of reference θ_B corresponding to the wavelength given by the Bragg relation, cf. Eq. 2.1. Whereas a very sharp peak near the Bragg angle is expected for a perfect crystal, defects like mosaicity, dislocations, curvature and absorption processes create disturbances in the perfect parallelism and layout of the atomic planes and cause a broadening of the peak. The physics behind the experimental process is well known now and according to [57] and [58], the computation of such diffraction profiles can be done for all types

of crystal.

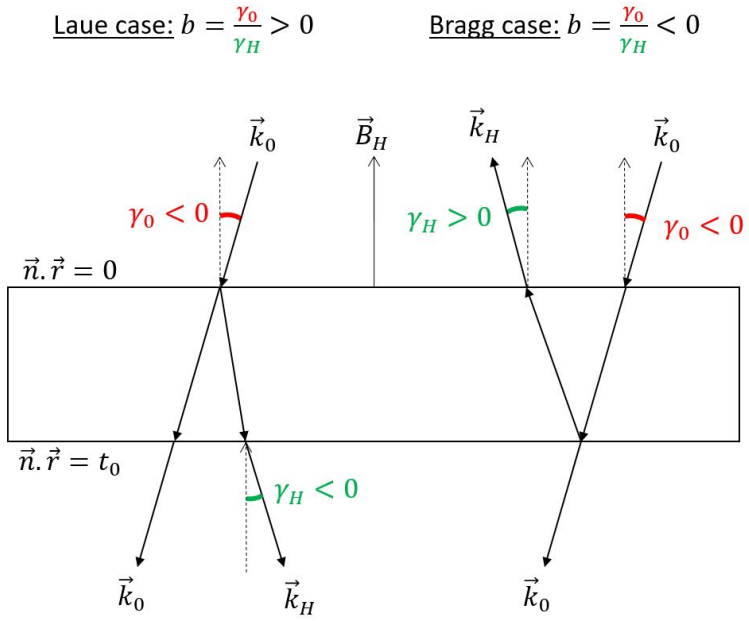

Figure 2.4. – *Two possible diffraction directions for the X-ray photons in a crystal of thickness t_0 depending on the sign of the asymmetry parameter b.*

In this Section, we use the relations defined in the Appendix A and Appendix B to quantify the Rocking-Curve of a Bragg crystal. The dynamical theory of X-ray diffraction describes the behavior of the incident radiation when it enters the crystal medium in order to describe its behavior on the way out. We need to distinguish between two cases of crystal wave exit, as described in Fig. 2.4, where a crystal modelled as a set of parallel flat plates of finite thickness t_0 is shown. Here, the incident beam $\vec{k}_0$ is described by an angle γ_0 to the reciprocal vector $\vec{B}_H$ and we define an angle γ_H for the resulting diffracted beam $\vec{k}_H$. These two cases are the following:

i/ the diffracted beam $\vec{B}_H$ emerges through the entrance plane $\vec{n}.\vec{r} = 0 \rightarrow$ angle of incidence $\gamma_0 = -\gamma_H \rightarrow$ asymmetry parameter $b = -1 \rightarrow$ the Bragg case,

ii/ the diffracted beam $\vec{B}_H$ emerges through the opposite plane $\vec{n}.\vec{r} = t_0 \rightarrow$ angle of incidence $\gamma_0 = \gamma_H \rightarrow$ asymmetry parameter $b = +1 \rightarrow$ the Laue case.

Depending on the crystal plane where the diffracted wave comes out, an asymmetry parameter called b can take two values, ± 1. This parameter is expressed as:

$$b = \frac{cos(\vec{B}_H.\vec{k}_0)}{cos(\vec{B}_H.\vec{k}_H)} \tag{2.3}$$

where $\vec{B}_H$ is the reciprocal vector normal shown in Fig. 2.2, $\vec{k}_0$ and $\vec{k}_H$ are respectively the incident and diffracted wave vectors. If the Bragg diffraction occurs for the Miller

indices (hkl), the asymmetry parameter becomes:

$$b = \frac{\vec{n}.\vec{k}_0}{\vec{n}.\vec{k}_H} \approx \frac{\gamma_0}{\gamma_H} = -1 \tag{2.4}$$

where γ_0 and γ_H are respectively the direction cosines of the incident and diffracted waves and n the refractive index of the medium defined in Appendix B Eq. B.10. This parameter is extremely important because its value gives the information about the supposed parallelism between the optical surface and the atomic planes. We will come back on this subject in Sect. 3.2.1.

According to [58], the general solution for the Bragg reflection intensity ratio of a perfect crystal, with plane parallel geometry and without absorption processes, can be expressed as follows:

$$\frac{I_H}{I_0} = \frac{K^2 b^2 |\psi_H|^2 \left(sin^2(av) + sinh^2(aw)\right)}{|q+z^2| + \left(|q+z^2| + |z|^2\right) sinh^2(aw) - \left(|q+z^2| - |z|^2\right) sin^2(av)} \times \frac{1}{+\frac{1}{2}\left[(|q+z^2| + |z|^2)^2 + |q|^2\right]^{1/2} sinh(2aw) + \frac{1}{2}\left[(|q+z^2| - |z|^2)^2 + |q|^2\right]^{1/2} sin(2av)} \tag{2.5}$$

with the following parameters:

- K is a factor depending on the polarization of the radiation, equal to 1 for a normal polarization and $cos(2\theta_B)$ for the parallel one,
- b is the asymmetry parameter defined in Eq. 2.3,
- ψ_H is the Fourier coefficient of the polarizability defined in Appendix B Eq. B.7,
- $a = \pi k_0 \frac{t_0}{\gamma_0}$ with the crystal thickness t_0 and γ_0 the angle of incidence of the incident beam $\vec{k}_0$,
- $v + iw = \sqrt{q+z^2}$,
- $q = b\psi_{\overline{H}}\psi_H$,
- $z = \frac{1-b}{2}\psi_0 + \frac{b}{2}\alpha$,
- ψ_0 is the zero-order coefficient of the Fourier development of the polarizability Appendix B Eq. B.3,
- $\alpha_\theta = 2(\theta_B - \theta_i) sin(2\theta_B)$

We call I_H/I_0 the intensity ratio between the diffracted beam and the incident. The power ratio P_H/P_0 can thus be defined as the product of the intensity ratio Eq. 2.5 with the inverse of the value of the asymmetry parameter b Eq. 2.3:

$$\frac{P_H}{P_0} = \frac{1}{|b|}\frac{I_H}{I_0} \tag{2.6}$$

which depends on the $\alpha\theta$ variable, also variable of the diffracting angle θ. Then, the Rocking-Curve is the variation of the power ratio with the diffracting angle.

Taking into account the absorption processes that may happen when the incident wave penetrates the crystal, we must integrate to the power ratio Eq. 2.6 the fractional

decrease of the intensity of the incident beam. As we already defined in Appendix B Eq. B.13 the linear absorption coefficient μ_0 by a crystal medium, the intensity ratio can be written as:

$$\frac{I_H}{I_0} = e^{-\mu_0 \frac{t_0}{\gamma_0}} \tag{2.7}$$

A simplification, that one can find in [58], can be made for the expression of the modified power ratio Eq. 2.6:

$$\frac{P_H}{P_0} = \Lambda - \sqrt{\Lambda^2 - \left(1+4\kappa^2\right)} \tag{2.8}$$

where Λ is a function of three new parameters:

$$\Lambda = \sqrt{\left(-1+y^2-v^2\right)^2 + 4\left(yv-\kappa^2\right)^2} + y^2 + v^2 \tag{2.9}$$

- $\kappa = \left(\psi''_H\right) / \left(\psi'_H\right)$ is the ratio between imaginary and real parts of the Fourier coefficient of the polarization expressed in Appendix B Eq. B.3,
- $y = \left(\frac{1-b}{2}.\psi'_0 + \frac{b\alpha}{2}\right) / \left(\sqrt{|b|}.K.|\psi'_H|\right)$ a term corresponding to a new angular variable for the computation of the power ratio,
- $v = \left(\frac{1-b}{2}.\psi''_0\right) / \left(\sqrt{|b|}.K.|\psi'_H|\right)$

The numerical value of the integrated reflectivity is deduced by integrating the power ratio over the glancing angles, defined as the angle between the incident beam and the crystal surface:

$$R_y^H = \int d\vartheta \frac{P_H}{P_0} \tag{2.10}$$

The associated Rocking-Curve can then be plotted as a function of the term y but it is not very convenient. In order to convert the variable y to the glancing angle $(\theta - \theta_B)$, we use the conversion formula following:

$$y = \frac{\frac{1-b}{2}.\psi'_0 + \frac{b}{2}(2(\theta_B - \theta)sin(2\theta_B))}{\sqrt{(|b|)}.K.|\psi'_H|} \tag{2.11}$$

$$(\theta - \theta_B) = \frac{K.|\psi'_H|}{sin(2\theta_B)}.y - \frac{\psi'_0}{sin(2\theta_B)} \tag{2.12}$$

Since the asymmetry parameter $b = -1$ for the Bragg case, Eq. 2.8 gives directly the Rocking-Curve. The integrated reflectivity is then transformed R_y^H into R_v^H by:

$$R_v^H = \frac{K.|\psi_H|}{\sqrt{|b|}.sin(2\theta)}.R_y^H \tag{2.13}$$

Fig. 2.5 shows the computed Rocking-Curve of the He-like Ar resonance line w at $\lambda = 3.9490$ Å, cf. Table 2.3. The area under the curve is called the integrated reflectivity

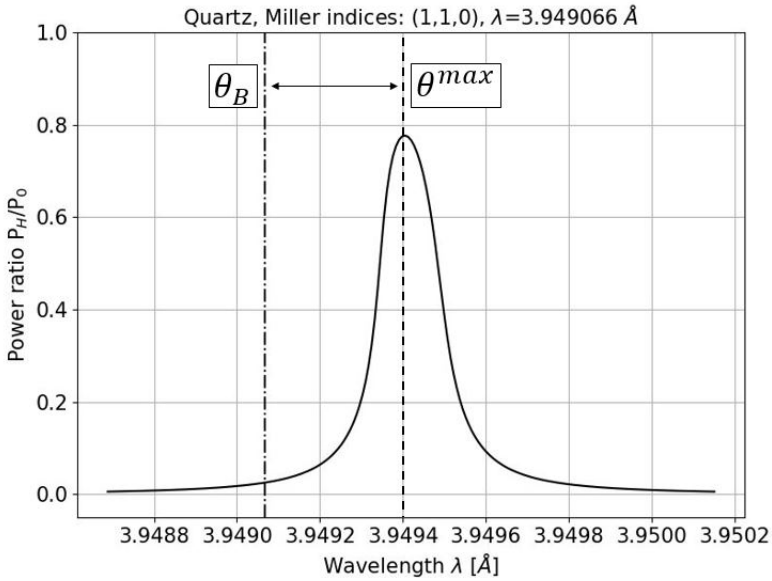

Figure 2.5. – *Rocking-Curve of an α-Quartz Bragg crystal of hexagonal mesh, Miller indices (1,1,0), for the He-like Ar resonance line wavelength* $\lambda_w = 3.9491$Å *[37].*

R_H. The total diffraction peak, obtained by summing both polarization component contributions through the parameter K, is broadened by the absorption and extinction processes taking place inside the crystal as expected from the dynamical theory of diffraction. The whole pattern is also shifted from the Bragg angle of reference by ≈ 23.9" in this specific example. This shift can be explained by the proportionality of the asymmetry parameter b to the center of the Rocking-Curve:

$$\theta_B + \frac{1-b}{2b.sin^2(\theta_B)}.\psi_0 \tag{2.14}$$

where θ_B is the Bragg angle of reference and ψ_0 is the averaged real-part refractive index of the crystal medium. The integrated reflectivity computed for both the He-like Ar w and z lines, at the Ar XVII spectrum extremities, are respectively 2.34×10^{-5} and 2.45×10^{-5}. A difference of 4% between those two values is found and we can make the approximation that the reflectivity of the crystal does not vary in wavelength over the width of the Ar^{16+} spectrum.

Since no surface or volume characterization technique could be used to determine the instrument function of the crystals, we are now able to determine the theoretical Rocking-Curve of the Ar XVII crystal for the spectral lines measured over the entire spectral band. This is a very important tool to characterize the crystal diffraction properties in terms of intensity and diffraction angle.

2.2.2. Johann configuration of X-ray spectrometer

Historically, there exist a few types of configuration for X-ray spectrometers. The conventional Johann spectrometer consists in a crystal cylindrically bent in the meridional plane (the toroidal section of the tokamak) with the lattice planes parallel to the crystal surface (or optical surface). The curvature in the meridional plane allows to focus the wavelengths on a plane detector. As it is shown in Fig. 2.6, all the rays which

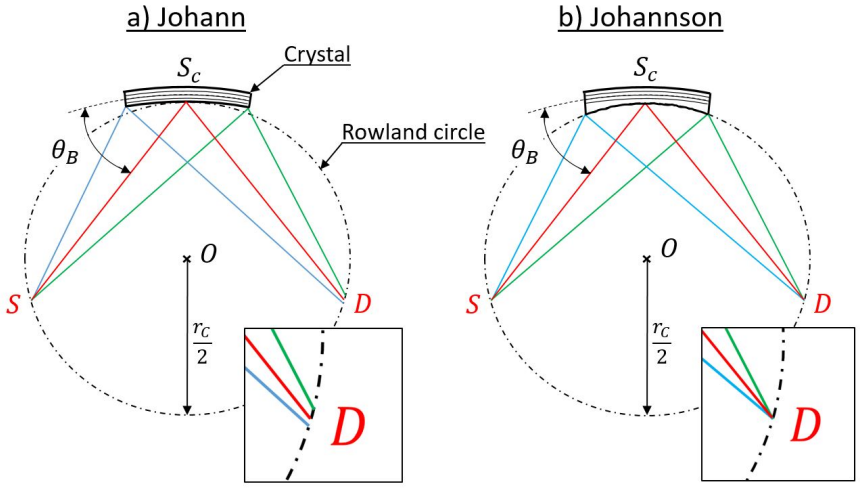

Figure 2.6. – *Sketches of a) the Johann configuration and b) the Johansson configuration.*

come from a same source point on the Rowland circle and diffracted at the same Bragg angle are focused on the same image point. Only the crystal summit is tangent to the Rowland sphere in this configuration, leading to a focusing error which distorts the measurement on the detector.

Another configuration, the Johansson kind, consists in crystals with the optical surface completely tangent to the Rowland circle, removing any focusing error. However, this configuration cannot be adapted to provide spatial resolution. For this purpose, another curvature is needed perpendicular to the meridional plane, in the sagittal plane. We choose to use an imaging spectrometer with spherically bent crystals, instead of a cylindrically bending, since it allows one to use the astigmatism to separate the meridional and sagittal foci [59].

2.2.2.1. Outline of the diagnostic geometry

In the Johann configuration, the crystal and the detector are tangent to the Rowland sphere of radius $r_c/2$ [60]. The use of spherically bent crystals allows the focal lengths to be separated: the photons are focused at a single point on the detector in the meridional plane and a symmetrical image of the plasma height is created in the sagittal plane. This property comes from the astigmatism of the spherical crystal and

is described by the lens equation [61] :

$$\frac{1}{f} = \frac{1}{s} + \frac{1}{s'} \qquad [\mathrm{m}^{-1}] \tag{2.15}$$

where s is the crystal-to-detector distance, s' is the crystal-to-source distance and f is the focal length of the crystal. Taking into account the astigmatism of the crystal, the focal length f is written differently for the meridional and sagittal planes:

$$f_m = \frac{r_c sin(\theta_B)}{2} \qquad [\mathrm{m}] \tag{2.16}$$

$$f_s = \frac{r_c}{2.sin(\theta_B)} \qquad [\mathrm{m}] \tag{2.17}$$

It leads to the following imaging equations:

$$\frac{1}{f_m} = \frac{2}{r_c sin(\theta_B)} = \frac{1}{A} + \frac{1}{l_m} \tag{2.18}$$

$$\frac{1}{f_s} = \frac{2sin(\theta_B)}{r_c} = \frac{1}{A} + \frac{1}{l_s} \tag{2.19}$$

Considering $A = r_c sin(\theta_B)$ as the crystal-to-detector distance $s = r_c.sin(\theta_B)$, we can obtain the distance from the crystal to the meridional and sagittal foci:

$$l_m = r_c sin(\theta_B) \qquad [\mathrm{m}] \tag{2.20}$$

$$l_s = \frac{-l_m}{cos(2\theta_B)} \qquad [\mathrm{m}] \tag{2.21}$$

The values of the distances for each crystal are detailed in Table 2.1 and a sketch of the locations of both foci is shown in Fig. 2.7. The location of the sagittal image depends on the Bragg angle value. Three cases are distinguished:

- For $\theta_B = 45°$, $l_s = \infty$, the reflected rays never cross and the sagittal image point is at infinity;
- For $\theta_B < 45°$, $l_s < 0$, the sagittal image point is located behind the crystal and the Rowland sphere;
- For $\theta_B > 45°$, $l_s > 0$, the sagittal image point is located in front of the crystal and further away than the meridional focus since $l_s > l_m$.

The Bragg angle and radius of curvature of the crystals have to be chosen to make sure the sagital focus is located close to the plasma center, which is the necessary condition to ensure vertical resolution of the diagnostic. The crystal here has a spherical symmetry around the axis between its summit and the center of the Rowland sphere. The rays are thus emitted at the sagittal point in the plasma, forming a cone whose axis of symmetry is normal to the crystal surface. The measured rays on the two-dimensional detector is thus the intersection of a cone with a plane surface. The condition for the

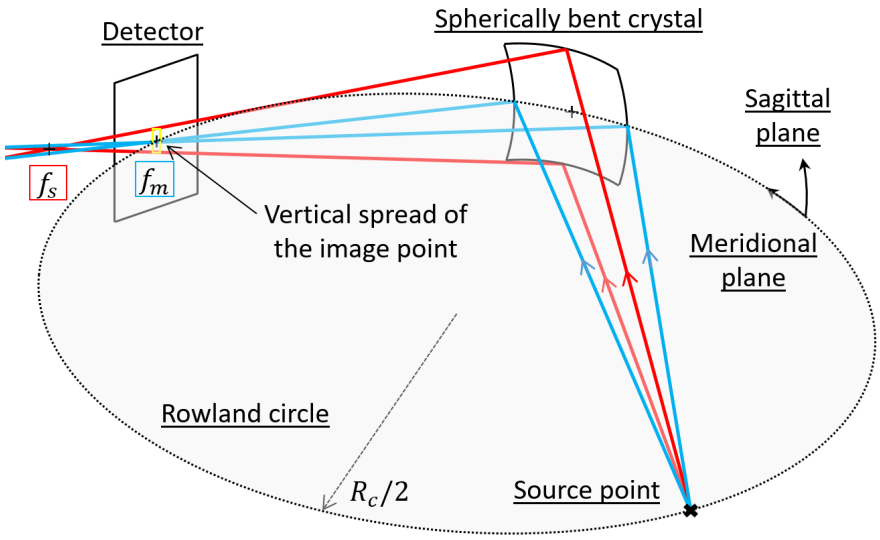

Figure 2.7. – *Sketches of a spectrometer in the Johann configuration with a spherically bent crystal.*

geometrical nature of the intersection of a conic with a plane is resumed as:

$$sin^2(2\theta_B) \leq sin^2(\theta_B) \tag{2.22}$$

which leads to three possible shapes of the rays on the detector, tangential to the Rowland sphere and with a normal vector that points to the center of the Rowland sphere:

- For $\theta_B > 60°$, the intersection is an ellipse;
- For $\theta_B = 60°$, the intersection is a parabola;
- For $\theta_B < 60°$, the intersection is a hyperbola.

An important point needs to be considered with regard to the Johann configuration, with cylindrical or spherical crystals. In Fig. 2.6 two different configurations are shown and the main difference between them is the shape of the crystal. The Johansson configuration exhibits a crystal which is entirely tangent to the Rowland sphere. The technique of manufacturing is different and the main change comes from the condition of diffraction at every point of the crystal which are not tangent to the Rowland sphere.

On the other hand, in the Johann configuration, the lattice planes are parallel to the optical surface of the crystal and it is tangent to the Rowland sphere only at its summit, which creates a focusing error. The extremities of the crystal, both in the meridional and sagittal direction, are the most distant points from it. This leads to an error of focusing of each wavelength on their theoretical point on the detector. A general expression of the Johann focusing error is found in [62] and expressed as:

$$\Delta\theta = \frac{w_c^2 \times cos(\theta_B)}{8 r_c} \qquad \text{[m]} \tag{2.23}$$

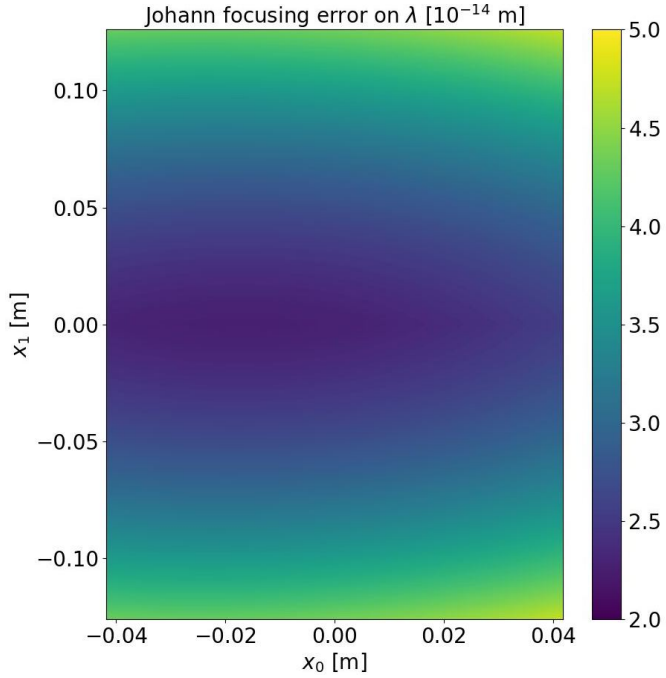

Figure 2.8. – *Map of the Johann error computed with the Ar XVII crystal parameters in Table. 2.1.*

where w_c is the total width of the crystal, r_c is the crystal curvature radius and θ_B is the Bragg angle. We can see that this error can be reduced with narrower crystals and for larger Bragg angles. We can compute easily the value of the Johann error discretised in every pixel on the detector. Fig. 2.8 shows a two-dimensional map of the Johann error computed for $\theta_B = 53.7\,^\circ$ and $r_c = 2.745$ m. It is calculated considering all the wavelengths diffracted from every point of the crystal to the detector pixels. The absolute error is thus computed by subtracting the maximum and minimum value of wavelength received by each pixel.

A spherical shape of the map is noticeable. It arises from the intersection of the Rowland sphere with the detector. The maximum values are found for the most distant points from the center of the detector. The spherical shape is not located at the center of the detector, which shows that the position of the each component of the instrument is not perfectly aligned in the synthetic diagnostic. We will come back to the effect of the Johann error on the spectral resolution in Sect. 2.2.4, comparing the order of magnitude of the Johann error ($\approx 10^{-14}$ m) with the spectral resolution of the instrument. We will also come back to the lack of knowledge about the real position of the detector, implemented in the synthetic diagnostic of the instrument in Sect. 2.2.4.

2.2.2.2. Line position on the detector calculation

The alignment of the diagnostic in the Johann configuration means that the crystal and detector are positioned on the same Rowland sphere, both tangent to it at their center, or summit. Taking into account a precise description of the spectrometer, a

model is written here to describe the position where the diffracted beam will intersect the 2D detector in the meridional plane. The general equations for a single crystal in a simple geometry are first established. But as the crystals are manufactured in two parts and then brought together side by side on a substrate, the summits of the two crystal halves are therefore no longer tangent to the Rowland sphere. An adaptation of the general equation must then be made to take account of this new geometry.

With the single crystal approximation: In this approximation, the crystal is modelled by its summit C, as shown in Fig. 2.9. The detector is placed tangentially

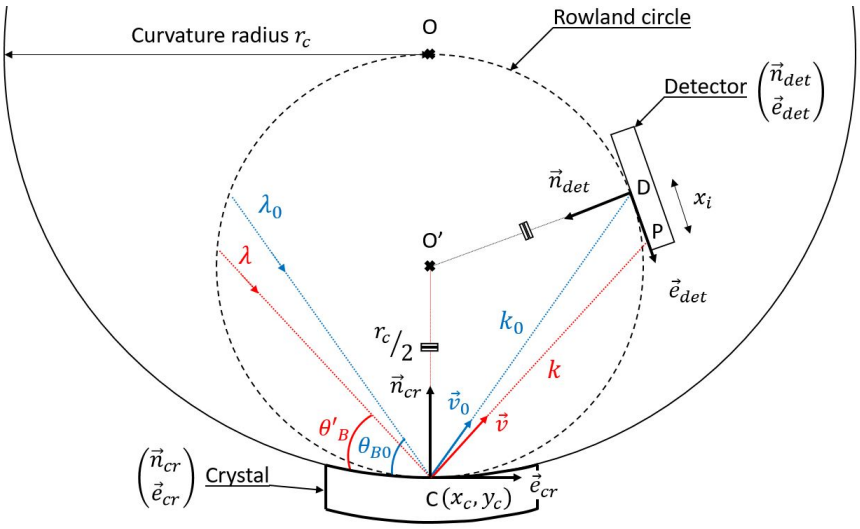

Figure 2.9. – *Sketch of the XICS spectrometer geometry in the Johann configuration, in the single crystal approximation.*

to the Rowland circle at its center D. Only a two-dimensional plane is considered here, to focus on the position of the diffracted beam in the meridional plane. Let us consider an incident beam of reference wavelength λ_0 coming from the plasma and diffracted at the center of the crystal C according to the Bragg relation Eq. 2.1. The incident beam is diffracted to the detector center D with an angle θ_{B0}. Only the diffraction at the crystal summit is represented but the process takes place on every point of the crystal where the angle of diffraction is the same. To simplify the diagram, only diffraction at the summit is shown. Considering the coordinates of the summit C (x_c, y_c) from the spectrometer frame origin O and the unit vectors of the crystal $(\vec{n}_{cr}, \vec{e}_{cr})$ with $\vec{n}_{cr} = -\vec{n}_{in}$, we can define the diffraction vector $\vec{SC}$ as :

$$\vec{CD} = k_0 . \vec{v}_0 \tag{2.24}$$

with the propagation unit vector $\vec{v}_0$:

$$\vec{v}_0 = \begin{vmatrix} sin(\theta_{B0})\vec{n}_{cr} \\ cos(\theta_{B0})\vec{e}_{cr} \end{vmatrix} \tag{2.25}$$

The unit vectors of the detector can be expressed as a function of the crystal unit vectors as:

$$\begin{cases} \vec{n}_{det} = \begin{vmatrix} cos(2\theta_{B0})\vec{n}_{cr} \\ -sin(2\theta_{B0})\vec{e}_{cr} \end{vmatrix} \\ \vec{e}_{det} = \begin{vmatrix} -sin(2\theta_{B0})\vec{n}_{cr} \\ -cos(2\theta_{B0})\vec{e}_{cr} \end{vmatrix} \end{cases} \tag{2.26}$$

Thus, we can compute the norm k_0 of the diffraction vector $\vec{CD}$ with the product to $\vec{n}_{det}$:

$$k_0 = \frac{\vec{CD}.\vec{n}_{det}}{\vec{v}_0.\vec{n}_{det}} = r_c.sin(\theta_{B0}) \qquad [m] \tag{2.27}$$

which demonstrates the same relation for the crystal-to-detector distance as that found in Sect. 2.2.2 Eq. 2.20. It can be also easily found from geometrical perspectives, considering the $\widehat{CO'D}$ isocele triangle with CO' = DO' = $r_c/2$ and $\vec{CO'}.\vec{CD} = ||\vec{CO'}|| \times ||\vec{CD}|| \times cos(-\theta_{B0}+\pi/2)$.

The diffraction vector $\vec{CD}$ can be generalized as $\vec{CP}$ to any vector between the summit C of the crystal and any point P on the detector, i.e. corresponding to a narrow range of angles $\theta_B = \theta_{B0} + \Delta\theta_B$, as:

$$\vec{CP} = k(\Delta\theta_B).\vec{v}(\Delta\theta_B) = k_0 \frac{\vec{v}_0.\vec{n}_{det}}{\vec{v}(\Delta\theta_B).\vec{n}_{det}}.\vec{v}(\Delta\theta_B) \tag{2.28}$$

Finally, the relation which gives the position of the diffracted beam of wavelength λ near the reference wavelength λ_0 is the following:

$$x(\Delta\theta_B) = (\vec{CP} - \vec{CD}).\vec{e}_{det} = r_c.sin(\theta_{B0}).\left[cos(\theta_{B0}) - \frac{sin(\theta_{B0})}{tan(\theta_{B0}-\Delta\theta_B)}\right] \qquad [m] \tag{2.29}$$

This relationship gives the position of the diffracted wavelength λ_0 beam, relative to the detector center.

We consider now a small deviation of the Bragg angle of reference within the crystal lattice, defined by an angle α, due to the crystal characteristics and affecting the unit vectors of the crystal as follows:

$$\begin{cases} \vec{n}'_{cr} = -cos(\alpha)\vec{n}_{cr} + sin(\alpha)\vec{e}_{cr} \\ \vec{e}'_{cr} = cos(\alpha)\vec{e}_{cr} + sin(\alpha)\vec{n}_{cr} \end{cases} \tag{2.30}$$

This modification affects the propagation vector $\vec{v}_0$:

$$\vec{v}(\alpha) = \begin{vmatrix} sin(\theta_{B0}+\alpha)\vec{n}_{cr} \\ cos(\theta_{B0}+\alpha)\vec{e}_{cr} \end{vmatrix} \tag{2.31}$$

and thus the position relation Eq. 2.29 according to the angle α becomes:

$$x(\Delta\theta_B,\alpha) = [k_0(\Delta\theta_B,\alpha).\vec{v}(\Delta\theta_B,\alpha) - k_0.\vec{v}_0].\vec{e}_i$$
$$= r_c.sin(\theta_{B0}).\left[cos(\theta_{B0}) - \frac{sin(\theta_{B0})}{tan(\theta_{B0}-\Delta\theta_B-\alpha)}\right] \quad [m] \quad (2.32)$$

with

$$k_0(\Delta\theta_B,\alpha) = k_0.\frac{\vec{v}_0.\vec{n}_{det}}{\vec{v}(\Delta\theta_B,\alpha).\vec{n}_{det}} = k_0.\frac{sin(\theta_{B0})}{sin(\theta_{B0}-\Delta\theta_B-\alpha)} \quad [m] \quad (2.33)$$

The general solution for the diffracted beam crossing the meridional plane of the detector is established. It is a function of the curvature radius of the crystal r_c, the Bragg angle of reference θ_{B0} and the angle α. This solution is the first approximation for a single crystal, which is not relevant for the case studied here. The next step is to take into account both half-crystals in the general geometry.

With the real crystal geometry: The crystals used for the XICS spectrometer are actually manufactured in two identical stripes, see Sect. 2.2.1.2. This is no mere technical detail, as the crystal must be tangent to the Rowland sphere at its summit to validate the Johann configuration. However, two crystals side by side do not constitute a single crystal, since they both have their own summit. We investigate here what this means in terms of the diffraction direction of a wave on each half-crystal.

We shall consider now two distinct summits for the two half crystals and modify the simpler geometry studied previously, as shown in Fig. 2.10. A zoom on the crystals

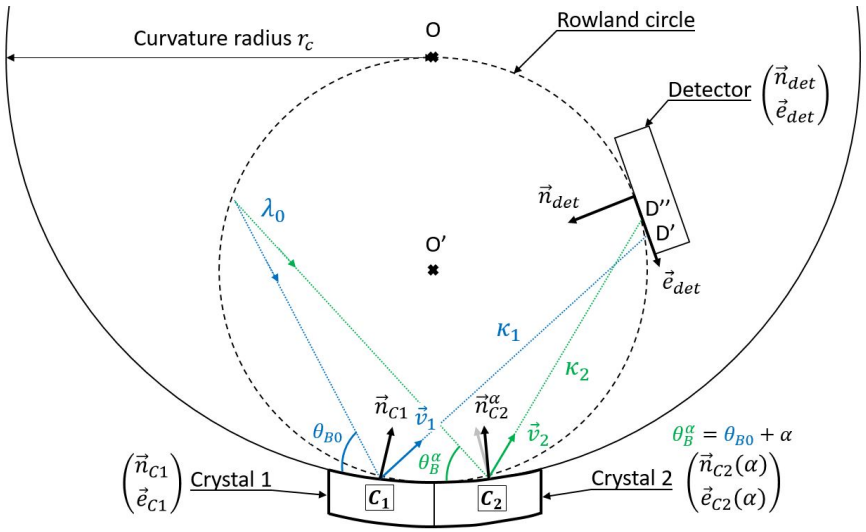

Figure 2.10. – *Sketch of the XICS spectrometer geometry in the Johann configuration considering a splitted crystal, both halves located next to each other.*

location is made in Fig. 2.11 to illustrate the unit vectors of each summit and the angular aperture between them. Because of the change of summit position, both C_1 and C_2 are not anymore perfectly on the Rowland sphere. It leads to different diffraction

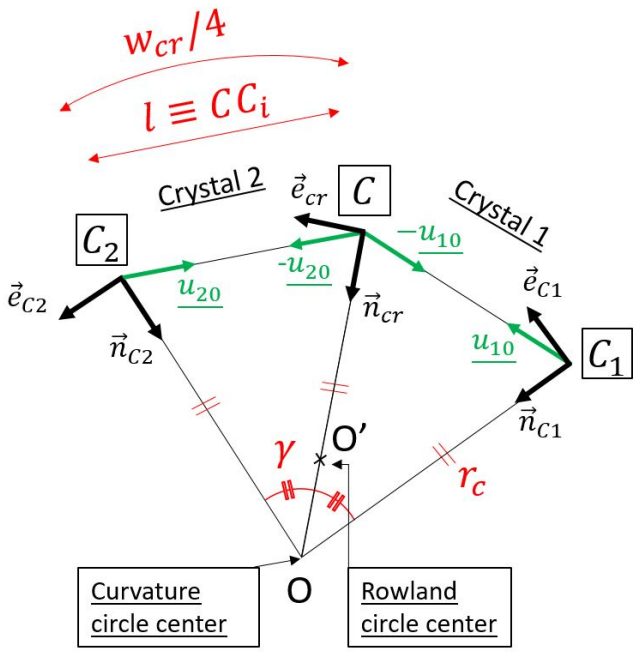

Figure 2.11. – *Zoom on the crystal location in Fig. 2.10: the positioning of each half-crystal summit S_1 and S_2 according to the single crystal summit S on the curvature circle of origin O'. The unit vectors are shown for all the summits.*

directions to the detector, which moves the theoretical center of the detector to two distinct new positions. In addition, a miscut angle α is applied to the second crystal. It changes the Bragg angle of diffraction by $\theta_B^\alpha = \theta_{B0} + \alpha$. The theoretical centers of the detector for the two halves are thus different, at D' for the crystal 1 and D'' for the second. We thus expect that the two spectra from the two crystals do not overlap perfectly. It is summarized in Fig. 2.10. Let us proceed to the establishment of the proper position relations for each half.

The norm of the propagation vector k_0 was used to locate precisely the detector on the Rowland sphere but considering the splitting, the distance between each summit C_i and the center of the detector C has to be reevaluated. The diffraction vectors $(\vec{S_1C}, \vec{S_2C})$ can be written as:

$$\vec{C_1D} = l.\vec{u_{10}} + r_c.sin(\theta_{B0}).\vec{v}(\theta_{B0}) \tag{2.34}$$

$$\vec{C_2D} = l.\vec{u_{20}} + r_c.sin(\theta_{B0}).\vec{v}(\theta_{B0}) \tag{2.35}$$

considering an angular aperture $\gamma = r_c/(w_c/4)$ between $(\vec{O}, \vec{O_i})$, as shown in Fig. 2.11. The distance l is related to the curvature radius of the crystal used by:

$$l = 2.r_c.sin(\gamma/2) = 2.r_c.sin(\phi) \qquad [m] \tag{2.36}$$

The unit vectors related to the space between (C_1, C_2) and C can be written as a

function of the single crystal unit vectors as:

$$\begin{cases} \vec{u}_{10} = -sin(\phi).\vec{n}_{cr} + cos(\phi).\vec{e}_{cr} \\ \vec{u}_{20} = -sin(\phi).\vec{n}_{cr} - cos(\phi).\vec{e}_{cr} \end{cases} \tag{2.37}$$

The expression of the diffraction vectors C_1C and C_2C can be as well rewritten:

$$\begin{cases} \vec{C_1D} = \begin{vmatrix} \mathrm{r_c}.\left[-2.sin^2(\phi) + sin^2(\theta_{\mathrm{B0}})\right]\vec{n}_{cr} \\ \mathrm{r_c}.\left[sin(2.\phi) + \frac{1}{2}sin(2\theta_{\mathrm{B0}})\right]\vec{e}_{cr} \end{vmatrix} \\ \vec{C_2D} = \begin{vmatrix} \mathrm{r_c}.\left[-2.sin^2(\phi) + sin^2(\theta_{\mathrm{B0}})\right]\vec{n}_{cr} \\ \mathrm{r_c}.\left[-sin(2.\phi) + \frac{1}{2}sin(2\theta_{\mathrm{B0}})\right]\vec{e}_{cr} \end{vmatrix} \end{cases} \tag{2.38}$$

Computing the norm of each of these diffraction vectors leads to the reworked expression of the propagation vector norm $\mathrm{k_0}$ for each summit:

$$\kappa_1(\phi,\theta_{\mathrm{B0}}) = \{\frac{{\mathrm{r_c}}^2}{4}.\left[6 - 4cos(2\theta_{\mathrm{B0}} + 2\phi) + 2cos(2\theta_{\mathrm{B0}}) - 4cos(2\phi)\right]\}^{1/2} \quad [\mathrm{m}] \tag{2.39}$$

$$\kappa_2(\phi,\theta_{\mathrm{B0}}) = \{\frac{{\mathrm{r_c}}^2}{4}.\left[6 - 4cos(2\theta_{\mathrm{B0}} - 2\phi) + 2cos(2\theta_{\mathrm{B0}}) - 4cos(2\phi)\right]\}^{1/2} \quad [\mathrm{m}] \tag{2.40}$$

Considering the deviation angle α affecting each half crystal, the propagation vectors become:

$$\begin{cases} \vec{v}_1 = cos(\theta_{\mathrm{B0}})\vec{u}_{10}(\alpha) + sin(\theta_{\mathrm{B0}})\vec{n}_{S1}(\alpha) \\ \vec{v}_2 = -cos(\theta_{\mathrm{B0}})\vec{u}_{20}(\alpha) + sin(\theta_{\mathrm{B0}})\vec{n}_{S2}(\alpha) \end{cases} \tag{2.41}$$

$$\vec{v}_1(\alpha) = \begin{vmatrix} \left[sin(\theta_{\mathrm{B0}})cos(2\phi - \alpha) - cos(\theta_{\mathrm{B0}})sin(\phi - \alpha)\right]\vec{n_{cr}} \\ \left[cos(\theta_{\mathrm{B0}})cos(\phi - \alpha) + sin(\theta_{\mathrm{B0}})sin(2\phi - \alpha)\right]\vec{e_{cr}} \end{vmatrix} \tag{2.42}$$

$$\vec{v}_2(\alpha) = \begin{vmatrix} \left[sin(\theta_{\mathrm{B0}})cos(2\phi - \alpha) + cos(\theta_{\mathrm{B0}})sin(\phi - \alpha)\right]\vec{n_{cr}} \\ \left[cos(\theta_{\mathrm{B0}})cos(\phi - \alpha) - sin(\theta_{\mathrm{B0}})sin(2\phi - \alpha)\right]\vec{e_{cr}} \end{vmatrix} \tag{2.43}$$

Thus, the norm of the diffraction vectors, affected by a α angle, can be rewritten as follows:

$$\kappa_1(\phi,\Delta\theta_{\mathrm{B}},\alpha) = \kappa_1(\phi).\frac{\vec{v}_1(\phi).\vec{n}_{det}}{\vec{v}_1(\phi,\Delta\theta_{\mathrm{B}},\alpha).\vec{n}_{det}} \tag{2.44}$$

$$\kappa_2(\phi,\Delta\theta_{\mathrm{B}},\alpha) = \kappa_2(\phi).\frac{\vec{v}_2(\phi).\vec{n}_{det}}{\vec{v}_2(\phi,\Delta\theta_{\mathrm{B}},\alpha).\vec{n}_{det}} \tag{2.45}$$

$$\kappa_1(\phi,\Delta\theta_B,\alpha) = \kappa_1(\phi).\left[sin(\theta_{B0})cos(2\theta_{B0}+2\phi) - cos(\theta_{B0})sin(2\theta_{B0}+\phi)\right] \\ / \left[sin(\theta_B)cos(2\theta_{B0}+2\phi-\alpha) - cos(\theta_B)sin(2\theta_{B0}+\phi-\alpha)\right] \quad (2.46)$$

$$\kappa_2(\phi,\Delta\theta_B,\alpha) = \kappa_2(\phi).\left[sin(\theta_{B0})cos(2\theta_{B0}-2\phi) - cos(\theta_{B0})sin(2\theta_{B0}-\phi)\right)] \\ / \left[sin(\theta_B)cos(2\theta_{B0}-2\phi+\alpha) - cos(\theta_B)sin(2\theta_{B0}-\phi+\alpha)\right] \quad (2.47)$$

Finally, as for the single crystal approximation, we can compute the new position solution for each half-crystal of a spectral line of Bragg angle of reference θ_{B0} as a set of the angular aperture between the summits γ, the nearby diffraction angle $\Delta\theta_B$ and the angle α:

$$x_1(\phi,\Delta\theta_B,\alpha) = \left(\vec{C_1P} - \vec{C_1D}\right).\vec{e}_{det} \\ = \left(\kappa_1(\phi,\Delta\theta_B,\alpha).\vec{v}_1(\phi,\Delta\theta_B,\alpha) - \kappa_1(\phi).\vec{v}_1\right).\vec{e}_{det} \quad (2.48)$$

$$x_2(\phi,\Delta\theta_B,\alpha) = \left(\vec{C_2P} - \vec{C_2D}\right).\vec{e}_{det} \\ = \left(\kappa_2(\phi,\Delta\theta_B,\alpha).\vec{v}_2(\phi,\Delta\theta_B,\alpha) - \kappa_2(\phi).\vec{v}_2\right).\vec{e}_{det} \quad (2.49)$$

$$x_{i,1}(\phi,\Delta\theta,\alpha) = \kappa_1(\phi) \times [-\frac{sin(\theta_0)cos(2\theta_0+2\phi) - cos(\theta_0)sin(2\theta_0+\phi)}{sin(\theta_0)cos(2\theta_0+2\phi-\alpha) - cos(\theta_0)sin(2\theta_0+\phi-\alpha)} \times \\ [sin(\theta)sin(2\theta_0+2\phi-\alpha) + cos(\theta)cos(2\theta_0+\phi-\alpha)] \\ + sin(\theta_0)sin(2\theta_0+2\phi) + cos(\theta_0)cos(2\theta_0+\phi)] \quad [\text{m}] \quad (2.50)$$

$$x_{i,2}(\phi,\Delta\theta,\alpha) = \kappa_2(\phi) \times [-\frac{sin(\theta_0)cos(2\theta_0-2\phi) - cos(\theta_0)sin(2\theta_0-\phi)}{sin(\theta_0)cos(2\theta_0-2\phi+\alpha) - cos(\theta_0)sin(2\theta_0-\phi+\alpha)} \times \\ [sin(\theta)sin(2\theta_0-2\phi+\alpha) + cos(\theta)cos(2\theta_0-\phi+\alpha)] \\ + sin(\theta_0)sin(2\theta_0-2\phi) + cos(\theta_0)cos(2\theta_0-\phi)] \quad [\text{m}] \quad (2.51)$$

This set of equations describe the position of every spectral line on the detector from a diffraction for each incident wavelength, $\lambda = \lambda_0 + \Delta\lambda$, and for any deviation angle α. The fact that the crystals are manufactured in two identical stripes means that the wavelengths cannot be focused at the same point as predicted with the Johann configuration. In fact, there are two foci for each half-crystal, and we will see in the Sect. 3.2 that it has a non-negligible effect on the measured spectra.

2.2.3. X-ray photons measurement

Now that the dispersing element has been chosen to focus on the energy range of the Ar XVII spectrum and the configuration of the spectrometer is established, the filtering and the detecting elements must be determined. The energy range is about [3.93, 4.00] Å, which is very narrow. The crystals actually acts like an energy filtering element but to ensure it can not be worn by some high energy photons coming from

the plasma, an additional filter has be to placed between the crystal and the tokamak vessel. This is the role of the Be window.

2.2.3.1. Beryllium filter

A Be window of 150μm thickness and of size 220 × 140 mm^2 is placed between the crystal box and the vacuum vessel. An exploded-view drawing is shown in Fig. 2.12. The Beryllium foil is held between two flanges and reinforced with twenty-one rods

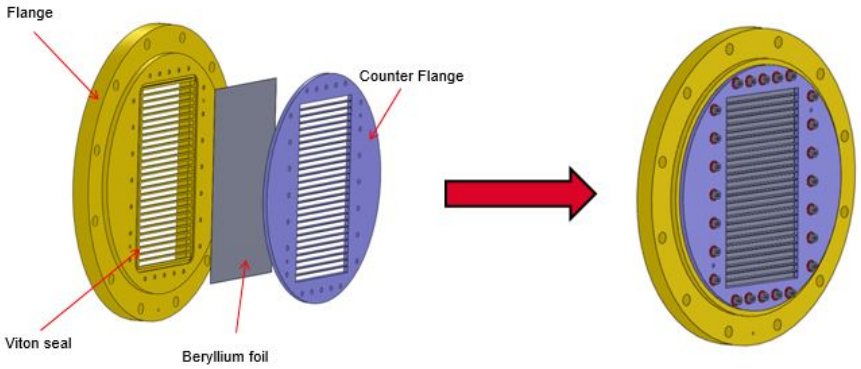

Figure 2.12. – *Exploded-view drawing of the Be window.*

made in stainless steel, of 2 mm of width and 6.7 mm of thickness distributed on all the surface. These rods are placed to ensure a mechanical resistance to the pressure gradient between the spectrometer and the vessel vacuum conditions. This is a major security condition to avoid any break of the Be foil and any contamination of the tokamak vessel for both the experiments and human health.

This Be window has two aims. The first is to separate the two vacuum conditions of the diagnostic (about less than 10^{-4} Pa) and of the tokamak vessel (about less than 10^{-5} Pa). This separation ensures that the integrity of the vacuum on one side is not compromised in the event of a failure on the other. The second is to filter out the photons with low energies, i.e. all the UV and Infrared (IR) spectral range. Fig. 2.13 shows the transmission coefficient of Beryllium (Z=4) for photon energies up to 10 keV, as well as for Fe (Z=26). The transmission coefficient corresponding to the wavelength of reference of the Ar XVII crystal, or the energy of reference here, is about 60% at 3130 eV. 40% of the incident photons of the Ar^{16+} spectrum are lost at this step. A mean value can be extracted for the entire Ar XVII spectrum knowing the corresponding energies of the boundary spectral lines measured on the Ar XVII spectrum, $E_w \approx 3140$ eV and $E_z \approx 3104$ eV, shown in Fig. 2.13. The mean transmission coefficient is estimated to $T_{Be}(ArXVII) = 0.595$.

On the contrary of Be, the Fe bars block entirely the photon energies below 5 keV. The thickness of the reinforcements is sufficient to block completely the incident X-ray photons. The total area covered by the twenty-one bars represents 30% of the total Be

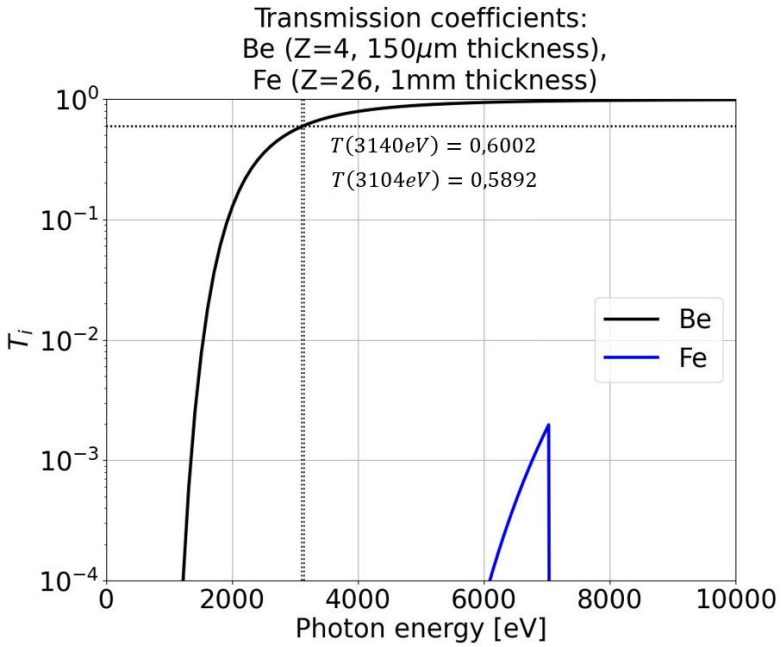

Figure 2.13. – *Transmission coefficient of (black) a Be (Z=4) window of 150 μm thick and (blue) of Fe (Z=26) bars of 1 mm thick.*

window area so we can estimate the total transmission coefficient of the Be window:

$$\eta_{Be} = T_{Be}(ArXVII) \times 70\% = 0.416 \tag{2.52}$$

The combined effect of the crystal and the Be window therefore filters out a maximum number of photons that are not useful for the spectrometer. All that remains is to define the photon-collecting element, in accordance with the geometric configuration of the spectrometer, i.e. a two-dimensional detector.

2.2.3.2. Two-dimensional semi-conductor detector

The parameters of the detector, according to the conditions expressed so far, must be the following:

— a large-size area to have the maximum spectral extension and spatial resolution,
— low pixel area combined with the highest number as possible to reduce the point-spread function,
— a high count rate to minimize the risk to saturate the signal,
— a high single-photon sensitivity to maximize the conversion between photons and counts,

To optimize the detector dynamics allowing to better resolve the image and the spectra, the XICS spectrometer is equipped with a PILATUS3 X700K detector. Table 2.2 summarizes the main parameters of the detector. The hardware is in single-photon counting mode. As shown in Fig. 2.14, the PILATUS3 hybrid pixel detector

Sensor	reverse-blased Si diode array
Sensor thickness	320 μm
Quantum efficiency at 5.4 keV at 8.0 keV at 17.5 keV	 94 % 97 % 37 %
Number of modules	7
Module size	83.8 × 33.5 mm^2
Number of pixels per module	487 × 195
Intermodule gap	17 pixels, 7% of the total area
Total number of pixels	487 × 1467
Total surface	118 × 402 mm^2
Dynamic range	20 bits
Counting rate per pixel	10^7 photons.s^{-1}
Energy range	2.4 - 36 keV
Energy resolution	500 eV
Readout time	0.95 ms
Point-spread function	1 pixel (FWHM)

Table 2.2. – *Technical specifications of the PILATUS3 detector.*

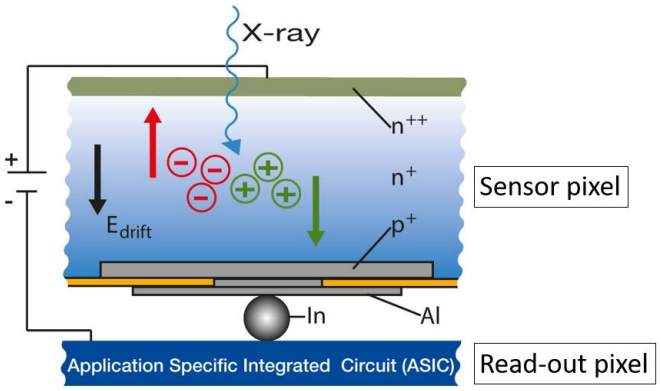

Figure 2.14. – *Cross-section of the PILATUS3 detector system* [1].

consists of a sensor and a two-dimensional array of p-n diodes [63] processed in a high-resistivity semiconductor. An incoming X-ray photon is directly converted into an electric charge in the sensor pixel of which a sketch is shown in Fig. 2.14. A charge-sensitive preamplifier amplifies the signal generated by the measurement of the photon and a comparator is used next to produce a digital signal if the incoming charge exceeds a pre-defined threshold. The dynamic of the detector is a twenty bits storage unit, which avoids any saturation of the signal. Each sensor pixel is connected to its corresponding readout channel through a microscopic indium ball, with a typical diameter of 18 μm. The advantage of small pixels leads to a point-spread function of one pixel. The interconnection between the sensor and the read-out pixels results

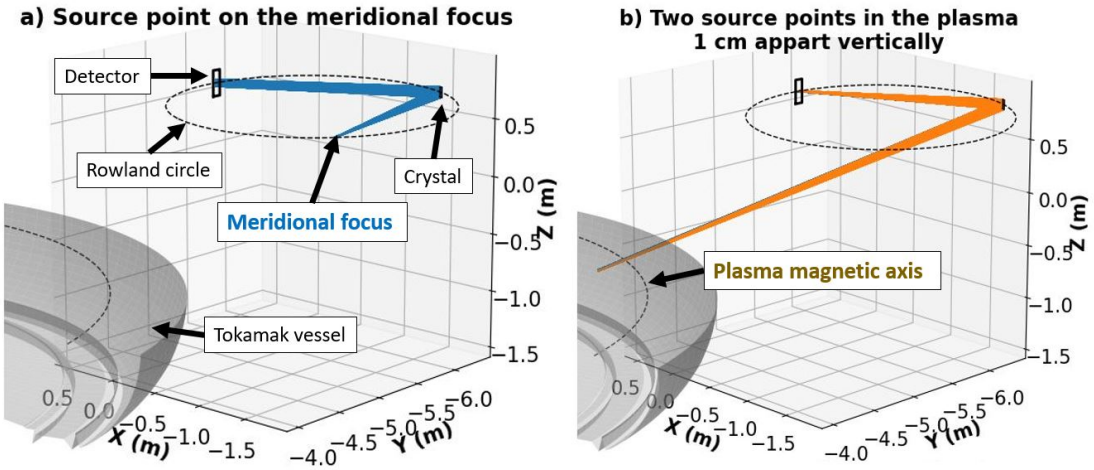

Figure 2.15. – *Reverse ray-tracing computations with the XICS configuration (a) from a source point source on the Rowland circle at the meridional focus and (b) from two source points located close to the magnetic axis, 1 cm apart vertically.*

also in a low capacitance which reduces the noise. The detector has to be operated in-vacuum and actively cooled during plasma discharges. Strict conditions of pressure and temperature are ensured, lower than 10^{-4} Pa and 25 °C, to avoid any critical damage of the sensor system.

2.2.4. Diagnostic resolution power

2.2.4.1. Spectral and spatial resolutions

In this Section, we explore the capabilities of this diagnostic in terms of spectral and spatial resolution. A synthetic diagnostic has been implemented using the ToFu open-source python library [1], taking into account the architecture of the WEST tokamak, to highlight the boundary conditions of use. This python library is dedicated to the design of synthetic diagnostics for fusion plasmas and also to perform tomographic inversions of line-of-sight integrated measurements. A synthetic diagnostic is a tool that recreates the configuration of a real diagnostic in a simulated tokamak environment. Validation of the processing of real diagnostic measurements is then possible by recreating a signal and simulating the action of the instrument to calculate synthetic images.

To do this, metrological data is required to scale up the various components of the instrument. This will be the subject of Sect. 2.3. With this tool, we will perform reverse ray-tracing calculations from the tokamak vessel to the detector to demonstrate the spatial and spectral limits available with this instrument. Fig. 2.15 shows two representations of a spectral emission diffracted to the detector. In Fig. 2.15 a), the

1. See https://github.com/ToFuProject for information about the ToFu library

emission starts from the meridional focus of the crystal on the Rowland sphere, as represented in Fig. 2.7. In Fig. 2.15 b), the emission point is split in two vertically-spaced points located at the plasma magnetic axis, one at the sagittal focus (orange) and the second 1 cm below (green), and play the role of the meridional focus. The intersection

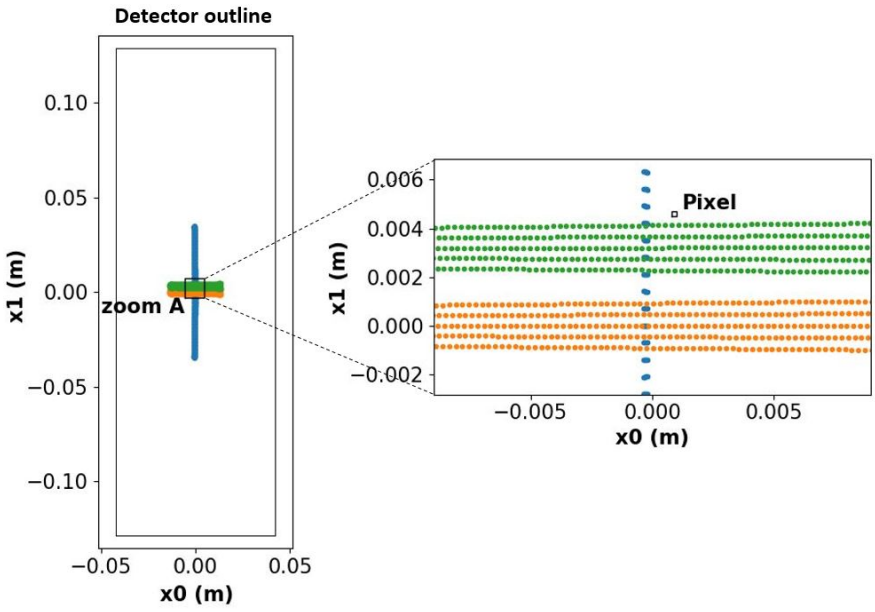

Figure 2.16. – *Computed position and broadening of two close spectral lines from a simulated bi-chromatic plasma volume of emission with the detector at the Ar XVII meridional focus.*

of the rays with the detector in both cases is displayed in Fig. 2.16 where the total detector outline is shown and exhibits the intersections of simulated rays for the two different cases. In the Fig. 2.15 a) case, the emission (in blue) from a source point on the Rowland circle at the meridional focus is well focused on the detector at the cost of a vertical spread due to the difference between the sagittal and meridional foci. We saw in Sect. 2.2.2.1 that the sagittal focus is placed behind the detector, leading to a vertical spread of the image. The width of the blue image appears to be of the size of the detector pixels. The pixel size could be a limiting factor for the spatial resolution if it was chosen larger.

About the Fig. 2.15 b) case, the two source points are located in the plasma, very close to the sagittal focus of the Ar XVII crystal. The rays no longer intersect the Rowland sphere at one point, but are spread out in the meridional plane, creating the green and orange images on the detector. The one centimeter spacing between the two emission points at the sagittal focus is therefore well resolved on the camera, at the expense of the spectral resolution. Finally, considering now a whole uniform plasma emitting bi-chromatically to the detector, in Fig. 2.17, we emphasize that the conjunction of a finite volume source with focusing is the main limiting factor on the spectral resolution. The same simulated pattern has been observed and also

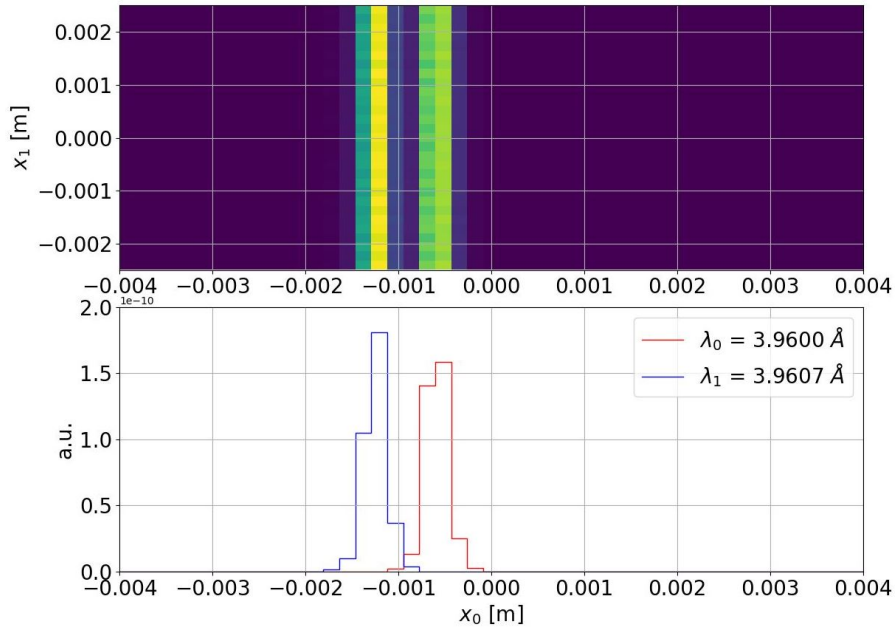

Figure 2.17. – *Intersection of the two reverse ray-tracing computations shown in Fig. 2.15 wit the detector outline (left) and (right) zoom on a reduced area to show the line spreading.*

detailed in [64]. The images of the two wavelengths are separated by a local minimum that is ~ 80% of their maxima, from which a spectral resolution of $\Delta\lambda/\lambda \approx 10^{-4}$ can be defined. The corresponding lines of sight available in the plasma are shown in Fig. 2.18 for the poloidal and the toroidal cross-sections.

2.2.4.2. Doppler shift and broadening resolution

We saw that the spectral resolution of the instrument of $\Delta\lambda/\lambda \approx 10^{-4}$ is effective to resolve very close wavelengths. From this fact, we can also extrapolate the sensitivity of the measurements to a Doppler shift. To do that, we can compute the exact wavelength difference between two adjacent pixels and deduce the corresponding Doppler shift. Let us take the example of the Ar XVII crystal with an inter-reticular spacing of d_{hkl} = 2.457 Å and the wavelength of the Ar^{16+} resonance line w at λ_0 = 3.9490 Å. The corresponding Bragg angle of reference is found with the Bragg law Eq. 2.1 and is θ_{B0} = 53.477 ° = 0.9333 radians. Then, we use Eq. 2.29 that governs the position of a specific wavelength on the detector that has been expressed in Sect. 3.2.2. It allows to find the angular difference $\Delta\theta_B$ that corresponds to a shift in one pixel of size 172 μm in any direction across the detector width:

$$x(\Delta\theta_B) = \pm 172\mu m = r_c . sin(\theta_{B0}) . \left[cos(\theta_{B0}) - \frac{sin(\theta_{B0})}{tan(\theta_{B0} - \Delta\theta_B)} \right] \quad \text{[m]} \qquad (2.53)$$

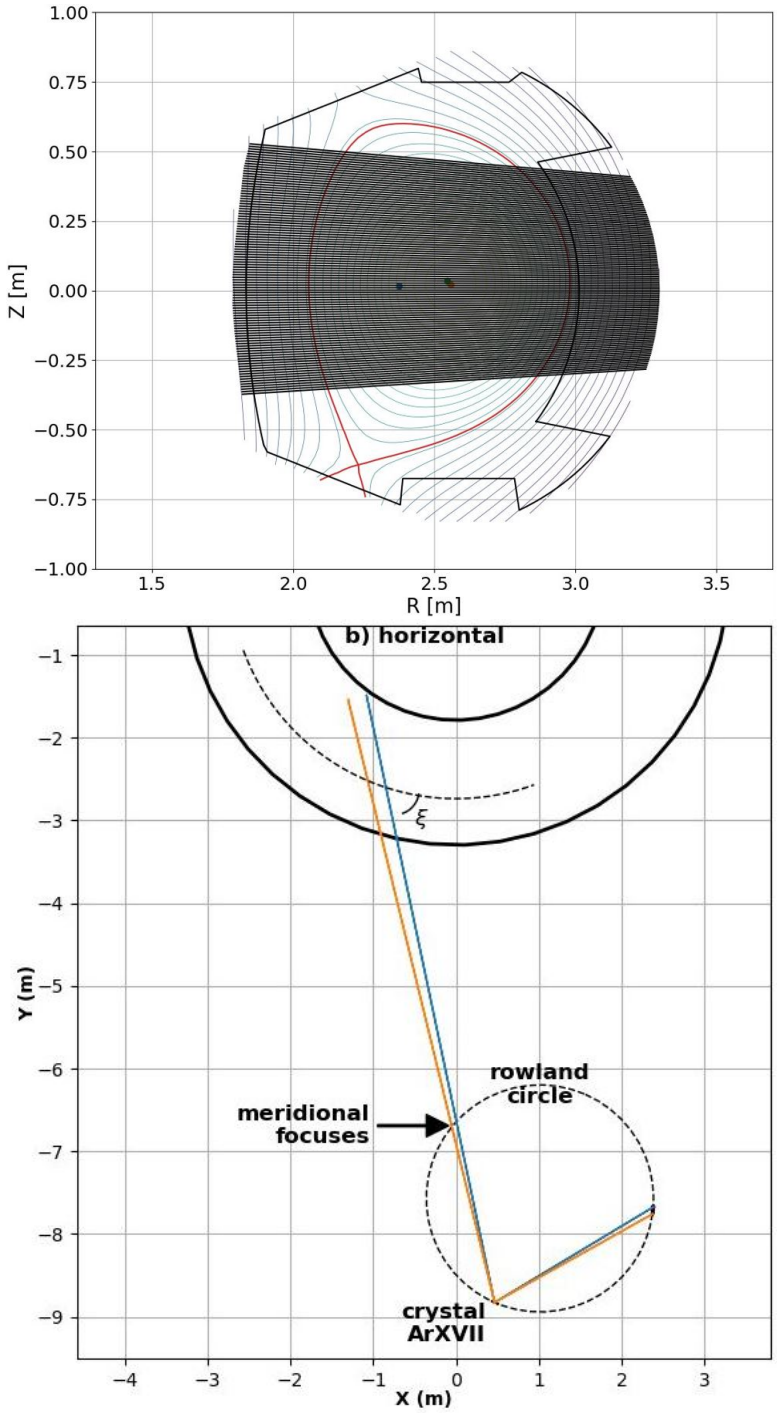

Figure 2.18. – *Plasma coverage by the XICS spectrometer in (top) the poloidal cross-section using 100 lines of sight covering the central part of the WEST vacuum vessel and (bottom) in the toroidal cross-section of WEST tokamak. The two colors represent the two wavelengths measured at the extreme edges of the detector.*

The unknown of the equation is the $\Delta\theta_B$ term so knowing θ_{B0}, we can express its value as $\Delta\theta_B \approx \pm 6.266 \times 10^{-5}$ radians with $r_c = 2.745$ m. It corresponds with Eq. 2.1 to a change in wavelength of $\pm 1.832 \times 10^{-14}$ m. In addition, along each LOS in the plasma, one can compute the value of the angle between the LOS and the local toroidal direction, which is relevant to compute the local Doppler shift. Fig. 2.18 (bottom) shows the direction of the lines of sight of the XICS in the toroidal cross-section. An mean angle $\bar{\xi} \approx 38° \approx 0.663$ radians is computed and has to be introduced in the Doppler shift equation Eq. 1.79 to obtain the change of toroidal rotation velocity for a change of one pixel:

$$\frac{\Delta\theta_B}{\theta_B} = \frac{\vec{v} \wedge \vec{l}}{c} = \frac{v \times cos(\bar{\xi})}{c} \implies v \approx 10.9\,\text{km/s} \tag{2.54}$$

with $\vec{l}$ the direction of the line of sight. The value of the Doppler shift change with one pixel is high, which means that the spectrometer cannot determine toroidal rotation speeds below this value. In the same way, an estimation of the minimal Doppler broadening measured that corresponds to a one-pixel broadening is:

$$\frac{\Delta\lambda_D}{\lambda_0} = \sqrt{\frac{2k_B T_i}{m_i c^2}} \implies T_i \approx 4.65 \times 10^5\,\text{K} \approx 40.1\,\text{eV} \tag{2.55}$$

Compared to the Doppler shift resolution, the Doppler broadening resolution is far more accurate and therefore much more sensitive to spectrum modelling errors. In addition to modelling uncertainties, an additional broadening source can be added by the position of the detector relative to the Rowland sphere. Indeed, as we will see in the next Sections, the position of the detector relative to its theoretical position can cause a focusing error.

2.2.5. Limitations of the spectrometer

2.2.5.1. Differences caused by the different crystals

This study has been performed with the Ar XVII crystal but it can also be done with the other two crystals. As it is referenced in Table 2.1, the values of the meridional and sagittal focus distances differ from one crystal to another from the value of the curvature radius and the Bragg angle of reference. Fig. 2.19 shows the fixed positions of the three crystal sagittal foci in the WEST tokamak frame, computed with Eq. 2.20. It is clear that with a same curvature radius, the position of the sagital and meridional foci are affected by the different Bragg angles. The difference is particularly visible for the sagital focus which have a larger dependency on the Bragg angle. The difference is smaller for the meridional focus and is compatible with the use of a single fixed detector. It has been shown previously that to keep the detector position fixed with a multi-crystal configuration, all the crystals are mounted on a rotating table [65] that allows to place all the crystals at the same position facing the plasma.

This choice is very convenient to avoid to change the position of the detector each

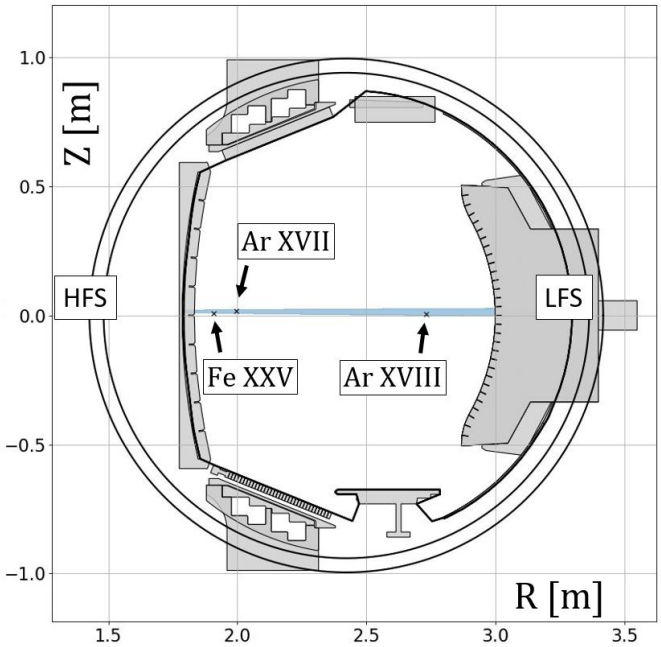

Figure 2.19. – *Poloidal cross-section of WEST tokamak with the three positions of the sagittal foci for the three XICS crystals. The blue area represents the focus of simulated rays from the detector.*

time the crystal is changed. As a result, the detector position is not optimal for the other two because of the different foci. Fig. 2.20 shows a toroidal cross-section of the

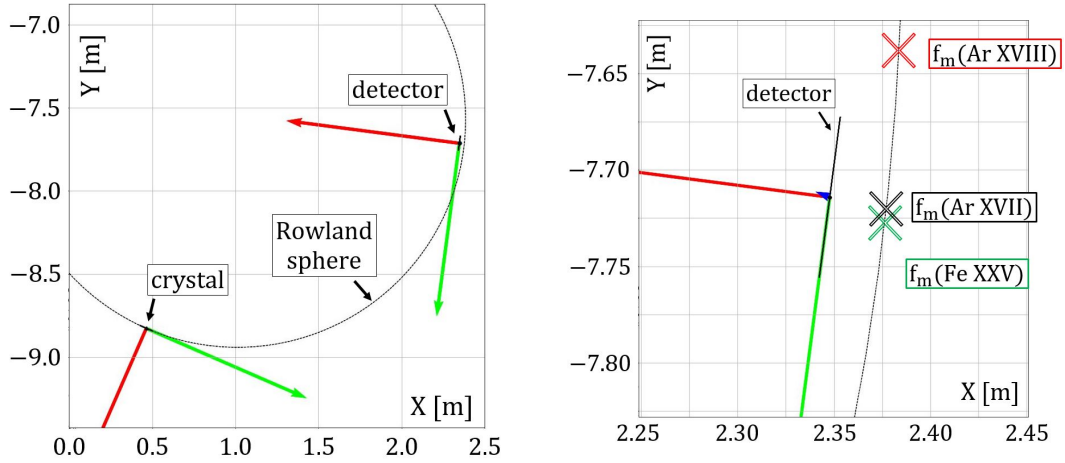

Figure 2.20. – *Left: Toroidal cross-section of the XICS spectrometer with a common position for all the crystals in the tokamak frame and the approximated position of the detector. Right: zoom in to the location of the detector to highlight the difference to the Rowland sphere and meridional foci.*

XICS spectrometer in the tokamak frame (WEST's symmetry axis at $X = Y = 0$). As for the positions of the sagittal foci in Fig. 2.19, the three crosses represent the theoretical

positions of the respective meridional foci for the three crystals. We make here the approximation that all the crystals have the same in-line position facing the plasma, which is not exactly the case because of the uncertainties of the rotating table. Thus, due to the same curvature radius, the Rowland sphere are common to all. However, we can see that the recomputed position of the detector is neither perfectly tangent to the Rowland sphere, nor at the location of one of the three meridional foci. Due to the lack of knowledge of the real position of the detector in the absence of spectral calibration as expressed in the last Section, we cannot know accurately its real position for now but we can still estimate the broadening due to this fact.

2.2.5.2. Broadening due to the detector position

The fact that the detector position is probably not exactly located at a meridional focus of one of the three crystal induces a broadening of the spectral lines. To visualize this effect, we propose to compare the bi-chromatic emission for a uniform volume of plasma for the computed position of the detector and its ideal position at the meridional focus of the Ar XVII crystal, as shown in Fig. 2.15.

The aim is to study the broadening of the spectral line as measured and deduce the importance of this effect on the measured width. Fig. 2.21 shows the broadening induced by the position of the detector on two close wavelengths measured. At the top, the detector is placed at the computed, and approximated, position and at the bottom, at the meridional focus of the Ar XVII crystal. We can notice first that the positions of the wavelengths are shifted by approximatively 2 cm. The intensity measured on the simulated detector, in arbitrary unit, is approximately 42% weaker when the detector is not modelled on the meridional focus on the Rowland sphere but few centimeters ahead.

In addition, when the detector is located at the meridional focus, the lines are spread on two pixels on the detector while at the approximated position, this spread is multiplied by a factor four. It is equivalent to an effective broadening of $\Delta\lambda \approx 1.5\times10^{-13}$ m while in the ideal case, it is $\Delta\lambda \approx 3.6\times10^{-14}$ m. This broadening, induced by an unknown detector position, is therefore prejudicial and increases the measured line width and thus the inferred ion temperature. This makes spectral calibration all the more essential to determine the instrumental causes of spectral broadening and their significance.

2.3. Spectrometer commissioning

The installation and testing phase of a new diagnostic is an important one, as it generally provides us with valuable information about what is known as the instrument function. It is during this phase that we gather as much information as possible on each component of the measuring instrument and that we can judge their intended operation. The quality and accuracy of the measurements then depend on an instrument function that is perfectly, partially or not at all known, because it must be

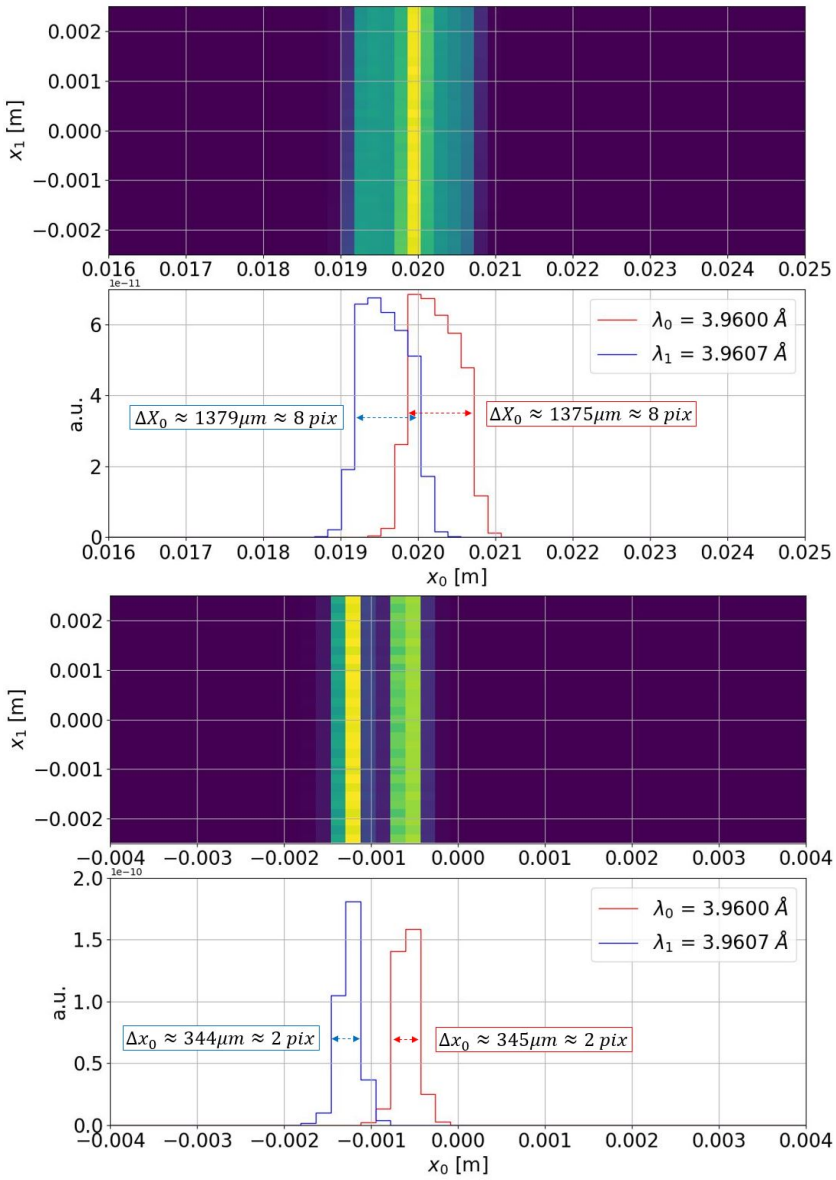

Figure 2.21. – *Computed position and broadening of two close spectral lines on (top) the computed position of the detector and (bottom) its optimal location at the Ar XVII meridional focus.*

possible to distinguish the physical information in the signal from the information added by the instrument. In this section, we will describe the processes used, and not used, during the XICS installation and their effects on the instrument function.

2.3.1. Alignment

A view of the instrument and its main components is shown in Fig. 2.22. The Be window is inserted between the vacuum vessel and the crystal box where the Bragg

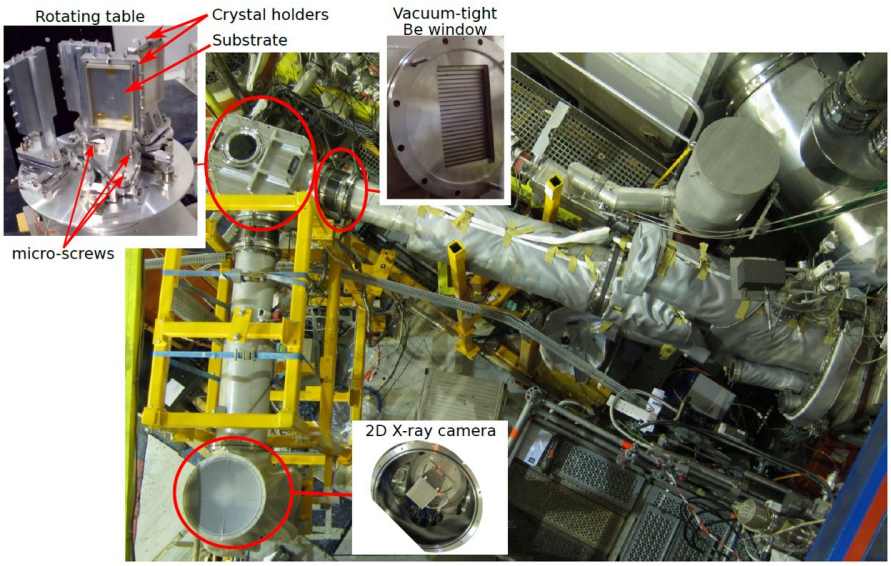

Figure 2.22. – *Top view picture of the XICS instrument on WEST tokamak [37].*

crystals are placed on a patented rotating table [65]. It is remotely-controlled and can hold up to four crystals. The rotating table allows to choose which crystal is in use for each plasma discharge. All crystals have very close Bragg angles for their target wavelength, so that the Rowland circles are very similar, see Sect. 2.2.4. It allows a fixed position of the detector to remain relevant whatever crystal is chosen. Micrometric screws allow to fine-tune the position and orientation of each crystal holder individually. On each holder, a spherically-curved substrate supports two thin quasi-transparent half-crystals. The two stripes are positioned side by side on a substrate, forming a single crystal with the same surface and volume characteristics. Its installation and alignment were carried out in several steps, in air and using bright visible sources.

First, the radius of curvature of each crystal was checked experimentally using autofocusing of a slit-like source at the center of the crystal's sphere of curvature. The resulting radius of curvature is 2745 mm, value referenced in Table 2.1, and differs from the specifications by ≈ 29 mm. Then, once all crystals are installed on the rotating table, three micro-screws are used to fine-tune their positions and orientations individually by focusing a fixed slit-like source on a fixed visible detector. This is the individual alignment phase. It is performed first in the laboratory and then again in the tokamak hall, with LEDs mounted on a plate, once the rotating table has been installed in its vacuum chamber.

After the alignment, two more steps were undertaken as verifications:

1. A set of colored LEDs is placed at the detector location to represent a set of lines of sight directed to the inside of the tokamak vessel. This step serves as a check for vignetting due to structures inside the vessel or the spectrometer.
2. A laser metrology campaign was later carried out to accurately locate, in the tokamak frame, all crystals at their 'in-line' positions.

The use of visible light implies that the approximation of the crystals as spherical mirrors is correct. The crystal cuts have to be perfect, meaning that the crystal lattice must be perfectly parallel to the crystal's optical surface. We can see from Table 2.1 that there are actually intrinsic parallelism defaults within the crystal lattice and that a true X-ray alignment as described in [66] would further reduce uncertainties, as well for the alignment as for the surface characterization of the crystals used. Finally, some useful information for the model can be obtained by scanning the rotation table angle from shot to shot during experimental campaigns. It helps constrain geometrical uncertainties. In that sense, a common mobile platform, finely controlled with a patented design [65], turns out more informative than non-mobile crystals.

2.3.2. Argon impurity injection

Here in WEST among other tokamaks, the problem with the measurement of an Ar spectrum is that there is no natural Ar in a D-D plasma in a W environment. It is therefore necessary to inject in the plasma emitting ions to increase the line dynamics. Argon was chosen because it is a fairly light noble gas (Z=18) that does not disturb the plasma too much, can ionise quickly (see the Ar fractional abundances as a function of the plasma temperature in Fig. 1.12) and is easy to pump out.

The need to inject Ar impurities in the plasma is essential for the signal-to-noise ratio of the instrument during experimental campaigns. Ar injections are performed when the Ar XVII or Ar XVIII crystals are 'in-line'. They generally involve between 10^{-1} and 1Pa m^3 of a D_2/Ar 0.01% pre-mix. An injection of 1Pa m^3 corresponds from the ideal gas law to an injection of 7.3×10^{21} particles, of which one ten-thousandth corresponds to Ar atoms. This is equivalent to a concentration of 10^{-3} in relation to an averaged electron density in WEST of 5×10^{19}m^{-3}. Experience shows that one injection every 3-5 shots or a large one at the start of the day are enough. Particular care must be taken to inject argon at strategic times in a plasma scenario, since too high an Ar concentration can lead to a large fraction of power radiated by these impurities and even to a disruption. The end of a plasma discharge, or during a heating plateau with the LHCD system, would appear to be ideal moments for the plasma to receive these injections without too much risk to the experiment in progress. Fig. 2.23 shows the time variation of Ar^{16+} concentration for two plasma discharges from the same day, one has a D_2/Ar injection of approximately 0.3Pa m^3. The injection time is marked with a green arrow for the #59974 plasma discharge. The concentration increases with a strong gradient, multiplied by a factor ten for the first pulse ($c_{Ar,16+}(t = 2s) = 2.92 \times 10^{-4}$ and $c_{Ar,16+}(t = 2.4s) = 2.89 \times 10^{-3}$). The injection has led to an early plasma disruption. The concentration time profiles, for which the computation method is detailed in Sect. 3.4, also display the lowering of the concentration after a few consecutive discharges.

An acceptable concentration of Ar in the vacuum chamber can be maintained at an acceptable level to guarantee a good signal-to-noise ratio during a few consecutive plasma discharges, or even consecutive whole days without injection from the experiments. No Fe injection is needed for the Fe XXV crystal since Fe ions are intrinsically

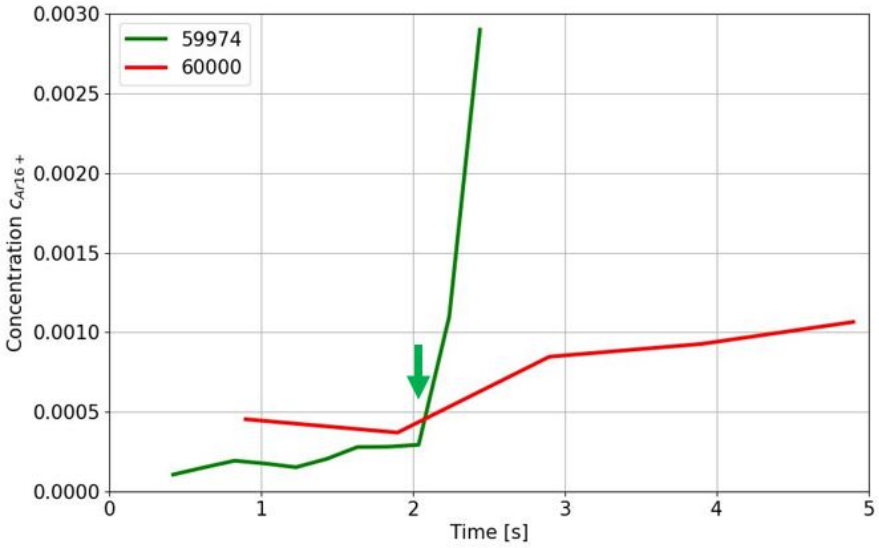

Figure 2.23. – *Time variation of the Ar^{16+} line-averaged concentration for the WEST #59974 and #60000 plasma discharges from the same experimental day of operation. D_2/Ar injection is marked with a green arrow for the #59974 discharge.*

present in the tokamak vessel from its structural materials. The plasma parameters such as the electron temperature and density must be large enough for the ions of interest to exist in significant concentrations. According to [28] and the Ar fractional abundance plot in Fig. 1.12, although the fractional abundance of Ar XVII has a maximum at ≈ 0.9 keV, it remains high enough in a wide range of electron temperature, to make that ion a suitable target for multiple plasma scenarios. The lower boundaries for the electron and Ar densities, as well as for the electron temperature, are determined by the intensity of the photon flux, i.e. the SNR.

This instrument allows to control the signal-to-noise ratio, by increasing the acquisition time as necessary in the cost of time resolution. The detector allows a fairly broad acquisition time range, from a few milliseconds to seconds. The compromise between the temporal and spatial (vertical binning) resolutions and signal-to-noise ratio typically allows for integration time around 200 – 500 ms, for the reasons explained previously.

2.3.3. Discussion on calibration methods

Calibration has not been performed during the first commissioning of the instrument and cannot be performed at the moment due to a lack of technical resources. However, spectral calibration must be carried out with a specific and well-known X-ray source to allow absolute rotation measurements since the position of each spectral line must be known perfectly. We can find in the literature some examples for XICS systems at W7-X [67] or K-STAR [68].

An innovative design for a wavelength calibration system that allows routine calibrations between plasma pluses has been proposed in [69]. It consists in the installation of an X-ray tube between the plasma vessel and the crystal, the closer to the sagittal focus as shown in Sect. 2.2.2, to simulate a plasma emission. The calibration system provides the emission of two well-known spectral lines to be measured and a ray-tracing simulation code that simulates the X-ray source, the crystal and the detector. The estimated error in the measurement is low, approx 10^{-7} Å, to ensure with high accuracy the position of the lines on the detector. A similar system can be installed in the WEST XICS spectrometer, the X-ray tube located inside the crystal box between the rotating table and the vacuum vessel and the Be window.

The ray-tracing algorithm provided with the ToFu library code, already used to model the synthetic diagnostic, can provide simulated ray positions, as shown in Fig. 2.24. The top figure displays a part of a 2D spectrum from the WEST #56683

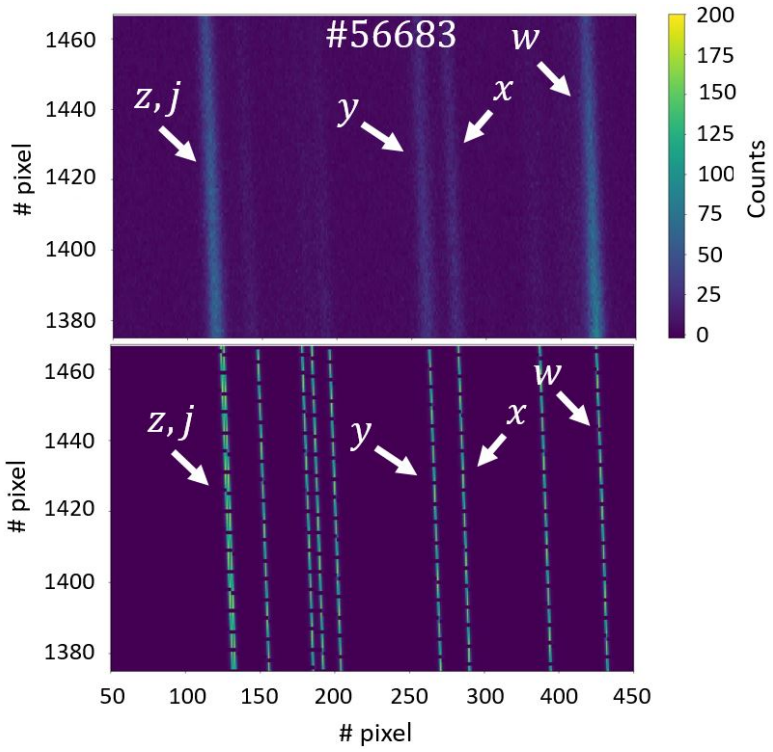

Figure 2.24. – *Comparison of the Ar spectral line positions on the detector between (top) a measured 2D spectrum and (bottom) a simulated one.*

plasma discharge. Five spectral lines from Ar^{15+} and Ar^{16+} are marked with white arrows. The simulated spectral lines shown in Fig. 2.24 (bottom) are created by combining the ray-tracing with a synthetic diagnostic of the instrument and extracting the Rocking-Curve computed for each Ar spectral line, as studied in Sect. 2.2.1. The ray-tracing algorithm takes into account the value of the non-zero Rocking-Curve for all the diffracting angles and uses these values as pseudo-intensity of lines to be traced. According to the position of the lines measured with the calibration system,

optimization algorithm could lead to the most reliable position of the detector, since the alignment procedure with visible light did not provide such information.

A different approach is proposed in [70], not based on a X-ray tube installed in the XICS instrument but that uses directly the rotational properties of the plasma discharges to perform absolute spectral calibration. Three different ways to perform a wavelength calibration are detailed. A mode-locking [71] tracking is done since it is the sign of a drop of the toroidal rotation to zero and thus of the Doppler shift. A comparison with Magneto Hydro Dynamics (MHD) mode rotation could also provide an estimation of the toroidal rotation of the plasma. Unfortunately, it is commonly known that in WEST plasma discharges, the toroidal rotation is expected to be significantly smaller (and thus harder to measure) than in other tokamaks like Korea Superconducting Tokamak Advanced Research (KSTAR) due to the absence of any NBI heating [72] that would transfer momentum to the plasma.

Similarly, a brightness calibration could also be useful in order to convert the counts in brightness unit. In addition, more information about the quantum efficiency of the detector would have been useful to the energy range of the Ar XVII spectrum for example, $E \approx 3.1$ keV, where the only data in our possession about this parameter are given in Table. 2.2. Such an operation to calibrate a VUV (Vacuum Ultra-Violet) spectrometer installed on WEST has been performed and described in [73]. Details about the spectrometer will be given in Sect. 3.4. As we are currently unable to perform a brightness calibration in the same way as described previously, we can refer to the work of [32] in which a calibration transfer has been performed from an EUV spectrometer to another, also equipping the WEST tokamak. The EUV spectrometer to XICS calibration transfer will be the main topic of Sect. 3.4 where we will detail the procedure and the resulting computations of Ar and W impurity density profiles.

2.3.4. Discussion about defective detector modules

During the introduction of the detector used in the XICS spectrometer made in Sect. 2.2.3.2, we introduced the main characteristics of the detector. Among all data gathered in Table 2.2, one of them became critical for the spectrometer operation. The whole detector is made of seven modules stacked together in the vertical direction. Fig. 2.25 shows two different 2D spectra measured for two different plasma discharges from two consecutive experimental campaigns. The left one is extracted from the first experimental campaign and the right one from the next one.

Two important results are noticed. First, the spectral lines appear larger on the left spectrum. This is due to a line-doubling phenomenon that will be introduced in Sect. 3.2 and which has been solved between the first two campaigns of the instrument hiding one half-crystal facing the plasma, restoring the spectral resolution to its best. The second is the loss of two modules, second and third from the top.

From the geometrical considerations expressed in Sect. 2.2.2, the top of the detector corresponds to the bottom of the plasma. The loss of these two modules prevents the measurement of the Ar and W spectral emission from the lower part of the plasma, which, according to Fig. 2.18, corresponds to the lines of sight below the axis $Z = 0$.

One can also notice that the spectral lines are not perfectly symmetrical in the vertical direction of the image. It means that the central module is not sufficient to measure the emission from a sufficiently large area around the magnetic axis of the plasma. In other words, we have to deal with a truncated measurement of the plasma center, which is very inconvenient given that this diagnostic was designed to measure plasma temperature and rotation from the plasma center emission.

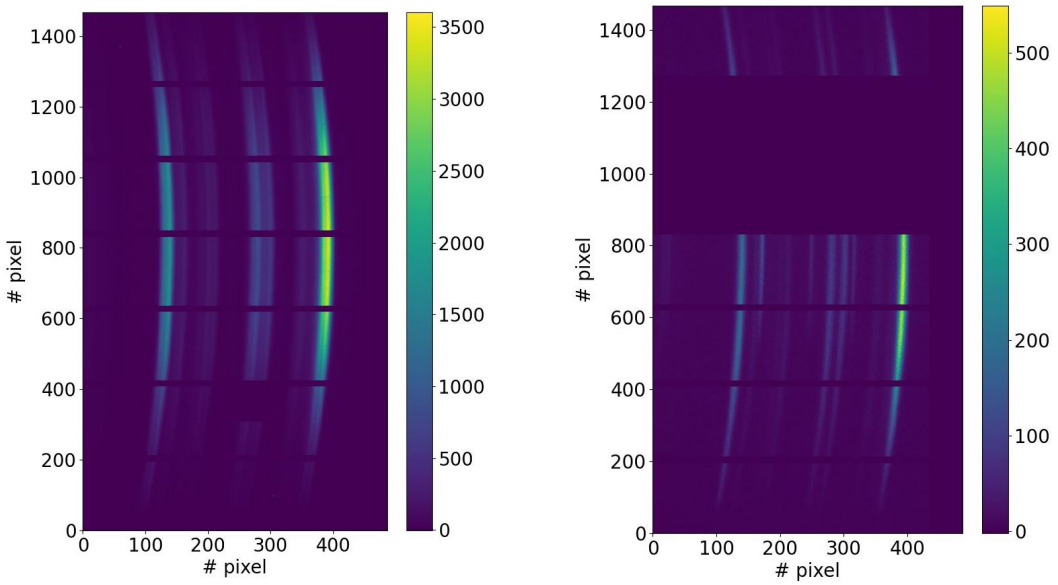

Figure 2.25. – *2D spectra measured for the (left) WEST* #55076 *plasma discharges at t = 55.8s with a line-doubling issue, cf. Sect. 3.2, and (right) WEST* #56683 *plasma discharges at t = 37.7s.*

The loss of modules can have multiple causes and has occurred on several time since its installation. First of all, make sure that the detector is switched off between campaigns. In fact, between campaigns, electrical work in the building may lead to sudden, unannounced cuts in the general power supply. These shut-downs (and subsequent power-ups) are strongly suspected of inducing current transients in the cables, which may not be properly protected by the detector electrical protections. After such events, a module was deactivated and iterations with DECTRIS revealed that an internal electrical fuse had probably blown. These are very small fuses and replacing them, which requires careful opening of the control unit, allowed to solve the problem.

Second, the data cables that connect the detector to its control unit via the feed-through have been identified as a weak spot. The cables themselves are very high-quality but the connectors on the feed-through are very fragile and can be easily damaged if any significant force. A module could be retrieved by interchanging the data cables by the feed-through, but that remains quite random and the fact we are not able to retrieve all modules suggests that some connections are probably damaged. A short-term solution would probably be to disassemble the feed-through and send

it back to DECTRIS for inspection with the data cables and possible repair. A good long-term solution would be to mechanically protect the cables and connections from any stress.

2.4. Spectral modeling

In this Section, the data treatment algorithm used to model the Ar XVII spectrum is introduced in several points. Due to the number of spectral lines measured and the different plasma conditions for which they appear, the algorithm is based on a non linear fitting approach. First, in Sect. 2.4.1 the preparation of the data is outlined. The two-dimensional (space and wavelength) measured spectra must be transformed, i.e. an image axis conversion step is performed in order to straighten the spectral lines and thus process two-dimensional spectra. A pixel filtering step is also added to measure the signal-to-noise ratio.

The aim is to fit a mathematical model to the experimental data with prior information concerning the measurements based on theoretical knowledge and/or experimental experience, several initial guesses and spectral constraints, to improve both the computation time and the accuracy of the algorithm. This is described in Sect. 2.4.2. The Ar XVII spectrum is composed by a background above which the spectral lines are measured so the modelling of this background becomes very important to obtain a good minimization of the difference between the model and experimental data. Definitions of the background and the lines modelling are given in this Section. Finally, the tomographic inversion process is used to compute radial emissivities from the line-integrated measurements and explained in Sect. 2.4.3.

2.4.1. Preparation of the data

2.4.1.1. 2D image transformation

The detector returns 2D arrays corresponding to the intensity collected by each pixel. Fig. 2.26 (a) shows a measured image with the XICS instrument for the WEST #59975 plasma discharge, at t = 2.07 s. It shows the number of counts per pixel, for the 487 pixels in the horizontal direction and 1467 in the vertical direction. We observe several spectral lines with a hyperbolic shape. The wide dark stripe around the 1000th pixel row represents a defective module and the other narrower ones are the blank spaces between the neighbouring modules. From that image, we can extract for each individual row a lineout as shown in Fig. 2.26 (b). We can already identify several peaks which have to be identified as spectral lines, i.e. converting the pixel axis to a wavelength scale.

The measured images are the intersections between the planar detector surface and the spectral lines, Bragg-diffracted along cones having the crystal as apex, as demonstrated in Sect. 2.2.2. The spectral lines thus appear as hyperbolic arcs (for Bragg angles $\leq$ 60 degrees), as seen in the 2D image shown in Fig. 2.26 (a). A geometrical transformation is performed in order to straighten the spectral lines by converting the

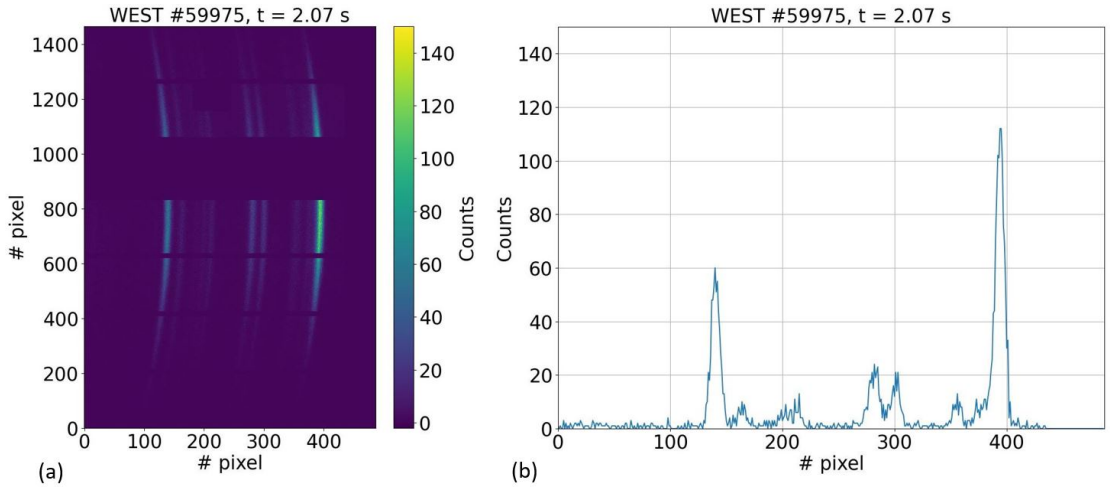

Figure 2.26. – *(a) Raw image measured for the WEST #59975 plasma discharge at t = 2.1 s and (b) associated spectrum taken for* 800th *row of pixels.*

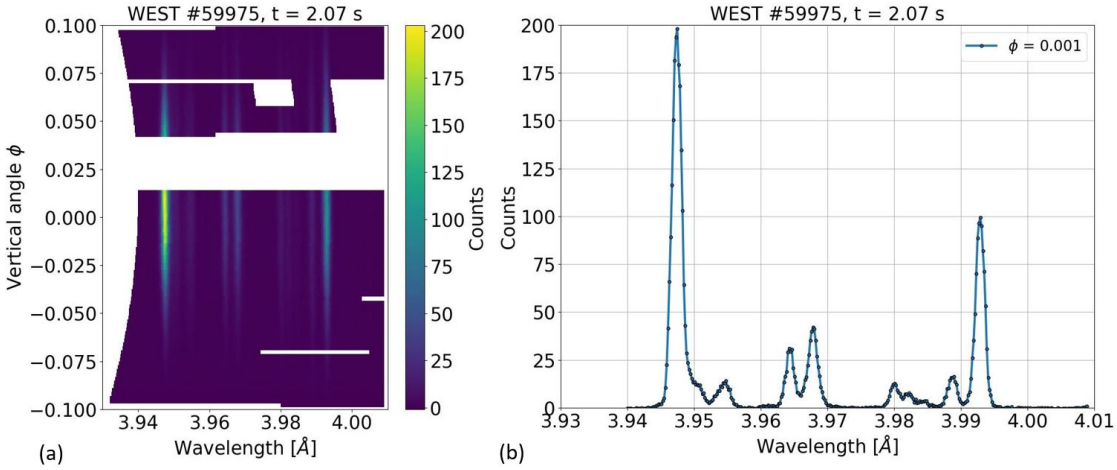

Figure 2.27. – *(a) Re-scaled image for the WEST #59975 plasma discharge at t = 2.1 s and (b) associated spectrum taken for* $\phi = 0.001$.

x- and y-axes into wavelength and vertical angle scales, as shown in Fig. 2.27. The (a) sub-figure represents the 2D spectrum after the axes conversion.

In the case shown here, one entire module is unavailable, causing the wide white stripe and missing data relative to a particular plasma volume. The other white areas represent masked pixels area due to some defects. The corresponding central spectrum is shown in the sub-figure (b), which corresponds to a 50 rows binning. The x-axis transform is done according to the Bragg relation which associates the highest wavelengths to the highest Bragg angles of diffraction (Eq. 2.1). Relatively to the Johann configuration, the highest wavelengths appear on the left side of the 2D image. The x-axis transform rebuild a correct scale where the lines are now straightened to allow a two-dimensional modeling.

The y-axis is first converted into a vertical angle ϕ corresponding to the angle

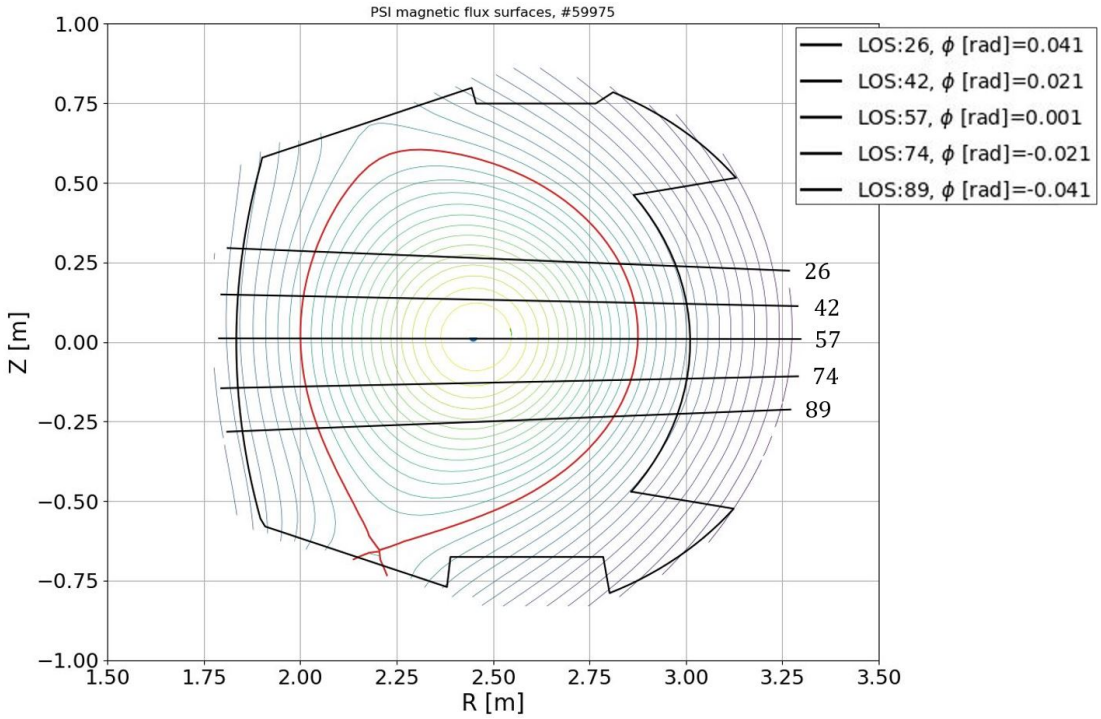

Figure 2.28. – *Vertical angle ϕ that defines the lines of sight with respect to the toroidal plane $Z = 0$.*

between the LOS and the horizontal plane, see Fig. 2.28. Each line of sight corresponds to a specific ϕ value, which crosses several magnetic surfaces, with their own radial coordinate ρ_{tor} defined in Sect. 1.2.4, along its path. It is thus used to derive the impact parameter knowing the magnetic equilibrium. The impact parameter h, illustrated in Fig. 2.29, is defined as the normalized radius of the magnetic surface to which the line of sight is tangential. This coordinate transform provides an estimate of the wavelength scale shown in Fig. 2.27 (b) and thus allows to identify the spectral lines. It also interpolates missing pixel values in inter-module spaces by applying B-splines over the entire image height. This process is automatically done for all plasma discharges processed by the dedicated synthetic diagnostic.

2.4.1.2. Data selection and signal-to-noise

For each time (or each image), an automated pixel selection is performed. As we can see in Fig. 2.30, the image is cut into several horizontal bands, defined by the black horizontal lines. In each horizontal band, the algorithm detects all the pixels and apply a SNR condition. The SNR is measured as the ratio between the peak height and the standard deviation value of the background (noise). A SNR of 3σ is generally the minimum acceptable with a probability, also called the confidence level, that the peak is ~ 99.7 % non-random noise. This way, we can set a minimum percentage of pixels in the band that must satisfy the SNR condition to be accepted. The SNR

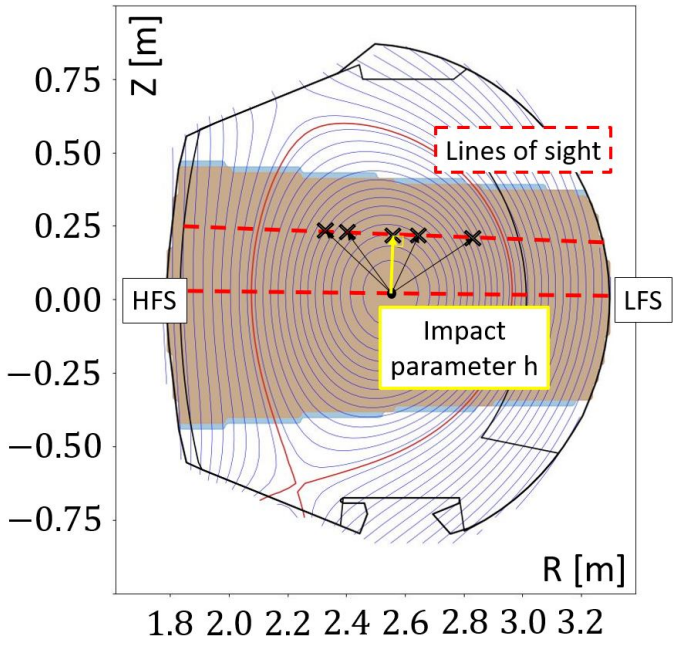

Figure 2.29. – *Geometric coverage of the diagnostic lines of sight in the poloidal cross-section (brown) and definition of the impact parameter. The black crosses define the intersections of the line of sight with the magnetic surfaces [37].*

condition must be chosen carefully taking into account the Ar concentration in the plasma. The lower the signal, the less strict the condition must be to exploit the data. Here, the pixels for which the condition is fulfilled appear in green. Other pixels where the condition is not fulfilled can also be accepted (in orange) because no signal from any spectral line is measured there and they can be used to model the background.

2.4.2. 2D images processing

In this section, we explain the main algorithm that is used to model the Ar XVII spectrum. As in Sect. 1.3.1.3, the spectra have two main components: a continuum due to Bremsstrahlung and a discrete set of lines. Multiple spectral constraints are used to improve processing speed and quality. These constraints give prior information about the theoretical wavelengths, the line width, shift and experimental line ratios. The aim is to give all the information we have to improve the data treatment.

2.4.2.1. Spectral constraints

The treatment algorithm is not based on a peak-finding model to identify the total number of spectral lines on the spectrum. It requires a former identification of the spectral lines with their expected wavelength in the Ar XVII spectral range. Table 2.3 lists the various Ar and W spectral lines that have been identified so far in the Ar XVII spectrum from the literature [52]. The W lines have been identified by [74] and [75]. The wavelengths referenced are used as initial guesses in the algorithm on which it is

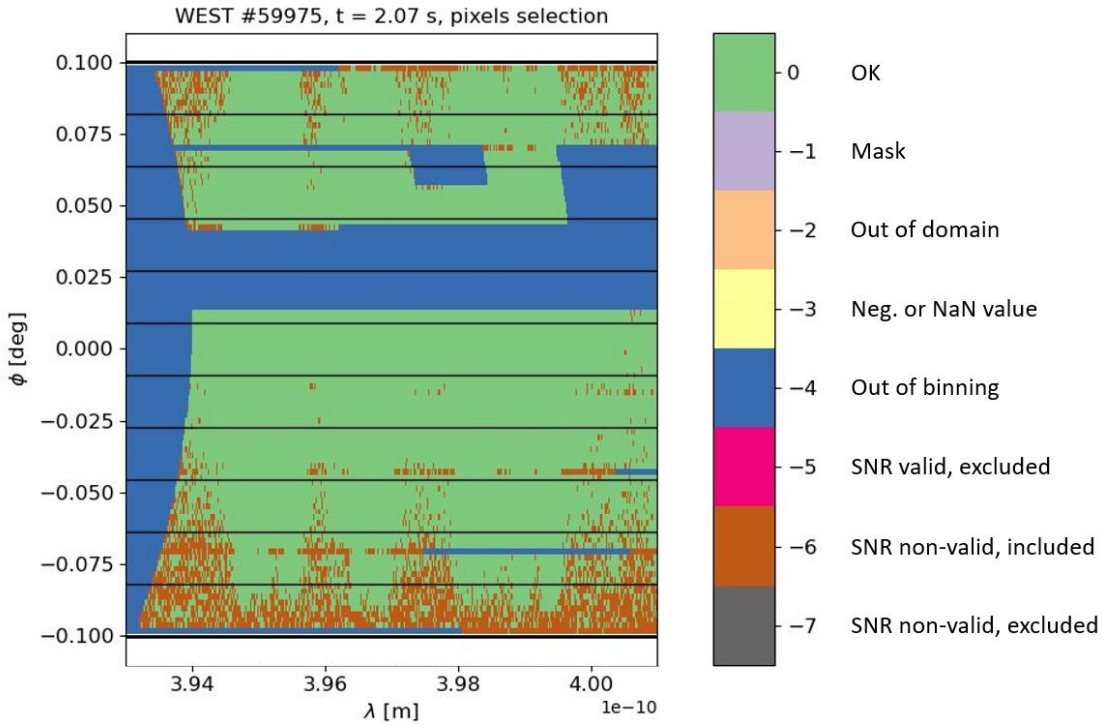

Figure 2.30. – *Automated pixel selection of the 2D XICS images. The color code displays the different values attributed to each pixel in all the horizontal bands (black lines).*

Ion	Name	Transition	λ [Å]
Ar XVII	w	$1s^2\,{}^1S_0$ - $1s2p\,{}^1P_1$	3.9490
Ar XVII	x	$1s^2\,{}^1S_0$ - $1s2p\,{}^3P_2$	3.9658
Ar XVII	y	$1s^2\,{}^1S_0$ - $1s2p\,{}^3P_1$	3.9693
Ar XVII	z	$1s^2\,{}^1S_0$ - $1s2s\,{}^3S_1$	3.9946
Ar XVI	k	$1s^22p\,{}^2P_{1/2}$ - $1s2p^2\,{}^2D_{3/2}$	3.9898
Ar XVI	j	$1s^22p\,{}^2P_{3/2}$ - $1s2p^2\,{}^2D_{5/2}$	3.9938
Ar XVI	q	$1s^22s\,{}^2S_{1/2}$ - $1s2s2p\,{}^2P_{3/2}$	3.9813
Ar XVI	r	$1s^22s\,{}^2S_{1/2}$ - $1s2s2p\,{}^2P_{1/2}$	3.9834
Ar XVI	a	$1s^22p\,{}^2P_{3/2}$ - $1s2p^2\,{}^2P_{3/2}$	3.9857
Ar XV	n=3	$1s^23l$ - $1s2p3l$	3.9560
W XLIV	Ga-3	$3d^{10}4p\,{}^2P_{1/2}$ - $3d^94p6f\,{}^2D_{3/2}$	3.963
W XLV	Zn-2	$3p^64s^2\,{}^1S_0$ - $3p^54s^25d\,{}^1P_1$	3.975
W XLV	Zn-3	$3d^{10}4s^2\,{}^1S_0$ - $3d^94s^26f\,{}^1P_1$	3.988

Table 2.3. – *Theoretical transitions and wavelengths of the Ar [42] and W [74] spectral lines identified in the Ar XVII spectrum.*

based to compute the Doppler shift and width of all the lines. However, this method leaves open the possibility of excluding certain spectral zones from the modeling, or

of considering only certain lines.

Since the Doppler broadening is the dominant broadening effect, all the spectral lines are modelled with Gaussian functions for this first version of the data treatment. For the modelling of the width of the lines, we choose to group the spectral lines by element to better constraint the algorithm. From the Gaussian function, the line width depends on the impurity ion temperature as $\sqrt{T_i}$ that is extracted by the FWHM of the curve. In general, the brightest line of the Ar XVII spectrum, the resonance line w, is used for the determination of the observed Doppler width. However, [76] chose the $j+z$ feature because no dielectronic satellites are located on the wings of the feature, contrary to the w line with the $n \geq 3$ dielectronic satellites located at its right side. As the Ar^{15+} j and Ar^{16+} z lines are close, less than 1 Å, the authors found that treating them as a single line only led to an overestimation of the temperature of 10% at $T_i = 0.5$ keV. Comparisons between the apparent widths of the w and j,z features, alone and in the same width group, is done in Sect. 3.3.2.

About the spectral shift, the algorithm uses the theoretical wavelengths referenced in Table 2.3 as initial guesses. The choice of grouping them by ion species or by element is also applicable, but since no spectral calibration has been carried out to know perfectly the wavelength scale of the spectrum, it is difficult to arbitrarily guide the algorithm without more information. We will see in Sect. 3.3.1 that the algorithm is efficient enough to find common shift values to all the ion species measured.

2.4.2.2. The Bremsstrahlung background

Bremsstrahlung has been identified in Sect. 1.3.1.3 as an important part of the background measured on the XICS spectra. The expression of the Bremsstrahlung emissivity in Eq. 1.47 can be retrieved to obtain a brightness measurement along a line of sight l according to Eq. 1.71:

$$B_l(\lambda) = \frac{1}{4\pi} \int dl \times b_l(\lambda) exp\left(-\frac{\alpha_l}{\lambda}\right) \tag{2.56}$$

where $b_l(\lambda)$ and α_l are defined as:

$$b_l(\lambda) = G_{ff}(Z, T_e, \lambda) \frac{n_e \times \sum_Z n_Z \times Z^2}{\lambda \sqrt{k_B T_{e,l}}} \tag{2.57}$$

$$\alpha_l = \frac{hc}{k_B T_{e,l}} \tag{2.58}$$

where from Eq. 2.57 can be expressed the effective charge Z_{eff} that represents the concentration of impurities in the plasma:

$$Z_{eff} = \frac{\sum_Z n_Z Z^2}{\sum_Z n_Z Z} = \frac{\sum_Z n_Z Z^2}{n_e} \tag{2.59}$$

In general on WEST, the effective charge Z_{eff} can reach almost a value of 5 due to the presence of various impurities in the plasma, of which tungsten. In a pure D-D plasma, this coefficient is 1.

Here, the approximation of quasi-neutrality is used as $n_e = n_i = \sum_Z n_Z Z$ between the electron and ions populations. The background modelling is a critical aspect of the overall spectrum modelling because an over-estimated background level can reduce the fitted intensity of low-intensity lines such as the dielectronic satellites $n = 3$. We constrain the background modelling in two steps. First, precautions had to be taken to filter out the noise measured on the images and originating from all the defective pixels on the detector surface. Fig. 2.31 shows a typical image recorded a few seconds

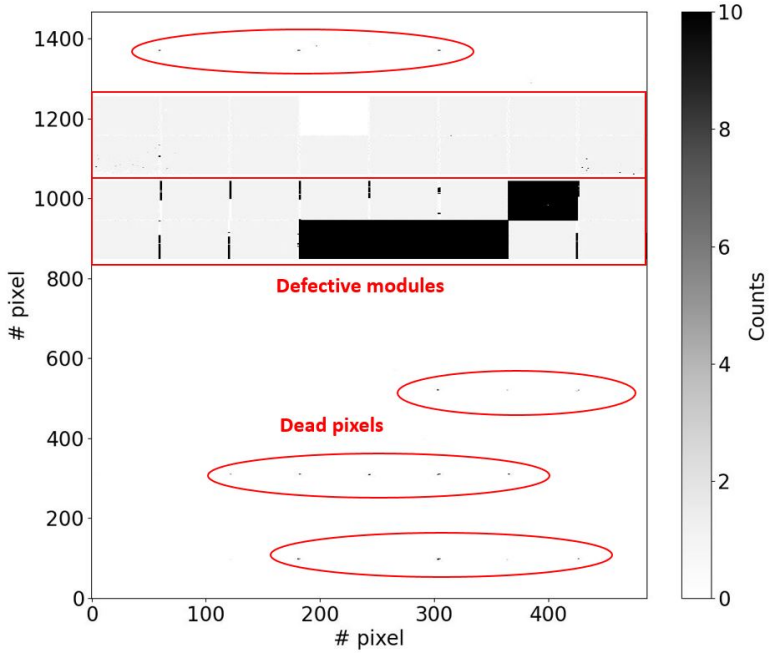

Figure 2.31. – *Pre-plasma image recorded by the detector, showing multiple dead pixel and two (partly) defective modules*

before a plasma start-up. It shows many isolated pixels with a non-zero signal and two modules where almost all the pixels measure a meaningless signal. The upper limit of the color bar representing the measured signal has been deliberately reduced to ten counts to better visualize the saturated pixels.

Second, the method used to model the background when processing spectra was based on its characterization in spectral areas where no lines are expected. As a result, the number of counts measured there are attributed to the background. It turns out that the list of spectral lines referenced in the table is not exhaustive and, on the contrary, an unknown number of additional lines are measured, often hidden by those of high intensity. Fig. 2.32 displays three different spectra of the WEST #59920 plasma discharge. The y-axis representing the number of counts is in a logarithmic scale to highlight the fit error on the experimental points. Two spectral domains are deliberately ignored as they do not bring anything important to this stage: $\lambda =$

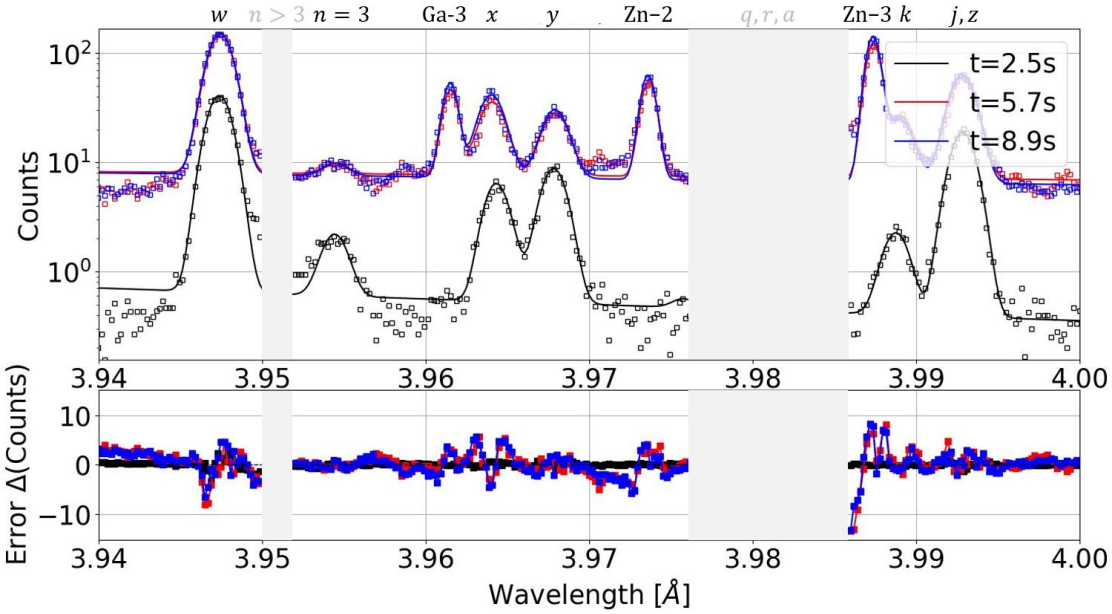

Figure 2.32. – *WEST* #59920 *plasma discharge where three spectra are extracted at three different time acquisitions. The line intensities are in counts per time unit, of 200ms of integration, and in a logarithmic scale. The residual of the spectra modelling is shown in the lower sub-figure. Two spectral intervals are grayed out as they are not taken into account.*

[3.950, 3.952] Å for the dielectronic satellites $n > 3$ and λ = [3.979, 3.986] Å for the (q, r, a) feature. We can easily notice that the background modelling is well performed on the long wavelength side but much less on the short wavelength side. As we previously said, the algorithm targets the spectral domains where no spectral lines are expected. This applies to the left wing of the resonance line, the right wing of the $j + z$ feature and all the spaces between lines. However, several features are noticed, at the left wing of the Ga-3 line at ~ 3.958 Å and between the y and Zn-2 lines at ~ 3.971 Å for example. The non-identification of these features misleads the algorithm and causes an increase of the background level, resulting in an overestimation on the left side of the spectrum. This implies an underestimation of low-intensity lines such as the dielectronic satellites $n = 3$.

To avoid this bias, we decided to model the background independently of the spectral lines. A first data treatment is applied on pre-defined spectral domains to avoid any spectral line, identified or not, to interfere. The results of this first procedure gives the Bremsstrahlung background modelled for each image. As a result, background-cleaned spectra are obtained with the subtraction of the original 2D spectra with the 2D background spectra. Fig. 2.33 shows a resulting spectrum for the WEST #59920 plasma discharge at t = 10.13 s. Here, the discrete spectrum fitting is plotted after subtraction of the background level from the measurements. The description of the multi-Gaussian model in the next Section do not take into account anymore the background modelling.

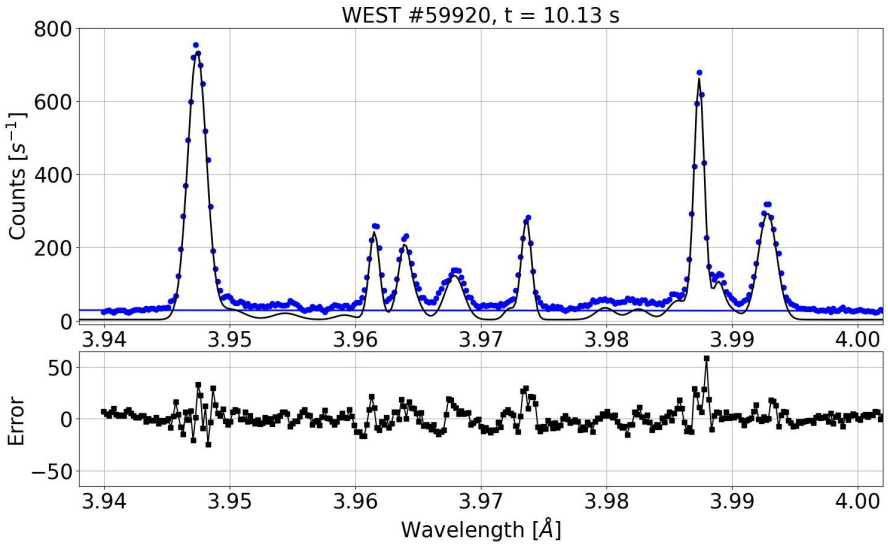

Figure 2.33. – *Typical spectrum for the WEST #59975 plasma discharge at t = 10.13 s (black) fitted on the experimental points (blue dots) reduced by the Bremsstrahlung background (blue line).*

2.4.2.3. The multi-Gaussian function

The Gaussian function that is used to model in first approximation the spectral lines has been introduced in Sect. 1.3.5. Eq. 1.78 takes into account both the Doppler shift and the Doppler broadening that affects the shape of the lines. In order to interpret the spectrum, each line is modeled with a Gaussian function and the total spectrum by a sum of Gaussian functions:

$$F_l(\lambda) = \sum_j A_j(\lambda) \times exp\left[-\frac{\left(\lambda - \lambda_{0,j}\right)^2}{2\omega_j^2}\right] \tag{2.60}$$

where the suffix l refers to the line of sight considered, ω_j^2 is the Doppler broadening defined in Eq. 1.80, $\lambda - \lambda_{0,j}$ represents the Doppler shift between the theoretical and measured wavelengths and the summation is performed on all the spectral lines measured j. A common least-squares computation, based on the sum of squared residuals, is used to minimize the error between the measured data y_l and the model F_l for all the lines of sight l:

$$\chi^2 = \sum_i \left(y_i - F_i\right)^2 \tag{2.61}$$

The choice to fit in advance the background has been discussed just above and the resulting spectrum only contains discrete components. It implies that two different minimizing functions are defined, one for the Bremsstrahlung background as explained in the last Section and a second for the over-all spectrum. They are expressed

respectively as follows:

$$\chi^2_{ff} = \left(y_l - B_l(\lambda)\right)^2 = \left(y_l - b_l(\lambda) \times exp\left(-\frac{\alpha_l}{\lambda_l}\right)\right)^2 \tag{2.62}$$

$$\chi^2_{sp} = \left(y_l - F_l(\lambda)\right)^2 = \left(y_l - \left[\sum_j A_j.exp\left(-\frac{\left(\lambda - \lambda_{0,j}\right)^2}{2\omega_j^2}\right)\right]\right)^2 \tag{2.63}$$

The separation of the two components of the spectrum allows to reduce the number of parameters to be minimized by each modelling procedure, two parameters b and α for the background and j times the three parameters of the Gaussian function $(A_j, \lambda_{0,j}, \omega_j)$ for the discrete spectrum. The result of the procedures gives the intrinsic residue:

$$Re_l = y_l - F_l \tag{2.64}$$

The optimization problem that is posed to minimize the residuals between the experimental data and the theoretical model is by nature non-linear by the summation over j Gaussian functions and l lines of sight. Generally, to improve the accuracy of non-linear fitting algorithms, a Jacobian matrix is needed. In vector analysis, the Jacobian matrix is the matrix of first-order partial derivatives of a vector function. The determinant of this matrix, known as the Jacobian, plays an important role in solving non-linear problems. The general form can be written for a general function F containing x_n variables as:

$$J(F) = \left[\frac{\partial F}{\partial x_1}, \cdots, \frac{\partial F}{\partial x_n}\right] \tag{2.65}$$

There are as many partial derivatives as variables in the function f_1 considered. The Jacobian associated to the multi-Gaussian function $F_l(\lambda)$ for every LOS l takes thus the following form:

$$J(F_l(\lambda)) = \left[\frac{\partial F_l}{\partial A_j}, \frac{\partial F_l}{\partial \lambda_{0,j}}, \frac{\partial F_l}{\partial \omega_j}\right] \tag{2.66}$$

with

$$\frac{\partial F_i}{\partial A_j} = \sum_j exp\left[-\frac{\left(\lambda - \lambda_{0,j}\right)^2}{2\omega_j^2}\right] \tag{2.67}$$

$$\frac{\partial F_i}{\partial \lambda_{0,j}} = -\sum_j \frac{A_j \times \left(\lambda - \lambda_{0,j}\right)}{\omega_j^2} exp\left[-\frac{\left(\lambda - \lambda_{0,j}\right)^2}{2\omega_j^2}\right] \tag{2.68}$$

$$\frac{\partial F_i}{\partial \omega_j} = \sum_j \frac{A_j \times \left(\lambda - \lambda_{0,j}\right)^2}{\omega_j^3} exp\left[-\frac{\left(\lambda - \lambda_{0,j}\right)^2}{2\omega_j^2}\right] \tag{2.69}$$

The implementation and the use of these analytical expressions for the Jacobian decreases the fitting computation time and increases the accuracy of the algorithm.

2.4.2.4. Vertical binning with B-splines function

The conversion of the image axes presented in Sect. 2.4.1 enables for a direct two-dimensional image processing. Each pixel row then corresponds to a line of sight l in the plasma, with a spatial resolution of the order of the centimeter, as shown in Sect. 2.2.4.1. We then obtain as many data points, or 1D spectra, as we have rows of pixels in the vertical direction of the image. However, as we saw in the previous Section, for l lines of sight, the multi-Gaussian function $F_l(\lambda)$ used has a very large number of variables to solve:

$$N_{var} = l \times (A_j, \lambda_{0,j}, \omega_j) \tag{2.70}$$

The computation time would then be greatly increased if we were to consider the 1467 lines of sight, but to the benefit of spatial resolution.

To reduce this computation time, rows of pixels are then grouped together, for a number chosen by the user. The choice of this number is a compromise since the lower the number of bins, the more rows of pixels will be included in it. Conversely, the greater the number of clusters and the better will be the spatial resolution. Fig. 2.34

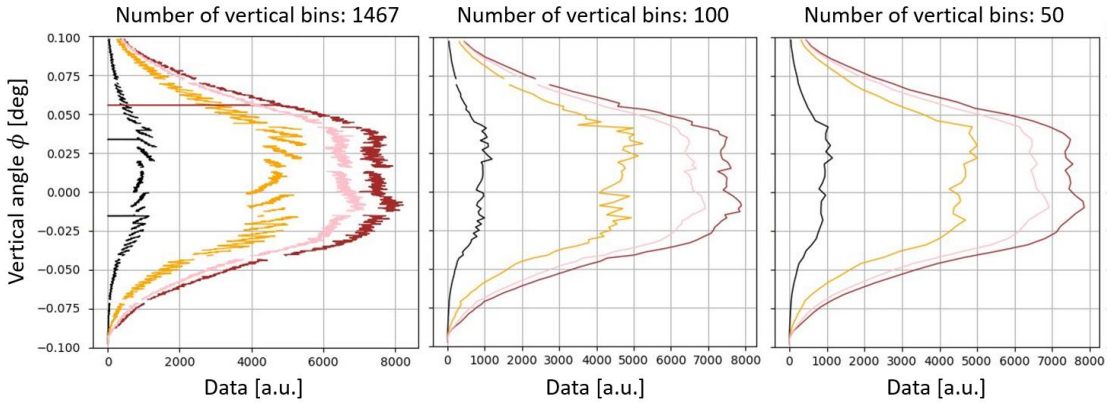

Figure 2.34. – *Smoothing induced by the number of vertical bins on a vertical section of the measured intensity of a line. 1467, 100 and 50 vertical bins are shown here.*

displays three numbers of vertical bins applied on the image and the smoothing induced on a vertical section of a spectral line intensity measured. For the case of the 1467 pixel rows selected, i.e. no vertical binning, the signal is highly noised. This is mainly a statistical noise characterised by the Poisson law which describes

an uncertainty on N measurements in $\sqrt{(N)}$. The effect of adding a greater number of pixels rows to a bin, and therefore tending towards a smaller total number of bins, increases the Poisson statistics per bin and thus reducing the associated noise. Particular care must be taken not to use a too small number of bins, in which case physical information could be lost through degradation of the spatial resolution.

The connection between the vertical bins during the data processing is made via B-splines (BS) functions to ensure a continuous solution between them. Basically, B-splines basis functions $B^{i,d}$ are described recurrently as a function of two parameters, the order d and a vector of k knots t_k as :

$$B^{i,d}(t) = \gamma^{i,d} \times B^{i,d-1}(t) + (1-\gamma^{i,d}) \times B^{i+1,d-1}(t) \tag{2.71}$$

where

$$\gamma^{i,d} = \frac{t - t_i}{t_{i+d-1} - t_i} \tag{2.72}$$

that satisfies:

$$B^{i,d} = \begin{cases} \gamma^{i,d} & \text{if } t_i \neq t_{i+d-1}, \\ 0 & \text{otherwise} \end{cases} \tag{2.73}$$

B-splines functions of second degree are represented in Fig. 2.35 where the sum of of all the amplitudes $\gamma^{i,d}$ must be one between all the functions for a specific value of x. The solution of each B-spline function is thus connected to its neighbours

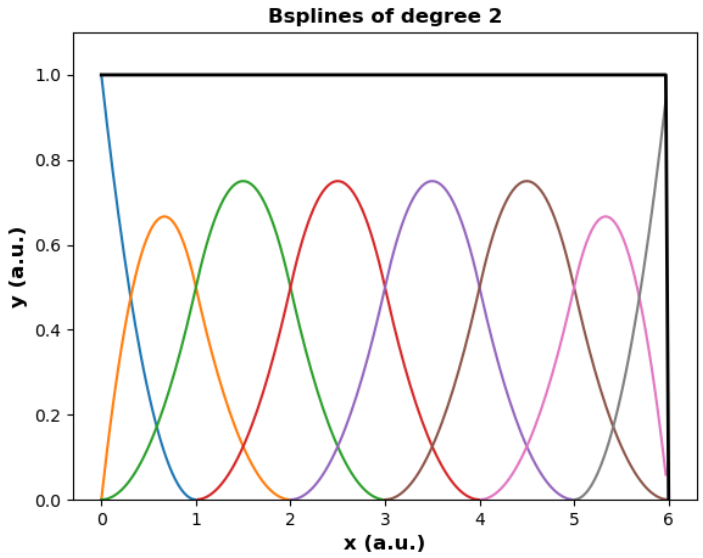

Figure 2.35. – *Sketch of B-splines functions $B^{i,d}$ of degree 2.*

and the smoothness model of the function on which we apply this method can be made. For our case, we apply a finite number of knots to the total height of the image,

with discretized values of the vertical angle ϕ shown in Fig. 2.30, and this allows the algorithm to process each information contained in the neighbouring bins as consistently as possible. Examples are shown in Fig. 2.36 of B-splines application

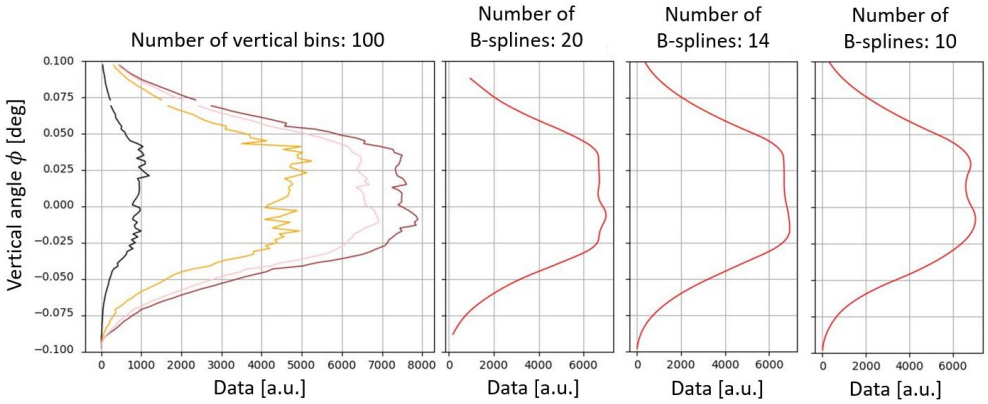

Figure 2.36. – *Different smoothing of the signal obtained with 100 bins presented in Fig. 2.34 with 10, 14 and 20 B-splines functions applied over the height of the image.*

on the signal weighted over 100 vertical bins presented in Fig. 2.34. The higher the number of BS, the more the amplitudes of each function correspond to the real fluctuations in the data. We can therefore play with these two parameters, the number of vertical bins and BS functions, to identify a compromise between spatial resolution and smoothness, while always ensuring a continuous solution.

Fig. 2.37 shows the result of the fitting procedure on the discrete spectrum. From left to right, the original spectrum image is displayed on which the non-linear algorithm is performed and the residuals that are computed are shown in the right side. The largest residual values are then deduced precisely at the wavelength values of the measured lines. From the fitted image in the middle, three 1D spectra are extracted and are shown in Fig. 2.37. The color code is the same for both figures, to highlight the greatest line intensities for the central part of the image, corresponding to the plasma central area. The corresponding residuals are also represented.

2.4.3. Tomographic inversions

The integration of photons along lines of sight causes a loss of local information in the plasma. As a result, temperature radial and time profiles, whether for electron or ion, deduced directly from the XICS measurements have to be compared with precaution with other local temperature measurements, such as with the ECE radiometer. We therefore need to convert LOS-integrated measurements to radial quantities by means of tomographic inversions. The measurement of a specific line of sight m_i is the sum of the local emissivities $\vec{f}_j$ from all the volume units V crossed by the Volume

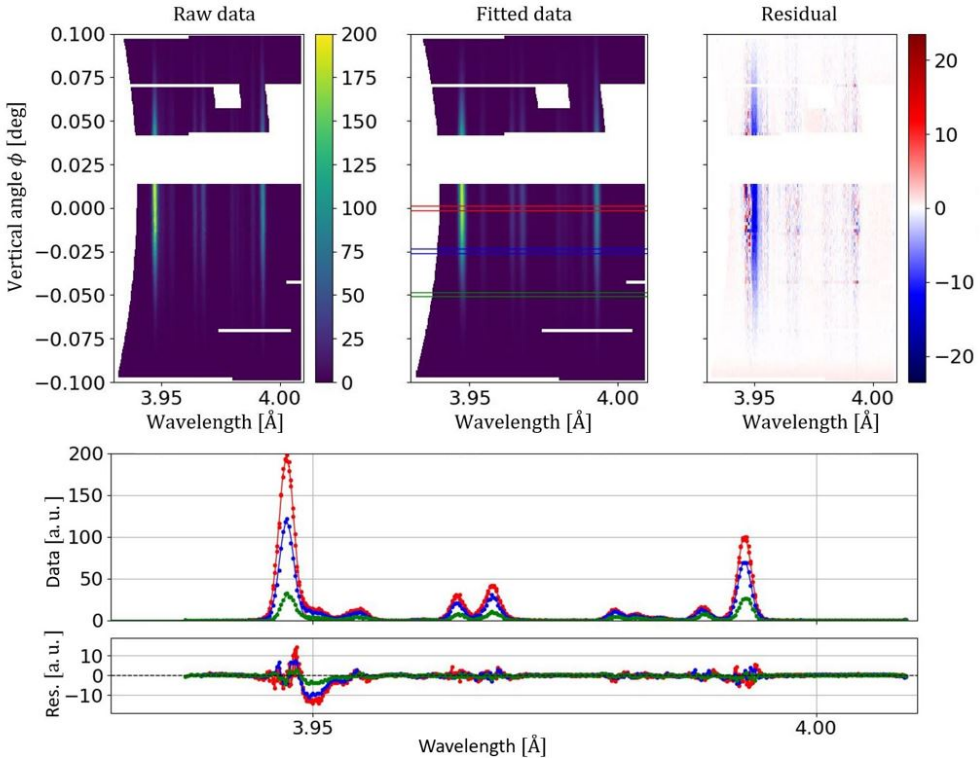

Figure 2.37. – *(Top left): Measured image on which (top middle) the fitting algorithm is applied and (top right) the corresponding residual map; (Bottom): Three spectra extracted from the fitted image and the associated residual profiles.*

Of Sight (VOS):

$$m_i = \iiint_V \iint_\Omega f_j \, d\Omega dV \tag{2.74}$$

A geometry (or transfer) matrix $L_{i,j}$, which describes the relationship between the plasma volume and the diagnostic geometry, is computed taking into account the magnetic equilibrium of the plasma and the spectrometer lines, or volumes, of sight. This linear problem is under-determined, in the sense that there are an infinite number of solutions due to the sparsity of the measurement. It is also ill-posed by the nature of the equations which are Fredholm equations of the first kind [77]. It means that even a square matrix would lead to highly noise sensitive solutions. This difficulty is solved by performing an inversion-regularization. The approach used here is the very classic Phillips-Tikhonov regularization [78] [79], which consists in minimizing a potential made of the sum of two terms, one quantifying the residue (χ^2) and the other one quantifying the irregularity of the solution. The second term is weighted by a positive scalar quantity (μ) called the regularization parameter:

$$\phi(f) = \chi^2(f) + \mu R(f) \tag{2.75}$$

This can be understood as a way of finding the most regular solution for a given set of measurements. The regularity functional $R(f)$ is a choice of the user and thus contains a prior information about the solution. A good way of testing the robustness of a solution is to run inversions with several different regularity functionals and compare them to find which of their features are robust and which are not. Details and relative merits of various regularity functionals and algorithms for choosing the value of the regularization parameter can be easily found in the literature. The references [80, 81, 82, 83, 84, 85, 86, 87, 88, 89] will provide details for the interested reader.

In our particular case, the radial emissivity function is a linear combination of a set of fifteen radial B-splines of degree 2:

$$f(x,y) = \sum f_i . B_i(\rho) \tag{2.76}$$

where $f(x,y)$ is the continuous 2D scalar emissivity field and the radial B-splines B_i are weighted by the unknown coefficients f_i. Thus, the functional integral Eq. 2.74 becomes a matrix equation involving the geometry or transfer matrix $L_{i,j}$ which contains the contribution of each B-spline to a given measurement:

$$m_i = \sum_j f_j B_j L_{i,j} \tag{2.77}$$

Thus the functional Eq. 2.75 becomes the following matrix equation:

$$J(\vec{f}) = ||\vec{m} - L\vec{f}||^2 + \mu R(\vec{f}) \tag{2.78}$$

In the following, the emissivity field f is approximated by discretized components $\vec{f}$, each associated with a discrete value of ρ. The method for determining the value of the regularization parameter is based on Bayesian inference and is described in [90]. Two different regularity functionals are tested:

— D1N2: $R(f(\rho)) = \int \nabla(f(\rho))^2$
— D2N2: $R(f(\rho)) = \int \Delta(f(\rho))^2$

In practice, we will see that both regularity functionals give almost identical results.

The use of tomographic inversions for the XICS system is performed with the python library ToFu. The expression of the Gaussian distribution function has been introduced in Eq. 2.60 with A_i, ω_i^2 and $(\vec{v}_i.\vec{l})/c$ respectively the ith line intensity measured, the Doppler broadening and the Doppler shift. As described in [91], the profile of each of these three parameters can be recovered by performing iteratively three inversions on the three moments of each Gaussian:

$$M_{n,i} = \int d\lambda I_i(r)(\lambda - \lambda_0)^n \tag{2.79}$$

$$M_{n=0,i} = \int d\lambda I_i(r)(\lambda - \lambda_0)^0 = A_i(r) \tag{2.80}$$

$$M_{n=1,i} = \int d\lambda I_i(r)(\lambda - \lambda_0)^1 = A_i(r) \times \frac{\vec{v}_i.\vec{l}}{c} \tag{2.81}$$

$$M_{n=2,i} = \int d\lambda I_i(r)(\lambda - \lambda_0)^2 = A_i(r) \times \left(\left(\frac{\vec{v}_i.\vec{l}}{c}\right)^2 + \omega_i^2\right) \tag{2.82}$$

It is an iterative process where each moment is used to compute the next, and thus where errors can propagate. Work has been done in [91] to try and quantify that error propagation. Inverting each moment therefore allows us to find the associated quantities locally. In order to compute radial electron temperature profiles with the XICS instrument, the inversion of the He-like Ar resonance line w, He-like Ar dielectronic satellite line k and the He-like Ar dielectronic satellites $n = 3$ intensities are needed.

Fig. 2.38 shows the successive steps leading to the computation of the radial electron temperature profiles with the line ratio $(n = 3)/w$ (bottom), from the associated LOS-integrated line intensities (top) and the tomographic inversion applied on each (middle), with the two regularity functionals presented previously D1N2 and D2N2. Given that the LOS-integrated intensities decrease toward the center of the plasma, it is logical that the inverted intensities do so as well. Indeed, if the LOS-integrated profiles are hollow, the emissivity must be more hollow to compensate the fact that they are integrated along longer lines of sight. The results of the line intensity inversion is thus consistent in Fig. 2.38. The result on the temperature profiles is an upward revision of the values found by the integrated line ratio, especially at the center of the plasma for $\rho = [0., 0.5]$. It is also noticeable that both regularity functionals implemented and shown in Fig. 2.38 produce similar results.

2.4.4. Discussion of the effect of magnetic equilibrium reconstruction on inverted amplitudes

The data treatment allows to compute, for each quantity (spectral line amplitudes, T_e, T_i and V_p) both a line-of-sight integrated profile (expressed as a function of the impact parameter h of each line of sight), and an inverted profile (expressed as a function of the normalized minor radius ρ_{tor}. Without the magnetic equilibrium, we cannot access to the shape of the plasma and thus to the various magnetic surfaces that compose it. The magnetic equilibrium reconstruction, computed with the code Newton direct and Inverse Computation for Equilibrium (NICE) [92], has a key role in the interpretation of the XICS measurements.

We have seen that the maximum spatial resolution for the XICS diagnostic is of the order of a few millimeters in the plasma center (see Fig. 2.16 where two point-like sources in the plasma center separated by one centimeter project two images that are clearly fully decorrelated on the camera). The same precision is then expected for the magnetic equilibrium reconstruction. However, the error reported for this calculation is higher, of the order of 2-3 cm, making it the largest source of error in the

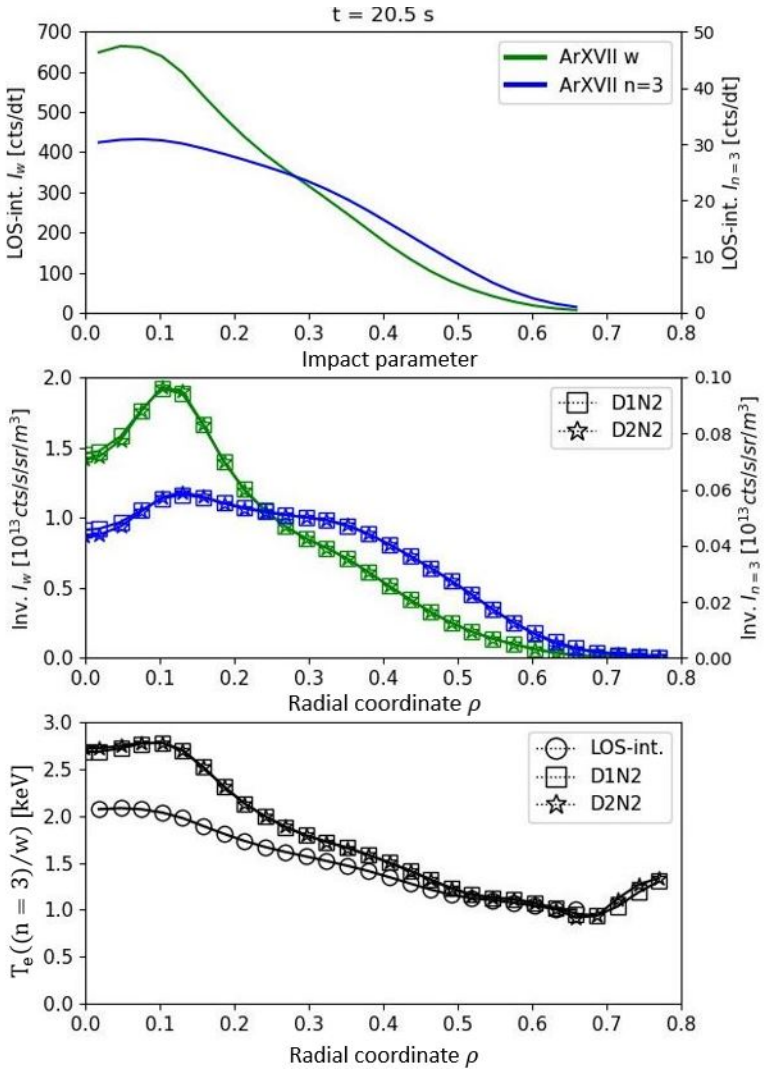

Figure 2.38. – *Top: LOS-integrated and middle: inverted (middle) line intensity of the Ar XVII w and (n=3) lines for the* #57796 *WEST pulse at t = 20.5 s for a time integration of 600 ms; Bottom: radial electron temperature T_e computed with both* $(n = 3)/w$ *and* k/w *line ratios [37].*

inversion routine. It means that an erroneous position of the magnetic axis of a few centimetres necessarily affects the calculation of the impact parameter h. To visualise the effects on the profiles, Fig. 2.39 shows the intensity profiles of the w resonance line for the WEST #59920 plasma discharge for three different times. The LOS-integrated profiles are distinguished with three different colors from corresponding reconstructed retrofitted profiles. The latter are the results of the integration along the lines of sight of the radial emissivities, taking into account the magnetic equilibrium of the plasma. Discrepancies in the impact parameter h were observed on two times marked in red and green lines. The axes of symmetry of the profiles do not coincide, resulting in a non-zero Δh which also differs between the two times. It is zero for t = 4.9 seconds after

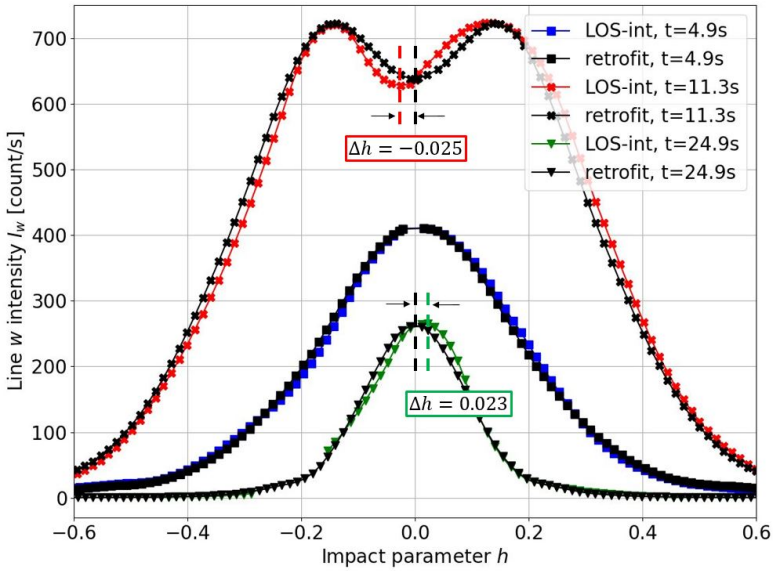

Figure 2.39. – *Line-integrated (coloured) and retrofitted profiles (black) of the He-like resonance line w intensity for three different times of the WEST #59920 plasma discharge.*

the discharge beginning, decreases to $\Delta h = -0.025$ at t = 11.3 seconds and increases to $\Delta h = 0.023$ at the very end of discharge. This discrepancies correspond to an error of 2-3 lines of sight, i.e. an angle of view that differs by only 0.17-0.22 °. This is due to the fact that the plasma does not stay fixed along the discharge, so as for the magnetic axis of the plasma and the reconstruction of its position therefore does not correspond with the axis of symmetry of the lines measured. An additional error is then added to the data processing because of the error in the magnetic balance reconstruction. Note that the uncertainty in the calculation of the magnetic axis affects to varying degrees all WEST diagnostics that use magnetic equilibrium reconstruction in their program, including the ECE radiometer, whose electronic temperature profiles we will use in the next Chapter. For the rest of this study, the impact parameter variable used to plot the integrated profiles will be corrected on a case-by-case basis for the value of Δh.

In addition to the uncertainty on the magnetic equilibrium reconstruction, another source of discrepancy could come from the slow time resolution of the XICS. An varying integration time between 100-500 ms is needed to achieve a good signal-to-noise ratio. If the magnetic equilibrium is undergoing dynamic changes faster than that, a seemingly random discrepancy might appear due to the fact the XICS is not able to capture that dynamic.

2.4.5. Discussion of the modelling of the Ar dielectronic satellite group of lines $n = 3$ and $n = 4$

In the previous Sections, we used the approximation that the dielectronic satellite groups of lines $n \geq 3$, in the wavelength range $\lambda \in [3.949, 3.960]$ Å, can be modelled by single Gaussian functions. This modeling method has already been tested in [93] where the electron temperature estimated with the line ratio between the dielectronic satellite group of lines $n = 3$ and the resonance line w has been validated against measurements with Thomson Scattering and ECE diagnostics. Actually, the use of a Gaussian function to fit the $n = 4$ and $n = 3$ groups is a rather coarse approximation since each group is the sum of several unresolved spectral lines.

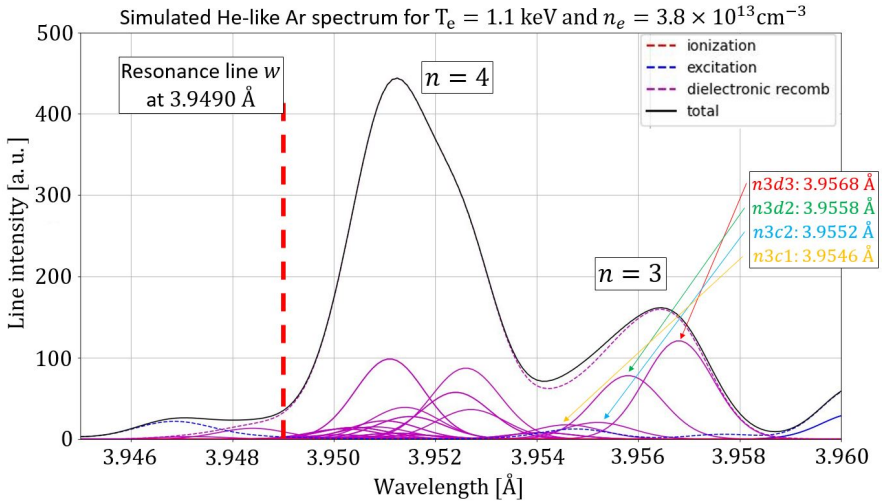

Figure 2.40. – *Simulated Ar spectrum in the spectral range of the $n = 4$ and $n = 3$ dielectronic satellite groups of lines, computed with the Aurora code [35] and the ADAS datasets [47] [48].*

Fig. 2.40 shows a simulated Li-like Ar spectrum in a reduced spectral range $\lambda \in [3.945, 3.960]$ Å where a large number of spectral lines that compose the $n = 4$ and $n = 3$ dielectronic satellite groups of lines are plotted. The PEC data used to model this spectrum are from the ADAS datasets that will be used in Sect. 3.3 to extract the electron temperature from experimental line ratios. Typical WEST values of electron temperature and density are used here, respectively $T_e = 1.1$ keV and $n_e = 3.8 \times 10^{19}$ m^{-3}. The value of n which characterizes each dielectronic satellite group refers to the spectator electron in the dielectronic recombination process, and to its energy level, of the form $1s2p\ nl$. The most intense lines of the $n = 3$ and $n = 4$ satellite line groups can be extracted in an attempt to model these groups more precisely. The very large number of spectral lines that make up these groups produces a non-Gaussian shape. Four of the most intense spectral lines of the $n = 3$ group are identified from [94], marked with different colors and referenced in Table 2.4 with names beginning by $n3$, as well as sixteen lines that belongs to the $n = 4$ group of satellites.

Name	Transition	λ [Å]
n3c1	$1s^2 3s\ ^2S_{1/2}$ - $1s2p3s\ ^2P_{1/2}$	3.9546
n3c2	$1s^2 3s\ ^2S_{1/2}$ - $1s2p3s\ ^2P_{3/2}$	3.9551
n3d2	$1s^2 3p\ ^2P_{1/2}$ - $1s2p3p\ ^2D_{3/2}$	3.9559
n3d3	$1s^2 3p\ ^2P_{3/2}$ - $1s2p3p\ ^2D_{5/2}$	3.9568
n4a1	$1s^2 4d\ ^2D_{5/2}$ - $1s2p4d\ ^2P_{3/2}$	3.9489
n4a2	$1s^2 4d\ ^2D_{3/2}$ - $1s2p4d\ ^2P_{1/2}$	3.9491
n4a3	$1s^2 4p\ ^2P_{1/2}$ - $1s2p4p\ ^2S_{1/2}$	3.9500
n4a4	$1s^2 4p\ ^2P_{3/2}$ - $1s2p4p\ ^2S_{1/2}$	3.9505
n4a5	$1s^2 4d\ ^2D_{3/2}$ - $1s2p4d\ ^2F_{5/2}$	3.9508
n4a6	$1s^2 4d\ ^2D_{5/2}$ - $1s2p4d\ ^2F_{5/2}$	3.9509
n4a7	$1s^2 4d\ ^2D_{3/2}$ - $1s2p4d\ ^2D_{5/2}$	3.9513
n4a8	$1s^2 4d\ ^2D_{3/2}$ - $1s2p4d\ ^2D_{3/2}$	3.9514
n4a9	$1s^2 4d\ ^2D_{5/2}$ - $1s2p4d\ ^2D_{5/2}$	3.9515
n4b1	$1s^2 4d\ ^2D_{5/2}$ - $1s2p4d\ ^2F_{7/2}$	3.9516
n4b2	$1s^2 4s\ ^2S_{1/2}$ - $1s2p4s\ ^2P_{3/2}$	3.9518
n4b3	$1s^2 4s\ ^2S_{1/2}$ - $1s2p4s\ ^2P_{1/2}$	3.9518
n4b4	$1s^2 4p\ ^2P_{3/2}$ - $1s2p4p\ ^2P_{3/2}$	3.9523
n4b5	$1s^2 4p\ ^2P_{1/2}$ - $1s2p4p\ ^2P_{1/2}$	3.9525
n4b6	$1s^2 4p\ ^2P_{1/2}$ - $1s2p4p\ ^2D_{3/2}$	3.9528
n4b7	$1s^2 4p\ ^2P_{3/2}$ - $1s2p4p\ ^2D_{5/2}$	3.9532

Table 2.4. – *Theoretical transitions and wavelengths from [94] of the Ar $n = 3$ and $n = 4$ spectral lines added to the modelling algorithm.*

The relative intensity of these groups is by definition much weaker than the resonance line, which reduces the contribution of each component in the overall intensity measured. As the spectral resolution of the instrument does not allow us to clearly resolve the lines in each group, the Gaussian approximation is a sensible choice, even if we will see later that it does not perfectly model the experimental points. In order to constrain the modelling of the lines in the $n = 3$ group, and since we have PEC files of the Ar lines we are studying here, we can study the temperature variations in the intensity of the lines in the $n = 3$ group. The aim is to extract PEC ratios constants over a wide range of temperatures to incorporate into our multi-Gaussian model and constrain all the line intensities relative to each other.

Fig. 2.41 (left) shows the PECs of the five most intense lines in the $n = 3$ group as a function of the electron temperature. The $n3d1$ line at 3.9556 Å appears much weaker than the other four, which justifies that it is neglected in the data treatment. All the PECs seem to have the same temperature variation, which can be checked in right Fig. 2.41. In a large range of T_e, the PEC ratios do not vary between 500 and 4000 eV, which allows to use constant values of PEC ratios in the data treatment algorithm. We can then directly compare the two models, the original single-Gaussian and the new multi-Gaussian. Fig. 2.42 displays the experimental points of the $n = 3$ and

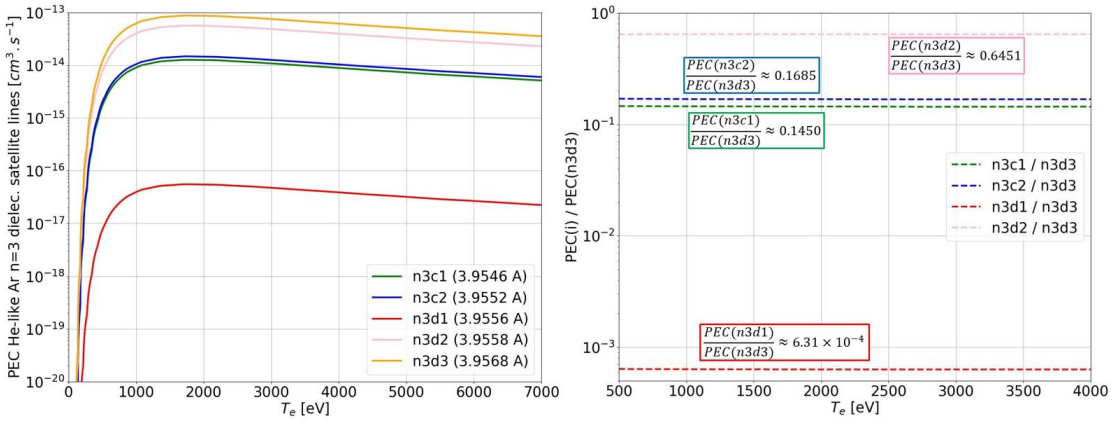

Figure 2.41. – *Left: PECs of the spectral lines that belong to the $n = 3$ group of dielectronic satellite lines; Right: PEC ratios without variation over a large electron temperature range.*

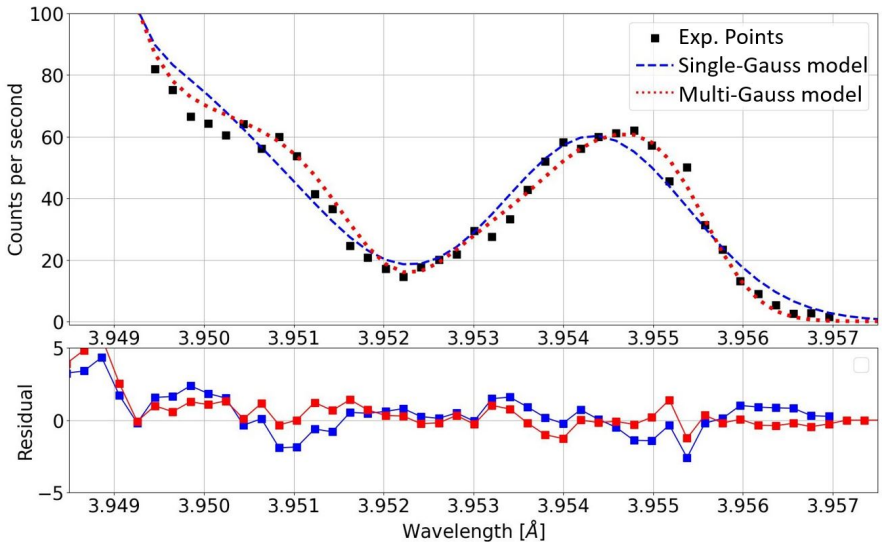

Figure 2.42. – *Comparison of the two models used to fit the $n = 3$ and $n = 4$ groups of dielectronic satellite lines: single-Gaussian (blue) and multi-Gaussian (red) models.*

$n = 4$ groups of dielectronic satellites for the WEST #59975 discharge and the two models tested to fit them, in blue the single-Gaussian approximation and in red the multi-Gaussian model. It can be seen that taking into account some of the different lines in each group improves the accuracy of the fitting routine. On the other hand, we can see that this improved model does not bring any significant change in the total modeled intensity of the $n = 3$ group, since it is the maximum intensity of the line group that interests us. Variations of a few counts per second are noticed, which do not infer great differences of the maximum intensity of the $n = 3$ group of lines. Therefore, the original single-Gaussian model can still be used to model this group

without major inaccuracies.

2.5. Conclusions

This Chapter was dedicated to the presentation of the XICS diagnostic, how to measure the Ar XVII spectrum and to model it. To do so, a full description of the instrument has been done, detailing all the components. A study of the diagnostic configuration has allowed to determine the spatial and spectral resolutions, of respectively few millimeters in the plasma and $\Delta\lambda/\lambda \approx 10^{-4}$. However, a few limitations has been exposed, relative to the position of the detector. Its positioning is a compromise between the three different crystals, each of which has different sagittal foci.

On the other hand, it has the advantage of keeping the detector in a constant position over the experimental campaigns, without the need to change it by changing the crystal facing the plasma. It is also an important advantage since no spectral calibration has been performed so the part of the instrument function that is unknown is constant also. In addition, we expressed the lack of brightness calibration performed during the XICS installation. However, we summarized a few techniques that can be done to remediate this issue and introduced a brightness calibration transfer with another spectrometer, which will be the subject of Sect. 3.4.

The last part of the chapter, relative to the description of the spectral modelling, exposed the data treatment as it is used to interpret the measurements. The data treatment is based on two-dimensional images modelling. The primary task is to deconvolve the measurements from geometric effects of the Johann configuration. As a consequence, the measured spectral lines are straightened. Then we ensure the signal-to-noise ratio is sufficient to extract reliable results. The various constraints applied to the data treatment aim to improve its accuracy and minimize the computation time based on experimental and theoretical knowledge of the spectra.

A first limitation to the process described is the need to predict in advance the maximum number of lines expected. However, unexpected events can distort the modeled spectra and make them stand out afterwards. Another sensitive point is the modeling of the Bremsstrahlung background, which is of low intensity in the Ar XVII spectrum in general, but which can cause modeling errors in low-intensity Ar lines such as the Li-like dielectronic satellites $n > 3$. Pre-treatment of the single background level enables it to be better constrained, and the following data treatment of argon and tungsten lines to be significantly improved. Finally, the tomographic method has been described, which is used to extract local emissivities and experimental temperature values.

3. Ar XVII spectrum analysis

Sommaire

3.1. Introduction . . . 140
3.2. Crystallographic study of Bragg crystals . . . 140
3.2.1. Line-doubling phenomenon during the first campaign . . . 141
3.2.1.1. Causes of angular offsets . . . 142
3.2.1.2. Crystal asymmetry . . . 143
3.2.1.3. Thermal expansion . . . 146
3.2.2. Modelling of the spectral shift parameter . . . 148
3.2.2.1. Extraction of experimental spectral shift and count ratio data . . . 148
3.2.2.2. Prediction model of the spectral shift variation . . . 151
3.2.3. Discussion on the count ratio parameter . . . 154
3.2.4. Discussion on a possible effect of heating system on the count ratio parameter . . . 155
3.3. Extraction of physical quantities from the Ar XVII spectrum . . . 156
3.3.1. Toroidal rotation velocity . . . 157
3.3.2. Ion temperature . . . 159
3.3.3. Electron temperature . . . 162
3.3.4. W impurity measurement . . . 169
3.3.5. Discussion on the role of the photon emission coefficients data 174
3.4. Experimental impurity density profiles . . . 177
3.4.1. Brightness calibration of the XICS spectrometer . . . 177
3.4.1.1. WEST Extreme-UV spectrometer . . . 177
3.4.1.2. Identification of the W spectral lines . . . 178
3.4.1.3. Brightness equivalence between two lines from the same ion species . . . 179
3.4.1.4. Line of sight selection criteria . . . 182
3.4.1.5. Cross-calibration from the SIR to the XICS diagnostic . 187
3.4.2. Mid- and high-Z impurity profiles . . . 188
3.4.2.1. Line-averaged density and concentration computation 188
3.4.2.2. Tungsten and argon density and concentration . . . 192
3.4.3. Discussion on an alternative brightness calibration . . . 194
3.5. Conclusions . . . 196

3.1. Introduction

This Chapter is dedicated to the results extracted from the Ar XVII spectrum. Fig. 3.1 shows a typical spectrum measured from the first experimental campaign of the instrument. This spectrum is similar to other Ar XVII spectra studied in the past by

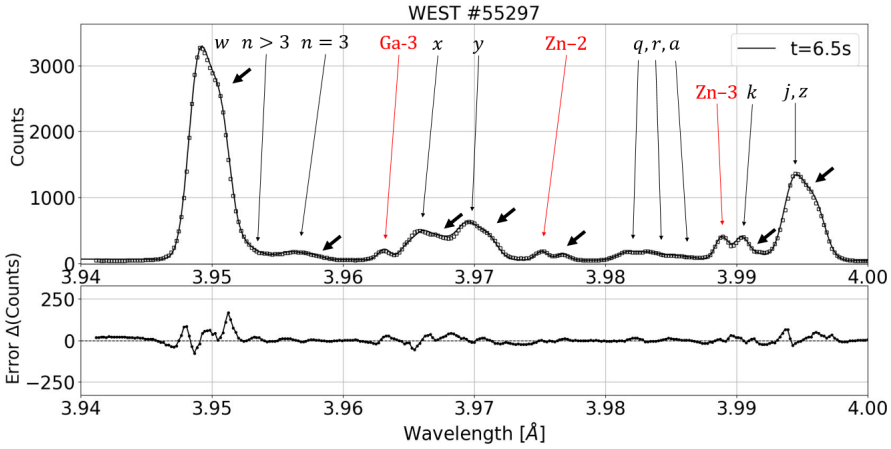

Figure 3.1. – *1D spectrum of the Ar XVII crystal and WEST #55297 pulse affected by line-doubling. The spectrum is extracted at t = 6.5 s, for a time integration of 600 ms. Measured values (black squares) and fitting results (black line) are shown superimposed. The fitting error is also shown below the 1D spectrum.*

[76] in Tokamak of Fontenay-aux-Roses (TFR), [52] in Tokamak Fusion Test Reactor (TFTR), [95] in TS, [91] in Alcator C-MOD or [96] in KSTAR except for two differences. First, a shoulder is measured on the most intense lines in the spectrum, marked with the black arrows, similar to a line doubling. The study of line doubling will be done in Chap. 3.2. To explain this phenomenon, we will focus our study on the crystals properties and more specifically using the Rocking-Curve demonstrated in Sect. 2.2. Then, from the data treatment, we will see in Sect. 3.3 the physical quantities that we can extract from this spectrum. Second, additional spectral lines are measured, around the He-like Ar x and y inter-combination lines and close to the Li-like dielectronic satellite k line, marked with black arrows. It has been shown by [74] that W emission lines contaminate the argon spectrum. Their measurement affects one of the two argon line ratios available to compute electron temperature profiles, in Sect. 3.3, but at the same time allows to cross-calibrate the XICS instrument in brightness with the measurements from another spectrometer and to recover tungsten and argon density profiles, in Sect. 3.4.

3.2. Crystallographic study of Bragg crystals

The first issue that has been reported in the spectrum Fig. 3.1 is the line-doubling measured on all the spectral lines observed during the first campaign. The aim of this

Section is to investigate the cause(s) of this phenomenon and to propose a method to remove this issue. As we will see in Sect. 3.3, we need to extract the line amplitudes, width and positions on the detector to compute the electron and ion temperature as well as the toroidal rotation velocity.

For this purpose, dealing with doubled lines is very complicated, as we do not yet know at this point what causes them, and extracting information from the line shape is risky. Multiple causes can affect the measured spectrum. Focusing on the crystal, we investigate the most probable ones and conclude that the spectrum doubling is mostly due to the two crystal halves having slightly different miscuts.

In Sect. 3.2.1, the analysis of the possible causes for this line-doubling deformation on the Ar XVII spectrum is done. Then, the line position on the detector computation done in Sect. 2.2.2.2 will be used to model the spectral components of the line-doubling. With experimental values of the two components of the line-doubling, extracted from several WEST pulses, we will study their wavelength dependence and try to model the spectral shift.

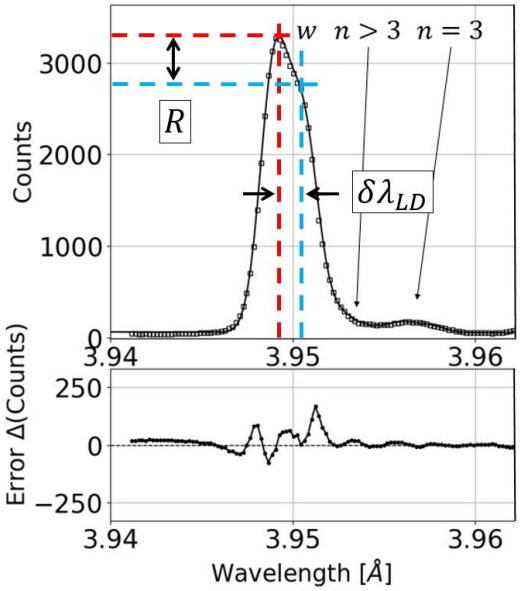

Figure 3.2. – *Line-doubling phenomenon affecting the Ar XVII spectral lines, defined with a count ratio R and a spectral shift $\delta\lambda_{LD}$.*

3.2.1. Line-doubling phenomenon during the first campaign

During the first experimental campaign in WEST, and in addition to the expected spectral lines of argon and tungsten, a line-doubling phenomenon was observed for all the plasma discharges with the original experimental set-up described in Sect. 2.2.1, i.e. both Ar XVII half-crystals mounted on the rotating table. It can be described with two parameters, a count ratio R and a spectral shift $\delta\lambda_{LD}$ between the doubled lines, as shown in Fig. 3.2.

In this part, we explore the different causes that may induce a deformation of the Rocking-Curve. Two main causes have been identified: non-parallelism between the optical surface and the crystal lattice due to the manufacturing process and internal deformations of the mesh due to thermal variations to which the crystals are exposed. Finally, we will integrate these two parameters into the Rocking-Curve calculations to determine their importance in the line-doubling of the spectrum Fig. 3.1.

3.2.1.1. Causes of angular offsets

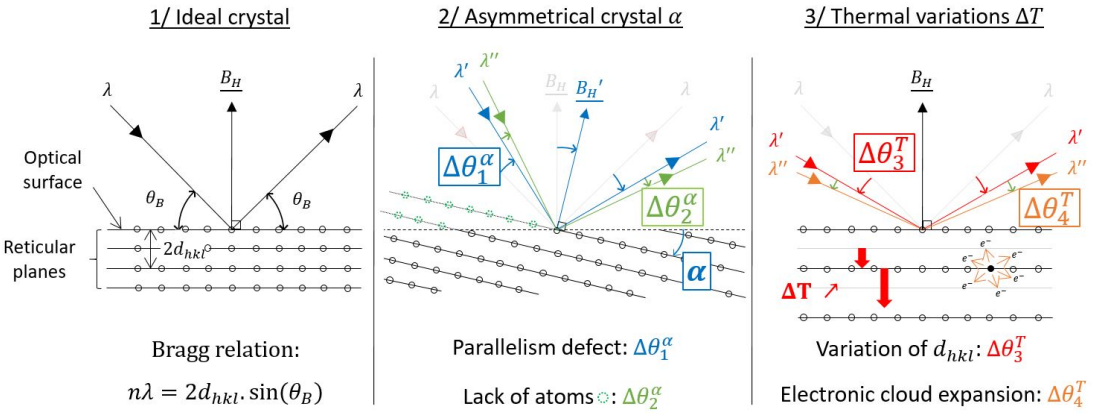

Figure 3.3. – *1/ Sketch of the Bragg diffraction with a perfect crystal of inter-reticular spacing d_{khl}. Two causes of angular offsets on the direction of diffraction are shown: 2/ non-parallelism between the optical surface and the layers characterized by a miscut angle α ($\Delta\theta_1^\alpha$ in blue) and the missing atoms of atomic layers (green dashed circles) also contribute to the total angular offset ($\Delta\theta_2^\alpha$ in green); 3/ thermal deformation of the inter-reticular spacing d_{khl} ($\Delta\theta_3^T$ in red) and a deformation of the total electronic cloud ($\Delta\theta_4^T$ in orange).*

The search for causes of angular offsets begins with a geometry analysis of the spectrometer Johann configuration. A Rowland sphere is computed to position and align all the different components of the instrument and for this computation we use the approximation that the two half-crystals mounted on the substrate form a single, whole crystal. This approximation is actually wrong because, as we will see in Sect. 2.2.2.2, each half-crystal leads to the creation of distinct Rowland spheres.

The main hypothesis to be checked is that both halves have the same default of parallelism between the optical surface and the crystal layers, characterized by the manufacturer and detailed in Table 2.1. We saw in Sect. 2.2.1 that the Miller indices of the crystal mesh determine the inter-reticular spacing d_{hkl} and therefore in the angle of diffraction of the incident X-ray beam. We can find also in the literature that thermal variations can affect the crystal mesh itself, as demonstrated in [97].

These hypothesis have to be studied because, in the end, these probable causes of crystal deformation can affect the real Rocking-Curve, induce a shifting of the spectral

lines of interest and therefore distort the physical quantities extracted. The count ratio R between the doubled lines makes the electron temperature computations very difficult. In addition, the spectral shift $\delta\lambda_{LD}$ parameter is added to a Doppler shift and estimations of the plasma toroidal rotation velocity may be biased.

Some studies in the literature treat both experimentally and numerically the Rocking-Curve experiments. [98] have numerically examined the dependence of the reflection curves of bent crystals with the crystal thickness and the bending radius, using a dynamical theory for a 1D deformation gradient. Their results showed that the bending radius of the crystal, as well as the bending shape, have a strong effect on the integrated reflectivity at a specific wavelength, confirmed by experimental data. In [64], the authors have coupled a ray-tracing algorithm, used to simulate the X-ray intensity profiles to be observed for a spherical Johann-type spectrometer, to the X-ray Oriented Programs (XOP) code [99] which computes the Rocking-Curve for various kinds of crystals. Nevertheless, scarce is the literature treating the effects of the miscuts on the diffraction profiles and the temperature changes affecting the crystal lattice itself.

Based on [58] and [57], a study is made here of the Rocking-Curve dependence on the spectrometer parameters. Fig. 3.3 summarises the main causes studied here, in comparison with the ideal Bragg diffraction with crystal defects. An asymmetrical crystal has a miscut angle α between the optical surface and the reticular planes. This defect tilts the whole mesh and the direction of the reciprocal lattice vector $\vec{B_H}$. This leads to the creation of a first component of the total angular offset $\Delta\theta_1^\alpha$. In addition, the missing atoms (green dashed circles) of the atomic layers create another angular component $\Delta\theta_2^\alpha$. Two other components originating from ambient temperature variations affecting the diffraction are added: the modification of the inter-reticular spacing d_{hkl} by thermal expansion ($\Delta\theta_3^T$) and the expansion of the electron clouds of the atoms involved in the Bragg diffraction phenomenon ($\Delta\theta_4^T$).

3.2.1.2. Crystal asymmetry

The presence of a miscut angle within the crystal lattice ($\Delta\theta_1^\alpha$) is one of the defects in crystals that has been shown experimentally to play an important part in the line-doubling. All the Ar spectral lines, as well as the W lines, are doubled with a count ratio R of the two components different from 1. This line-doubling phenomenon causes some troubles for the spectral line ratio computations and Doppler effect, shift and broadening, determination.

From simple geometrical considerations, it can be shown that the miscut angle modifies the position of the meridional focus, changing the value of the Bragg angle of reference of the crystal. Therefore, it affects the ideal position of the detector, characterized by the crystal-to-detector distance $l_m(\alpha) = r_c.sin(\theta_B + \alpha)$, with positive values of α representing a larger crystal-to-detector distance. Each half-crystal possess its own miscut angle and to model, see the parallelism row in Table 2.1, so we consider twice the value indicated for the entire crystal. This miscut angle issue induces a new crystal-to-detector distance $l_m(\alpha) = 2.2139$ m, i.e. a difference of 1.418 mm. This means that the spectral line is shifted by eight pixels on the detector, or $\Delta\lambda \simeq 1.5$ mÅ,

which is consistent with the experimental observations.

A more detailed study of this effect shows another physical phenomenon which may affect the direction of diffraction in the same way as the parallelism defect: a lack of atoms in the missing parts of the reticular planes ($\Delta\theta_2^{\alpha}$). We want to estimate here if this consequence of the miscut angle contributes also to the spectral shift on the spectra. Since it is quite difficult to estimate the total number of missing atoms without a precise surface characterization, we can still try to estimate the total number of SiO_2 molecules missing, if we consider a maximum miscut angle of $1.5'$ across the width of the crystal. From [54], we know that the elementary mesh of Quartz crystals contains one molecule of SiO_2 per approximately 113×10^{-30} m^{-3}. The volume of each Ar XVII half-crystal being $V_{cr} = 8\times10^{-7}$ m^3, the total number of molecules contained amounts to approximately 7.1×10^{21}. The volume loss, due to a maximum miscut angle of 1.5' across the width of the crystal, is estimated to 3.5×10^{-8} m^3, which only represents 1/23 of the total volume V_{cr}. This loss reveals a decrease of about 4% in the number of SiO_2 molecules. Given the small amount of atoms removed, the magnitude of this offset source is considered negligible compared to the angular deviation caused by the parallelism defect studied previously.

Taking into account only the miscut angle α, we can explore how this parameter affects the Rocking-Curve as it is computed in Sect. 2.2.1.3. The incident and diffracted angles θ_i and θ_d are modified as $\theta_i = \theta_B+\alpha$ and $\theta_d = \theta_B-\alpha$. The asymmetry parameter b defined in Eq. 2.3 thus needs to be rewritten as:

$$b = \frac{sin(\theta_i)}{sin(\theta_d)} \tag{3.1}$$

As a result, the angular width of the Rocking-Curve, the integrated reflectivity, as well as the asymmetry parameter, become dependent on the miscut angle as shown in Fig. 3.4. For very large positive values of α, the asymmetry parameter diverges quickly to $+\infty$ and as $R_H \propto |b|^{-1/2}$ (see Eq. 2.13), the integrated reflectivity decreases at the same time. The angular width of the curve follows the same behaviour as the integrated reflectivity. For miscut values of $\alpha = \pm1.5' = \pm0.025°$, very low variations of less than 2% are expected for the curve parameters. Fig. 3.5 displays the effect of a miscut angle $\alpha = \pm5° = \pm300$ arcmin on the Rocking-Curve of the Ar XVII w line. We can see that even for angles a hundred times larger than the maximum expected value given by the manufacturer, a very small difference is noticed, of the order of 2×10^{-15} m between the curve with non-zero α and the original one. With this spectral shift value, we reach the limits of the spectral resolution of the spectrometer. So it can be concluded that the expected low miscut angle of our crystals does not significantly modify either the shape or the location of the Rocking-Curve on the diffraction angle scale. Further investigation of potential sources of angular displacement must then be carried out in order to also take into account the geometry of the spectrometer and the crystals. Finally, a natural spectral shift is expected from the theoretical Bragg angle due to the intrinsic diffraction properties of Bragg crystals. We found a shift of ≈ 23.9" for the Ar XVII w line and ≈ 24.5" for the Ar XVII z line, which makes a difference of

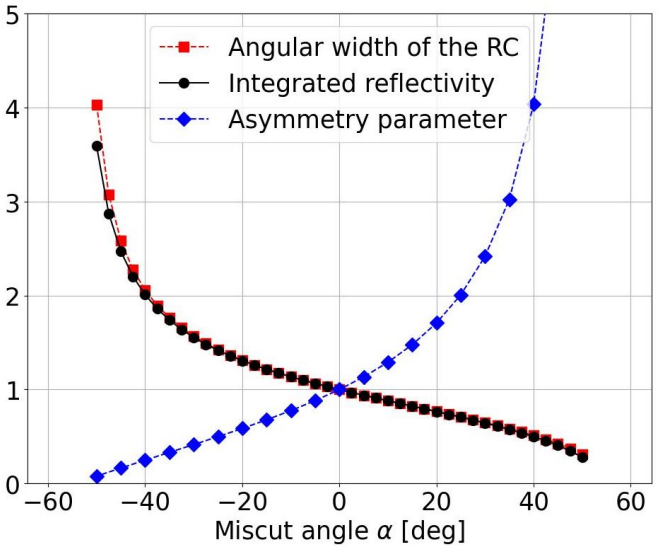

Figure 3.4. – *Rocking-Curve (RC) parameters curves as a function of the miscut angle α: angular width of the RC (red squares), integrated reflectivity (black dots) and asymmetry parameter b (blue diamonds). The curves are normalized to their value at α = 0.*

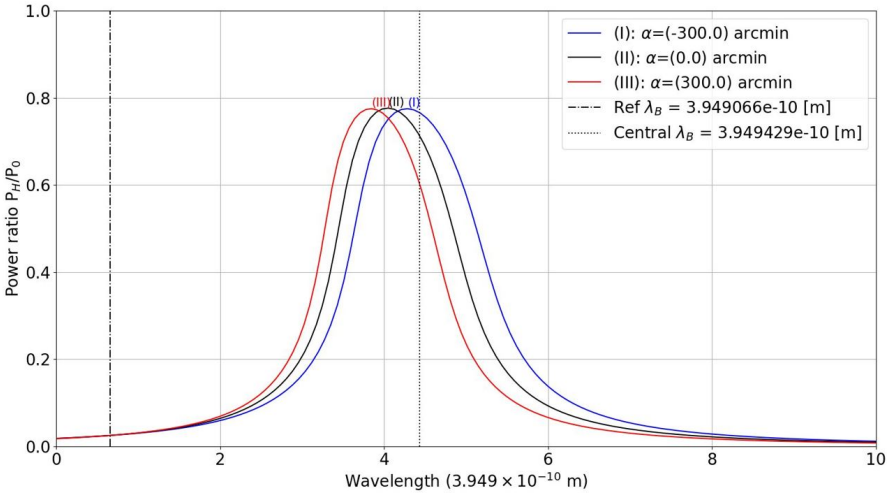

Figure 3.5. – *The original Rocking-Curve of the He-like Ar resonance line wavelength in Fig. 2.5 affected by a miscut angle of α ± 300 arcmin. The miscut value used is 200 times greater than the value specified in Tab. 2.1.*

only 2.5% over the whole spectral range. We will study now how the crystal mesh is deformed by the thermal variations to which it can be exposed and if it contributes to the spectral shift.

3.2.1.3. Thermal expansion

On Alcator C-Mod tokamak [100], [97] have estimated the effect of the temperature on the spectral diffraction of a crystal used on their X-ray spectrometer. It affects the crystal lattice and causes a spectral shift, as shown in Fig. 3.3 ($\Delta\theta_3^T$). They found that a temperature difference of about 12 °C has caused a spectral shift of the order of a pixel on all the observed spectral lines on their detector, similar to the one installed in the WEST XICS. The crystal-to-detector distance is also affected by temperature changes. The computations take their origin from the Bragg relation Eq. 2.1. The wavelength derivation can be performed keeping either the inter-reticular spacing constant or keeping the wavelength constant in the spectral resolution :

$$\frac{\Delta\lambda}{\lambda} = \frac{\Delta\theta_B}{tan(\theta_B)} = -\frac{\Delta d}{d}. \tag{3.2}$$

This linear expansion can also be described at first approximation by the product of a temperature change ΔT and a coefficient of linear thermal expansion noted γ_{eff} which will induce an additional spectral shift:

$$\gamma_{eff} = \frac{1}{d_{hkl}}\frac{\Delta d_{hkl}}{\Delta T} \qquad [^\circ C^{-1}]. \tag{3.3}$$

The computation of the lattice spacing is usually done as follows, for a hexagonal mesh:

$$\frac{1}{d_{hkl}^2} = \frac{4(h^2+k^2+hk)}{3a_0^2} + \frac{l^2}{c_0^2} \qquad [m^{-2}]. \tag{3.4}$$

where (h,k,l) are the Miller indices, $a_0 = 4.913$ Å and $c_0 = 5.404$ Å the lattice constants at 25 °C from [54]. The new lattice constants affected by a temperature change are then computed with Eq. 3.3 with the linear thermal expansion coefficients $a_{para} = 7.97 \times 10^{-6}$ °C^{-1} and $a_{perp} = 13.37 \times 10^{-6}$ °C^{-1}, also from [54]. From Eq. 3.3, we can derive the relation between the inter-reticular spacing and the thermal variations, with a linear thermal expansion coefficient $\gamma_{eff} = 1.337 \times 10^{-5}$ °C^{-1}:

$$d_{hkl} = d_{hkl}^0.(1+\gamma_{eff}.\Delta T) \qquad [m] \tag{3.5}$$

Fig. 3.6 displays the variation of the inter-reticular spacing with respect to the thermal variations. A variation $\Delta T = 10$ °C of the crystal temperature can change the inter-reticular spacing of about 0.328×10^{-3} Å, which is equivalent to a change in the diffraction direction of about 0.182×10^{-3} rad. The effects of temperature differences of ±10 °C on the Rocking-Curve of the Ar XVII w line are shown in Fig. 3.7. Two additional Rocking-Curves are plotted for thermal deformation of $\pm 10°C$. From the original curve, spectral shifts of $\pm 5 \times 10^{-4}$ Å are noticed. In our case, this error is of the same order of magnitude than the spectral resolution of the spectrometer but four times smaller than the closest lines measured ($\Delta\lambda(q,r) = 2.1 \times 10^{-3}$ Å).

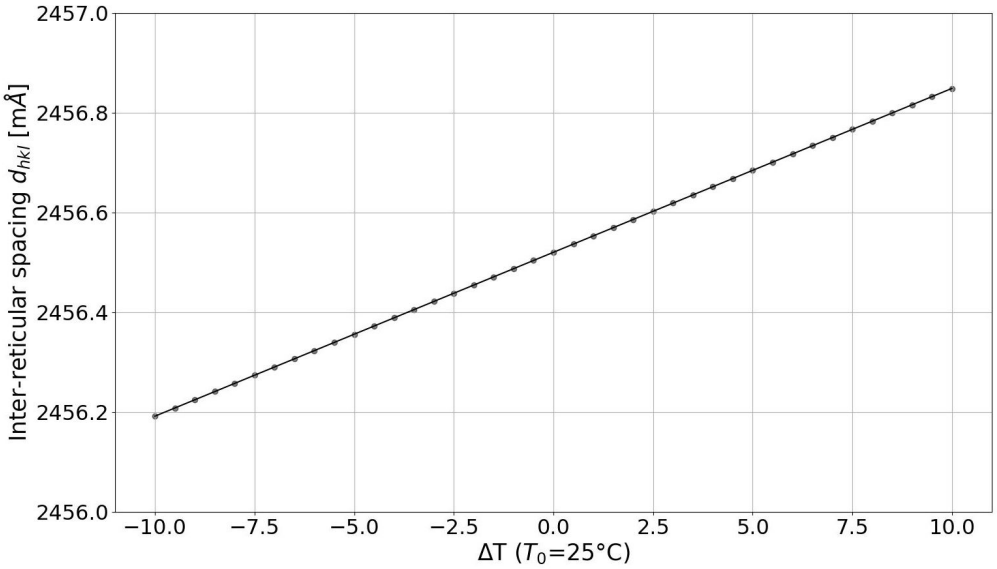

Figure 3.6. – *The inter-reticular spacing d_{hkl} versus the thermal variations affecting the crystal mesh.*

Fortunately, the temperature variations of the crystals on WEST are expected to be small thanks to an active water-cooling system placed under the crystal box. But despite this counter-measure, the temperature diffusion through the crystal successive supports may not be optimal. In addition, the sources of temperature variation include not only the ambient weather (and winter-summer cycles) but also the exposure to the plasma radiation, which on WEST can last several minutes. Hence, a valuable and relatively cheap safety measure would simply be to implement thermocouples as close as possible to the crystals to monitor their temperatures throughout operational time.

Thermal variations can also induce an expansion of the electronic clouds of atoms contained on the reticular planes. It can be produced by the direct thermal agitation of the atoms around their resting positions on the reticular plane, described by the Debye model [101]. Above the absolute zero, the atoms composing the solid vibrate more and more up to the Debye temperature at which all the vibration modes are excited. The combined motion of all the atoms of an elementary volume within the crystal is equivalent to an expansion of the associated electronic cloud. In the case of X-ray diffraction by crystals, it is convenient to use the Debye-Waller factor to describe the X-ray scattering attenuation, i.e. to study the behaviour of the atomic scattering factor when the medium is subject to ambient temperature variations. [102] have computed the order of magnitude of the Debye-Waller factor, $B \simeq 1 \times 10^{-47}$ for Quartz crystals, which leads to a negligible correction of the atomic scattering factor. For such values, the correction due to the thermal expansion of electronic clouds can be ignored and the component $\Delta\theta_4^T$ neglected.

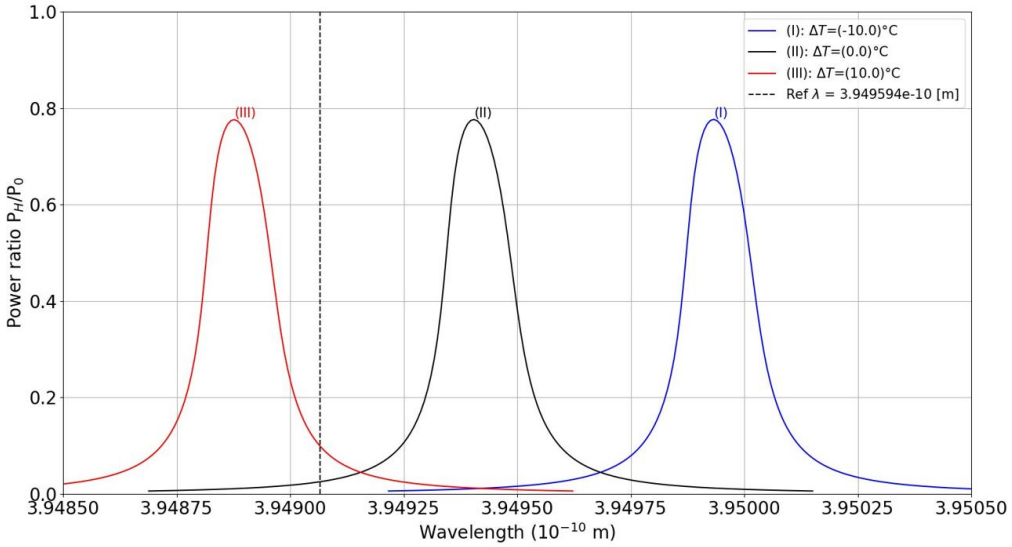

Figure 3.7. – *Diffraction pattern of the He-like Ar resonance line wavelength (Fig. 2.5), affected by a thermal variation of* $\pm 10\,^{\circ}C$.

3.2.2. Modelling of the spectral shift parameter

We saw that only two angular components must be kept for their theoretical effects on the Rocking-Curves. The miscut angle α induces an angular offset $\Delta\theta_1^{\alpha}$ that can change the shape and the integrated reflectivity of the crystal, but for very high values of α. It corresponds here to a simple geometrical angular shift of the Bragg angle of reference. However, the missing atoms of the atomic layers do not seem to have a great importance, even if it is difficult to estimate without a full surface and volume characterization. Also, some thermal variations that affect the crystal can change the inter-reticular spacing and thus the angle of diffraction of a specific wavelength. These verifications have been done through their effect on the Rocking-Curves.

At this point, we have estimated that the $\Delta\theta_1^{\alpha}$ component is the main cause of the observed spectral shift. We also know that a differential heating of the two crystal halves could make this spectral shift not constant in time. In the following section we investigate empirically and in more details how the spectral shift varies along the spectral range. Additionally to a spectral shift a count ratio different from unity is also observed and characterized.

3.2.2.1. Extraction of experimental spectral shift and count ratio data

Here, we use the geometrical relation that rules the position of the diffracted X-ray beam on the detector, according to the XICS geometry, and determined in Sect. 2.2.2.2 We do not take into account in the calculations the spectral shift inferred by the crystal as we saw in Sect. 2.2.1. The aim is to study how the miscut angle and the thermal variations could affect the direction of diffraction and if it can be modelled with accuracy. In Eq. 2.50 and Eq. 2.51, the deviation angle α becomes the miscut angle

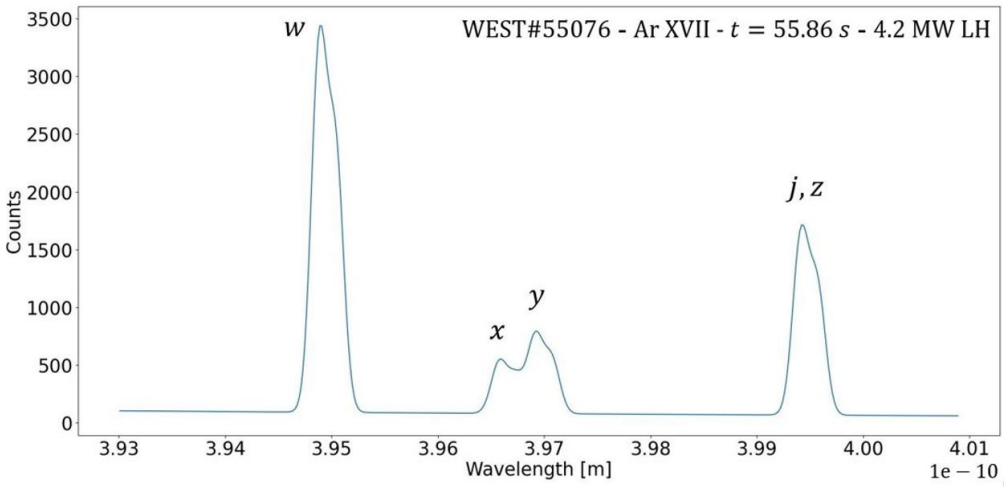

Figure 3.8. – *Example of a spectrum measured with the XICS during the WEST* #55076 *shot where three spectral areas are selected to study the line-doubling effect experimentally:* [3.945, 3.955] Å *for the resonance line* w, [3.965, 3.975] Å *for the intercombination lines* x *and* y *and* [3.992, 3.998] Å *for the forbidden line* z *and satellite line* j.

and the inter-reticular spacing change is taken into account in the Bragg angle of reference θ_{B0}. We will select a few plasma discharges from the WEST experimental campaigns when both half-crystals were facing the plasma and extract the data for the spectral shift and the count ratio parameters, the two parameters which describe the line-doubling phenomenon. Finally, we will try to deduce the set of miscut-thermal parameters which describe best the crystals used and the doubled spectrum in Fig. 3.1.

The spectral shift $\delta\lambda_{LD}$ represents the spacing between the two components of a given spectral line diffracted by each half-crystal with different lattice properties, especially miscuts. In this Section, we use the data from twenty-one WEST pulses, measured when both halves were facing the plasma. The main plasma parameters of the pulses examined here are detailed in Table 3.1. There is no particular reason, *a priori*, to think that the spacing is independent of the wavelength.

In order to quantify the variation of $\delta\lambda_{LD}$ over the entire spectral range allowed by the ArXVII crystal ([3.93, 4.01] Å), we choose to model independently three spectral areas corresponding to five Ar spectral lines. We selected the He-like resonance line w at [3.945, 3.955] Å, the doublet of He-like intercombination lines (x, y) at [3.965, 3.975] Å and the Li-like dielectronic satellite and He-like forbidden lines (j, z) at [3.992, 3.998] Å, as shown in Fig. 3.8. Our only motivation was to take into account the lines with a high count amplitude compared to the Bremsstrahlung background and a sufficient distance from other lines. The count ratio parameter is constrained between $0.5 < R < 0.9$ and the spectral spacing between $3 \times 10^{-4} \times \lambda < \delta\lambda_{LD} < 5 \times 10^{-4} \times \lambda$ from the doubled spectra. Each spectral area of interest is thus modelled with a multi Gaussian function taking into account the line-doubling parameters $\delta\lambda_{LD}$ and R

#	Δt [s]	t_{tot} [s]	I_p [MA]	B_T [T]	P_{LH} [MW]	P_{IC} [MW]	n_l [10^{20} m^{-2}]
54762	0.501	10.5	0.5	3.7	4.3	/	0.31
54765	0.501	11.5	0.5	3.7	3.4	/	0.32
54766	0.501	8.0	0.5	3.7	4.0	/	0.30
55045	0.501	6.0	0.5	3.6	4.2	/	0.35
55049	0.501	12.0	0.5	3.6	4.1	/	0.40
55076	0.501	24.0	0.5	3.6	4.2	/	0.40
55077	0.501	21.5	0.5	3.6	4.2	/	0.40
55080	0.501	16.5	0.5	3.6	3.1	/	0.39
55092	0.501	25.0	0.5	3.6	4.1	/	0.39
55095	0.501	15.0	0.5	3.6	4.5	/	0.39
55147	0.201	13.0	0.5	3.7	/	1.8	0.41
55160	0.201	12.0	0.5	3.7	/	1.9	0.40
55161	0.201	10.0	0.5	3.7	/	1.9	0.39
55164	0.201	12.0	0.5	3.7	/	1.8	0.50
55165	0.201	12.0	0.5	3.7	/	1.8	0.46
55166	0.201	10.0	0.7	3.7	/	1.8	0.58
55167	0.201	10.0	0.7	3.7	/	2.0	0.50
55292	0.201	14.0	0.5	3.6	1.8	/	0.35
55297	0.201	12.5	0.5	3.6	3.7	/	0.87

Table 3.1. – *List of studied shots measured with the ArXVII crystal set of the XICS spectrometer with the main plasma parameters associated: plasma discharge number, time acquisition, duration, plasma current, toroidal magnetic field, LHCD and ICRH power and line-averaged electron density.*

which affect respectively the Doppler shift and the intensity of the line measured:

$$F_i(\lambda, R, \delta\lambda_{LD}) = B(\lambda) + \sum_j A_j(\lambda) \times exp\left(-\frac{\left(\lambda_i - \lambda_{0,j}\right)^2}{2\omega_j^2}\right) + \sum_j A_j(\lambda) \times R_j \times exp\left(-\frac{\left(\lambda_i - \lambda_{0,j} + \delta\lambda_{LD,j}\right)^2}{2\omega_j^2}\right) \quad (3.6)$$

The fitting procedure follows the same trend as described in Sect. 2.4.2.3 by first determining all the components of the spectrum with the initial guesses, in particular the theoretical wavelengths. It then associates each pair of lines using the spectral shift parameter boundaries expressed just above and determines the count ratio between the two. In contrast to the normal multi-Gaussian fit, the two line-doubling variables are added to the others for each line of sight j:

$$N_{var} = b + \alpha + j \times (A_j, \lambda_{0,j}, \omega_j, R_j, \delta\lambda_{LD,j}) \quad (3.7)$$

As a result of the modelling process, a single value for each parameter is obtained

for each spectrum available. The experimental results are shown in Fig. 3.9. 2767 points are processed, more than 900 in each spectral area. Top and bottom plots of Fig. 3.9 respectively show the distribution of the spectral shift $\delta\lambda_{LD}$ and the count ratio R computed for each spectral range. The points are represented as a violin plot to show the distribution of the sample. 68% (green bar), 95% (red bar) and 99% (black bar) of the points of each distribution are shown. The number of points in each group is displayed with the distribution mean.

It can be seen that both doubling parameters depend on the wavelength. They are non-linearly decreasing functions of the wavelength. Every distributions studied in R and $\delta\lambda_{LD}$ are more or less spread out around the mean spectral area value. About the spectral shift, the distributions are almost symmetrical around a mean value, decreasing at large wavelengths. This is valid except for the (x, y) spectral range distribution where a non-symmetrical shape is noticed. This is also the case for the distribution of count ratio points in the w spectral range. Here, the decreasing function of the wavelength is different from the other parameter. For R, the change between the w and the (x, y) spectral ranges is more abrupt than between the (x, y) and the (k, j, z) spectral ranges. Only less than 1% of all the points are outside of the interval $1.50 \times 10^{-13} < \delta\lambda_{LD} < 1.66 \times 10^{-13}$ Å, giving little importance to extreme values. The following Subsection is related to the spectral variation of $\delta\lambda_{LD}$. The experimental data of the R parameter are shown here in order to get a full overview of the doubling parameters affecting the spectra and will be discussed in Sect. 3.2.4.

3.2.2.2. Prediction model of the spectral shift variation

In order to describe the spectral variation of $\delta\lambda_{LD}$, an analytical relationship has been determined, taking into account the crystal splitting and the miscuts. Eq. 2.50 and 2.51 describe the position of the spectral line diffracted by each half-crystal on the detector as a function of the angle of the incident beam $\theta = \theta_{B0} + \Delta\theta$, the angular aperture ϕ and the miscut angle α. The resulting shift on a pixel-scale is then computed as the difference between the two values:

$$\Delta x_i(\alpha, \Delta T) = x_{i,2}(\phi, \Delta\theta, \alpha) - x_{i,1}(\phi, \Delta\theta, \alpha) \qquad \text{[m]} \tag{3.8}$$

The thermal component is integrated by previously computing the resulting inter-reticular spacing d_{hkl} from Eq. 3.5 affecting the Bragg angle of reference θ_{B0}. Thus, the spectral shift function $\delta\lambda_{LD} \equiv f(\alpha, \Delta T)$ is found by converting the line position from pixel to wavelength thanks to the synthetic diagnostic implemented with the ToFu package. Doing so, a prediction of the value of $\delta\lambda_{LD}$ can be made for specific wavelengths, miscuts and thermal changes.

With the spectral shift distribution represented in Fig. 3.9 (top), a direct comparison between experimental and theoretical data is possible. We thus need to compute which couple of parameters $(\alpha, \Delta T)$ model the most the spectral distribution. A least-squares method is used to determine the couple of parameters which best model the

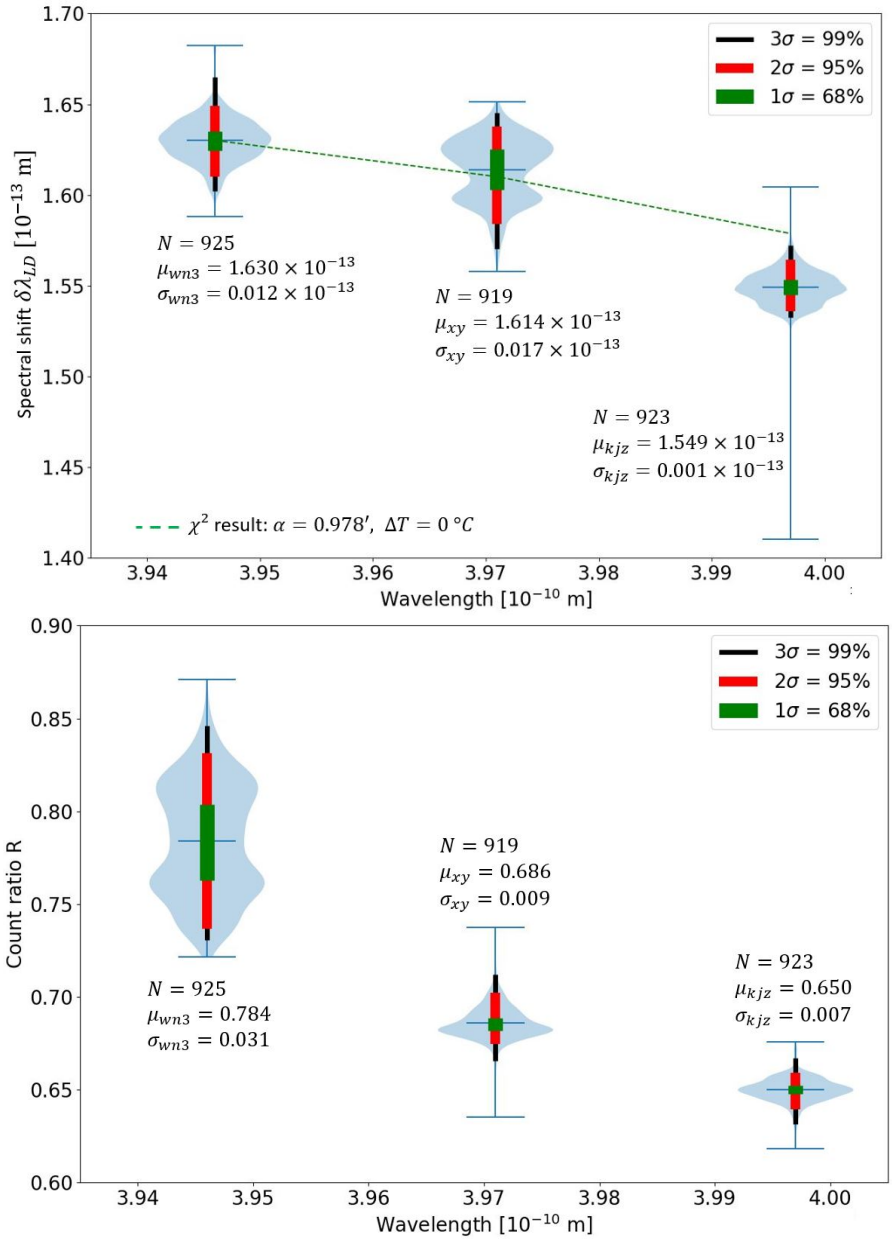

Figure 3.9. – *(Top) Experimental distribution of the spectral shift $\delta\lambda_{LD}$ as a function of the wavelength, overlaid with a best-fit model, and (bottom) the experimental values of the count ratio R parameter.*

experimental data, performing a residual reduction by minimising the quantity:

$$\chi^2 = \sum (y_i - f(\alpha, \Delta T))^2 \tag{3.9}$$

Boundaries are imposed for the miscut angle $\alpha = [-1.5', 1.5']$ and temperature changes ΔT = [0, 5] °C to constrain the results within a reasonable range. The miscut limits are imposed by the crystal specifications from the manufacturer. The temperatures

in both the crystal and the detector boxes are maintained with a cooling system to ensure 15°C inside both of them. This is done to prevent any internal degradation of the crystals by the plasma heat and to ensure an optimal detector operation. However, the hostile environment close to the tokamak means that we have to take into account an uncertainty about the actual temperature of the crystals, since no thermometer is installed in the crystal box. Thus a maximum acceptable temperature gradient of 5 °C can be envisaged.

The result of the least-squares method is shown in Fig. 3.9 (top) in green dashed line. We found an optimal value of the miscut angle for each half-crystal of $\alpha = 0.978'$ and no temperature change $\Delta T = 0\,°C$. It appears that the miscuts are the main component ruling the $\delta\lambda_{LD}$ spectral variation, while a thermal change affecting d_{hkl} has a minor effect on the curve gradient or amplitude. The limiting factor here is the spectral shift distribution in the (kjz) zone, which is lower than the other two.

As a result, the calculated optimum curve does not cross the center of the (kjz) point distributions, nor 99% of the total distribution. Nevertheless, the set of equations describing the line positions on the detector in the two-part crystal configuration describes reasonably well the decay of the spectral shift parameter towards the longer wavelengths. The $\delta\lambda_{LD}$ values represent a shift of, for increasing wavelengths, about 1.54 to 1.46 mm between the two components, which is similar with the experimental spectra studied and the estimated value given in Sect. 3.2.1.2.

In summary, the variation of the spectral shift induced by the use of the two half-crystals with their own miscut angle and temperature properties can be studied through the twenty-one WEST pulses. The considerable number of points allows statistical studies and shot modelling to be performed in order to obtain a single value of the $\delta\lambda_{LD}$ for three different spectral areas. The order of magnitude of $\delta\lambda_{LD}$ is of the same order of magnitude than the spectral resolution of the spectrometer. This explains why the doubled lines are so easily noticed in such spectrum as in Fig. 3.1 and why we need to understand the mechanics of this doubling across the spectrum.

The statistical study shows that towards the larger wavelengths, $\delta\lambda_{LD}$ decreases non-linearly and can be well constrained as a function of the spectrometer geometry parameters. Depending on the incident wavelength, the main feature affecting all the spectral line positions is the miscut angle underlying the crystal lattice. While the temperature changes have a strong effect on line positions, they are less correlated with the spectral shift than the miscuts. The temperature control of the crystal box ensures that large temperature variations cannot happen.

A total miscut amount for both half-crystals of $\sim 2'$ is approximated in agreement with the technical specifications given by our supplier. Thus, the choice has been made to hide one half-crystal to remove the line-doubling. Although this reduces the available diffraction area, it is the most viable solution today, as it enables us to obtain simple spectra and thus extract physical quantities such as electron or ion temperature. Without it, the use of line amplitudes would be subject to considerable uncertainty because today we are not able to model the count ratio. The fact that the count ratio depends on the wavelength is a major obstacle that we cannot yet explain. It is the subject of the following Section.

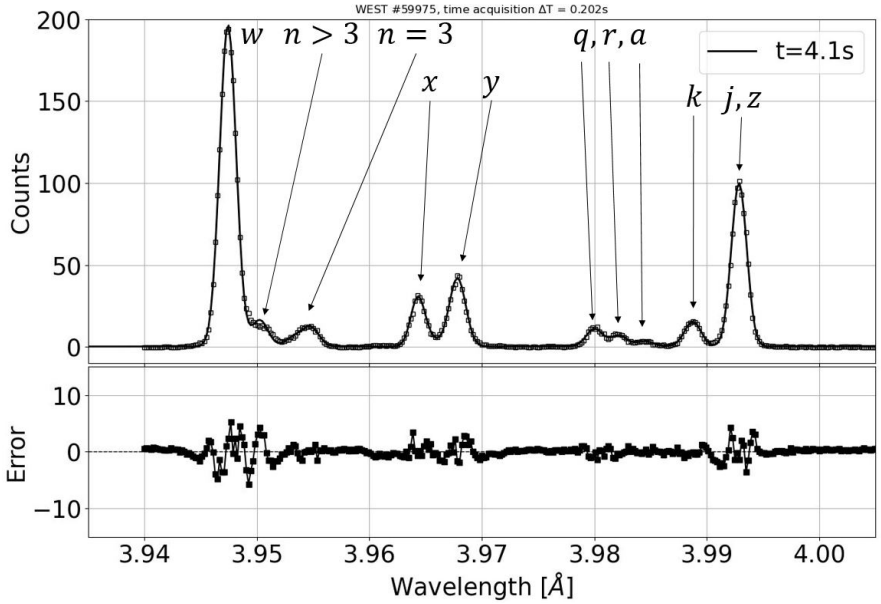

Figure 3.10. – *1D spectrum of the Ar XVII crystal and WEST #59975 pulse without line-doubling. This spectrum corresponds to a central electron temperature of* $T_{e,0} = 1.1$ *keV and a central electron density of* $n_{e,0} = 3.8 \times 10^{19}$ m^{-3}.

Despite the good understanding of the spectral shift parameter, the origin of the count ratio R and of its wavelength dependence is still unknown. In fact, it is very difficult for us to use the doubled lines to extract reliable information from the plasma. At the end of the first experimental diagnostic campaign, it was decided to hide one half of the crystal in order to remove this line-doubling. A typical spectrum is shown in Fig. 3.10. From this point, all the spectra shown were measured with only one half-crystal facing the plasma.

3.2.3. Discussion on the count ratio parameter

The doubled spectra can be modelled by adapting the Gaussian distribution as established in Eq. 3.6. The spectral component of the line-doubling is well described and can be used to interpolate possible miscut and inter-reticular spacing values for the two half-crystals for the specific plasma discharge conditions studied. The major issue is our current lack of understanding of what determines the count ratio parameter R.

If we assume that the two half-crystals are perfectly identical, then we should not observe a difference in counts between the two components of the doubled lines. However, in addition to the fact that the count ratio is less than 1 for all the plasma discharges studied, it also varies with the wavelength, in the same way as the spectral spacing parameter. The maximum difference between the ends of the spectrum is 20%, which means that 20% of the photons measured are lost, whether or not due to the diffraction of the two half-crystals. It would seem, then, that each half has a

different contribution to the overall instrument function of the diagnostic.

To determine the cause of this parameter, or at least try to exclude potential suspects, structural crystal characterization procedures could be employed. Some studies could be performed to characterize the layers of the multilayer crystal, as in [103]. Different techniques have been used to study buried layers and interfaces in a Fe/Si crystal. An X-ray diffraction experiment is used to measure an angular diffraction pattern of the crystal. The study of the angular peaks for specific angles of diffraction, with a well-known X-ray source, allows to compute the Miller indices of the layers within the crystals with Eq. 3.4. This is a good tool to probe the organization of crystal layers in depth. A second experiment consists in performing a X-Ray reflectivity experiment to determine the Rocking-Curve of the crystal. This technique is used to compute the thickness, roughness, density and composition of the different layers and interlayers of the crystal. All this information should help to identify the main cause of the count ratio.

3.2.4. Discussion on a possible effect of heating system on the count ratio parameter

An interesting aspect on the spectral shift $\delta\lambda_{LD}$ and count ratio R distributions, presented in Fig. 3.9, can be investigated. In both distributions and in certain spectral ranges, there are noticeable non-symmetrical shapes with respect to the parameters. Multi-humped shapes, symmetrical with the wavelength, are noticed in the (x, y) spectral range for the spectral shift and in the w spectral range for the count ratio. A deeper analysis of the shot properties shows a difference between plasmas heated by the joule effect (Ohmic heating), the LHCD and the ICRH systems. Table 3.1 shows the heating system and the power deposited in the plasma for each shot. We group the pulse numbers by their first three numbers, the 550XX series in green, the 551XX series in blue and in red the 552XX series. Note that during the 551XX series the ICRH system was employed and during the others, only the LHCD was used. To study what can differentiate them, the values of the R parameter computed for each time step are plotted in Fig. 3.11.

About the R parameter in Fig. 3.11, this method reveals two groups of values related to the heating systems used. A first trend represented by the blue ICRH points is noticed, for values of R greater than 0.8. The second is composed of the other two series of pulse (LHCD), for values of R lower than 0.8. One can easily notice that the R parameter values are higher for the ICRH pulses where the central electron temperature was found lower than the LHCD pulses. W^{43+} and W^{44+} spectral lines may be measured mixed or close to the Ar^{16+} w, x, y and z lines at the high LHCD pulses T_e, inducing a wrongly fitted set of lines and inducing an artificial modification of the count ratio parameter. We will indeed see in particular in Sect. 3.3 that the presence of W is in fact a strong source of uncertainty for the fitting and interpretation of this spectrum.

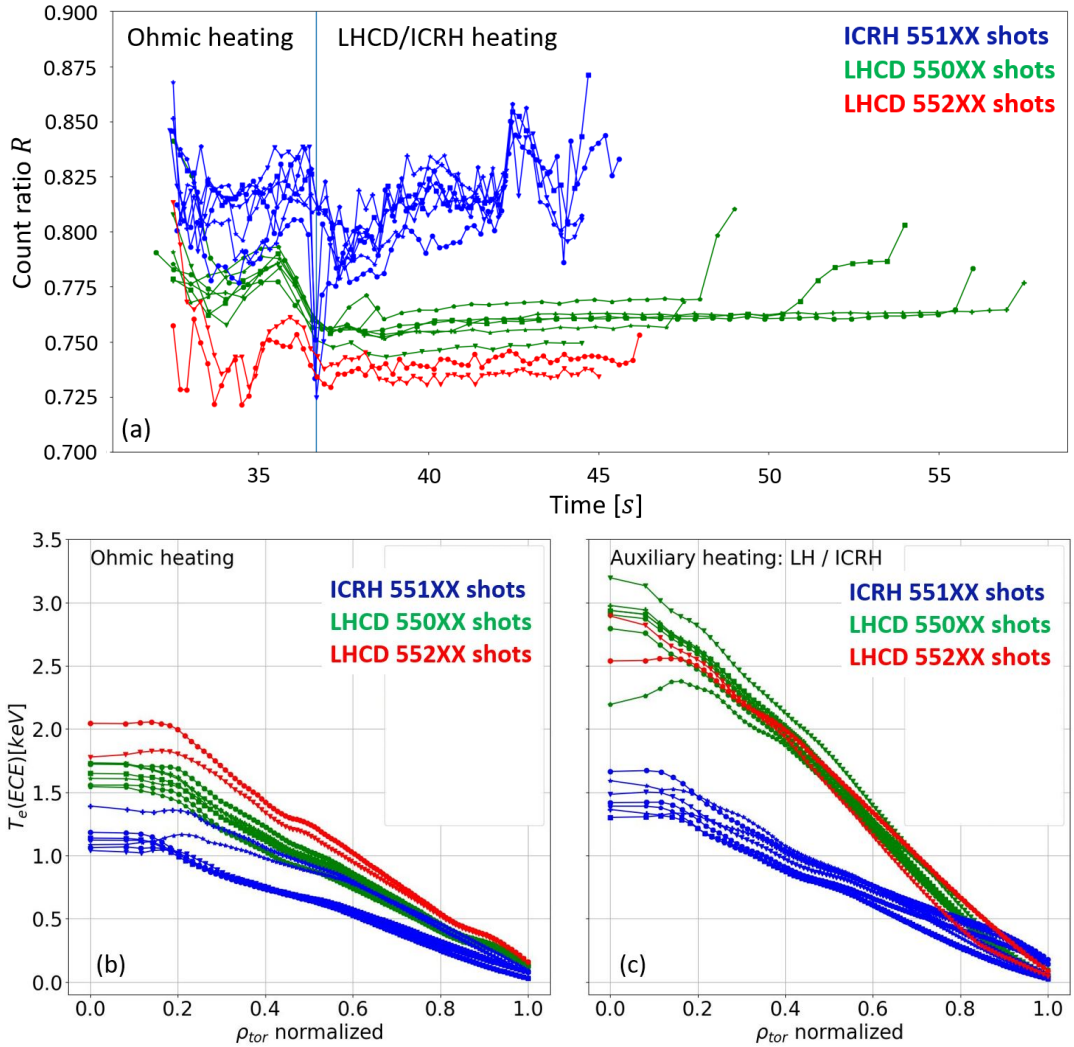

Figure 3.11. – *(a) R values computed for the WEST shots detailed in Table 3.1 and for the w spectral range. Color code shows the ICRH plasma discharges in blue and the LHCD plasma discharges in green and red. The electron temperature T_e measured with the ECE radiometer is thus plotted versus the toroidal radial coordinate ρ_{tor} during (b) the Ohmic heating phase and (c) during LHCD or ICRH heating.*

3.3. Extraction of physical quantities from the Ar XVII spectrum

This Section is dedicated to the extraction of the ion and electron temperature, rotation velocity profiles, in space and time, and W lines measurements from the Ar XVII spectrum. Here, we focus on the LOS-integrated measurements, expressed as a function of the impact parameter h defined in Sect. 2.4.1.

For this purpose, we base the study on the data treatment of two WEST plasma dis-

charges (#59975 and #59920) of which the time traces of the main plasma parameters are shown in Fig. 3.12. The #59975 pulse has a low electron temperature plateau

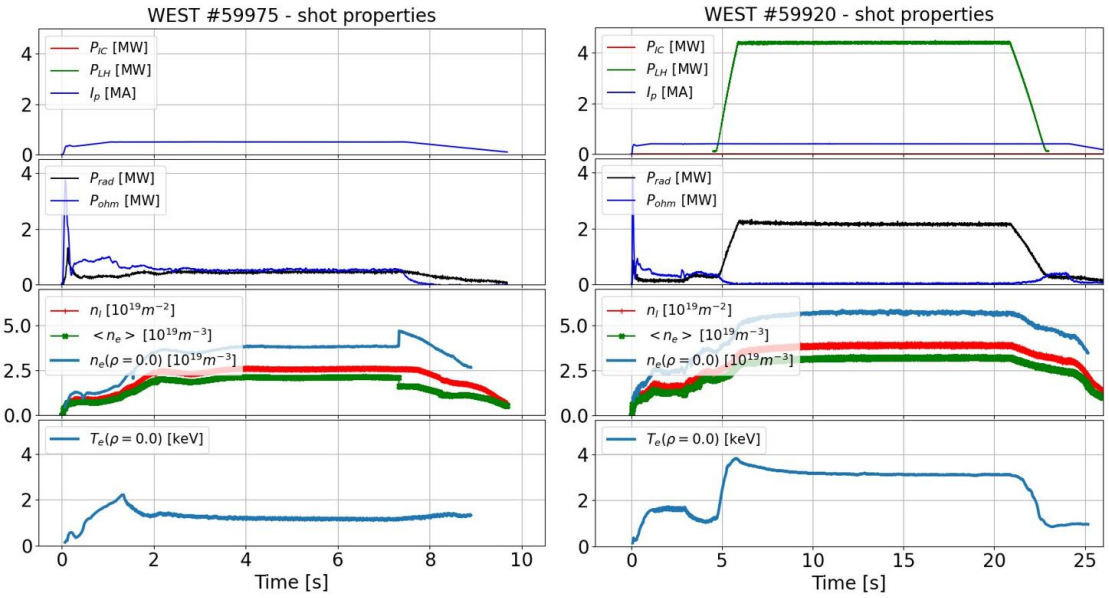

Figure 3.12. – *Time traces of the WEST #59975 and #59920 plasma parameters. From top to bottom: plasma current I_P and LH power P_{LH}, radiated P_{rad} and Ohmic P_{ohm} power, integrated electron density measured by the central interferometer chord n_l, volume averaged $< n_e >$ and central $n_e(\rho = 0)$ electron density and electron temperature measured by the most central ECE channel.*

from approximately t = 4 to 7.3 s at $T_{e0,max} \approx 1.1 - 1.2$ keV, which makes possible the measurement of the Ar spectral lines without contamination of the spectra by W lines. No additional heating system is used here to heat the plasma.

An example of spectrum extracted from this pulse is shown in Fig. 3.10 where all the He-like and Li-like Ar spectral lines are marked with black arrows. LH power has been injected in the plasma for the #59920 pulse between 4 and 22 s up to 4.4 MW, to increase the electron temperature up to 3.8 keV before a stable plateau at 3.1 keV. The electron density is also higher than for the Ohmic pulse and the radiated power increases by up to 50% of the LH power.

3.3.1. Toroidal rotation velocity

The estimation of the line shifts is made by the computation of the position of the lines. During the axes transformation of the 2D images described in Sect. 2.4.1, the spectral lines are straightened in order to process the spectra in two dimensions. Depending on their position across the width of the detector, the position of a line gives the Doppler shift by Eq. 1.79 relative to the column of pixels corresponding to its rest wavelength. Fig. 3.13 (top) shows the Doppler shift profiles of two different

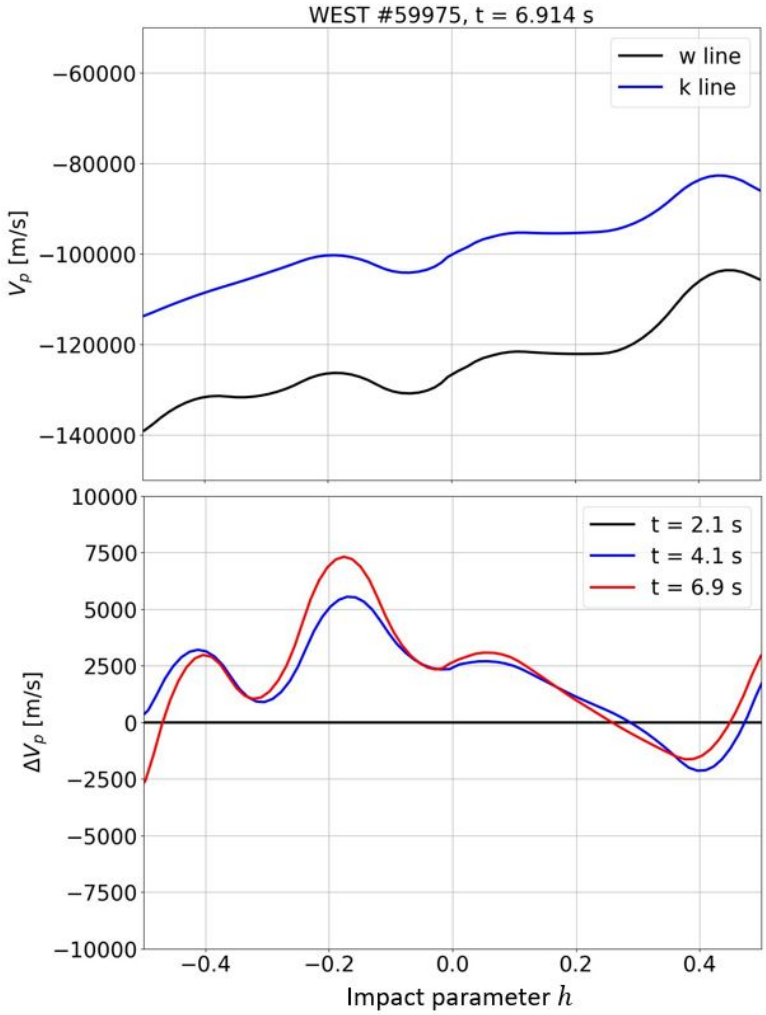

Figure 3.13. – *Top: Non-calibrated toroidal rotation velocity profiles of the Ar^{16+} w and Ar^{15+} k lines for the WEST #59975 pulse at t = 6.914 s; Bottom: relative profiles from the resonance line w data to t = 2.1s.*

lines, the Ar^{16+} resonance line w at $\lambda_0 = 3.94906$ Å and the Ar^{15+} dielectronic satellite line k at $\lambda_0 = 3.9898$ Å, as a function of the impact parameter h. We have there the rotation profiles for two different Ar ionization stages, distributed at both edges of the Ar XVII spectrum

The first result to notice is the very high apparent rotation velocities at the plasma center, $|V_p| \geq 100$ km/s which is higher than expected for the WEST plasmas in which no momentum transfer is performed with for example NBI heating. The relative values of rotation velocity here are not reliable because of the remaining uncertainty regarding the exact camera location with respect to the crystal, i.e. without spectral calibration, as discussed in Sect. 2.3.3. An up-down asymmetry is also noticed on these profiles of an order of approximately 20 $\mathrm{km\,s^{-1}}$ between h=±0.4. This result has to be discussed regarding the the lack of knowledge of the accurate orientation

of the detector, in addition to its position, in the tokamak frame. An error, or rather inaccuracy, in the positioning and/or orientation of the detector on its base in the dedicated box during the installation can lead to this kind of distorted result. From the results exposed in Sect. 2.2.4.2, a defect of a few pixels in the inclination of the detector between the high and low extremities can lead to the addition of a symmetrical Doppler shift artifact from top to bottom.

Taking into account this defect, we should expect similar Doppler shift profiles for all the Ar lines but a difference of $\Delta V_p \approx 22$ km/s is found between the w and the k shift profiles. This difference could be due to some physical transport phenomena affecting differently the Ar ionization stages in the plasma. Another source of this difference could be the different angle with respect to the toroidal direction of the LOS associated to both ends of the spectrum as described in Sect. 2.2.4.2. Finally, inaccuracies in the wavelength mapping on the camera due to uncertainties on the position of the camera could also contribute to this discrepancy, distort the recalculated wavelength scale and lead to this type of result. Relative profiles can be calculated to estimate variations in rotation velocity between each time step, as shown in Fig. 3.13 (bottom) with the data from the resonance line for three different times. With the exception of oscillations which we do not yet know if they are due to physical phenomena or to the transformation of images seen in Sect. 2.4.1, the amplitude of these changes in rotation does not exceed 10 km/s which is the minimum Doppler shift resolution of the instrument. It thus appears difficult then to extract reliable results from these rotation velocity profiles (and relative ones).

Several methods could be implemented to reduce this uncertainty, an absolute in-situ spectral calibration would be one of them. Alternatively a laser metrology on the camera would also help. Another rotation velocity measurement could also provide useful information to define accurately when a plasma discharge has absolutely no rotation to estimate the absolute positions of the lines on the detector.

3.3.2. Ion temperature

The ion temperature is extracted from the Doppler broadening of the line-integrated measurements, as a function of the squared line width $\propto \Delta\lambda_D^2$ (see Eq. 1.80). Several groups of broadening are applied, depending on the different mass of the ion species measured in the spectrum. In Sect. 2.4.2.1 we established according to [76] that the $j+z$ feature must be fitted together to extract the ion temperature. Fig. 3.14 shows two Doppler broadening of the resonance line w and the feature $j+z$ for the WEST #59975 plasma discharge.

We can see that the two profiles do not give the same ion temperature profile. Indeed, the close $n > 3$ dielectronic satellites on the long-wavelength side of the resonance line contribute to its apparent Doppler broadening. As Gaussian profile functions are applied to model the lines, which is an approximation compared to Voigt profile functions which suits better to the lines, the contribution appear more important and enough to use the $j+z$ feature to estimate the plasma ion temperature. Generally, it is also assumed that the width of the spectral lines observed is dominated by the Doppler

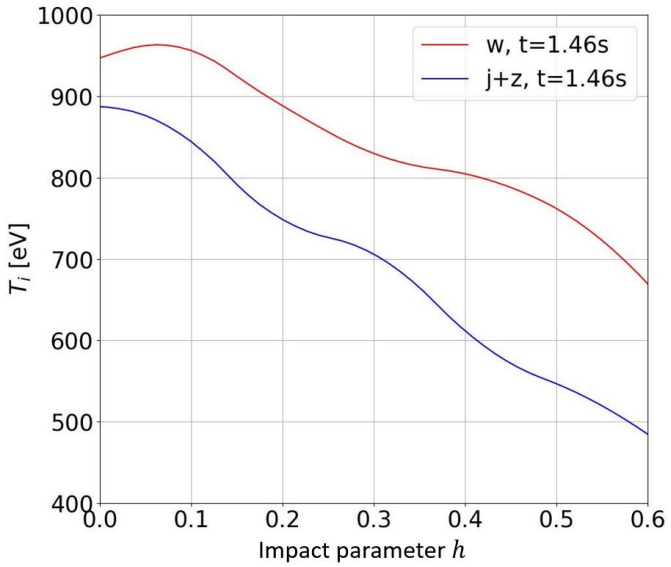

Figure 3.14. – *Doppler broadening profiles extracted from the He-like Ar resonance line w and j + z feature for the WEST #59975 pulse at t = 1.46 s.*

broadening in comparison to the natural line-width and the instrument function, see Sect. 1.3.5. However, the different contributions to the line width that we have seen so far cannot be verified since no calibration techniques have been performed on this diagnostic, cf. Sect. 2.3.3, i.e. the Rocking-Curve width, the Johann error and also the geometrical extent of the visible plasma of the detector pixels, which leads to a greater number of photons for the pixels with the greatest extent.

The comparison of our experimental ion temperature profiles is possible with a computation made with the WEST database from the D-D fusion producing neutrons using interpretative METIS simulations [104] [105]. The results of these computations of the central ion temperature is displayed in Fig. 3.15 in parallel of the XICS measurements and the T_e deduced from ECE measurements. During the Ohmic phase until t = 5 seconds, we can see that the electron and ion temperatures are similar, T_e reaches at its maximum 1.6 keV where the two T_i computations gives a maximum value around 1.2-1.3 keV. Once the LH waves are injected in the plasma, the electron temperature increases by almost a factor four between before and after the LH ramp-up phase. However, the ion temperature saturates at different plateau values, $T_i(XICS) \approx 1$ keV and $T_i(METIS) \approx 1.3$ keV. In fact, the two measurements also give a different magnitude of temperature rise.

It is shown in Fig. 3.16 where both METIS and XICS T_i time traces for the plasma center are plotted in red and blue respectively. During the ohmic phase, the $T_i(XICS)$ values are higher than the $T_i(METIS)$ data, which is reversed during the LH phase. Both temperatures reach a minimum just before t = 5 seconds at around 750-800 eV. We then see an increase in $T_i(XICS)$ by a factor of 1.3 up to 1keV, while the $T_i(METIS)$ data increase up to 1.35 keV by a factor of 1.7. Finally, at the end of the pulse, both calculations give the same temperature estimate. The ratio between both compu-

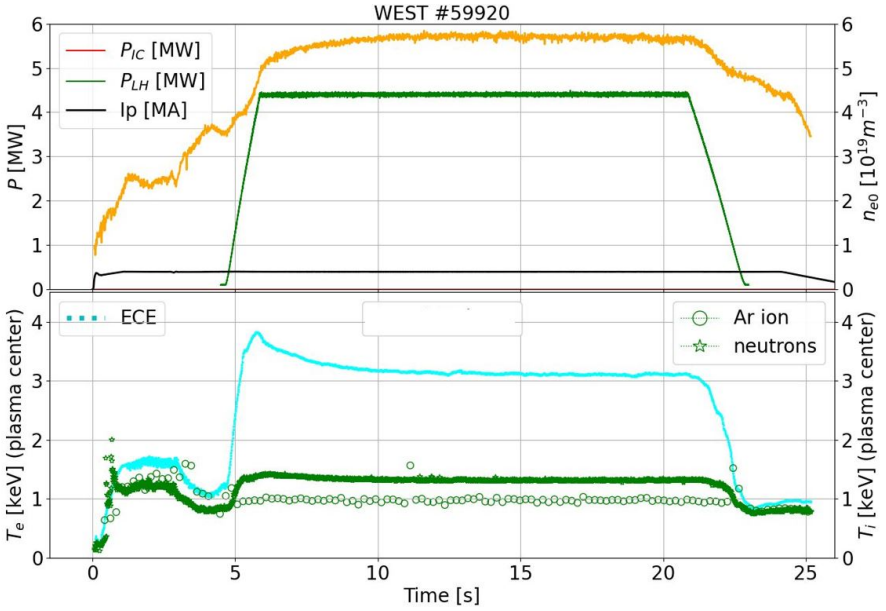

Figure 3.15. – *Time traces of the WEST #59920 plasma parameters. From top to bottom: plasma current (black) I_P and central electron density (orange) $n_{e,0}$, LOS-integrated ion temperature (green circle) $T_{i,0}$ computed with the $j+z$ feature Doppler width and the METIS simulations (green star). The electron temperature measured by the most central ECE channel $T_{e,0}(ECE)$ (cyan) is plotted to give an estimation of T_e.*

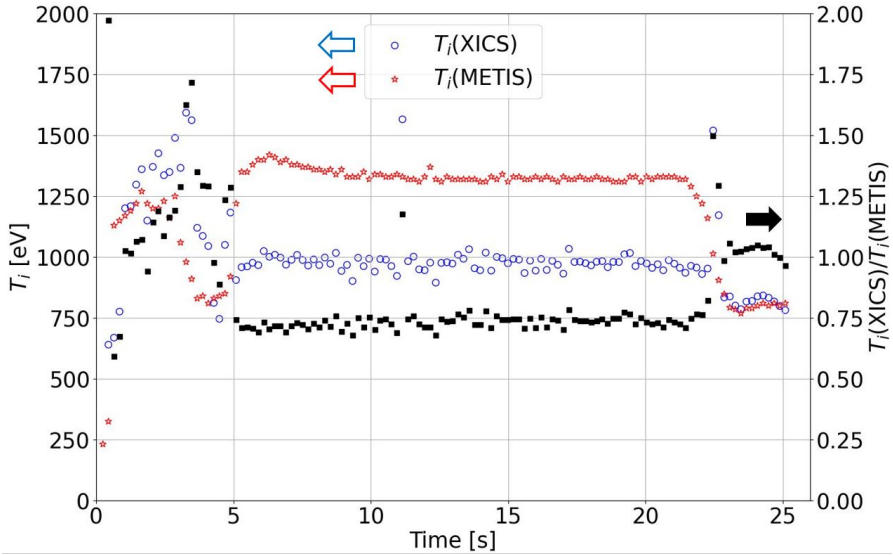

Figure 3.16. – *Time traces for the WEST #59920 plasma of the ion temperature (blue circle) $T_{i,0}$ computed with the $j+z$ feature Doppler width and the METIS simulations (red star). The ratio between the two (black dot) is also shown in the right y-axis.*

tations is displayed in black squares in the secondary y-axis. Leaving aside the first Ohmic phase, we can see that the ratio of $T_i(XICS)/T_i(METIS)$ fluctuates between 0.75 during the LH phase and 1 at the end. Finding the reason for these differences appears difficult since, from the XICS point of view, it would mean measuring line widths that are smaller than expected in order to recover the values of $T_i(METIS)$. A statistical study of all the plasmas from an experimental campaign, with a large range of plasma parameters, should provide useful information to converge to more reliable T_i profiles.

3.3.3. Electron temperature

Introduced in Sect. 1.3.4.3, the line emissivity is a function of the impurity n_Z and the electron n_e densities, the fractional abundance of the emitting ionization stage $f_{Z,z}$ and the PEC of the considered line. The last two terms depend on the plasma electron temperature. We have seen in Sect. 1.3.4.4 that the electron temperature can be extracted from ratios between lines from neighbouring ionization stages.

The theoretical sensitivity of various Ar line ratios to the electron temperature has been studied in [28] and the results are shown in Fig. 3.17. The line ratio the most

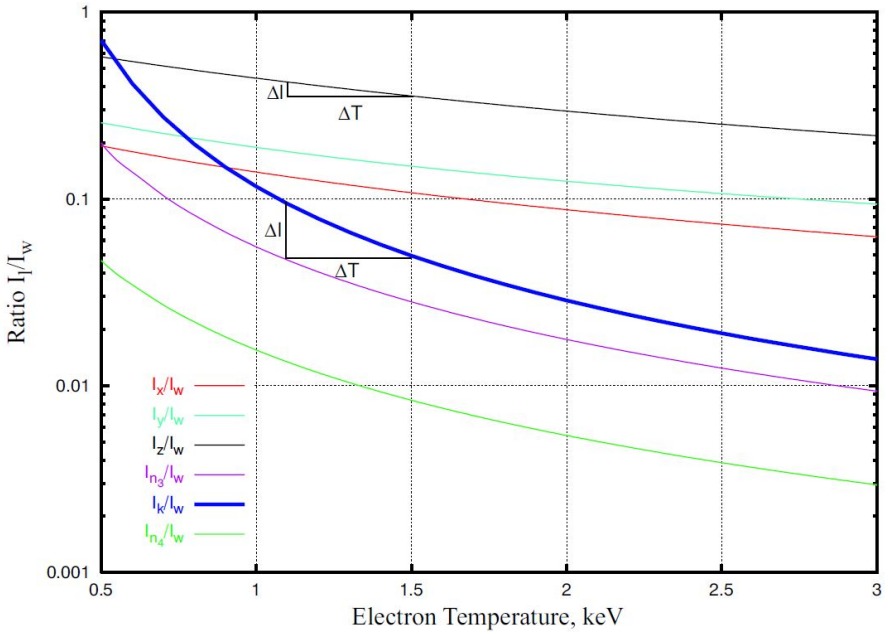

Figure 3.17. – *Theoretical line ratio of various He-like and Li-like Ar lines to the He-like Ar resonance line w as a function of the electron temperature [28].*

sensitive to the electron temperature appears to be between the dielectronic satellite line k and the resonance line w. The second most sensitive ratio is between the dielectronic satellites $n = 3$ and the w line. Historically, the first one is the most commonly used to extract the electron temperature profiles with XICS systems [52] and been experienced in [106] and [93] with the single-Gaussian approximation for

the $n = 3$ group of lines. Using the PEC files for the Ar^{15+} and Ar^{16+} ionization stages obtained from the OPEN-ADAS database [36], theoretical temperature sensitivities for the two line ratios $R^{th}_{k/w}$ and $R^{th}_{(n=3)/w}$ are computed from the excitation process and compared to the XICS experimental line ratios, as shown in Fig. 3.18.

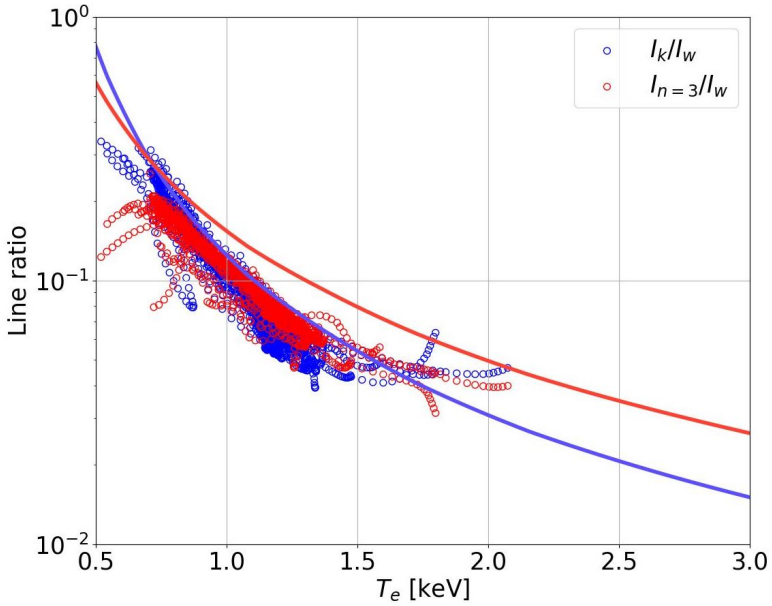

Figure 3.18. – *Ratios of the Ar^{15+} dielectronic satellite line $n = 3$ (red line) and Ar^{16+} dielectronic satellite line k (blue line) to the Ar^{16+} resonance line w as a function of the ECE electron temperature and comparison to the experimental line ratios (circles) with the WEST* #59975 *data.*

The experimental line ratios obtained from the measurement of the WEST #59975 plasma discharge are plotted in blue ($R^{exp}_{k/w}$) and red ($R^{exp}_{(n=3)/w}$) circles. First, different temperature dependences can be observed between the calculations of [28] and ours based on OPEN-ADAS database. This can be explained by the great complexity of the atomic physics codes that can be used for this purpose, as discussed in Sect. 1.3.4.3, and is not the subject of this thesis. That being said, the comparison between the experimental R^{exp}_i and the theoretical R^{th}_i line ratios displays a common trend. Both $R^{exp}_{(n=3)/w}$ and $R^{exp}_{k/w}$ are lower than their corresponding theoretical values and the gap increases with increasing T_e. Two possible explanations arise.

Either the resonance line intensity is overestimated or the atomic data we use to compute the theoretical line ratios, from which we deduce the temperature, are not optimal. The first hypothesis can be explained by the neglecting of the recombination process in the overall intensity and here for the theoretical line ratios. As shown in [107], the radiative recombination population of the upper level for the resonance line w can be very important for the cooler outer regions of the plasma and Fig. 1.16 in Sect. 1.3.4.3 shows close contributions from recombination to the excitation in the case of the resonance line. Here, only the excitation part of the He-like Ar resonance line PECs is used for the theoretical line ratios and the total $n = 3$ line ratio contribution

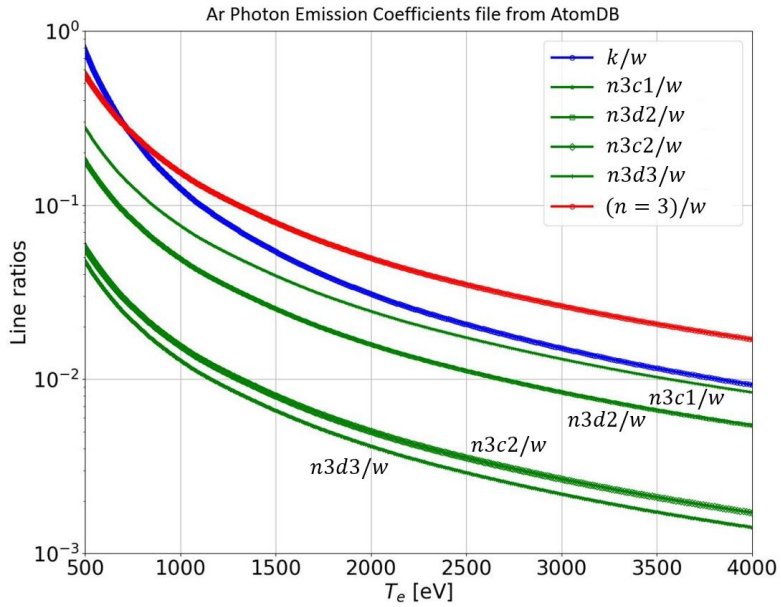

Figure 3.19. – *Theoretical line ratios between the excitation part of the He-like and Li-like Argon lines.*

is the sum of the PECs of the most intense lines that belongs to this group. Fig. 3.19 shows in detail the various contributions of the most intense lines in the $n=3$ group of dielectronic satellites, as discussed in Sect. 2.4.5. It appears that neglecting the recombination component for the w line can enhance the theoretical line ratios, leading to the discrepancies between experimental points and theoretical curves seen in the previous figure. While it is possible to sum the PECs of the lines in the $n=3$ group, since they originate from the same atomic process, it is not possible to sum different contributions from excitation, ionization and recombination. These theoretical line-ratio curves are therefore approximated and it is assumed that part of the total error in the T_e estimation comes from this approximation. The second hypothesis is difficult to demonstrate, since it would require testing several atomic physics codes and comparing their results with experimental data - a subject of study in its own but a subsection will be addressed to this topic in Sect. 3.3.5.

It should be noted that in [108], an alternative approach based on the simulation of the spectral emission has been proposed for the interpretation of X-ray argon impurity emission. The simulations have well demonstrated that radiative cascades are important, as well as spatial parameter variations and charge exchange with neutral hydrogen. Based on a fully collisional-radiative space resolved approach, excellent overall agreement between the simulation and the experimental data was obtained. In particular, the simulation included the Li-like satellite emission $1s2lnl' - 1s^2nl'$ for $n = 3,4,5,6,7$ that are located near the resonance line and a very good correlation between the k satellite line and these higher-order satellites near the w line was observed. Also, good agreement with the ECE measurements was observed in [109].

Another point that could be linked to the first hypothesis is that [110] authors has identified the contribution of non-thermal electrons, high-energy electrons on top of the Maxwellian electron distribution function, which enhance the intensity of the resonance line in case of low electron density plasmas and/or plasmas heated with RF waves (with LHCD). The latter is excluded here because of the absence of LHCD heating for this particular plasma discharge. However, [110] authors found a clear deviation of the R_i^{exp}/R_i^{th} ratio, increasing as the electron densities is decreased to $n_e = 5 \times 10^{19}$ m^{-3}, interpreted as an effect of non-thermal electron population. Further studies can be carried out on this subject, taking into account a complete characterisation of the electron energy distribution function in this type of Ohmic plasma discharges.

Finally, Fig. 3.20 shows the LOS-integrated temperature profiles obtained with the two XICS line ratios $R^{exp}_{k/w}$ and $R^{exp}_{(n=3)/w}$ and are compared with the corresponding ECE temperature profile at the same time. Here, the single-Gaussian function approximation is used to model the $n = 3$ group of dielectronic satellites as studied in Sect. 2.4.5. The $T_e((n = 3)/w)$ profile appears to be higher for the entire radial range studied

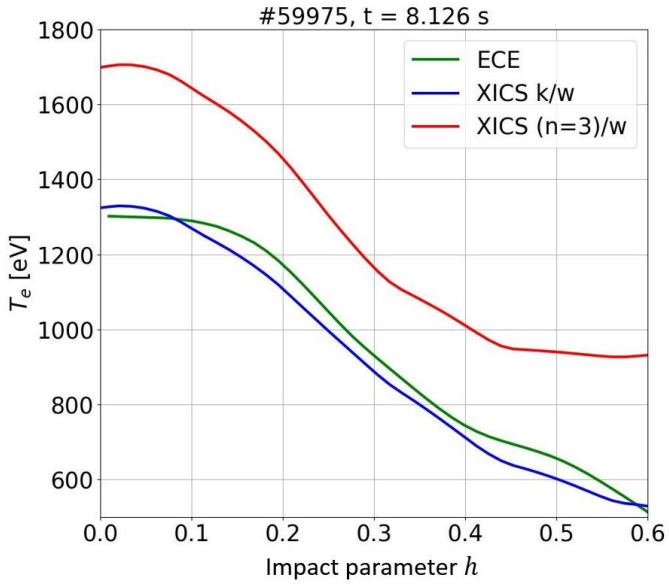

Figure 3.20. – *Electron temperature profiles deduced from the ECE (green line) and the XICS measurements, with the k/w (blue) and $(n = 3)/w$ (red) line ratios for the WEST #59975 data at $t = 8.126$ s.*

compared with the other two profiles. The $T_e(k/w)$ one is similar to the ECE profile but the maximum of the two is not located at the same ρ_{tor} coordinate. Both XICS profiles have their maximum slightly shifted to $\rho_{tor} \approx 0.03$. This shift is related to the discussion in Sect. 2.4.4 where we have seen that the computation of the ρ_{tor} radial coordinate is highly dependent on the magnetic equilibrium reconstruction method. Studying the temporal variation of these quantities, we find again that the ratio $R^{exp}_{(k)/w}$ gives an estimation of the temperature closer to the ECE measurements for the plasma center, as shown in Fig. 3.21. The central $T_e(k/w)$ electron temperature is about 1.13

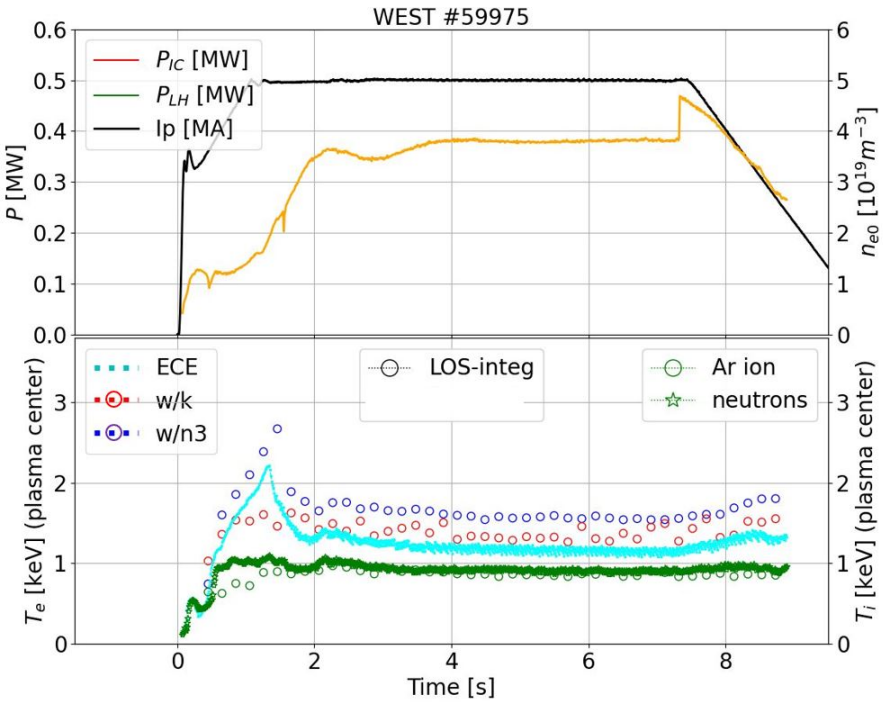

Figure 3.21. – *Time traces of the WEST #59975 plasma parameters. From top to bottom: plasma current (black) I_P and central electron density (orange) $n_{e,0}$, electron temperature measured by the most central ECE channel $T_{e,0}(ECE)$ (cyan) and from the two XICS LOS-integrated line ratios $T_{e,0}(k/w)$ (red) and $T_{e,0}((n=3)/w)$ (blue), and the LOS-integrated ion temperature (green circle) $T_{i,0}$ computed with the $j+z$ feature width and the total neutron flux interpolation (green star).*

times higher than the ECE measurements, on the electron density plateau between t = 4.0 s and t = 7.3 s, while a mean factor 1.3 is found between $T_{e,0}((n=3)/w)$ and ECE time traces.

In addition, between t = 0.5 and t = 1.5 s, the $T_{e,0}(k/w)$ time trace saturates at 1.5-1.6 keV when $T_{e,0}(ECE)$ increases above 1.8 keV to a maximum value of 2.2 keV and become close to the ECE values again when the temperature drops below 1.5 keV. The reason for this difference, in a specific T_e range, is the presence of W lines in the Ar XVII spectrum.

Indeed, the study of the #59920 plasma discharge allows to study XICS measurements for higher electron temperatures and to explore this behavior. Fig. 3.22 shows the time traces of LH power, central electron density, central electron temperature for the #59920 plasma discharge. It is a typical WEST plasma discharge during which 4.2 MW of Lower-Hybrid power maintains the plasma stable from 5 to 22 s. The electron density and temperature at the plasma core reach about 5×10^{19} m^{-3} and 3.1 keV respectively. During the Ohmic phase, up to 4 seconds, but also at the very end of the pulse from 23 seconds onwards, we notice the same discrepancies between the electron temperature measurements of the ECE and XICS diagnostics, as for the

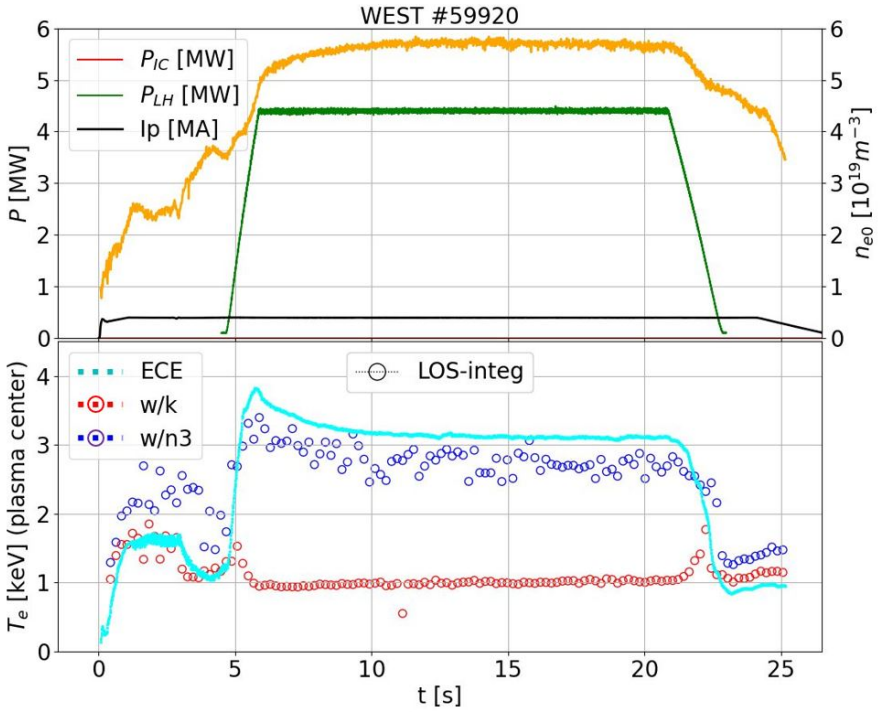

Figure 3.22. – *Time traces of the WEST #59920 plasma parameters. From top to bottom: plasma current (black) I_P, LH power P_{LH} (green) and central electron density (orange) $n_{e,0}$, electron temperature measured by the most central ECE channel $T_{e,0}(ECE)$ (cyan) and with the two XICS LOS-integrated line ratios $T_{e,0}(k/w)$ (red) and $T_{e,0}((n=3)/w)$ (blue).*

previous pulse studied.

Two phases are visible here: the Ohmic phase and the LHCD phase. During the Ohmic phase, the $R^{exp}_{(k)/w}$ line ratio gives a better match with the ECE temperatures. But during the LHCD phase, the roles are inverted and the $R^{exp}_{(k)/w}$ line ratio becomes completely irrelevant and saturates at ≈ 1 keV.

We can take a closer look at the experimental line ratios during the whole pulse duration, displayed in Fig. 3.23 and compare them directly to LH heating duration to study their behavior. Between t = 5 and t = 23 seconds, a clear discrepancy between the two XICS line ratios is noticed. $R^{exp}_{(n=3)/w}$ becomes very low, corresponding to higher temperatures as seen in Fig. 3.18 but the same behavior is not noticed for the other line ratio. We can conclude here that the LHCD heating has a clear effect on this line ratio estimation from the supra-thermal electrons increasing the intensity of the resonance line w as explained earlier.

Direct comparison of all the T_e points deduced is made between between the ECE and XICS measurements in Fig. 3.24. We plot the temperature points in red from the $R^{exp}_{(k)/w}$ line ratio and in blue from the $R^{exp}_{(n=3)/w}$ one. The distribution is plotted from corresponding times for the two diagnostics. The points introduced just above appear in this figure. About the $R^{exp}_{(n=3)/w}$ line ratio in blue, two branches are noticed, one

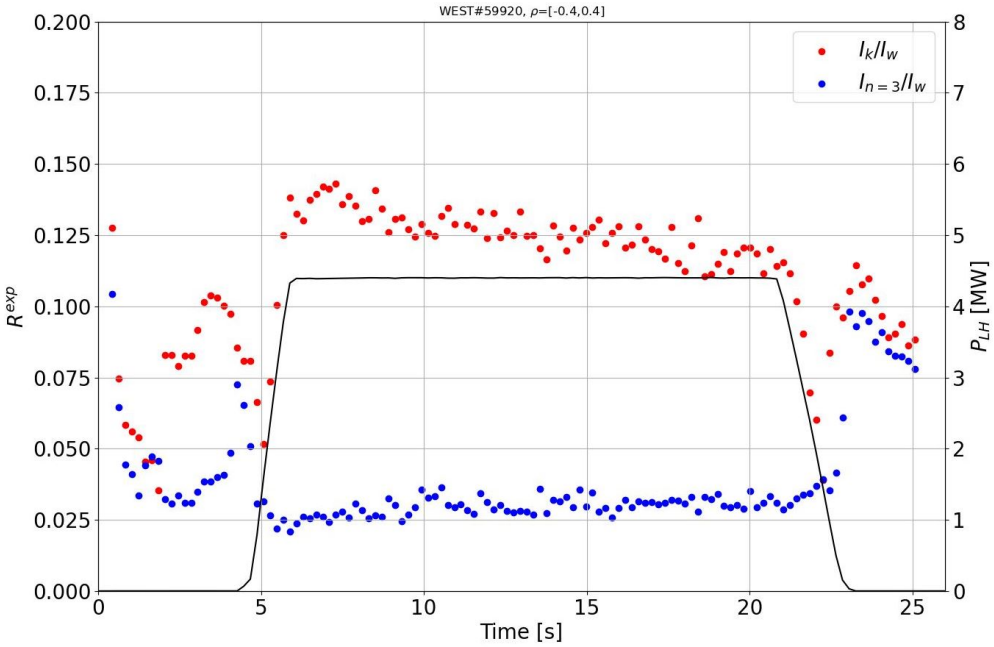

Figure 3.23. – $R^{exp}_{(k)/w}$ *and* $R^{exp}_{(n=3)/w}$ *line ratios variations with time for the WEST #59920 plasma discharge during LH heating. The time duration of the LH heating is plotted in black line.*

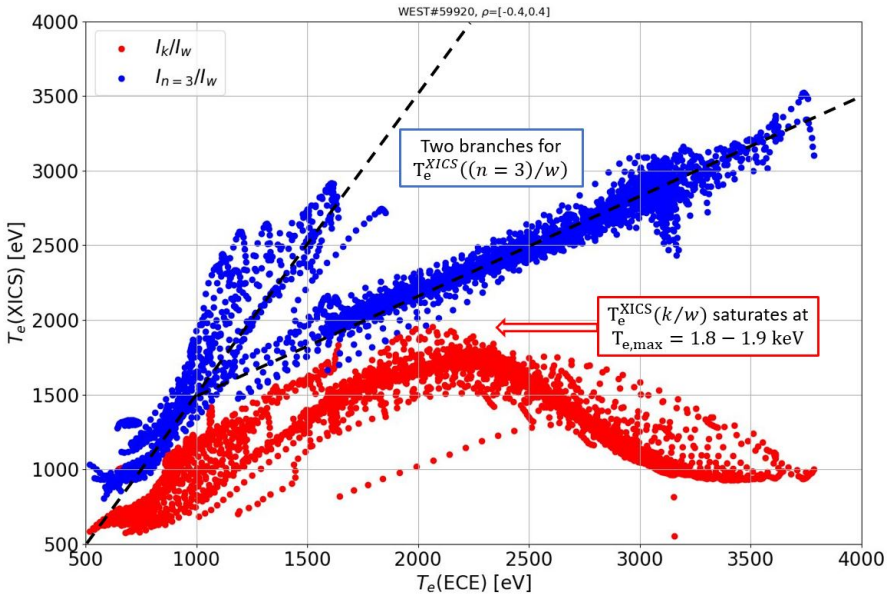

Figure 3.24. – *Comparison of the* T_e *deduced from both Ar line ratios to the ECE radiometer estimations.*

with a higher slope at low temperatures (T_e < 1.8 keV) than for another branch for the higher temperatures. The break of slope is abrupt and corresponds to the activation of LH heating. The low temperature branch illustrates the behavior of the T_e estimation

with this line ratio studied with the past Ohmic reference pulse. Concerning the $R^{exp}_{(k)/w}$ line ratio in red, the XICS values saturate at approximately 2 keV and an inversion of the slope is noticed at the highest electron temperatures. Here again, the main difference with the measurements of the Ohmic reference plasma is the RF waves in the plasma and so the higher electron temperature achieved.

As a result, we can conclude that the intensity of the resonance line w is not the cause of these discrepancies (otherwise we should observe an unusual behavior also with the $R^{exp}_{(n=3)/w}$ line ratio) on the contrary of the dielectronic satellite line k. Additional spectral lines are thus suspected to be present in the close vicinity of this line, which distort its modelling as a consequence. Nor can we conclude that this line ratio is unusable, as we will now show that we can identify new tungsten spectral lines across the spectrum that distort the fit.

3.3.4. W impurity measurement

Thanks to the results of the [74] and [75] works, three tungsten spectral lines have already been identified in the observed Ar XVII spectrum in WEST and integrated in the treatment algorithm, shown in Fig. 3.25 and referenced in Table 2.3 . Three are of high intensity, which means they can be well modeled and studied. They are emitted from the W^{43+} and W^{44+} ionization stages and labelled as Ga-3 for the W^{43+} and Zn-2 and Zn-3 for the W^{44+} ionization stages. Two spectral area selections are made and

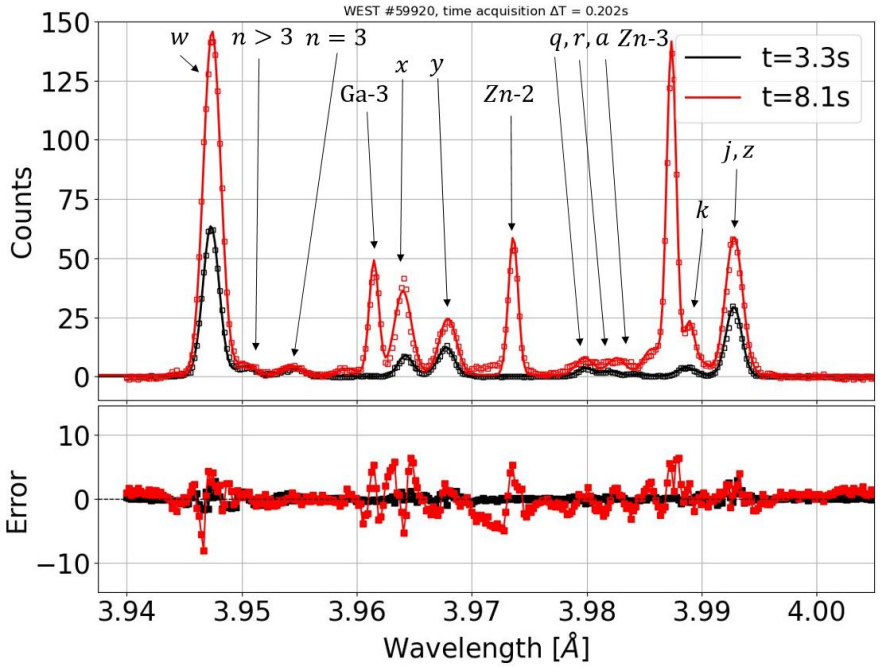

Figure 3.25. – *Two spectra extracted for the XICS central line of sight measured with the Ar XVII crystal and during the WEST #59920 for t = 3.3 and 8.1 s. All the Ar and W spectral lines referenced as initial guesses in the algorithm are marked with black arrows.*

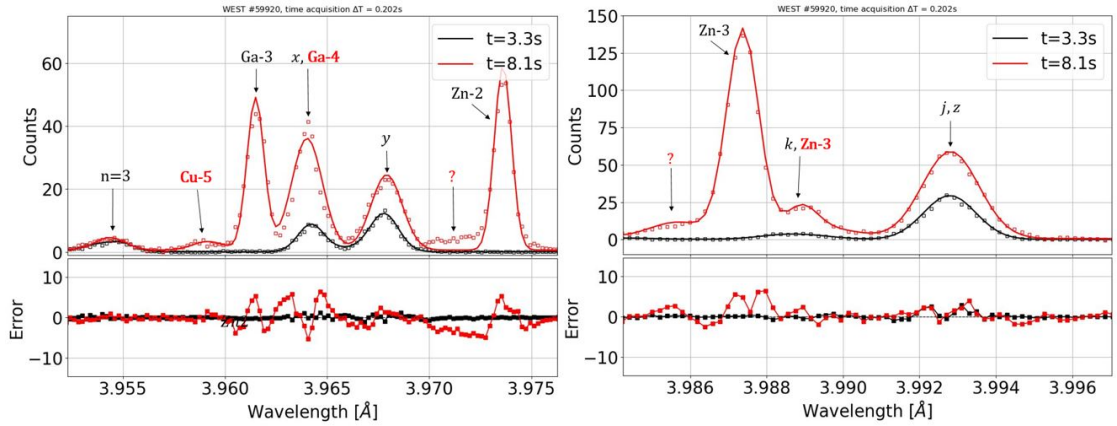

Figure 3.26. – *Spectral areas of the spectrum Fig. 3.25 selected to highlight additional spectral lines (in red) measured (left) around the He-like Ar feature $x + y$ and (right) close to the dielectronic satellite line k.*

displayed in Fig. 3.26 to better visualize the differences between the two spectra.

In the left subfigure, the spectra shows in detail the $x + y$ feature spectral range where two additional spectral lines are identified and labelled: Cu-5 ($3p^6 4p^2\ ^2P_{1/2}$ - $3p^5 4s5f^2\ ^2D_{3/2}$) as from the W^{45+} and Ga-4 ($3d^{10}4p^2\ ^2P_{1/2}$ - $3d^9 4p6f^2\ ^2P_{1/2}$) as from the W^{43+} ionization stages. These lines have already been observed in [74] and more recently in [111]. Another feature is also noticed between the He-like Ar intercombination line y and the W^{44+} Zn-2 line. Here, the spacing between these two lines is large so we do not expect them to participate in this emission with their wings. An unknown number of lines are measured here, probably from W impurity because the high electron temperature that corresponds to this time at t = 8.1 seconds, see Fig. 3.22.

About the Cu-5 spectral line measured approximately at $\lambda_{Cu-5} \sim 3.958$ Å, the number of counts per time unit is fairly low (25 counts.s^{-1}). This indicates that this W^{45+} line remains difficult to measure with the XICS instrument for the electron temperature achieved in this specific WEST plasma discharge. More work has to be carried out to find WEST plasma discharges where higher electron temperatures are reached. And for the Ga-4 spectral line measured at approximately $\lambda_{Ga-4} \sim 3.963$ Å, its evidence is provided by the fact that the x line becomes more intense than the y line for increasing temperatures.

In the right subfigure, the spectra show in detail the k and $j + z$ features where the W^{44+} Zn-3 line has already been identified. Here also, additional lines are measured, on the left wing of the Zn-3 line and also embedded in the dielectronic satellite line k. A second component of the Zn-3 transition ($3p^6 4s^2\ ^1S_0$ - $3p^5 4s^2 5f\ ^1D_1$) appears to be measured at a very low spectral spacing from the k line ($\sim 4 \times 10^{-4}$ Å). The work of [111] on KSTAR describes Ar XVII spectra measured in a W-environment with a new W divertor and their ability to measure the Ar XVII spectral range without Ar impurity lines. It results thus in spectra where only W lines are measured.

This gives important information about the low-intensity lines which are probably

embedded below the Ar lines in our spectra in WEST. They found a multitude of low- and medium-intensity additional spectral lines distributed in the entire spectral range. In addition to confirm our previous W line identification, they indicated that one or more additional spectral lines could be measured in the narrow range between the k line and the $j+z$ feature, without formal identification.

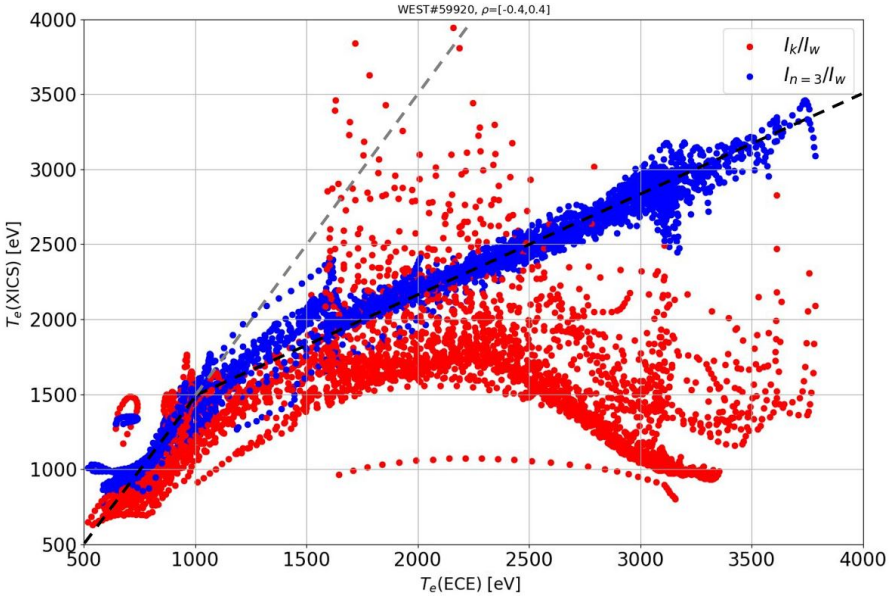

Figure 3.27. – *Comparison of the T_e deduced from both Ar line ratios to the ECE radiometer estimations after the integration of the second Zn-3 spectral line in the algorithm.*

Taking into account the second Zn-3 line in the data treatment allows to test the improvement in the k line modelling it could offer. Fig. 3.27 shows the modification of the electron temperature computed with both $R^{exp}_{(k)/w}$ and $R^{exp}_{(n=3)/w}$ line ratios after the integration of the second Zn-3 line in the treatment algorithm. The slope breaking noticeable for the $R^{exp}_{(n=3)/w}$ line ratio is attenuated but is still present for $T_e((n=3)/w) \approx 1.5$ keV. For the other line ratio, the dots distribution is more diffuse especially at higher temperatures ($T_e(ECE) > 1.5$ keV), making the shape more diffuse as seen in Fig. 3.24 around 1.8-1.9 keV. The slope inversion is still measured for a central temperature $T_e(XICS)$ between 2 and 2.5 keV. The fact that the maximum becomes ill-defined indicates that taking into account a second line juxtaposed to the k line seems to be the right way forward. However, no linearity between $T_e(k/w)$ and $T_e(ECE)$ seems yet to emerge.

Unfortunately, no PECs are available for this second Zn-3 component in order to constrain it more efficiently in the code. It is also difficult to conclude on the exact number of lines in the close vicinity of the dielectronic satellite line k since it would require a spectral resolution higher than the XICS one of 10^{-4} Å to measure them. It would be also difficult to predict the corresponding transitions from the atomic physics computations as there are too many energy levels that can be involved in such

ionization stages of W. The possibility of measuring spectra without Ar lines over a wide temperature range could help to identify or at least measure the lines.

However, we can still study the measured intensities of the three well-defined W^{43+} Ga-3, W^{43+} Zn-2 and Zn-3 spectral lines. This study allows to constrain them in the treatment algorithm. We use here measured intensities from experimental data extracted from several WEST plasma discharges. Fig. 3.28 shows the W^{44+} Zn-2 spectral line as a function of the W^{43+} Ga-3 and the W^{44+} Zn-3 spectral lines. The Zn-

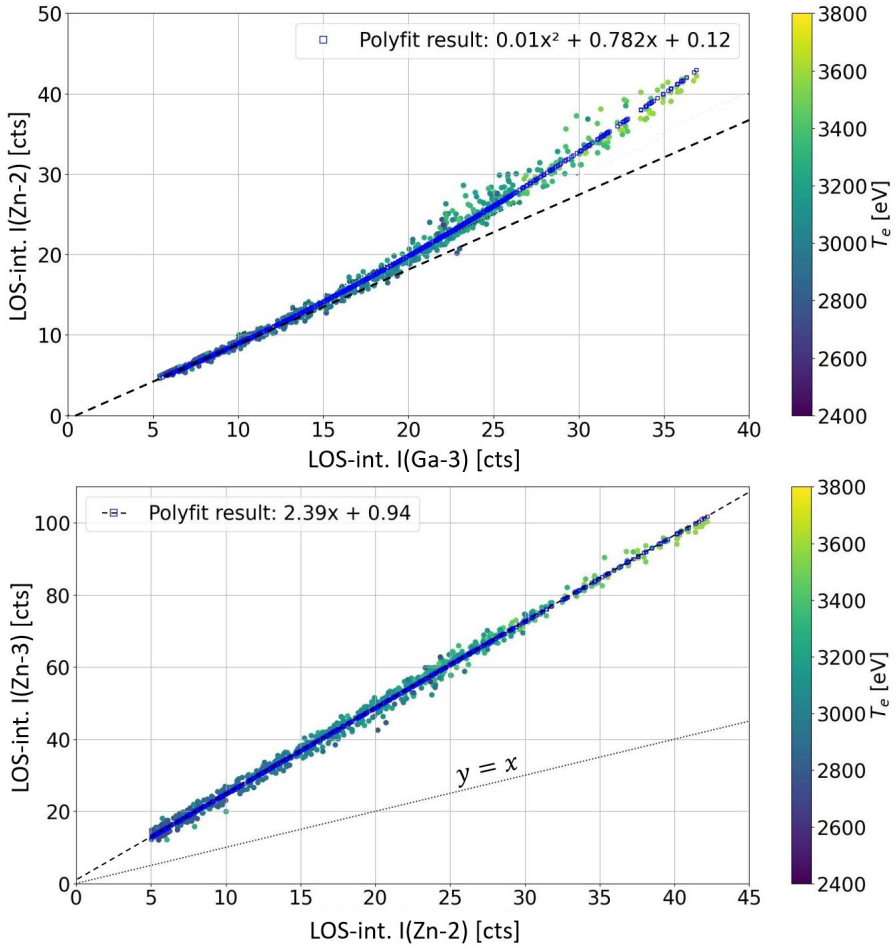

Figure 3.28. – *Spectral line ratios between (top) the W^{43+} Ga-3 and the W^{44+} Zn-2 and between (bottom) the W^{44+} Zn-2 and the Zn-3 spectral lines measured with the XICS diagnostic [37].*

3/Zn-2 line ratio is constant over a large range of electron temperature, $T_e = [2.4, 3.8]$ keV, while it is not the case for the Zn-2/Ga-3 ratio. The first can be approximated by a linear affine function with a slope coefficient of 2.39, as indicated on the bottom subfigure. This result is important as both Zn-3 and Zn-2 spectral lines are emitted from the ionization stage of W. From the expression of the line emissivity Eq. 1.65, only the PEC variables are different for these two lines and we have seen in Sect. 1.3.4 that the PECs for two lines from the same ionization (He-like resonance w and forbidden

z lines) stage do not have the same temperature dependence.

Here, there is a linear relation between these two and it can be used to constrain one line from the other in the data treatment. As for the Zn-2/Ga-3 line ratio, it appears only constant for low brightness, i.e. for low temperatures, and tends towards a higher intensity measured for the W^{44+} Zn-2 line at higher temperatures. The fractional abundances of these ionization stages are shown in Fig. 3.29, computed with the Aurora atomic physics code, taking into account ionization and recombination processes without transport. These curves are computed assuming a superstaging approximation for such complex W ions [35], by bundling multiple ionization stages together to reduce computational time and based on similar ionization potentials between neighbouring stages. Here, we can see that the fractional abundances of the

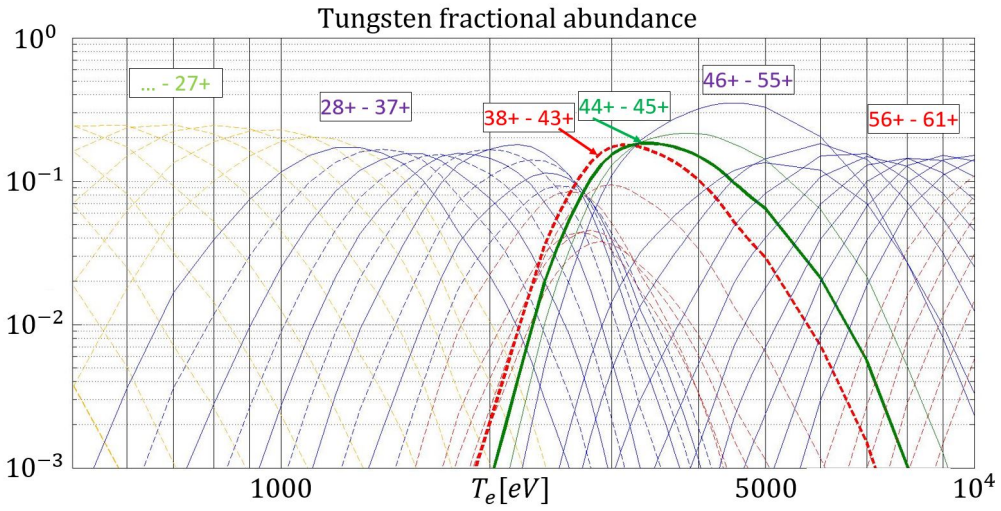

Figure 3.29. – *Fractional abundances of the W ionization stages as a function of the temperature [37].*

W^{43+} and W^{44+} increase in parallel until $Te = 3$ keV and decrease to the higher temperatures differently. This trend can explain the the line ratio behavior for temperature above 3 keV seen in top Fig. 3.28. The ratio can be approximated by a second-degree polynomial $0.01x^2 + 0.782x + 0.12$. To explore more in depth the dependence of the two line ratios with the temperature, the two Zn-2/Ga-3 and Zn-3/Zn-2 line ratios are plotted as a function of the electron temperature respectively in top and bottom Fig. 3.30. The comparison is made with the PECs for the two W^{44+} spectral lines, acquired from the OPEN-ADAS database [36]. A similar comparison is made of the other line ratio with the W^{43+} and W^{44+} fractional abundance ratio in the absence of PECs for the W^{43+} Ga-3 spectral line.

Two different behaviors are noticed for the two line ratios. The Zn-3/Zn-2 data distribution is consistent with the PEC ratio value, within 20-30%, with a similar trend as a function of T_e. However, we can notice that the behavior of the Zn-2/Ga-3 line ratio and of the fractional abundance ratio diverge with the increasing electron temperature. The main hypothesis to explain this difference would be the measurement

of one or more lines embedded in one of these two lines, which could lead to the distortion of their modelling. Nevertheless, no W line ratios appear to be usable to extract an electron temperature profile at this point. Future work on tungsten lines identification should help make progress in this direction, as well as improving the spectrum constraints and modelling.

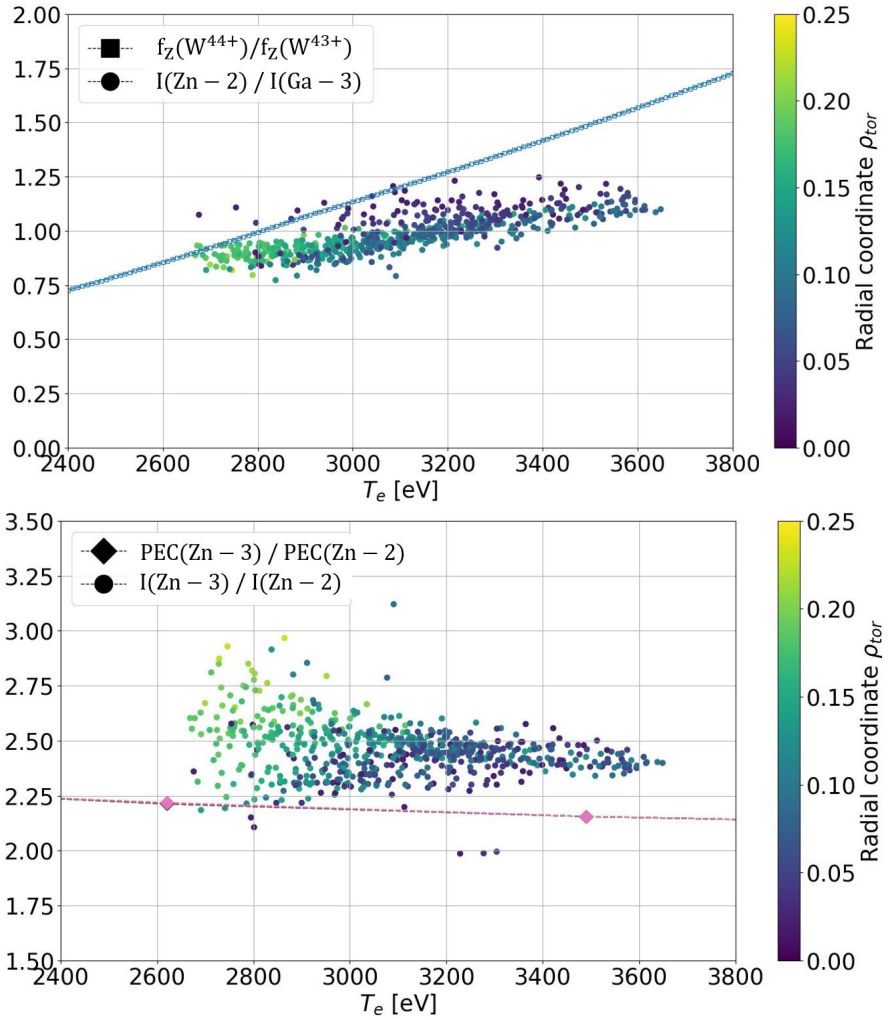

Figure 3.30. – *(Top) Ratios of the W^{43+} Ga-3 and W^{44+} Zn-2 line intensities and comparison with the associated fractional abundances ratio; (Bottom) Ratios of the W^{44+} Zn-2 and Zn-3 line intensities and comparison with the PEC ratio [37].*

3.3.5. Discussion on the role of the photon emission coefficients data

The treatment algorithm that we have introduced earlier is based on the use of PEC files for the estimation of the electron temperature from experimental line ratios.

The accuracy of the data used is thus fundamental for reliable computations and comparisons with other diagnostic measurements. The PEC data can be calculated using various atomic physics models, more or less adapted to the ions studied and therefore to the number of electrons. For example, the L-S coupling and intermediate-coupling models [112] should give similar results for simple ions such as Ar^{16+} (two electrons remaining), but the latter is better suited to more complex ions such as W^{44+} (thirty electrons remaining). A good knowledge of the codes thus allows a critical assessment of the data. In this thesis, we have mentioned two atomic physics databases from which we used so far some data: ADAS [113] and AtomDB [47]. It is not the point here to describe accurately what differentiate them but a comparison between those two data sources is a first step towards an uncertainty assessment.

Fig. 3.31 shows the comparison of the PECs for the He-like Ar resonance line w from AtomDB, ADAS and from [28]. Two different ADAS files are computed with the

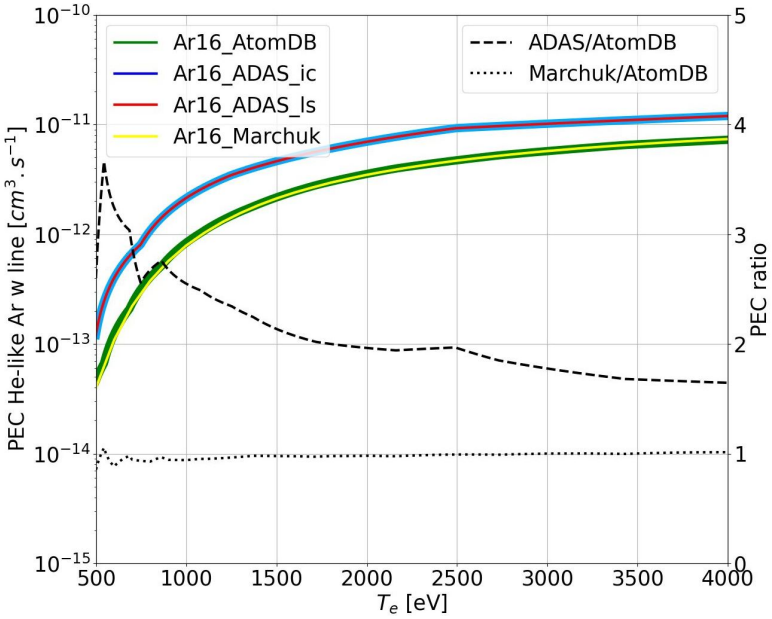

Figure 3.31. – *Comparison of the PECs of the He-like Ar resonance line w from (blue and red) two different OPEN-ADAS files, (green) AtomDB and (yellow) the work of Marchuk used at W7-X [28]. PEC ratios between each data source are also displayed in dashed and dotted black lines in the same temperature range.*

intermediate-coupling and L-S coupling schemes and give similar results, as expected for this case where only two electrons remain in this argon ion species. The L-S coupling is a method of applying perturbation theory to an electronic configuration in the central field approximation. For atoms with low Z number or strongly ionized ions such as the Ar^{16+} with two electrons remaining, the electrostatic interactions between the electrons are much stronger than the interaction between the spin of an electron and its own orbital motion. The coupling is thus preferentially between the orbital quantum numbers $\vec{L} = \sum_i \vec{l}_i$ on one side and spin $\vec{S} = \sum_i \vec{s}_i$ on the other,

notably due to the diagonalization of the perturbed Hamiltonian of the system, which commutes with the angular momentum operators. On the other hand, when the system becomes more complex, i.e. for larger Z or less ionized ions such as the W^{44+} with thirty electrons remaining, the spin-orbit interactions become more important and the coupling is preferentially between orbital and spin angular momenta, and the Hamiltonian commutes with $\vec{J} = \vec{L} + \vec{S}$. This gives us the "fine-structure levels" specified by the quantum number J, this is the j-j coupling. The intermediate-coupling is therefore required when the spin-orbit mixing of the levels is more important and all the momentum quantum numbers $\vec{L}, \vec{S}, \vec{J}, M_J$ are needed to resolve all the energy levels. Examples of matrix transformation from L-S coupling to intermediate-coupling model can be found in [114].

Here, Marchuk's $PEC_w(yellowline)atomicdatausedinFig.3.31, describedin[28]$, $havebeen Scouplingscheme.Thesamecouplingschemeisusedin theAUTOSTRUCTUREcode[[116]$, $likeionspecies.Thiscodealsocomputesatomicandionpropertiessuchasenergylevelsandato Scouplingandintermediate-couplingusingnon-orrelativisticwavefunctions.$

First, we see that, for an He-like ion species with only two electrons remaining, both ADAS datasets in L-S and intermediate-coupling give similar results, result expected since they are computed from the same atomic code. However, the ratio between L-S coupling data from ADAS and AtomDB shows a large difference at very low temperatures, up to a factor of 3.6, and decreases towards higher temperatures, whereas a ratio equal to 1 exists between data from AtomDB and Marchuk's thesis. This proves that even two different atomic physics codes using the same coupling scheme for the PEC of the Ar^{16+} resonance line can give different results. The choice of PECs is therefore more complex than simply selecting the right coupling scheme for the ion of interest.

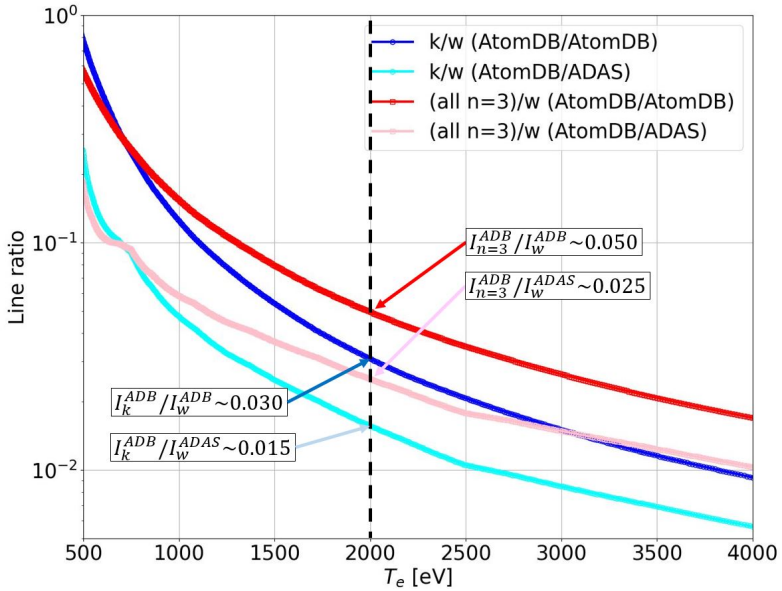

Figure 3.32. – *Comparisons of $(n = 3)/w$ and k/w line ratios as a function of the electron temperature from two different dataset sources.*

We can then study what the use of the different PEC datasets for the resonance line directly implies for theoretical line ratios in terms of electron temperature estimation. To do this, we can reuse Fig. 3.18, change the PEC of the w line and see how much the line ratio changes for the same temperature. The result is shown in Fig. 3.32 for the Li-like dielectronic satellite lines $n = 3$ and k from OPEN-ADAS. The w/k line ratios are plotted in blue and cyan and for the $w/(n = 3)$ line ratios in red and pink . For a $T_e = 2$ keV estimation for example, there is a factor of two of difference between the line ratios, in agreement with Fig. 3.31. The next step to complete this study should be to obtain complete PECs datasets from the ADAS database for all the Ar^{16+} lines useful for calculating the electron temperature. It appears important to check whether theoretical PEC ratios from different sources can give the same results, and if not, to try to explain these differences on the basis of the models and/or codes used. In conclusion, great care must be taken when using PEC data, and the user must be aware of the uncertainties they can generate, whether for the computation of the electron temperature from experimental line ratios or even for modelling spectra using atomic physics based forward models as in [119].

3.4. Experimental impurity density profiles

The identification and interpretation of the various W spectral lines performed in the previous Section do not allow yet to extract plasma parameter profiles as useful as the electron temperature profiles for example. However, a discussion has been made in Sect. 2.3.3 about the feasibility of a cross-calibration in brightness of the XICS instrument with the data of another WEST spectrometer. Indeed, we introduced the fact that a VUV spectrometer is already calibrated in brightness and is able to measure Ar and W spectral lines.

The aim of the Section is actually to perform this calibration transfer from one spectrometer to another. Such a procedure has already been performed, see [32], but between two spectrometers with the same spectral lines measured, i.e. same wavelengths. In Sect. 3.4.1, we will detail step by step the process performed by describing the spectral range measured by the VUV spectrometer and the spectral lines, or common impurity ionization stages, that we could use. Relationships for transferring this brightness calibration are presented, which will raise the question of the selection of similar lines of sight between the two diagnostics.

Once all these issues have been solved, a calibration transfer coefficient will be established, and the first impurity density profiles from XICS measurements will be presented.

3.4.1. Brightness calibration of the XICS spectrometer

3.4.1.1. WEST Extreme-UV spectrometer

One of the VUV spectrometers installed on WEST is called SIR [73]. The instrument is a high-resolution grazing incidence Schwob-Fraenkel [120] EUV spectrometer

mounted in the Rowland sphere configuration. It has two interchangeable concave gratings, one 600 grooves/mm grating which cover from 15 to 340 Å, the second 2400 grooves/mm to cover from 15 to 90 Å. The first has a spectral resolution of 0.18 Å at $\lambda = 25$ Å and 0.27 Å at $\lambda = 310$ Å, for a time resolution of 0.015 s.

Two operation modes can be used with this spectrometer: (i) a fixed mode where the line of sight crosses almost horizontally the plasma magnetic axis and (ii) an oscillating mode that scans the lower part of the plasma, from the magnetic axis to the lower divertor. These two spatial plasma coverages in the WEST poloidal cross-section

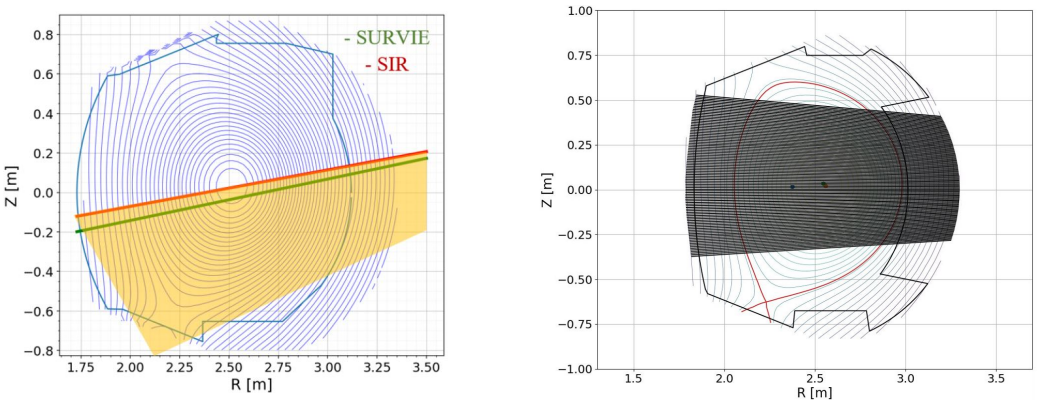

Figure 3.33. – *Left: Spatial coverage of the SIR diagnostic in the WEST poloidal cross-section. The fixed mode is represented in red and in yellow the area covered by the LOS in oscillating mode. Right: Spatial coverage by the XICS lines of sight already shown in Fig. 2.18.*

are illustrated in Fig. 3.33 (left) where the red line of sight corresponds to the fixed mode and the yellow area corresponds to the lines of sight available in the oscillating mode. The corresponding plasma coverage with the XICS instrument is shown for comparison in the right figure.

The SIR spectrometer is equipped with two mobile detectors. Each detector measure a narrow wavelength interval. The whole wavelength domain can be covered by moving the detectors between plasma discharges. In addition, an absolute brightness calibration has been performed with a Manson source [121] emitting Kα lines of six different elements in the lower part of the spectrometer domain ($\lambda \leq 113$Å), and a relative calibration has been performed above 113 Å using spectral line brightness ratios.

3.4.1.2. Identification of the W spectral lines

A typical SIR spectrum is shown in Fig. 3.34 where the identified tungsten lines are indicated. Four spectral lines from the W^{42+} to the W^{45+} ion species are measured in the [120, 160] Å spectral range and are referenced in Table. 3.2. They are all well spectrally resolved and intense enough to emerge from the background. The aim is to select one of these lines for the brightness calibration transfer but the choice is highly

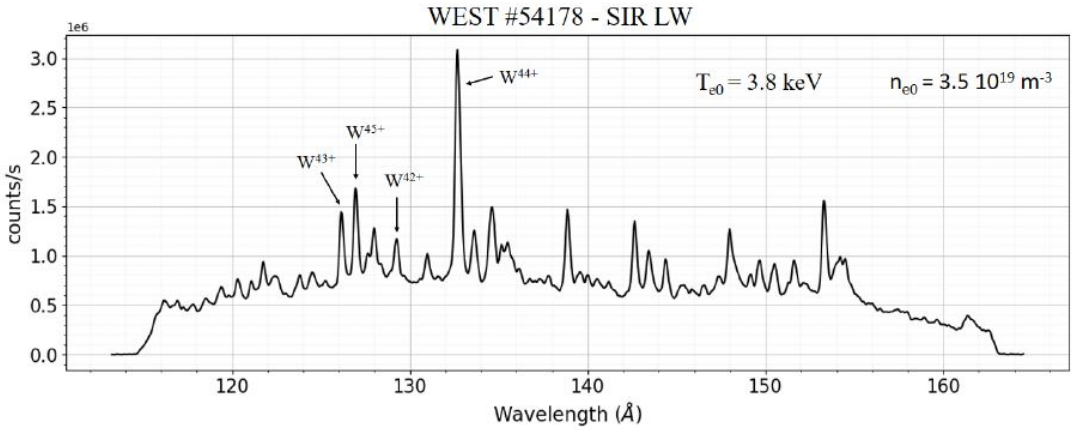

Figure 3.34. – *SIR spectrum from WEST #54178 plasma discharge with four W spectral lines marked with black arrows [32].*

Diagnostic	Ion	Transition	λ (Å)	Ref.
SIR	W^{42+}	$4s^2\ 4p^2\ ^3P_0$ - $4s^2\ 4p^2\ ^1D_2$	129.2	[32], [122]
	W^{43+}	$4s^2\ 4p\ ^2P_{1/2}$ - $4s^2\ 4p\ ^2P_{3/2}$	126.1	[32], [122]
	W^{44+}	$4s^2\ ^1S_0$ - $4s\ 4p\ ^3P_1$	132.6	[32], [122]
	W^{45+}	$4s\ ^2S_{1/2}$ - $4p\ ^2P_{1/2}$	126.8	[32], [122]
XICS	W^{43+}	$3d^{10}4p\ ^2P_{1/2}$ - $3d^9 4p6f\ ^2D_{3/2}$	3.963	[74], [75]
	W^{44+}	$3p^6 4s^2\ ^1S_0$ - $3p^5 4s^2 5d\ ^1P_1$	3.975	[74], [75]
	W^{44+}	$3d^{10}4s^2\ ^1S_0$ - $3d^9 4s^2 6f\ ^1P_1$	3.988	[74], [75]

Table 3.2. – *Theoretical transitions and wavelengths of the W spectral lines measured with the SIR and the XICS diagnostics.*

restricted by the acquisition of the corresponding PEC files and the saturation of the SIR signal as we will soon see.

About those measured in the Ar XVII spectrum shown in Fig. 3.25, three W spectral lines are spectrally resolved enough from the neighbouring lines, the W^{43+} Ga-3 and W^{44+} (Zn-2, Zn-3) referenced in Table 3.2. The W^{44+} Zn-2 spectral line appears to be the most promising candidate since it is the best spectrally resolved of the three, although not the most intense. In this case, the W^{44+} Zn-3 line is the most intense but it is much too close spectrally to the Ar^{15+} dielectronic satellite *k* line. In addition, no PEC file is available for the W^{43+} Ga-3 spectral line so it reduces our field of action to the study of the W^{44+} Zn-2 spectral line.

3.4.1.3. Brightness equivalence between two lines from the same ion species

Introduced in Sect. 1.3.5, the brightness of a line is a function of the corresponding line emissivity and thus depends on the electron density n_e, the impurity density n_Z, the fractional abundance of the ionization stage $f_{Z,z}(T_e)$ and the PEC $PEC(n_e, T_e)$.

The brightness is defined as the integration of the line emissivity along the line of sight:

$$\begin{aligned} B(\lambda_{ij}) &= \frac{1}{4\pi}\int \epsilon(\lambda_{ij}, l)dl \\ &= \frac{1}{4\pi}\int n_e(l)\times n_Z(l)\times f_{Z,z}(T_e(l))\times PEC_{ij}(, n_e(l), T_e(l))dl \qquad [\text{photons.s}^{-1}\,\text{m}^{-2}\,\text{sr}^{-1}] \end{aligned} \tag{3.10}$$

where $\epsilon_Z(\lambda_{ij}, l)$ is the emissivity of a spectral line of wavelength λ_{ij} for the l line of sight defined in Eq. 1.65 expressed in [photon.s^{-1}.m^{-3}].

We can express the brightness emitted by the same ion of the two diagnostics for spectral lines:

$$B^{SIR}(\lambda^{SIR}) = \frac{1}{4\pi}\int_{SIR} n_e n_W f_{W,44+}(T_e) PEC_{SIR}(n_e, T_e)dl \tag{3.11}$$

$$B^{XICS}(\lambda^{XICS}_{Zn-2}) = \frac{1}{4\pi}\int_{XICS} n_e n_W f_{W,44+}(T_e) PEC_{XICS}(n_e, T_e)dl \tag{3.12}$$

where n_e and n_W are respectively the electron and W densities, $f_{W,44+}(T_e)$ is the fractional abundance of the W^{44+} and $PEC_i(n_e, T_e)$ is the PEC corresponding to the spectral line studied for each spectrometers. If we compare the two brightness measurements for the same line of sight ($dl^{SIR} = dl^{XICS} = dl$) at the same time and so for the same plasma conditions (same T_e, n_e and n_W) and for two different wavelengths of the same ionization stage, we can express the brightness ratio as:

$$\begin{aligned} \frac{B^{SIR}(\lambda^{SIR})}{B^{XICS}(\lambda^{XICS}_{Zn-2})} &= \frac{\int_{SIR} n_e n_W f_{W,44+}(T_e) PEC_{SIR}(n_e, T_e)dl_{SIR}}{\int_{XICS} n_e n_W f_{W,44+}(T_e) PEC_{XICS}(n_e, T_e)dl_{XICS}} \\ &= \frac{\alpha^{SIR}\int_{SIR} n_e n_W f_{W,44+}(T_e) pec(n_e, T_e)dl_{SIR}}{\alpha^{XICS}\int_{XICS} n_e n_W f_{W,44+}(T_e) pec(n_e, T_e)dl_{XICS}} \end{aligned} \tag{3.13}$$

where PEC_{SIR} and PEC, assumed to have the same dependence on T_e and n_e, are described as the product of a constant characteristic of the transition with a reduced single function of T_e and n_e:

$$PEC_i(n_e, T_e) = \alpha^i \times pec(n_e, T_e) \tag{3.14}$$

This assumption will be treated immediately after the finalization of the calibration coefficient expression. Both integrals contain the same information related to the electron n_e and ion n_W density, temperature T_e, fractional abundance $f_{W,44+}(T_e)$ and reduced PEC $pec(n_e, T_e)$ if the lines of sight are equivalent:

$$\frac{B^{SIR}(\lambda^{SIR})}{B^{XICS}(\lambda^{XICS}_{Zn-2})} = \frac{\alpha^{SIR}\int_l n_e n_W f_{W,44+}(T_e) pec(n_e, T_e)dl}{\alpha^{XICS}\int_l n_e n_W f_{W,44+}(T_e) pec(n_e, T_e)dl} \tag{3.15}$$

Thus, the brightness ratio becomes:

$$\frac{B^{SIR}(\lambda^{SIR})}{B^{XICS}(\lambda^{XICS}_{Zn-2})} = \frac{\alpha^{SIR}}{\alpha^{XICS}} \tag{3.16}$$

In parallel, the brightness of a line is related to the measured photon count per time unit as follows:

$$B^i(\lambda^i) = \kappa^i(\lambda^i) \times N^i(\lambda^i) \tag{3.17}$$

where N^i is the photon count per time unit of the i diagnostic for the λ^i wavelength and κ^i is the brightness calibration coefficient, which has the following units:

$$\kappa^i(\lambda^i) \equiv \frac{photon}{s.m^2.sr}\frac{s}{count} \tag{3.18}$$

Inserting Eq. 3.17 in Eq. 3.16, the brightness ratio becomes:

$$\frac{B^{SIR}(\lambda^{SIR})}{B^{XICS}(\lambda^{XICS}_{Zn-2})} = \frac{\alpha^{SIR}}{\alpha^{XICS}} = \frac{\kappa^{SIR}(\lambda^{SIR}) \times N^{SIR}(\lambda^{SIR})}{\kappa^{XICS}(\lambda^{XICS}_{Zn-2}) \times N^{XICS}(\lambda^{XICS}_{Zn-2})} \tag{3.19}$$

Finally, the calibration coefficient can be expressed as:

$$\kappa^{XICS}(\lambda^{XICS}_{Zn-2}) = \frac{B^{SIR}(\lambda^{SIR})}{N^{XICS}(\lambda^{XICS}_{Zn-2})} \times \frac{\alpha^{XICS}}{\alpha^{SIR}} \tag{3.20}$$

As the brightness calibration of the SIR diagnostic has already been performed, all that remains is to compute the calibration coefficient κ^{XICS}. Before doing this, let us check the assumption on the PEC dependence on T_e and n_e. Fig. 3.35 shows the PECs for both transitions, the SIR one in red and the XICS one in blue, for a temperature range [1 - 6] keV deduced from the fractional abundance of the W^{44+} ion species in Fig. 3.29.

From Fig. 3.35, different temperature dependences are noticed and the ratio between them decreases over a wide temperature range, with a higher slope coefficient for the lowest temperatures. As we cannot extract easily a common factor, we need thus to find another way to reduce the PECs. For this ionization stage, we can extract from Fig. 3.29 a maximum abundance $f_{Z,max}$ and the temperature $T_{Z,max}$ at which the maximum is reached. Thus, a temperature range over which the ionization stage is dominant is determined, for $f_Z \geq f_{Z,max}/2$, as shown in Fig. 3.36. This temperature range is shown in blue in Fig. 3.35 where the temperature range corresponding to the temperatures of the WEST #59920 plasma discharge is also coloured in yellow. The comparison between the PECs must thus be done at the intersection of these temperature ranges, between 3 and 3.8 keV. We can thus perform a weighted integration of the PEC ratio with the electron temperature, which is more accurate than take a mean

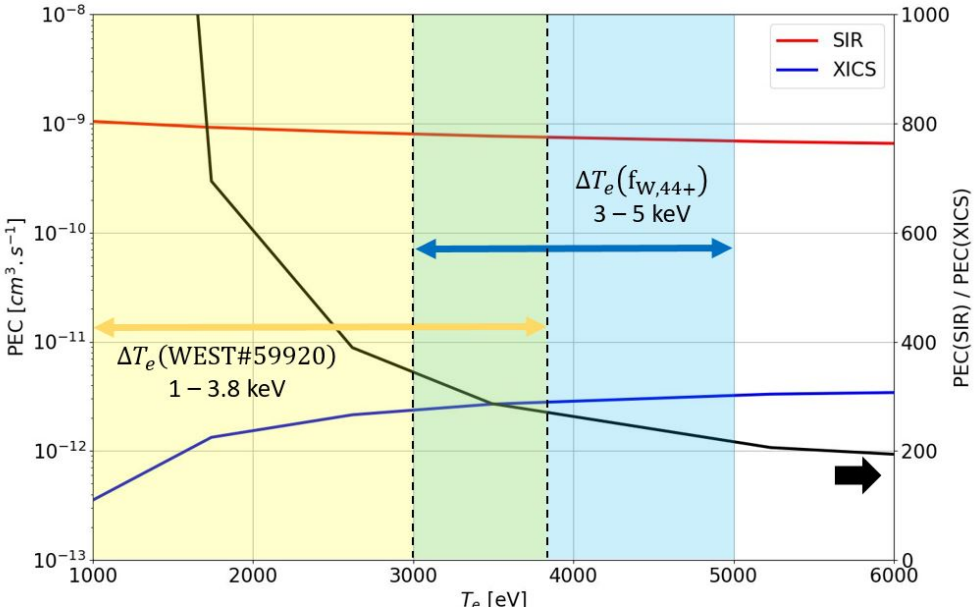

Figure 3.35. – *PECs for the XICS W^{44+} Zn-2 spectral line at $\lambda = 3.971$Å (blue) and the SIR spectral line at $\lambda = 132.273$Å (red), at $n_e = 4 \times 10^{19}$ m^{-3}; The ratio of the PECs is also shown in black with the secondary y-axis. Two temperature areas are coloured: in yellow the temperature range corresponding to the WEST 9920 plasma discharge used for the cross-calibration and in blue the temperature range over which the W^{44+} ionization stage is dominant.*

value of the ratio between the temperature range selected. It can be computed as:

$$\beta = \frac{\int T_e \times \frac{PEC_{SIR}}{PEC_{XICS}} dl}{\int T_e dl} \approx 301 \tag{3.21}$$

where we take a typical line of sight length of 1 m. The ratio between the PECs α^i constants expressed in Eq. 3.16 thus take the following averaged value:

$$\frac{\alpha^{XICS}}{\alpha^{SIR}} \approx 3.3 \times 10^{-3} \tag{3.22}$$

3.4.1.4. Line of sight selection criteria

In Sect. 3.4.1.1, we introduced the spatial coverage of the SIR diagnostic in the WEST poloidal cross-section. The SIR lines of sight cover all the lower part of the vacuum vessel, from the plasma center to the lower divertor, when it is operated in the oscillating mode. This mode allows to obtain a large number of integrated brightness points to compare with the XICS lines of sight that cover the same plasma area. Indeed, as shown in Fig. 3.33, the XICS lines of sight cover a large part of the central plasma region with a lower angle to the axis Z=0. The diagnostic geometries are

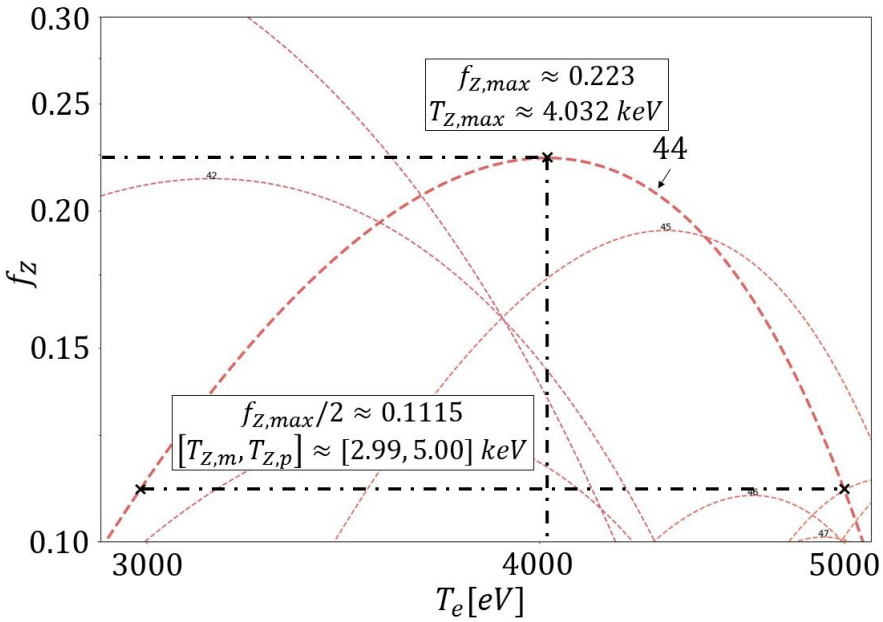

Figure 3.36. – *Fractional abundance of the W^{44+} ionization stage where are indicated the maximum abundance $f_{Z,max}$ and the temperature associated $T_{Z,max}$.*

thus sufficiently different that finding an identical line of sight with both spectrometers is not straightforward.

Fig. 3.37 shows the intensity of the XICS W^{44+} Zn-2 spectral line as a function of time and radial coordinate. A part of the measurement between $\rho_{tor} = [-0.03, -0.3]$ is missing because of two defective modules of the detector, see Sect. 2.3.4. The Bremsstrahlung background has been subtracted. The W^{44+} Zn-2 spectral line emission is measured between t = [5, 22] s when the electron temperature is high enough to allow this ionization stage to exist. Due to the missing signal, the XICS line of sight must then be selected between $\rho_{tor} = [0, 0.3]$ where a maximum intensity is measured at $\rho_{tor} = -0.02$.

Concerning the SIR measurement, Fig. 3.38 shows the W^{44+} line brightness as a function of the line of sight angles. The W^{44+} line chosen for the calibration transfer is so strong that it saturates in lines of sight close to the plasma center, for angles between 10° and 14°. The corresponding lines of sight are represented on the left Fig. 3.38. The three lines cover a wide area of the plasma, from the center to the lower divertor. The brightness saturation corresponds to the very center of the plasma, between $\rho_{tor} = [0, 0.2]$, where the W^{44+} ion species exists in majority. Extraction of SIR data in this range is thus impossible so we must then aim for more eccentric lines of sight and particularly between 14°, where the SIR brightness measurement is not saturated and non-zero, and 23° for the closest line of sight to the lower divertor. The restricted radial range where the SIR brightness measurement is usable is thus for $\rho_{tor} = [0.2, 0.3]$.

The quantities on which brightness depends are n_e and T_e. We must therefore look for lines of sight on which the profiles of n_e and T_e are identical for the two

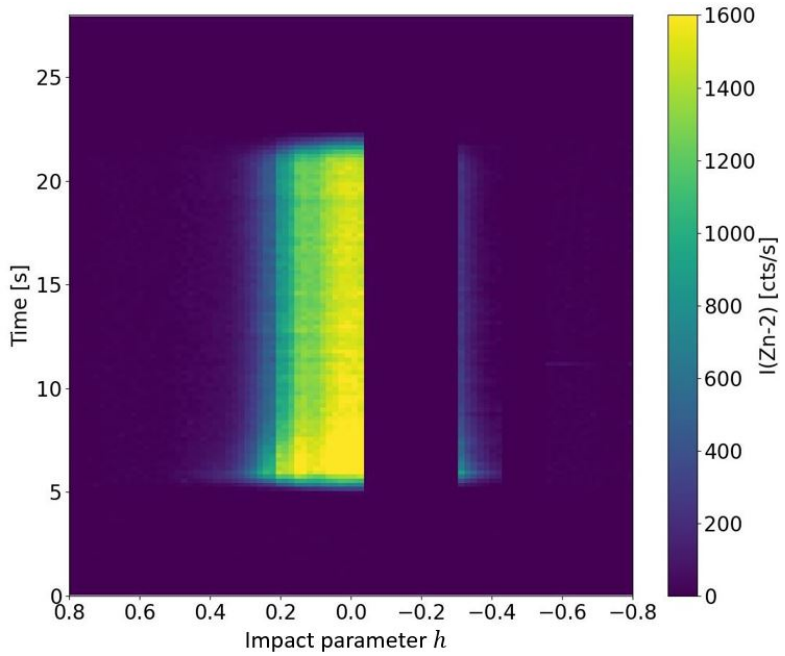

Figure 3.37. – *Intensity of the W^{44+} Zn-2 spectral line as a function of time and radial coordinate.*

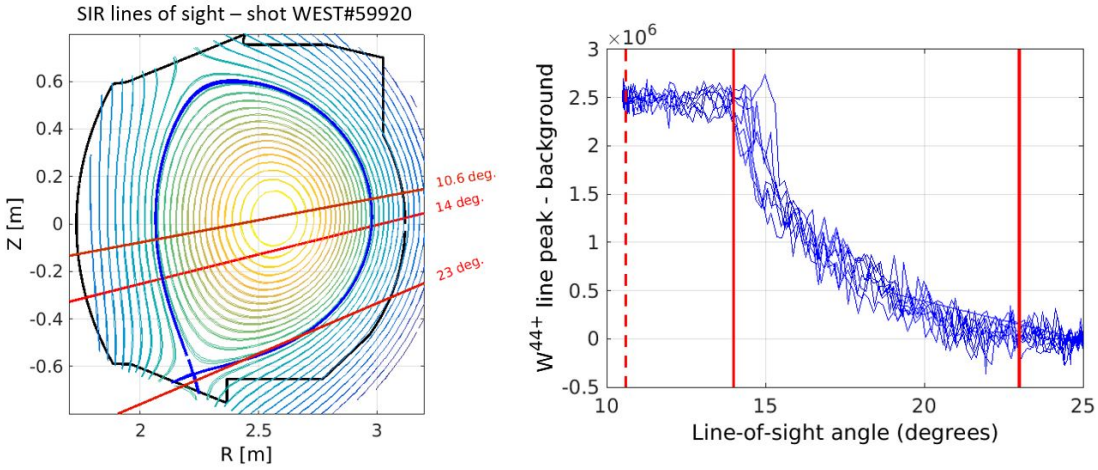

Figure 3.38. – *Intensity of the W^{44+} spectral line measured with the SIR spectrometer as a function of the radial coordinate.*

spectrometers, or at least homothetic. The plasma is discretised by concentric nested rings representing magnetic surfaces around a magnetic axis.

The magnetic equilibrium of the plasma is used to compute the points of intersection of each line of sight with all magnetic surfaces as a function of the total length of the line. Examples of a magnetic equilibrium are shown in Fig. 3.33 with the iso-contours plotted in the WEST poloidal cross-section. Each ring has an associated ρ_{tor} value, which we use to discretise the temperature and density values on the same

rings. The lines of sight cross a multitude of field surfaces and for each of them we can determine which ρ_{tor} values are crossed for each element of a line and the distance between each surface.

The comparison of the lines of sight of the two diagnostics can now be done in this range with this method. As the two diagnostic geometries are different, we propose to compare the lines of sight with the magnetic surfaces they cross along their path in the vacuum vessel. Fig. 3.39 shows the radial coordinates crossed by the hundred LOS of the XICS instrument. The XICS configuration, with a detector position not

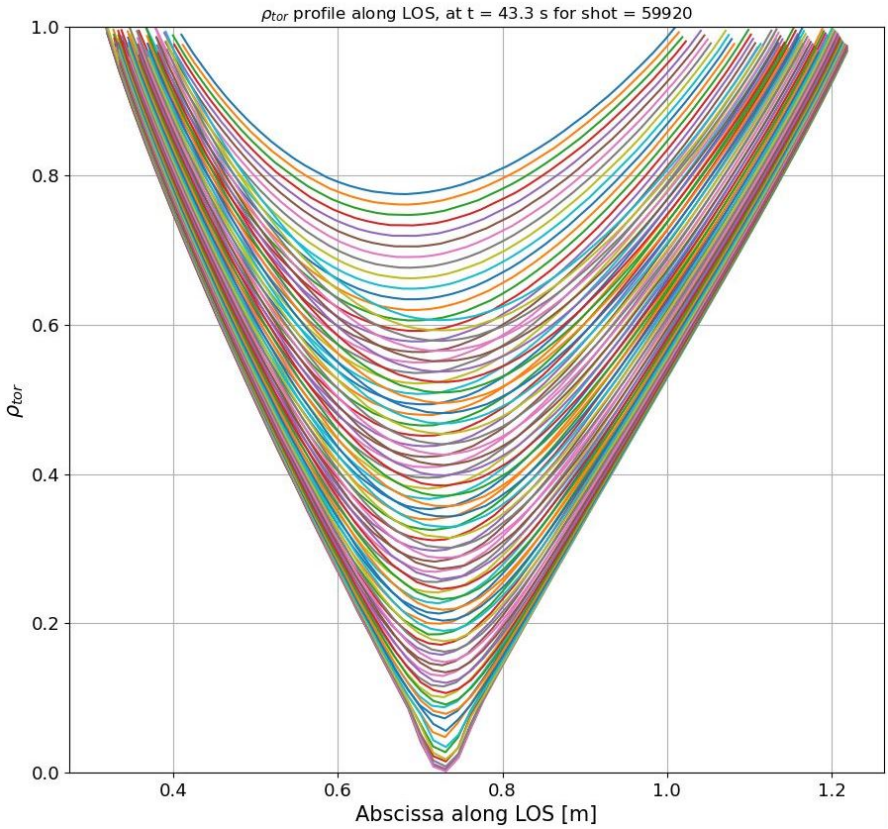

Figure 3.39. – *Magnetic surfaces crossed by the hundred XICS LOS as a function of their length.*

perfectly aligned with the Z axis, induces the non-symmetrical shape of the curves from the point of lower ρ_{tor} crossed. The lines of sight closest to the magnetic axis have a pointed shape around the minimum ρ_{tor} due to the shorter path travelled between successive magnetic surfaces. This method can be used to compare lines of sight belonging to instruments with different geometries.

The SIR lines of sight available are thus selected for $\rho_{tor,min} > 0.2$ where the SIR signal is not saturated. The most similar XICS lines are displayed in Fig. 3.40 where top Fig. 3.40 shows the comparison of the profiles of neighbouring magnetic surfaces crossed and the bottom one the distance travelled between the magnetic surfaces for each selected line.

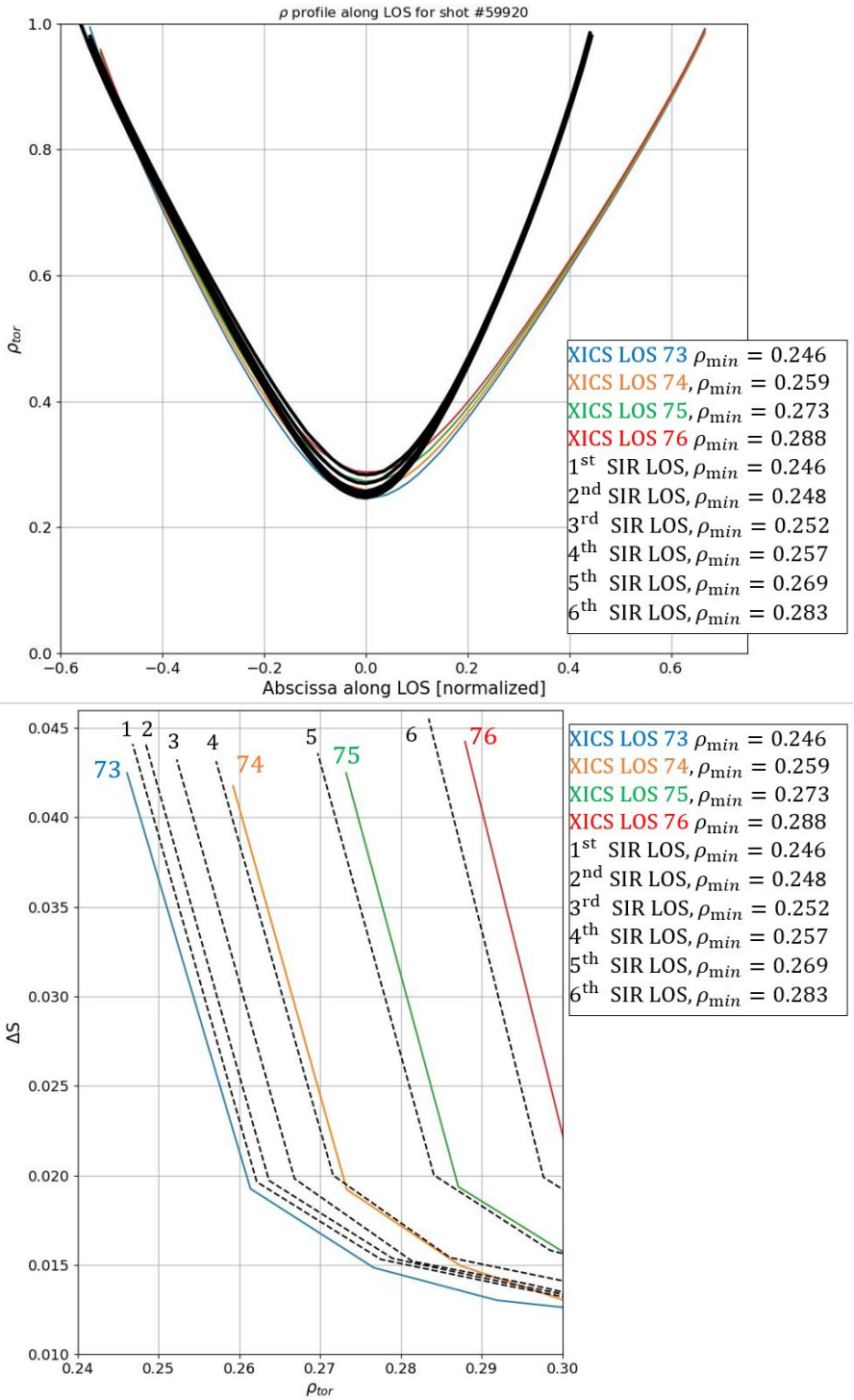

Figure 3.40. – *Top: Comparison between the SIR LOS for $\rho_{tor,min} = 0.25$ and the closest XICS LOS; Bottom: distance travelled between the various magnetic surfaces by the selected LOS.*

However, this study is not sufficient to be able to decide on the similarity of the lines compared and whether or not it is necessary to include a geometric factor between the two. Calculation of the distance ΔS crossed by each line of sight between neighbouring surfaces enables comparable lines to be associated, as shown in Fig. 3.40 (bottom). Several XICS lines are selected to be the closest to the SIR lines of sight for $\rho_{tor,min} = [0.246, 0.259, 0.273, 0.288]$. Each SIR line can be associated with another XICS line with a very similar ΔS profile. No need of geometrical compensation is thus needed between these lines of sight, at least in the poloidal cross-section. The geometrical coverage of the SIR instrument make a zero angle of their lines of sight with the magnetic axis where those of the XICS instrument make an angle $\bar{\xi} \approx 38° \approx 0.663$ radians. From the approximation that the SIR and XICS lines of sight in the toroidal cross-section form a right-angle triangle, we find $sin(\xi) = l^{SIR}/l^{XICS}$. Eq. 3.20 is thus updated adding the $sin(\xi)$ term in the expression of the SIR brightness. Eq. 3.16 takes the sine term in the numerator and finally the expression of the XICS brightness calibration constant Eq. 3.20 becomes:

$$\kappa^{XICS}(\lambda^{XICS}_{Zn-2}) = \frac{B^{SIR}(\lambda^{SIR}_{Zn-2})}{N(\lambda^{XICS}_{Zn-2})} \times \frac{\alpha^{XICS}}{\alpha^{SIR}} \times sin(\xi) \tag{3.23}$$

3.4.1.5. Cross-calibration from the SIR to the XICS diagnostic

To perform the cross-calibration of the XICS diagnostic with the brightness measurement of the SIR diagnostic, we investigate the WEST #59920 plasma discharge which has been studied in the Sect. 3.3. During this pulse, the SIR diagnostic was in oscillating mode, that allows to probe the lower part of the plasma and to get similar lines of sight with the XICS ones. We choose a time interval between t = [9, 20] s when a plateau of T_e and n_e is reached. The SIR brightness measurement is selected for the time acquisitions shown in Fig. 3.41 (top). The corresponding XICS LOS-integrated intensities of the W^{44+} Zn-2 spectral line are shown in the middle sub-figure and the corresponding ρ_{tor} coordinate on the bottom sub-figure. To compute the variable B^{SIR}/N^{XICS} in Eq. 3.23, the mean value of the ratio between the SIR brightness and the XICS intensity is made to obtain:

$$\overline{\frac{B^{SIR}(\lambda^{SIR}_{Zn-2})}{N^{XICS}(\lambda^{XICS}_{Zn-2})}} \approx 2.725 \times 10^{16} \frac{photon}{s.m^2.sr} \frac{s}{count} \tag{3.24}$$

The constant for the brightness calibration of the XICS diagnostic becomes:

$$\bar{\kappa}^{XICS} = \overline{\frac{B^{SIR}}{N^{XICS}}} \times \frac{\alpha^{XICS}}{\alpha^{SIR}} \times sin(\bar{\xi}) \tag{3.25}$$

$$\bar{\kappa}^{XICS} \approx 5.535 \times 10^{13} \frac{photon}{s.m^2.sr} \frac{s}{count} \tag{3.26}$$

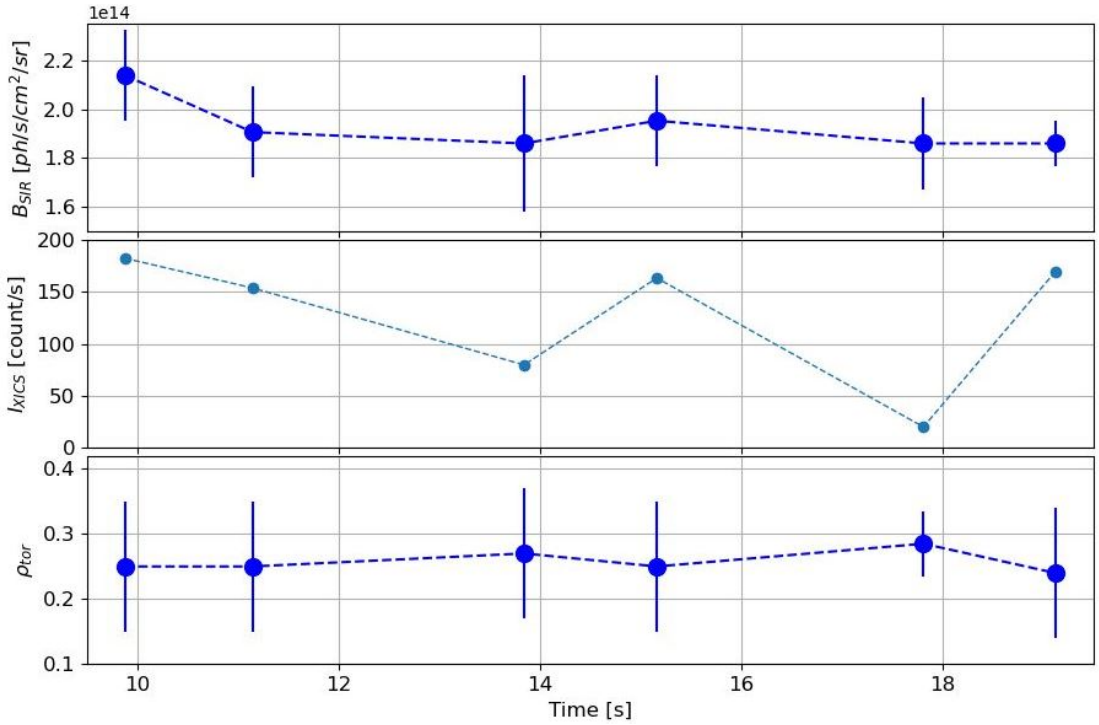

Figure 3.41. – *Top: brightness measurement (in photons.cm^{-2}s^{-1} sr^{-1}) of the SIR W^{44+} spectral line for multiple time acquisitions of the WEST #59920 pulse and associated XICS LOS-integrated intensity (in counts.s^{-1}) of the Zn-2 spectral line (middle) for the radial coordinate ρ_{tor} associated (bottom).*

3.4.2. Mid- and high-Z impurity profiles

3.4.2.1. Line-averaged density and concentration computation

The XICS diagnostic measures line emissions of various ionization stages integrated along the lines of sight. The brightness, already defined in Eq. 3.12, is proportional to the integral of the line emissivity along a line of sight:

$$B(\lambda) = \frac{1}{4\pi}\int n_e(l) n_Z(l) f_{Z,z}(T_e(l)) PEC(n_e(l), T_e(l)) dl \tag{3.27}$$

To extract the impurity density information out of the brightness, we need to retrieve integrated measurements of temperature and electron density, as well as PEC and fractional abundances for the studied ionization stage. Based on the calculation of the magnetic surfaces crossed by the XICS lines of sight, presented in Fig. 3.39, interpolation is performed to obtain the n_e, T_e, $f_{W,44+}$ and PEC profiles along the XICS lines of sight. The electron density and temperature profiles are deduced from interferometry [123] and ECE radiometer measurements. Fig. 3.42 shows the n_e, T_e, $f_{W,44+}$ and $PEC_{\lambda_{Zn-2)}}$ profiles along the XICS LOS which corresponds to $h = 0$. Profiles are plotted as a function of the line longitudinal and ρ_{tor} coordinates. The electron density and temperature reach high values at the plasma center, that allows

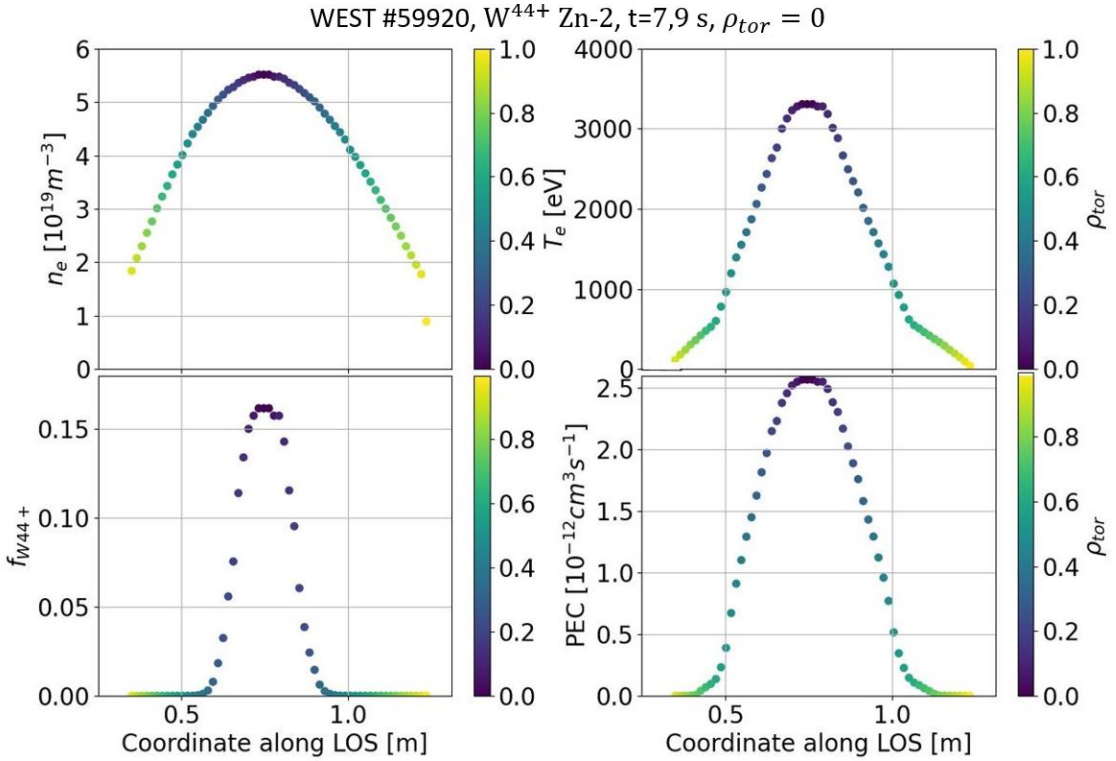

Figure 3.42. – *$n_e, T_e, f_{W,44+}$ and PEC_{Zn-2} profiles along the XICS LOS corresponding to $\rho_{tor,min} = 0.0$, as a function of the coordinate along the LOS and ρ_{tor}.*

to the W^{44+} to exist with a maximum fractional abundance of $f_{W,44+} \approx 0.16$. Note that the electron temperature profile is interpolated from the ECE measurements from $\rho_{tor} \approx 0.5$ to $\rho_{tor} = 1$, leading to this sudden break in slope. The W^{44+} fractional abundance and associated PEC profiles are interpolated from the temperature along the line.

The triple factor, as defined as the product between n_e, $f_{W,44+}$, PEC is computed and displayed in Fig. 3.43 for the four lines of sight used for the brightness calibration transfer. Here, the fractional abundance dominates the shape of the triple factor. The amplitude of the triple factor decreases by a factor 2.3 to the more eccentric line, which is in agreement with the lowest temperature found moving away from the center. The quantity is well defined within a narrow radial range $\rho_{tor} \leq 0.3$ and outside of which it can be approximated to zero.

Generally, and speaking of W impurity, the dependence of the photon emission coefficient is small for tokamak plasmas, which makes it only dependent on the electron temperature T_e. Thus, an approximation can be made over a restricted radial region of impurity emission in the plasma, in agreement with Fig. 3.43 where the triple factor can be considered constant for $\rho_{tor} \leq 0.3$. This approximation is generally valid for the W ion species, due to the large electron temperature at the very central area of the plasma $T_e \geq 2.2$ keV for $\rho_{tor} \leq 0.3$ as shown in Fig. 3.42. A line-averaged

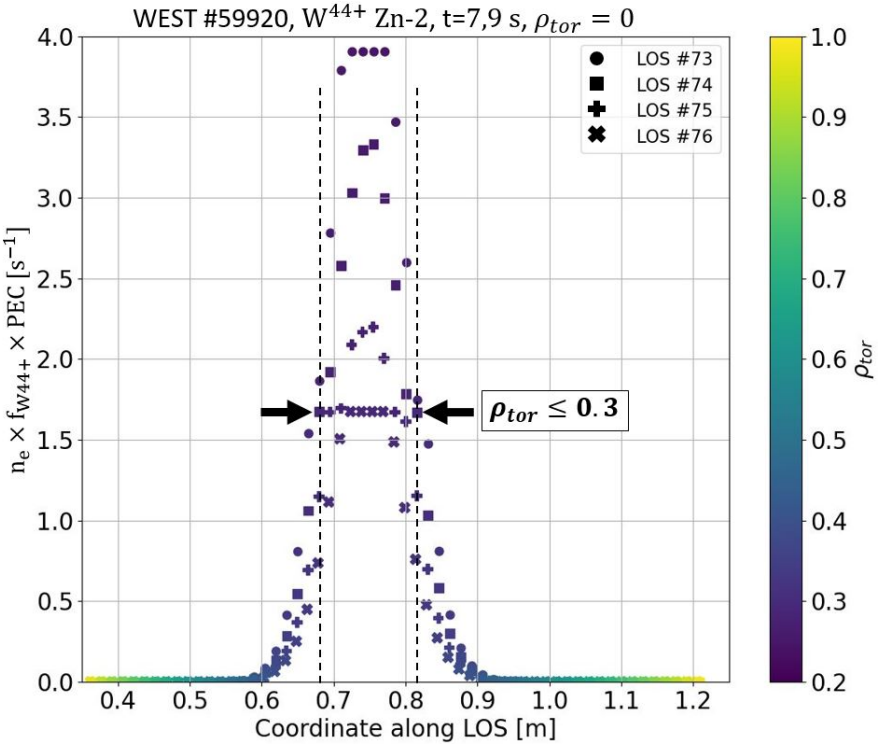

Figure 3.43. – *Triple factor $n_e \times f_{W,44+} \times PEC_{\lambda_{Zn-2}}$ profiles for the W^{44+} Zn-2 spectral line along the four XICS LOS presented in Fig. 3.40 as a function of the coordinate along the lines and ρ_{tor}.*

impurity density $\overline{n}_W$ is then extracted from the integral of the brightness:

$$B(\lambda) = \frac{1}{4\pi}\overline{n}_Z \int n_e(l) f_{Z,z}(T_e(l)) PEC(n_e(l), T_e(l)) dl \tag{3.28}$$

With the brightness calibration coefficient computed in the previous Section, an estimation of the line-averaged impurity density $\overline{n}_Z$ within the narrow range of ρ_{tor} can thus be obtained:

$$\overline{n}_Z = \frac{4\pi B(\lambda)}{\int n_e(l) f_{Z,z}(T_e(l)) PEC(n_e(l), T_e(l)) dl} \tag{3.29}$$

Concerning the Ar impurity, the triple factor that corresponds to the He-like Ar resonance line w is shown in Fig. 3.44. In comparison with the W^{44+} Zn-2 triple factor, the emission is defined within a larger radial range of $\rho_{tor} \leq 0.5$. The amplitude is a factor of twenty greater and fewer differences in the centre of the plasma between the lines of sight are noticed. On the other hand, a hole is formed for the most central region, corresponding to the shape of the $f_{Ar,16+}$ profile as shown in Fig. 3.45. The Ar^{16+} fractional abundance curve in Fig. 1.12 has its maximum below 1 keV and decreases quickly to 0.1 at 3.5 keV. For this time acquisition of this plasma discharges with $T_{e,max} = 3.3$ keV, this ionization stage then exists only to a very limited extent in

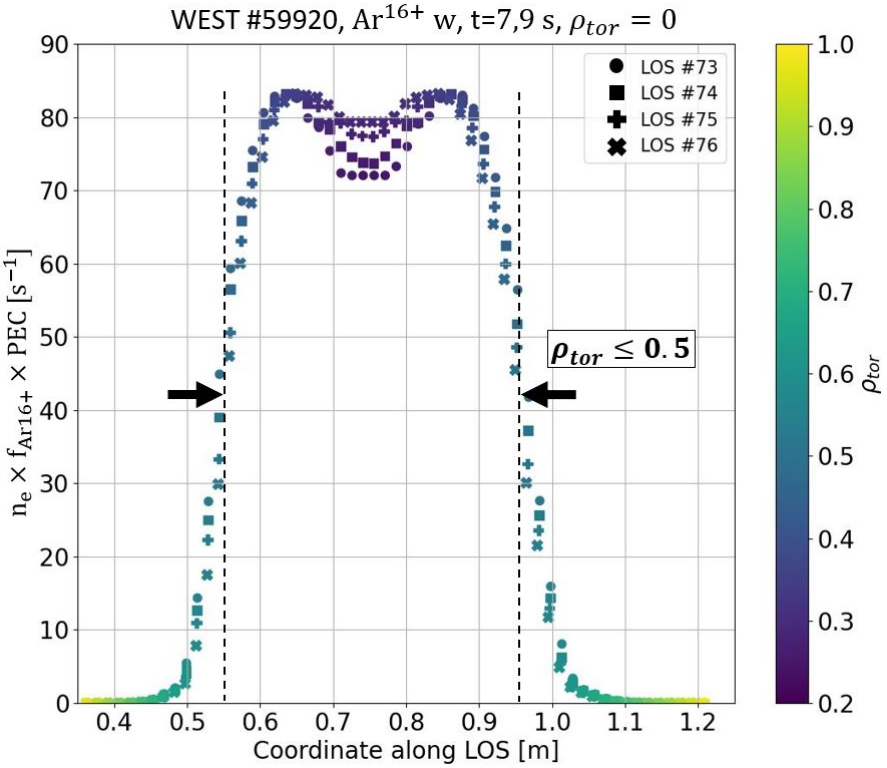

Figure 3.44. – *Triple factor $n_e \times f_{Ar,16+} \times PEC_w$ profiles for the Ar^{16+} w spectral line along the four XICS LOS presented in Fig. 3.40 as a function of the coordinate along the lines and ρ_{tor}.*

the most central region of the plasma and is the most abundant for $\rho_{tor} \approx 0.5 - 0.6$. However, the approximation made for the W^{44+} as emitting constantly over a narrow radial ρ_{tor} range can also be made for the Ar^{16+} for $\rho_{tor} \leq 0.5$. The resulting line-averaged impurity density $\overline{n}_{\mathrm{Ar}}$ is thus only valid for this radial range.

The averaged impurity concentration $\overline{c}_Z$ is obtained by dividing the averaged impurity density $\overline{n}_Z$ by the line-averaged electron density $\overline{n}_e$ for the radial area of impurity emission:

$$\overline{c}_Z = \frac{\overline{n}_Z}{\overline{n}_e} \tag{3.30}$$

where $\overline{n}_e$ is obtained from the integration of the profile along the line of sight l and divided by the total length L of the line:

$$\overline{n}_e = \frac{\int dl \times n_e(l)}{L} \tag{3.31}$$

However, the integration length of the electron density along the line of sight must be taken into account. The electron density varies between $n_e = 5.5 \times 10^{19} \mathrm{m}^{-3}$ for $\rho_{tor} = 0$ and $n_e = 0.9 \times 10^{19} \mathrm{m}^{-3}$ for $\rho_{tor} = 1$ with a stronger gradient for $\rho_{tor} \geq 0.5$.

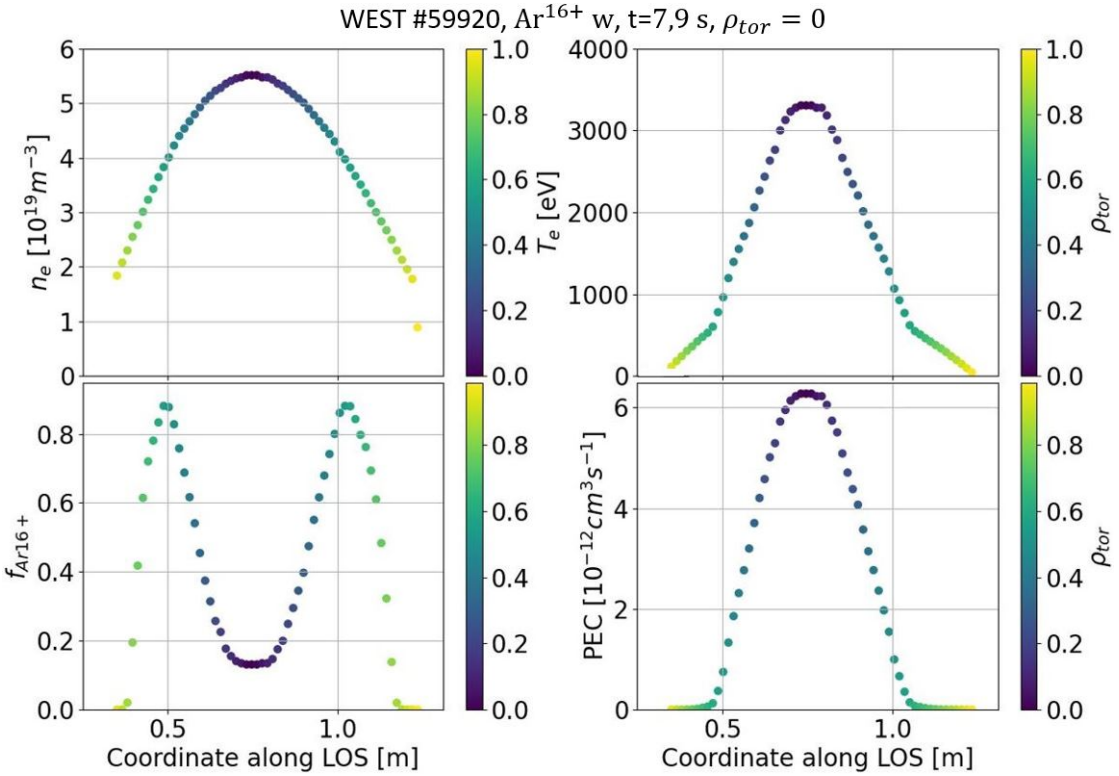

Figure 3.45. – $n_e, T_e, f_{Ar,16+}$ *and* PEC_w *profiles along the XICS LOS corresponding to* $\rho_{tor,min} = 0$*, as a function of the coordinate along the LOS and* ρ_{tor}*.*

The length of integration is taken for the W case for $\rho_{tor} \leq 0.3$ and for the W case for $\rho_{tor} \leq 0.5$. The resulting density profile then represents the respective emission zones defined above.

3.4.2.2. Tungsten and argon density and concentration

In the previous Section, the method used to transfer the brightness calibration from a VUV spectrometer to the XICS diagnostic has been detailed, allowing to measure brightness of mid- and high-Z impurities (argon and tungsten respectively). Hence, experimental data about the line-averaged density and concentration profiles of argon and tungsten can be studied.

Here, we propose to study the time variations of these quantities for two pulses. The first WEST #59920 plasma discharge is the one used to study the electron temperature profiles in the previous Chapter and for the transfer of the brightness calibration here. The second WEST #59667 is related to a radiative collapse of the plasma which is due to Ar accumulation in the plasma core.

The densities and concentrations for the WEST #59920 plasma discharge are shown in Fig. 3.46. About 4.2 MW of LHCD are delivered to the plasma between 5 seconds and 22 seconds, to reach an electron temperature of 3.1 keV and an electron density of $5 \times 10^{19} \mathrm{m}^{-3}$. For these temperatures, we expect to measure the W^{44+} spectral lines

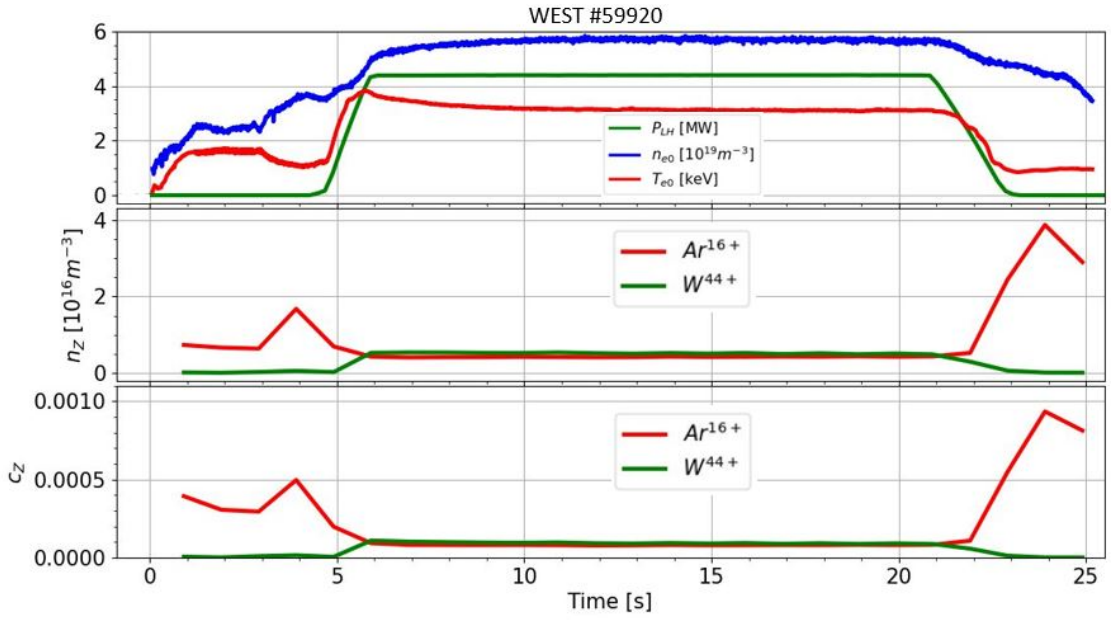

Figure 3.46. – *Temporal evolution of the line-averaged densities and concentrations of Ar^{16+} and W^{44+} for the WEST #59920 plasma discharge.*

at high intensities and this is validated by the line-averaged density time variation shown in green. At 6 seconds, stationary levels of $\overline{n}_{W,44+}$ and $\overline{c}_{W,44+}$ are found about $5.3 \times 10^{15} m^{-3}$ and 0.9×10^{-5} respectively, which is consistent with the results from [122] and [32].

The argon content is found higher and more correlated with changes within the plasma. The electron temperature variations affects almost instantaneously the content of argon. Before the LHCD phase, the decrease of T_e from 1.6 keV to 1 keV corresponds to a net local increase in time of $\overline{n}_{Ar,16+}$ of $1.6 \times 10^{16} m^{-3}$. The density levels of $\overline{n}_{Ar,16+}$ and $\overline{n}_{W,44+}$ are almost the same during the LH plateau and at the end of the discharge, the decrease in T_e and n_e corresponds to a net increase of the Ar^{16+} concentration. The $\overline{n}_{Ar,16+}$ density and $\overline{c}_{Ar,16+}$ concentration rise of about 3.3×10^{16} m^{-3} and 8.1×10^{-4} due to the combined loss in $n_{e,0}$ of 1.2×10^{19} m^{-3} and $T_{e,0}$ of 2.2 keV. The W^{44+} ionization stage no longer exists at these electron temperatures.

Concerning the WEST #59667 plasma discharge shown in Fig. 3.47, no LHCD heating was used, leading to a lower $T_{e,max}$ reached of about 2.5 keV after 1 second. Oscillations of the central T_e and n_e time traces are noticed and are related to the highest Ar concentrations during the discharge. No W lines has been measured during this pulse, leading to W^{44+} density and concentration profiles equal to zero. Here, the level of line-averaged Ar^{16+} density and concentration are one hundred times higher than those observed for the previous discharge studied. A mean Ar^{16+} concentration of about 0.012 is computed, with a peak at 0.016 at 1.6 seconds. The Ar density increases in parallel of the electron density before an abrupt disruption just before 5 seconds of discharge. At t = 4.7 seconds, we measure a density ratio n_{Ar}/n_e of about 0.011.

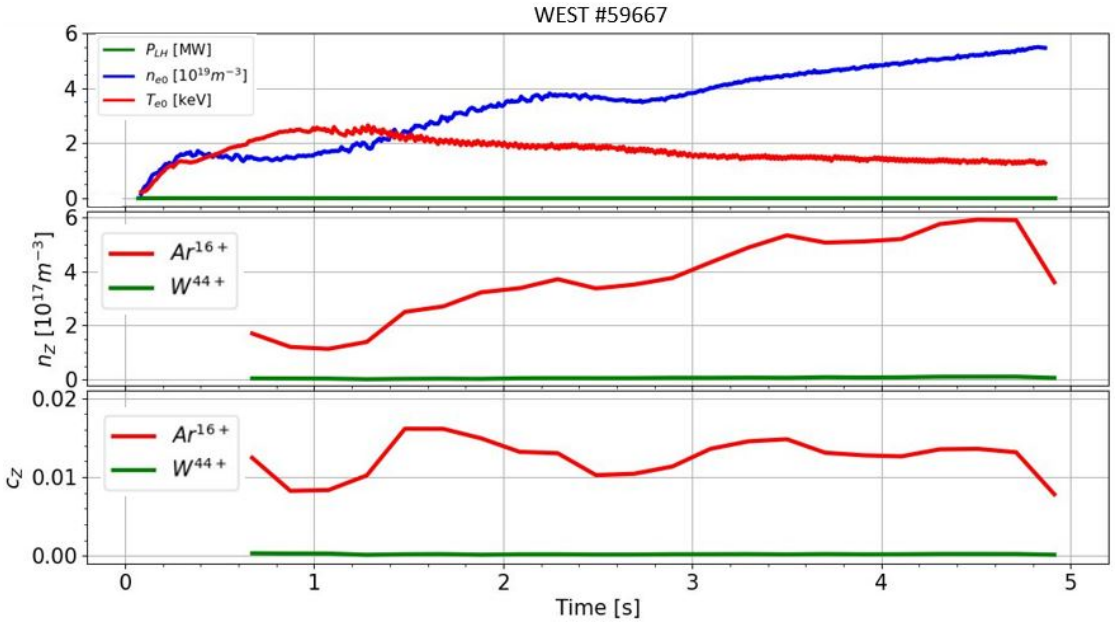

Figure 3.47. – *Temporal evolution of the line-averaged densities and concentrations of Ar^{16+} and W^{44+} for the WEST #59667 plasma discharge.*

For this specific discharge, the reason for this very high concentration of argon was a technical one, since a defect in the pre-vacuuming of the injection channels was observed, leading to an accumulation of argon in the channel before it was used to inject He into the plasma. This amount of argon atoms was then injected into the vacuum chamber one second before start-up and leads to an early disruption of the plasma.

The D_2/Ar injections are also sometimes responsible for disruptions. Examples of disruptions due to excessive injections has been presented in Sect. 2.3.2 where during the WEST #59981 plasma discharge, over-injection has led to an Ar concentration multiplied by a factor 20 just before the plasma to disrupt because of the radiative losses.

3.4.3. Discussion on an alternative brightness calibration

The proposed brightness calibration transfer between the VUV and the XICS diagnostic has provided very interesting results about Ar and W impurity content. However, an alternative method could be performed also based on the SIR measurements. Less assumptions could be made regarding the PECs of the two lines but maybe with more dependency on the quality of the magnetic equilibrium reconstruction A simple sketch of the brightness calibration transfer method is displayed in Fig. 3.48. The method presented in the previous Section rely on the brightness measurement of the EUV spectrometer. The SIR brightness coefficient is already known and permits to convert the number of counts per time unit into brightness units. The transfer from SIR to XICS follows in Fig. 3.48 the red arrows, from the lower to the upper branch.

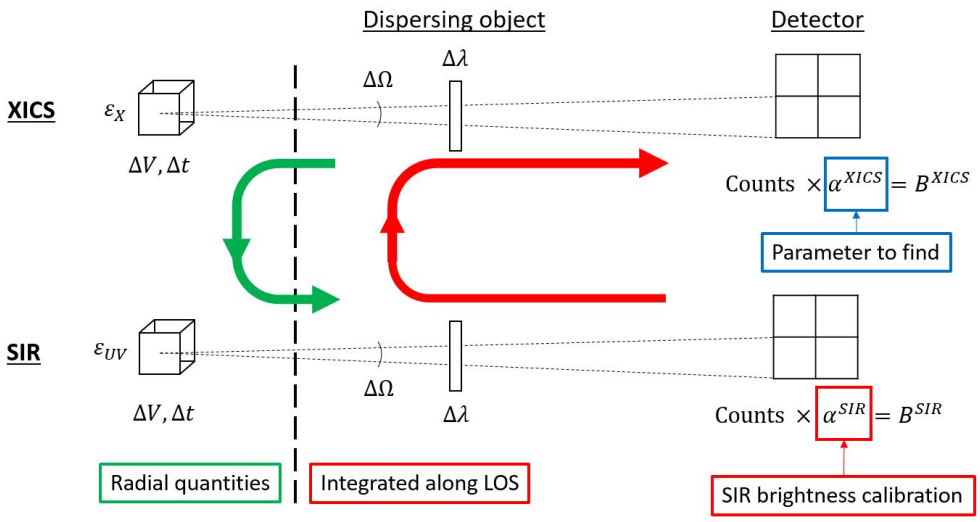

Figure 3.48. – *Sketch of the brightness calibration transfer from the EUV SIR spectrometer (lower branch) to the XICS spectrometer (upper branch). The performed method is represented by red arrows and the alternative with green arrows.*

Radial emissivities of the SIR spectral lines are not available so we used LOS-integrated measurements to perform the brightness calibration transfer.

However, the tomographic inversions introduced in Sect. 2.4.3 make it possible to recompute radial emissivities of the spectral lines measured on the Ar XVII spectrum. The alternative method would be to first compute the radial emissivities of the W^{44+} Zn-2 spectral line. Then, as the PECs are available for both W^{44+} lines for the two diagnostics, interpolation of the SIR spectral line could be performed taking into account the ratio between the two PECs as shown in Fig. 3.35. As this ratio is not constant with the electron temperature, we have computed, for the calibration transfer, a single function dependent on T_e and n_e to reduce the brightness ratio as a function of two coefficients as done in Eq. 3.16.

With this alternative method, we would take into account directly the PEC ratio to interpolate the radial emissivity of the SIR W^{44+} spectral line. Thus, and with the implementation of a synthetic diagnostic for the VUV spectrometer, the computation of LOS-integrated brightness would be possible and be compared with the real measurements. Doing so, another brightness calibration coefficient would been acquired from radial values of emissivities. The approximations concerning the length of integration of the electron density for the concentration computations and for the radial range of emission of the W^{44+} spectral lines would become obsolete and more accurate density and concentration profiles could been computed.

3.5. Conclusions

The analysis of the Ar XVII spectrum with the measurements of the XICS diagnostic has permitted to both extract information about the instrument function and studied plasmas. The first spectra measured for the first experimental campaigns were distorted because of the crystal function. We saw that the combination of a manufacturing in two parts and a defect of parallelism between the crystal planes and the optical surface induced a line-doubling characterized by a spectral shift and a count ratio. The crystallographic study performed in Sect. 3.2 allowed to identify the causes of the line-doubling and to determine the wavelength dependence of the spectral shift parameter. However, without a full characterization of either the volume or surface state of the crystals, it is difficult to express hypothesis about the cause(s). A simple solution has enabled the Ar XVII spectrum to be analyzed with a single Gaussian shape hiding one half-crystal facing the plasma, and thus removing the second component of the lines.

We were then able to look at the quantities to be extracted from the Gaussian functions used to model the lines in order to calculate the ion and the electron temperatures and the toroidal rotation velocity profiles. We demonstrated that the lack of spectral calibration meant that the latter could not be used for now but did not prevent the temperature profiles from being used. The ion temperature extracted from the line widths gave satisfactory results compared with temperatures calculated from neutron fluxes. As for the electron temperatures, they are in good agreement with those calculated with the ECE radiometer up to a certain temperature limit. Indeed, above 2 keV, one of the line ratios used becomes unusable as extremely close spectral lines merge with the *k* dielectronic satellite line. Despite having proved that W lines, or lines from another impurity, disturb the modelling of the k line, it is still not possible to identify both the number of lines and the emitting ion.

Finally, we have described a method to transfer the brightness calibration from one spectrometer to another. Based on the work carried out by [32], the transfer took place between diagnostics measuring different wavelength ranges and with different geometries. The detailed process for the similar lines of sight selection and the computation of the calibration transfer coefficient was then used to extract density and concentration profiles for the impurities measured on the Ar XVII spectrum, argon and tungsten. Here again, the orders of magnitude of these quantities were satisfactory, proving that this transfer method was carried out in the right way. We were able to link the disruption of a plasma discharge to a too large Ar concentration in the plasma, something that had not been done before on WEST.

SUMMARY

This thesis is dedicated to the modelling of a X-ray imaging crystal spectrometer (XICS) installed on WEST and the study of the spectral lines measured on the Ar XVII spectrum. To do so, it is necessary to understand the physical processes that occur in a tokamak plasma, at the origin of the lines measured and by extension the basic principles of a tokamak. The collisional processes between the electrons and Ar ions in a plasma lead to the emission of a great number of spectral lines in the wavelength range of the Ar XVII spectrum (3.1 keV < E < 3.15 keV) and imply several Ar ionization stages. The way we described the emissivity of a spectral line identifies the various dependences in the electron density and temperature. We saw that we can deduce from the line components (intensity, width and shift) the electron and ion temperature and toroidal rotation velocity from respectively spectral line ratios, Doppler broadening and shift. The very narrow spectral range in which all these lines are measured requires a measuring instrument capable of separating all the lines with a high accuracy, while collecting a maximum number of photons possible.

The XICS diagnostic was installed in replacement of a former X-ray line spectrometer in order to obtain, in addition to an excellent spectral resolution, a high spatial resolution by means of a very large number of lines of sight covering a broad volume of plasma. All the spectrometer components have been chosen with the precise aim of maximizing these resolutions. We have detailed the principles of the Bragg crystals by the Rocking-Curve computation. Diffraction is a complex process which induces a yield of less than one in terms of diffracted photons and a line broadening in addition to Doppler broadening. The implementation of the synthetic diagnostic has permitted to show the excellent spatial and spectral resolutions (about the centimeter and $\Delta\lambda \approx 10^{-4}$ respectively) but also highlights the main limitations due to the lack of spectral and brightness calibrations and due to crystals defects. Indeed, two defects (manufacturing in two pieces and miscut angle) have created a distortion of the instrument function, i.e. a line-doubling measured on all the spectral lines characterized by a spectral shift and a count ratio. We have been able to demonstrate our understanding of spectral shift by identifying its wavelength dependence, but that of the count ratio is still under study. This distortion was easily corrected by hiding one of the crystal halves, but at the expense of half the total diffraction surface. We also have seen that the lack of spectral calibration implies a large uncertainty in the instrument function, making the toroidal rotation velocity profiles unusable today.

However, the computations of the ion and electron temperatures profiles with the Ar spectral lines measurement showed very interesting results. First, they contribute to building a consistent estimate of these profiles using the various diagnostics installed in WEST. Second, they allow the effect of W emission in the Ar XVII spectrum to

be evaluated. Indeed, only three W lines from the W^{43+} and W^{44+} ionization stages were identified in the Ar XVII spectrum, with very high intensities at temperatures above 2 keV and relatively well spectrally resolved. However, the spectrum of W in the spectral range $3.93 < \lambda < 4.00$Å contains an unknown number of lines at varying relative intensities, some of which are mixed with Ar lines. This makes it impossible, for now, to use, above $T_e = 2$ keV, the Ar line ratio between the He-like resonance line w and the $n = 2$ dielectronic satellite line k, which has historically been used to determine the electron temperature in Carbon environment. Another Ar line ratio, between the He-like resonance line w and the $n = 3$ dielectronic satellite lines, gives temperature estimations which are more affected by high Bremsstrahlung emission. A very interesting use of these identified W lines has been proposed to calibrate the brightness of the spectrometer, another uncertainty of the instrumental function, and to deduce concentrations and densities of the two impurities argon and tungsten. The method detailed was to transfer the brightness calibration of a VUV spectrometer to the XICS as both diagnostic measure W^{43+} and W^{44+} lines. The method described in [32] has been adapted to take into account different diagnostic geometries and line wavelengths. As a result, consistent Ar and W densities and concentrations have been computed first for a typical LHCD plasma discharge where we found line-averaged concentrations and densities of $n_{Ar^{16+}} \approx 4.2 \times 10^{15} m^{-3}$, $c_{Ar^{16+}} \approx 7.8 \times 10^{-5}$, $n_{W^{44+}} \approx 5.3 \times 10^{15} m^{-3}$ and $c_{W^{44+}} \approx 9.5 \times 10^{-5}$.

The results presented in this thesis do not reflect the chronological order of the work carried out. Indeed, certain difficulties were encountered during the three years of the thesis, some sudden and others imposed by the workload of the diagnostics manager. The latter implies great dedication to the experiments that may have been carried out on WEST, and much of the personal experience gained has been difficult to transcribe into this thesis. Despite this, this diagnostic, which is relatively young since it was first commissioned in 2016, is a very important tool for the study of WEST plasmas and still requires substantial efforts to fully characterize its instrument function but also to get the most out of it. A few limitations on the overall XICS operation have been discussed along this thesis which have to be reminded:

- The different properties of the three crystals used on the XICS instrument, in terms of sagittal and meridian foci, result in an optimal averaged detector position, a few centimetres away from each meridian focus. This choice was made so as not to change the position of the detector each time a new crystal was placed in front of the plasma;
- The approximate position of the detector on the Rowland sphere can cause an artificial broadening of the lines, adding to the Doppler broadening and adding a systematic error to ionic temperature calculations;
- The lack of spectral calibrations adds an unknown component to the instrument function and makes it impossible to obtain absolute Doppler shift measurements;
- Defects in the detector, namely the loss of two central modules, mask a large part of the emission from the plasma's center-bottom;
- The origin of the count ratio parameter R characterizing half of the line-doubling

problem could not be established with certainty. However, the most plausible hypothesis is that there is an internal structural defect, i.e. on the reticular planes distribution within the crystal, on one of the two crystals, causing the loss of diffracted photons of same energy and angle of incidence between the two halves;

All these instrumental limitations leave plenty of scope for future improvements in performance. We can therefore list, in a non-exhaustive and non-prioritized manner, several areas for further work:

- Perform a spectral calibration by designing a device integrated into the diagnostics system, enabling wavelength calibration of the detector during commissioning phases;
- Include a calibrated X-ray source in the spectral calibration system to produce experimental Rocking-Curves and validate the theoretical. Comparing them with the theoretical ones determined in this work would reveal more about the diffraction properties of each half-crystal half and thus determine whether volume and/or surface inhomogeneities affect the measurements;
- Perform the alternative brightness calibration transfer method in order to verify the method described in this thesis and validate our results;
- Highlight the weaknesses of the current data processing algorithm based on 2D image modelling, by performing 1D fits on each pixel row of the images, at the cost of speed of execution;
- Perform again a metrology procedure in order to determine with high accuracy the real location of the detector in the tokamak frame;
- Use various atomic physics codes to study several PEC data sets and determine whether the differences in the electron temperature estimations with the two Ar line ratios can be resolved
- Study the living conditions of argon in the tokamak, in terms of recycling and storage in the vessel walls, to determine whether Ar-clean spectra could be obtained and thus study the entire W spectrum in this wavelength range;
- Consider the possibility of enhancing this diagnostic as a real-time instrument by significantly improving the speed and robustness of the data processing for a more accurate study of plasma discharges during experimental sessions;
- Study the possibility to perform some experiments in tokamaks as KSTAR or stellarators as W7-X where scientists are able to measure the Ar XVII spectrum without any argon impurity injection to reference as many other impurity lines as possible (especially from W ionization stages);
- Synchronize the XICS measurements with those of two new off-axis X-ray spectrometers soon to be installed on WEST in collaboration with Princeton Plasma Physics Laboratory (PPPL)/Massachusetts Institute of Technology (MIT);
- Search for a spectral range where several W ionization states can be measured with a new dedicated crystal, as for the High Resolution X-ray Imaging Spectrometer (HR-XIS) W^{64+} crystal mounted at W7-X [124] and try to extract temperatures from them, as it could be installed on ITER to measure the Ne-like W spectrum between 8.3 and 9.1 keV ($1.66 < \lambda < 1.49$) [62].

Appendices

A. Scattering on a unit cell of the crystal lattice

The diffraction by crystals is mainly governed by its atomic composition. There is a difference between the scattering by an electron, an atom or an ensemble of atoms. It results from the combined effect of all the electrons belonging to one or more atoms on the diffraction phenomenon. To characterize the influence of the material organization on the diffracted amplitude of a wave, we will need to introduce the notion of structure factor F. It can be described as the Fourier transform of the electronic distribution in the elementary mesh, for the case of X-ray photons.

Before expressing this quantity, let us focus on the atomic scale to define the atomic scattering factor f_0 [55]. This factor represents the ratio between the amplitudes of the radiation scattered on the one hand by an atom and on the other hand by a free electron. It only depends on the type of atom considered and the direction of scattering. According to the Bragg relation Eq. 2.1, we can now compute the parameter $sin(\theta_B)/\lambda$ with θ_B the Bragg angle of reference of the crystal. The value of this parameter is important because it is the main variable of the atomic scattering factor, as shown in Fig.A.1. Among the two species that compose the Quartz crystals, the atomic scattering factor is higher for the Silicon. It is due to its higher number of electrons, $Z(Si) = 14$ and $Z(O) = 8$, and decreases slowly as the scattering angle increases. The amplitude of the wave scattered by an atom with Z electrons becomes Z times the amplitude of the wave scattered by a single electron in the forward scattering direction ($2\theta = 0$). The waves scattered by all the electrons are then in phase. So if we call E_e the amplitude of the wave scattered by a single free electron, the amplitude E_{at} of the wave scattered by an atom becomes $E_{at} = f.E_e$ with:

$$f_0 = \int \rho(\vec{r}).e^{i2\pi.(\vec{B}_H.\vec{r}_j)} dr^3 \tag{A.1}$$

where the scalar product $\vec{B}_H.\vec{r}_j$ defines the phase difference between the radiation scattered by the jth electron and that scattered by an electron at the origin, and the vector $\vec{r}_j$ describes the position of the considered atom. When the electron distribution function $\rho(\vec{r})$ has a spherical symmetry, we shall introduce the radial distribution function $U(\vec{r})$ defined by $U(\vec{r}) = 4\pi.r^2.\rho(\vec{r})$ so that $U.dr$ represents the number of electrons between spherical shells of radii r and $r + dr$. Using spherical coordinates with $\vec{s} = 2\pi.\vec{B}_H$, we have $dv = 2\pi.r^2.sin(\phi).dr.d\phi$ and $\vec{s}.\vec{r} = sr.cos(\phi)$ where ϕ is the

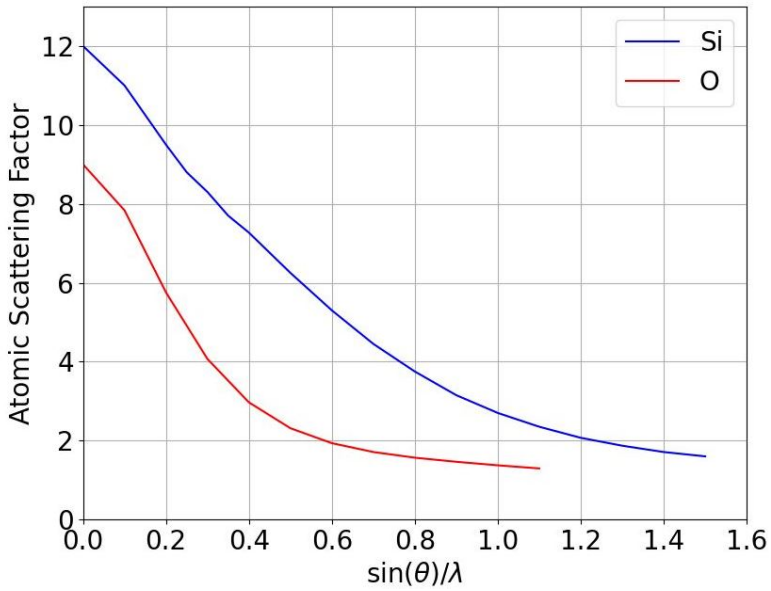

Figure A.1. – Atomic scattering factor values for O and Si species.

angle between $\vec{s}$ and $\vec{r}$, half the scattering angle. Hence,

$$f_0 = \int \frac{U(r).sin(sr)}{sr} dr = \int 4\pi.r^2.\rho(r).\frac{sin(sr)}{sr} dr \tag{A.2}$$

with $s = 4\pi.sin(\theta)/\lambda$. If now we consider the modifications to apply to the equations when the electronic binding forces are taken into account, like a binding force of the electron $-m.w_j^2.\vec{x}_j$ and a damping term $-m.\kappa_j.(d\vec{x}_j/dt)$, the revised expression for the atomic scattering factor becomes:

$$f = f_0 + \sum_j \frac{\phi_j}{1 - \frac{w_j^2}{w_0^2} - i\frac{\kappa_j}{w_0}} \approx f_0 + \sum_j \phi_j(\zeta_j + i\eta_j) \tag{A.3}$$

where the term inside the parenthesis is called the anomalous contribution to the atomic scattering power due to the jth electron with $\zeta_j = w_j^2/w_0^2$ and $\eta_j = \kappa_j/w_0$.

The next step is to consider now not anymore the case of the scattering by an atom but the case of an unit cell of the crystal. As we saw earlier, the amplitude of scattering from a single atom can be expressed in terms of the amplitude of scattering by the Z electrons that compose it. The ratio between those two amplitudes is called the atomic scattering factor. The amplitude of scattering from a unit cell may in a similar manner be written as $F.E_e$ with F the structure factor. The waves scattered in any order of diffraction (hkl) by different atoms will have phase differences with respect to each other, $\delta = 2\pi/d_{hkl}$. The value of x can be obtained by forming the scalar product

between $\vec{r}_n$ and $\vec{H}_{hkl}/H_{khl}$ and then:

$$\delta = \frac{2\pi}{d_{hkl}}.\frac{\vec{H}_{hkl}}{H_{khl}}.\vec{r}_n = 2\pi.(hu + kv + lw) \tag{A.4}$$

where $\vec{r}_n$ is the position vector of the considered atom within the unit cell $\vec{r}_n = u_n.\vec{a} + v_n.\vec{b} + w_n.\vec{c}$ and $\vec{H}_{hkl}$ is the normal vector to the reticular planes (hkl). The amplitude of each wave is given by the atomic scattering factor of the atom scattering it. As described by the relation of the phase difference Eq. A.4, the phase of each wave is related to the Miller indices of the reflecting planes and the coordinates of the scattering atom. If a unit cell contains a total of N atoms, the resultant wave scattered by all the N atoms in the direction of the (hkl) reflection is:

$$F = f_1.e^{i\delta_1} + f_2.e^{i\delta_2} + ... + f_N.e^{i\delta_N} \tag{A.5}$$

The magnitude $|F|$ of the structure factor represents the amplitude of the resultant wave. For a (hkl) reflection, the structure factor is more concisely expressed as:

$$F_{hkl} = \sum_{n=1}^{N} f_n.e^{2i\pi.(hu+kv+lw)} = \sum_{n=1}^{N} f_n.e^{2i\pi.\vec{B}_H.\vec{r}} \tag{A.6}$$

where f_n is the atomic scattering factor of the nth atom and (u_n, v_n, w_n) represent its coordinates. $|F_{hkl}|$ is defined as the ratio to the amplitude of the wave scattered by all the atoms of a unit cell to the amplitude of the wave scattered by a single electron. When the Bragg relation is satisfied for a set of (hkl) planes, the diffraction intensity from these planes is proportional to $|F_{hkl}|^2$. In general, F_{hkl} is a complex quantity, i.e. the phase of the scattered wave may have any phase difference with respect to that of a wave scattered by an atom at the origin of the unit cell. Then,

$$|F_{hkl}|^2 = \left(\sum f_{0,r}.cos(2\pi.(hx_r + ky_r + lz_r))\right)^2 + \left(\sum f_{0,r}.sin(2\pi.(hx_r + ky_r + lz_r))\right)^2 \tag{A.7}$$

This relation can be used as well as for the real part of the structure factor as the imaginary part. The interpolation of the value of the atomic scattering factor for Si and O species can be done from a database [125]. Hence, the total atomic structure factor for each species can be expressed as:

$$\begin{aligned} f_{Si} &= f_0^{Si} + 2\zeta_K^{Si} + i2\eta_K^{Si} = f_0^{Si} + f_{re}^{Si} + i.f_{im}^{Si} \\ f_O &= f_0^{O} + 2\zeta_K^{O} + i2\eta_K^{O} = f_0^{O} + f_{re}^{O} + i.f_{im}^{O} \end{aligned} \tag{A.8}$$

with the real and imaginary parts (ζ_K^i, η_K^i) which are dispersion terms and the index K refers to the K-electron of each species. These contributions can be calculated from the formulas developed by [126]. The formula for the imaginary contribution is:

$$2\eta_K^i = \pi.\frac{2^7.e^{-4}}{9}.\left(\frac{4x^2}{(1-\Delta)^2} - \frac{x^3}{(1-\Delta)^3}\right) \tag{A.9}$$

where the functions ϕ_K in Eq. A.3 have been set equal to unity since the volume containing the K-electrons has smaller dimensions than the X-ray wavelengths, $x = \lambda/\lambda_K$ (λ_K is the closest K-absorption wavelength for each species) and $\Delta^{Si} = 0.276, \Delta^{O} = 0.3$. Interpolating first values of atomic scattering factors according to the values of $sin(\theta_B)/\lambda$ from the database for each species, we are then able to compute the real and imaginary terms of the atomic scattering factor. With the phase terms for each atom in the unit cell, the calculation of the real F_{re} and imaginary F_{im} parts of the structure factor is done as mentioned above. The intrinsic response of a Quartz material that composes the Bragg crystals for the XICS spectrometer is now established. But this quantity alone cannot fully describe a material response to interaction with an electromagnetic wave. We then need to determine the attenuation of the diffracted wave by the thickness of material traversed, leading us to define the absorption coefficient of the crystal.

B. Fourier coefficients of the crystal polarization

Here, we describe the effect of a non-zero thickness material on the diffraction of a incident electromagnetic wave. As a first approximation, the diffraction process can be studied with an ideal crystal, approximated as a mirror of thickness $< 1\mu m$. This leads to a diffraction process where the entire amplitude of the incident is diffracted by the first layers. This simplified theory of X-ray diffraction neglects absorption and attenuation of the wave that enters the crystal mesh. In reality, all the atoms layer of atoms in addition to the crystal surface are involved in the diffraction.

Due to the real thickness of the crystal used (197 μm) and because the wavelength of the incident wave may be very close to the inter-reticular spacing value (d_{hkl}(Ar XVII) = 2.457 Å compared to λ_{ref}(Ar XVII) = 3.96 Å), the radiation may penetrate into the bulk of the crystal. Traversing the matter, the X-ray photon beam will be subjected to absorption. Photons can be absorbed by the electrons of the mesh, leading sometimes to the ejection of bound electrons. We speak of normal absorption when ejection of photo-electrons and/or Compton scattering happen. Coherent scattering also happens when the incident photon gives its energy to a bound electron, which vibrates and emits a new photon of the same wavelength by elastic diffraction. We can also introduce the notion of extinction that may happen in thick crystals. It leads to back diffraction of the beam in the incident direction, which causes a reduced diffracted radiation.

The theory that takes into account the absorption and extinction processes within a thick crystal is said dynamical [58]. It differs from the Darwin approximation for non-absorbing crystals or also the mosaic thick crystal approximation, treating of small mosaic structures within the mesh which are not exactly oriented in the same direction. The absorption phenomena of incident radiation into the matter are well represented by the factor $e^{-\mu.x}$ with μ the normal linear absorption coefficient and x the path through the matter.

In order to quantify the linear absorption coefficient of Bragg crystals, we start by explaining the polarizability of a material. It is the reaction of a charge distribution, like a part of the total electron cloud of all the atoms of a crystal, to be distorted from its normal shape by an external electromagnetic wave. The polarizability α can be related to the dielectric constant ϵ of a material by:

$$\epsilon = 1 + \frac{4\pi\alpha}{1 - \frac{4\pi}{3}\alpha} \approx 1 + 4\pi\alpha \qquad [\mathrm{C\,m^{-1}\,V^{-1}}] \tag{B.1}$$

since $4\pi\alpha = \psi \ll 1$. The polarizability can be written as the sum of the k contributions of the k electrons that compose it:

$$\alpha = \frac{-e^2}{m_e w^2} \sum_{k,l} \Omega_{k,l} = \frac{-e^2}{m_e w^2} \sum_{k,l} \rho_{k,l}(\vec{r} - \vec{r}_k) \qquad [\mathrm{C\,m^2\,V^{-1}}] \tag{B.2}$$

with $\rho_{k,l}$ the distribution function of the kth electron in the lth unit cell of the crystal. When the electron binding forces are also taken into account, the polarizability takes the same form as Eq. A.3:

$$\alpha = \frac{-e^2}{m_e w^2} \sum_{k,l} \rho_{k,l}(\vec{r} - \vec{r}_k)(1 + \zeta_j + i\eta_j) \tag{B.3}$$

and the ψ term can be deduced as:

$$\psi = \frac{-4\pi e^2}{m_e w^2} \sum_{k,l} \rho_{k,l}(\vec{r} - \vec{r}_k)(1 + \zeta_j + i\eta_j) \tag{B.4}$$

The polarizability parameter ψ is a scalar and a function of the position. It has the same periodicity as the crystal lattice itself. So since α is periodic, it can be written as a Fourier series:

$$\psi = 4\pi\alpha = \sum_H \psi_H . e^{-2i\pi \vec{B_H}.\vec{r}} \tag{B.5}$$

$$\psi_H = \frac{1}{V} \int \psi . e^{2i\pi \vec{B_H}.\vec{r}} dv \tag{B.6}$$

The Fourier coefficient of the polarizability ψ_H can also be written from Eq. B.2 as:

$$\psi_H = \frac{-4\pi . e^2}{m w^2} . F_H \tag{B.7}$$

Separating the real and the imaginary parts of ψ, we obtain as definition:

$$Re(\psi) = \psi' = \frac{-4\pi . e^2}{m w^2} . \sum (1 + \zeta_j) . \Omega_j \tag{B.8}$$

$$Im(\psi) = \psi'' = \frac{-4\pi . e^2}{m w^2} . \sum \eta_j . \Omega_j \tag{B.9}$$

As we wrote $\epsilon = 1 + \psi$, the refractive index n of the medium can be expressed as:

$$n = \sqrt{\epsilon} = \sqrt{1 + \psi} \approx 1 + \frac{\psi}{2} \tag{B.10}$$

since $\psi \ll 1$. The refractive index becomes a complex quantity as well and a periodic function of the position:

$$n \approx 1 + \frac{\psi'}{2} + \frac{i\psi''}{2} \tag{B.11}$$

The real averaged refractive index $1+\frac{\psi'}{2}$ can be written as:

$$\psi' = \psi_0 = -\frac{e^2.\lambda^2}{\pi.mc^2V}\sum(1+\zeta_j)Z_j \tag{B.12}$$

The imaginary part of the refractive index $\frac{\psi''}{2}$ is called the absorption index and it is related to the linear absorption coefficient by:

$$\mu = \frac{-2\pi}{\lambda}.\psi'' \qquad [\mathrm{m}^{-1}] \tag{B.13}$$

Its averaged true absorption coefficient throughout the crystal medium is then:

$$\mu_0 = -2\pi.k_0.\psi_0'' = \frac{2e^2\lambda}{mc^2V}.\sum(\eta_j Z_j) \tag{B.14}$$

with Z_j the number of electrons in the unit cell considered.

The use of the dynamical theory of X-ray photon diffraction allows us to model the absorption effect of the crystal on an incident electromagnetic wave. This model is a good intermediate solution, since it takes into account the penetration of the wave into the material and its attenuation, unlike the Darwin approximation. On the other hand, when no technical approach can be used to accurately determine the true state of a crystal internal mesh, as in our case, the mosaic model should be used with caution. Although the manufacturing processes for this type of crystal are becoming increasingly sophisticated, without any means of characterization, we do not have enough information to use a mathematical model that takes internal deformations into account.

We have now introduced and determined all the physical quantities and relations needed to establish the general equation for the Bragg diffraction intensity ratio between the incident and the diffracted wave.

Bibliography

[1] IPCC. *Climate Change 2013: The Physical Science Basis. Contribution of Working Group I to the Fifth Assessment Report of the Intergovernmental Panel on Climate Change*. NY, USA, 2013 (cit. on p. 43).

[2] Geng S. et al. "An Overview of the ITER Project". In: *Journal of Physics: Conference Series* 2386.1 (2022), p. 012012. DOI: 10.1088/1742-6596/2386/1/012012. URL: https://dx.doi.org/10.1088/1742-6596/2386/1/012012 (cit. on p. 42).

[3] Baeten P. et al. *Physics of nuclear reactors*. 2006 (cit. on p. 45).

[4] Wesson J. and Campbell D.J. *Tokamaks*. Vol. 149. Oxford Univerty Press, 2011 (cit. on pp. 46, 47, 56).

[5] Fleurot N. et al. "The Laser Mégajoule (LMJ) Project dedicated to inertial confinement fusion: Development and construction status". In: *Fusion Engineering and Design* 74.1 (2005). Proceedings of the 23rd Symposium of Fusion Technology, pp. 147–154. ISSN: 0920-3796. DOI: https://doi.org/10.1016/j.fusengdes.2005.06.251. URL: https://www.sciencedirect.com/science/article/pii/S0920379605003297 (cit. on p. 47).

[6] Azizov E. A. et al. "Tokamaks: from A D Sakharov to the present (the 60-year history of tokamaks)". In: *Physics-Uspekhi* 55.2 (2012), p. 190. DOI: 10.3367/UFNe.0182.201202j.0202. URL: https://dx.doi.org/10.3367/UFNe.0182.201202j.0202 (cit. on p. 47).

[7] Vallet A. "Hydrodynamic modelling of the shock ignition scheme for inertial confinement fusion". PhD thesis. 2014 (cit. on p. 48).

[8] Vezinet D. "Mesure et analyse du rayonnement Xmou d'un plasma de Tokamak en vue d'un contrôle en temps réel". 2013AIXM4749. PhD thesis. 2013. URL: http://www.theses.fr/2013AIXM4749/document (cit. on p. 48).

[9] Decker J. et al. "Calculations of lower hybrid current drive in ITER". In: *Nuclear Fusion* 51.7 (2011), p. 073025. DOI: 10.1088/0029-5515/51/7/073025. URL: https://dx.doi.org/10.1088/0029-5515/51/7/073025 (cit. on p. 51).

[10] Ohkawa T. et al. *Steady-state operation of tokamaks by RF heating*. Tech. rep. General Atomic technical report, G1-A13847, 1976 (cit. on p. 51).

[11] Landau L.D. "On the vibrations of the electronic plasma". In: *J.Phys. (U.S.S.R.)* 10.26 (1946) (cit. on p. 51).

[12] Dumont R.J. et al. "Variational approach to radiofrequency waves in magnetic fusion devices". In: *Nuclear Fusion* 49.7 (2009), p. 075033. DOI: 10.1088/0029-5515/49/7/075033. URL: https://dx.doi.org/10.1088/0029-5515/49/7/075033 (cit. on p. 51).

[13] Bucalossi J. et al. "Operating a full tungsten actively cooled tokamak: overview of WEST first phase of operation". In: *Nuclear Fusion* 62.4 (2022), p. 042007. DOI: 10.1088/1741-4326/ac2525. URL: https://dx.doi.org/10.1088/1741-4326/ac2525 (cit. on p. 51).

[14] Saoutic B. et al. "Tore Supra: Toward Steady State in a Superconducting Tokamak". In: *Fusion Science and Technology* 56.3 (2009), pp. 1079–1091. DOI: 10.13182/FST09-A9169. eprint: https://doi.org/10.13182/FST09-A9169. URL: https://doi.org/10.13182/FST09-A9169 (cit. on p. 51).

[15] Gilet C. al. "Diagnostic Systems on Tore Supra". In: *Fusion Science and Technology* 56.3 (2009), pp. 1219–1252. DOI: 10.13182/FST09-A9175. URL: https://doi.org/10.13182/FST09-A9175 (cit. on p. 51).

[16] Delpech L. et al. "Evolution of the Tore Supra Lower Hybrid Current Drive System for WEST". In: *Fusion Engineering and Design* 96-97 (2015). Proceedings of the 28th Symposium On Fusion Technology (SOFT-28), pp. 452–457. ISSN: 0920-3796. DOI: https://doi.org/10.1016/j.fusengdes.2015.01.020. URL: https://www.sciencedirect.com/science/article/pii/S0920379615000393 (cit. on p. 51).

[17] Hillairet J. et al. "WEST actively cooled load resilient ion cyclotron resonance heating system results". In: *Nuclear Fusion* 61.9 (2021), p. 096030. DOI: 10.1088/1741-4326/ac1759. URL: https://dx.doi.org/10.1088/1741-4326/ac1759 (cit. on p. 51).

[18] Firdaouss M. et al. "First feedback during series fabrication of ITER like divertor tungsten components for the WEST tokamak". In: *Physica Scripta* 96.12 (2021), p. 124037. DOI: 10.1088/1402-4896/ac2978. URL: https://dx.doi.org/10.1088/1402-4896/ac2978 (cit. on p. 51).

[19] Pütterich T. et al. "Calculation and experimental test of the cooling factor of tungsten". In: *Nuclear Fusion* 50.2 (2010), p. 025012. DOI: 10.1088/0029-5515/50/2/025012. URL: https://dx.doi.org/10.1088/0029-5515/50/2/025012 (cit. on p. 53).

[20] Ségui J.L. et al. "An upgraded 32-channel heterodyne electron cyclotron emission radiometer on Tore Supra". In: *Review of Scientific Instruments* 76.12 (2005), p. 123501. ISSN: 0034-6748. DOI: 10.1063/1.2140225. eprint: https://pubs.aip.org/aip/rsi/article-pdf/doi/10.1063/1.2140225/15902628/123501_1_online.pdf. URL: https://doi.org/10.1063/1.2140225 (cit. on p. 53).

[21] Janicki C. et al. “Electron temperature measurement from the ECE diagnostics in tokamak plasmas under transient conditions”. In: *Nuclear Fusion* 33.3 (1993), p. 513. DOI: 10.1088/0029-5515/33/3/I14. URL: https://dx.doi.org/10.1088/0029-5515/33/3/I14 (cit. on p. 53).

[22] Chelihi B. et al. “Analysis of the New Thomson Scattering Diagnostic System on WEST Tokamak”. In: *Applied Sciences* 12.3 (2022). ISSN: 2076-3417. DOI: 10.3390/app12031318. URL: https://www.mdpi.com/2076-3417/12/3/1318 (cit. on p. 53).

[23] Aftanas M. et al. “High-resolution Thomson scattering system on the COMPASS tokamak: Evaluation of plasma parameters and error analysisa)”. In: *Review of Scientific Instruments* 83.10 (2012), 10E350. ISSN: 0034-6748. DOI: 10.1063/1.4743956. URL: https://doi.org/10.1063/1.4743956 (cit. on p. 53).

[24] Scannell R. et al. “A 130 point Nd:YAG Thomson scattering diagnostic on MASTa)”. In: *Review of Scientific Instruments* 81.10 (2010), p. 10D520. ISSN: 0034-6748. DOI: 10.1063/1.3460628. URL: https://doi.org/10.1063/1.3460628 (cit. on p. 53).

[25] Bozhenkov S.A. et al. “The Thomson scattering diagnostic at Wendelstein 7-X and its performance in the first operation phase”. In: *Journal of Instrumentation* 12.10 (2017), P10004. DOI: 10.1088/1748-0221/12/10/P10004. URL: https://dx.doi.org/10.1088/1748-0221/12/10/P10004 (cit. on p. 53).

[26] Chellaï O. et al. “Design of a multi-energy soft X-ray diagnostic for profile measurements during long-pulse operation in the WEST tokamak”. In: *Fusion Engineering and Design* 203 (2024), p. 114390. ISSN: 0920-3796. DOI: https://doi.org/10.1016/j.fusengdes.2024.114390. URL: https://www.sciencedirect.com/science/article/pii/S0920379624002436 (cit. on p. 53).

[27] Delgado-Aparicio L.F. et al. “Multi-energy reconstructions, central electron temperature measurements, and early detection of the birth and growth of runaway electrons using a versatile soft x-ray pinhole camera at MST”. In: *Review of Scientific Instruments* 92.7 (2021), p. 073502. ISSN: 0034-6748. DOI: 10.1063/5.0043672. eprint: https://pubs.aip.org/aip/rsi/article-pdf/doi/10.1063/5.0043672/16017577/073502_1_online.pdf. URL: https://doi.org/10.1063/5.0043672 (cit. on p. 53).

[28] Marchuk O. “Modeling of He-like spectra measured at the tokamaks TEXTOR and TORE SUPRA”. doctoralthesis. Ruhr-Universität Bochum, Universitätsbibliothek, 2004 (cit. on pp. 54, 76, 81, 113, 162, 163, 175, 176).

[29] Rutherford E. “LXXIX. The scattering of and particles by matter and the structure of the atom”. In: *The London, Edinburgh, and Dublin Philosophical Magazine and Journal of Science* 21.125 (1911), pp. 669–688. DOI: 10.1080/14786440508637080. eprint: https://doi.org/10.1080/14786440508637080. URL: https://doi.org/10.1080/14786440508637080 (cit. on p. 55).

[30] Kunze H.J. "Collisional Processes". In: *Introduction to Plasma Spectroscopy*. Berlin, Heidelberg: Springer Berlin Heidelberg, 2009, pp. 115–134. ISBN: 978-3-642-02233-3. DOI: 10.1007/978-3-642-02233-3_7. URL: https://doi.org/10.1007/978-3-642-02233-3_7 (cit. on pp. 57, 76).

[31] Porquet D. et al. "Line ratios for helium-like ions: Applications to collision-dominated plasmas*". In: *AA* 376.3 (2001), pp. 1113–1122. DOI: 10.1051/0004-6361:20010959. URL: https://doi.org/10.1051/0004-6361:20010959 (cit. on p. 57).

[32] Boumendjel M. Y. "Investigation of tungsten emission and its density determination in magnetically confined plasmas". Theses. Aix Marseille University, 2023. URL: https://cea.hal.science/tel-04412004 (cit. on pp. 60, 115, 177, 179, 193, 196, 198).

[33] Armstrong G.S.J. et al. "Ab initio calculation of the non-relativistic free–free Gaunt factor incorporating plasma screening". In: *High Energy Density Physics* 10 (2014), pp. 61–69. ISSN: 1574-1818. DOI: https://doi.org/10.1016/j.hedp.2013.10.005. URL: https://www.sciencedirect.com/science/article/pii/S1574181813001766 (cit. on p. 60).

[34] Hilborn R.C. et al. *Einstein coefficients, cross sections, f values, dipole moments, and all that*. 2002. arXiv: physics/0202029 [physics.atom-ph] (cit. on p. 62).

[35] Sciortino F. et al. "Modeling of particle transport, neutrals and radiation in magnetically-confined plasmas with Aurora". In: *Plasma Physics and Controlled Fusion* 63.11 (2021), p. 112001. DOI: 10.1088/1361-6587/ac2890. URL: https://dx.doi.org/10.1088/1361-6587/ac2890 (cit. on pp. 62, 135, 173).

[36] *The ADAS User Manual, version 2.6, http://www.adas.ac.uk* (cit. on pp. 62, 163, 173).

[37] Da Ros A. et al. "Electron and ion temperature measurement with a new x-ray imaging crystal spectrometer on WEST". In: *Review of Scientific Instruments* 95.4 (2024), p. 043505. ISSN: 0034-6748. DOI: 10.1063/5.0179905. URL: https://doi.org/10.1063/5.0179905 (cit. on pp. 63, 89, 111, 120, 133, 172–174).

[38] Griem H.R. "Principles of Plasma Spectroscopy". In: *Fast Electrical and Optical Measurements: Volume I — Current and Voltage Measurements / Volume II — Optical Measurements*. Ed. by James E. Thompson and Lawrence H. Luessen. Dordrecht: Springer Netherlands, 1986, pp. 885–910. ISBN: 978-94-017-0445-8. DOI: 10.1007/978-94-017-0445-8_34. URL: https://doi.org/10.1007/978-94-017-0445-8_34 (cit. on p. 65).

[39] Mewe R. et al. "X-ray spectroscopy of stellar coronae". In: *The Astron Astrophys Rev* 3 (1991), pp. 127–168. DOI: https://doi.org/10.1007/BF00873539 (cit. on p. 65).

[40] Kramida A. et al. NIST Atomic Spectra Database (ver. 5.11), [Online]. Available: https://physics.nist.gov/asd [2024, May 21]. National Institute of Standards and Technology, Gaithersburg, MD. 2023 (cit. on pp. 68, 73).

[41] Goryaev F.F. et al. "Atomic data for doubly-excited states 2lnl of He-like ions and 1s2lnl of Li-like ions with Z=6–36 and n=2,3". In: *Atomic Data and Nuclear Data Tables* 113 (2017), pp. 117–257. ISSN: 0092-640X. DOI: https://doi.org/10.1016/j.adt.2016.04.002. URL: https://www.sciencedirect.com/science/article/pii/S0092640X16300092 (cit. on pp. 68, 73).

[42] Saloman E.B. "Energy Levels and Observed Spectral Lines of Ionized Argon, ArII through ArXVIII". In: *Journal of Physical and Chemical Reference Data* 39.3 (2010), p. 033101. ISSN: 0047-2689. DOI: 10.1063/1.3337661. eprint: https://pubs.aip.org/aip/jpr/article-pdf/doi/10.1063/1.3337661/15766032/033101_1_online.pdf. URL: https://doi.org/10.1063/1.3337661 (cit. on pp. 68, 73, 121).

[43] Gabriel A.H. "Dielectronic Satellite Spectra for Highly-Charged Helium-Like Ion Lines". In: *Monthly Notices of the Royal Astronomical Society* 160.1 (1972), pp. 99–119. ISSN: 0035-8711. DOI: 10.1093/mnras/160.1.99. eprint: https://academic.oup.com/mnras/article-pdf/160/1/99/8079457/mnras160-0099.pdf. URL: https://doi.org/10.1093/mnras/160.1.99 (cit. on pp. 68, 69, 74).

[44] Shevelko V.P. "Oscillator Strengths and Transition Probabilities". In: *Atoms and Their Spectroscopic Properties*. Berlin, Heidelberg: Springer Berlin Heidelberg, 1997, pp. 40–89. ISBN: 978-3-662-03434-7. DOI: 10.1007/978-3-662-03434-7_3. URL: https://doi.org/10.1007/978-3-662-03434-7_3 (cit. on p. 69).

[45] Porquet D. et al. "He-like Ions as Practical Astrophysical Plasma Diagnostics: From Stellar Coronae to Active Galactic Nuclei". In: *Space Science Reviews* 157.1–4 (2010), pp. 103–134. ISSN: 1572-9672. DOI: 10.1007/s11214-010-9731-2. URL: http://dx.doi.org/10.1007/s11214-010-9731-2 (cit. on p. 70).

[46] Hansen S.B. et al. "SCRAM: not a line shape code." In: (2019). URL: https://www.osti.gov/biblio/1640166 (cit. on p. 71).

[47] Foster A.R. et al. "Updated Atomic Data and Calculations for X-ray Spectroscopy". In: *The Astrophysical Journal* 756 (2 2012). NULL, p. 128. ISSN: 0004-637X. DOI: 10.1088/0004-637X/756/2/128. URL: http://adsabs.harvard.edu.ezp-prod1.hul.harvard.edu/abs/2012ApJ...756..128F (cit. on pp. 71, 135, 175).

[48] Smith R.K. et al. "Collisional Plasma Models with APEC/APED: Emission-Line Diagnostics of Hydrogen-like and Helium-like Ions". In: *The Astrophysical Journal* 556 (2 2001), pp. L91–L95. ISSN: 0004637X. DOI: 10.1086/322992. URL: http://stacks.iop.org/1538-4357/556/i=2/a=L91%20http://adsabs.

harvard.edu.ezp-prod1.hul.harvard.edu/abs/2001ApJ...556L..91S (cit. on pp. 71, 135).

[49] De Michelis C. and Mattioli M. "Soft-X-ray spectroscopic diagnostics of laboratory plasmas". In: *Nuclear Fusion* 21.6 (1981), p. 677. DOI: 10.1088/0029-5515/21/6/007. URL: https://dx.doi.org/10.1088/0029-5515/21/6/007 (cit. on p. 72).

[50] Dubau J. and Volonte S. "Dielectronic recombination and its applications in astronomy". In: *Reports on Progress in Physics* 43.2 (1980), p. 199. DOI: 10.1088/0034-4885/43/2/002. URL: https://dx.doi.org/10.1088/0034-4885/43/2/002 (cit. on pp. 74, 75).

[51] Zschornack G. *Handbook of X-Ray Data*. Springer, 2006 (cit. on p. 78).

[52] Bitter M. et al. "X-ray diagnostics of tokamak plasmas". In: *Physica Scripta Volume T* 47 (1993), pp. 87–95. DOI: 10.1088/0031-8949/1993/T47/014 (cit. on pp. 81, 120, 140, 162).

[53] Bragg W.H. "X-rays and Crystals". In: *Nature* 90 (1912), p. 219. DOI: 10.1038/090219a0. URL: https://doi.org/10.1038/090219a0 (cit. on p. 82).

[54] Wyckoff R.W.G. *Crystal Structures*. Crystal Structures. Wiley, 1963. ISBN: 978-0-470-96860-4. URL: https://books.google.fr/books?id=40uGpwAACAAJ (cit. on pp. 84, 85, 144, 146).

[55] MacGillavry C.H. and Rieck G.D. *International Tables for Crystallography*. The Kynoch Press, 1969 (cit. on pp. 84, 202).

[56] Antao S. M. et al. "STATE-OF-THE-ART HIGH-RESOLUTION POWDER X-RAY DIFFRACTION (HRPXRD) ILLUSTRATED WITH RIETVELD STRUCTURE REFINEMEN OF QUARTZ, SODALITE, TREMOLITE, AND MEIONITE". In: *The Canadian Mineralogist* 46.6 (Dec. 1, 2008), pp. 1501–1509. ISSN: 0008-4476, 1499-1276. DOI: 10.3749/canmin.46.5.1501. URL: http://www.canmin.org/cgi/doi/10.3749/canmin.46.5.1501 (visited on 02/01/2022) (cit. on p. 84).

[57] Bartiromo R. et al. "The asymmetric Johann spectrometer and its application to plasma diagnostic in tokamaks". In: *Nuclear Instruments and Methods in Physics Research* 221.2 (1984), pp. 453–459. ISSN: 0167-5087. DOI: https://doi.org/10.1016/0167-5087(84)90019-X. URL: https://www.sciencedirect.com/science/article/pii/016750878490019X (cit. on pp. 85, 143).

[58] Zachariasen W. *Theory of X-ray Diffraction in Crystals*. Wiley, New York, 1945 (cit. on pp. 85, 87, 88, 143, 206).

[59] Bitter M. et al. "Numerical studies of the imaging properties of doubly focussing crystals and their application to ITER". In: *Review of Scientific Instruments* 66.1 (1995), pp. 530–532. ISSN: 0034-6748. DOI: 10.1063/1.1146341. eprint: https://pubs.aip.org/aip/rsi/article-pdf/66/1/530/19254159/530_1_online.pdf. URL: https://doi.org/10.1063/1.1146341 (cit. on p. 90).

[60] Bertschinger G. et al. “Compact imaging Bragg spectrometer for fusion devices”. In: *Review of Scientific Instruments* 75.10 (2004), pp. 3727–3729. DOI: 10.1063/1.1781755. eprint: https://doi.org/10.1063/1.1781755. URL: https://doi.org/10.1063/1.1781755 (cit. on p. 90).

[61] Bertschinger G. et al. “High Spectral Resolution X-Ray Imaging Crystal Spectrometer for Tokamaks and Stellarators”. In: *Advanced Diagnostics for Magnetic and Inertial Fusion*. Ed. by P. E. et al. Stott. Boston, MA: Springer US, 2002, pp. 269–276. ISBN: 978-1-4419-8696-2. DOI: 10.1007/978-1-4419-8696-2_50. URL: https://doi.org/10.1007/978-1-4419-8696-2_50 (cit. on p. 91).

[62] Beiersdorfer P. et al. “The ITER core imaging x-ray spectrometer”. In: *Journal of Physics B: Atomic, Molecular and Optical Physics* 43.14 (2010), p. 144008. DOI: 10.1088/0953-4075/43/14/144008. URL: https://doi.org/10.1088/0953-4075/43/14/144008 (cit. on pp. 92, 199).

[63] Shockley W. “The theory of p-n junctions in semiconductors and p-n junction transistors”. In: *The Bell System Technical Journal* 28.3 (1949), pp. 435–489. DOI: 10.1002/j.1538-7305.1949.tb03645.x (cit. on p. 102).

[64] Jagodziński P. et al. “Ray-tracing simulations of spherical Johann diffraction spectrometer for in-beam X-ray experiments”. In: *Nuclear Instruments and Methods in Physics Research Section A: Accelerators, Spectrometers, Detectors and Associated Equipment* 753 (2014), pp. 121–130. ISSN: 0168-9002. DOI: https://doi.org/10.1016/j.nima.2014.04.004. URL: https://www.sciencedirect.com/science/article/pii/S0168900214003805 (cit. on pp. 105, 143).

[65] Colledani G. *patent number 1653710*. 2016 (cit. on pp. 107, 111, 112).

[66] Bertschinger G.et al. “Alignment and absolute wavelength calibration of imaging Bragg spectrometers”. In: *Review of Scientific Instruments* 87.11 (2016), 11E343. DOI: 10.1063/1.4963163. eprint: https://aip.scitation.org/doi/pdf/10.1063/1.4963163. URL: https://aip.scitation.org/doi/abs/10.1063/1.4963163 (cit. on p. 112).

[67] Sunn Pedersen T. et al. “Plans for the first plasma operation of Wendelstein 7-X”. In: *Nuclear Fusion* 55.12 (2015), p. 126001. DOI: 10.1088/0029-5515/55/12/126001. URL: https://dx.doi.org/10.1088/0029-5515/55/12/126001 (cit. on p. 113).

[68] Park H.K. et al. “Overview of KSTAR research progress and future plans toward ITER and K-DEMO”. In: *Nuclear Fusion* 59.11 (2019), p. 112020. DOI: 10.1088/1741-4326/ab20e2. URL: https://dx.doi.org/10.1088/1741-4326/ab20e2 (cit. on p. 113).

[69] Kring J. et al. “In situ wavelength calibration system for the X-ray Imaging Crystal Spectrometer (XICS) on W7-X”. In: *Review of Scientific Instruments* 89.10 (2018), 10F107. ISSN: 0034-6748. DOI: 10.1063/1.5038809. URL: https://doi.org/10.1063/1.5038809 (cit. on p. 114).

[70] Lee S.G. et al. “Calibration methods of X-ray imaging crystal spectrometer on KSTAR”. In: *Review of Scientific Instruments* 89.10 (2018), 10F108. ISSN: 0034-6748. DOI: 10.1063/1.5034023. URL: https://doi.org/10.1063/1.5034023 (cit. on p. 115).

[71] Qingwei Y. et al. “Studies of mode lock instability in the HL-1M tokamak”. In: *Brazilian Journal of Physics* 32.1 (2001), pp. 160–164. URL: https://doi.org/10.1590/S0103-97332002000100027 (cit. on p. 115).

[72] Lee S.G. et al. “Validation of Toroidal Rotation and Ion Temperature in KSTAR Plasmas”. In: *Fusion Science and Technology* 69.2 (2016), pp. 555–559. DOI: 10.13182/FST15-174. eprint: https://doi.org/10.13182/FST15-174. URL: https://doi.org/10.13182/FST15-174 (cit. on p. 115).

[73] Guirlet R. et al. “Absolute sensitivity calibration of an extreme ultraviolet spectrometer for tokamak measurements”. In: *Journal of Instrumentation* 12.01 (2017), P01006. DOI: 10.1088/1748-0221/12/01/P01006. URL: https://dx.doi.org/10.1088/1748-0221/12/01/P01006 (cit. on pp. 115, 177).

[74] Rice J.E. et al. “Contamination of argon x-ray spectra by tungsten and other elements commonly found in tokamaks”. In: *Journal of Physics B: Atomic, Molecular and Optical Physics* 54.9 (2021), p. 095701. DOI: 10.1088/1361-6455/abecd2. URL: https://dx.doi.org/10.1088/1361-6455/abecd2 (cit. on pp. 120, 121, 140, 169, 170, 179).

[75] Clementson J. et al. “Spectroscopy of M-shell x-ray transitions in Zn-like through Co-like W”. In: *Physica Scripta* 81.1 (2009), p. 015301. DOI: 10.1088/0031-8949/81/01/015301. URL: https://dx.doi.org/10.1088/0031-8949/81/01/015301 (cit. on pp. 120, 169, 179).

[76] Group TFR et al. “Dielectronic satellite spectrum of heliumlike argon: A contribution to the physics of highly charged ions and plasma impurity transport”. In: *Phys. Rev. A* 32 (4 1985), pp. 2374–2383. DOI: 10.1103/PhysRevA.32.2374. URL: https://link.aps.org/doi/10.1103/PhysRevA.32.2374 (cit. on pp. 122, 140, 159).

[77] Hansen P.C. et al. “Numerical tools for analysis and solution of Fredholm integral equations of the first kind”. In: *Inverse Problems* 8.6 (1992), p. 849. DOI: 10.1088/0266-5611/8/6/005. URL: https://dx.doi.org/10.1088/0266-5611/8/6/005 (cit. on p. 130).

[78] Tikhonov A.N. “Solution of Incorrectly Formulated Problems and the Regularization Method”. In: *Soviet Mathematics. Doklady* 5 (1962) (cit. on p. 130).

[79] Tikhonov A. N. "Regularization of incorrectly posed problems". English. In: *Doklady Akademy Nauk SSSR* 153.1 (1963), p. 49. ISSN: 0002-3264 (cit. on p. 130).

[80] Anton M. et al. "X-ray tomography on the TCV tokamak". English. In: *Plasma physics and controlled fusion* 38 (1996), p. 1849 (cit. on p. 131).

[81] Chattopadhyay A. K. et al. "Tomography for SST-1 tokamak with pixel method". English. In: *Review of Scientific Instruments* 76.6 (2005), p. 063502. ISSN: 00346748. DOI: 10.1063/1.1938853. URL: http://link.aip.org/link/RSINAK/v76/i6/p063502/s1&Agg=doi (visited on 02/15/2013) (cit. on p. 131).

[82] Granetz R.S. et al. "X-ray tomography on JET". English. In: *Nuclear fusion* 28 (1988), p. 457 (cit. on p. 131).

[83] Hanke M. et al. "Limitations of the L-curve method in ill-posed problems". English. In: *BIT Numerical Mathematics* 36.2 (1996), pp. 287–301. URL: http://www.springerlink.com/index/V40MJ4L5Q1252504.pdf (visited on 02/15/2013) (cit. on p. 131).

[84] Hansen P.C. et al. "An adaptive pruning algorithm for the discrete L-curve criterion". English. In: *Journal of Computational and Applied Mathematics* 198.2 (2007), pp. 483–492. ISSN: 03770427. DOI: 10.1016/j.cam.2005.09.026. URL: http://linkinghub.elsevier.com/retrieve/pii/S0377042705007284 (visited on 02/14/2013) (cit. on p. 131).

[85] Ingesson L.C. et al. "Tomography diagnostics: bolometry and Soft X-Ray detection". English. In: *Fusion Science and Technology* 53.2 (2008), p. 528. ISSN: 1536-1055 (cit. on p. 131).

[86] Ingesson L.C. et al. "Comparison of basis functions in Soft X-ray tomography and observation of poloidal asymetries in impurity density". English. In: *Plasma Physics and Controlled Fusion* 42.2 (2000), p. 161 (cit. on p. 131).

[87] Junghee K. et al. "Comparison of the three tokamak plasma tomography methods for high spatial resolution and fast calculation". English. In: *Review of Scientific Instruments* 77.10 (2006), 10F513. ISSN: 00346748. DOI: 10.1063/1.2229277. URL: http://link.aip.org/link/RSINAK/v77/i10/p10F513/s1&Agg=doi (visited on 02/16/2012) (cit. on p. 131).

[88] Odstrci M. et al. "Modern numerical methods for plasma tomography optimisation". English. In: *Nuclear Instruments and Methods in Physics Research Section A: Accelerators, Spectrometers, Detectors and Associated Equipment* 686 (2012), p. 156 (cit. on p. 131).

[89] Wang Y. and Xiao T. "Fast realization algorithms for determining regularization parameters in linear inverse problems". English. In: *Inverse Problems* 17.2 (2001), pp. 281–291 (cit. on p. 131).

[90] Bangti J. et al. "Augmented Tikhonov regularization". In: *Inverse Problems* 25.2 (2009), p. 025001. ISSN: 0266-5611, 1361-6420. DOI: 10.1088/0266-5611/25/2/025001. URL: http://stacks.iop.org/0266-5611/25/i=2/a=025001?key=crossref.60309c8993ce053853ab3d70df290316 (visited on 11/07/2014) (cit. on p. 131).

[91] Reinke M.L. et al. "X-ray imaging crystal spectroscopy for use in plasma transport research". In: *Review of Scientific Instruments* 83.11 (2012), p. 113504. ISSN: 0034-6748. DOI: 10.1063/1.4758281. eprint: https://pubs.aip.org/aip/rsi/article-pdf/doi/10.1063/1.4758281/13711357/113504_1_online.pdf. URL: https://doi.org/10.1063/1.4758281 (cit. on pp. 131, 132, 140).

[92] Faugeras B. et al. "An overview of the numerical methods for tokamak plasma equilibrium computation implemented in the NICE code". In: *Fusion Engineering and Design* 160 (2020), p. 112020. ISSN: 0920-3796. DOI: https://doi.org/10.1016/j.fusengdes.2020.112020. URL: https://www.sciencedirect.com/science/article/pii/S0920379620305688 (cit. on p. 132).

[93] Rosen A.S. et al. "Validation of x-ray line ratios for electron temperature determination in tokamak plasmas". In: 47.10 (Apr. 2014), p. 105701. DOI: 10.1088/0953-4075/47/10/105701. URL: https://dx.doi.org/10.1088/0953-4075/47/10/105701 (cit. on pp. 135, 162).

[94] Goryayev F.F. et al. *Atomic data calculations by Z-expansion method for doubly excited states 2lnl' and 1s2lnl' of highly charged ions with Z=6-36. I. Transitions from the states with n=2,3*. 2006. arXiv: physics/0603164 [physics.atom-ph]. URL: https://arxiv.org/abs/physics/0603164 (cit. on pp. 135, 136).

[95] Platz P. et al. "X-ray line diagnostics on the Tore Supra tokamak". In: *Review of Scientific Instruments* 70.1 (1999), pp. 308–311. ISSN: 0034-6748. DOI: 10.1063/1.1149326. URL: https://doi.org/10.1063/1.1149326 (cit. on p. 140).

[96] Lee S.G. et al. "Experimental results from x-ray imaging crystal spectrometer utilizing double crystal assembly in Korea Superconducting Tokamak Advanced Research (KSTAR)". In: *Review of Scientific Instruments* 93.8 (2022), p. 083508. ISSN: 0034-6748. DOI: 10.1063/5.0098520. eprint: https://pubs.aip.org/aip/rsi/article-pdf/doi/10.1063/5.0098520/16612618/083508_1_online.pdf. URL: https://doi.org/10.1063/5.0098520 (cit. on p. 140).

[97] Delgado-Aparicio L.F. et al. "Effects of thermal expansion of the crystal lattice on x-ray crystal spectrometers used for fusion research". In: *Plasma Physics and Controlled Fusion* 55.12 (2013), p. 125011. DOI: 10.1088/0741-3335/55/12/125011. URL: https://doi.org/10.1088/0741-3335/55/12/125011 (cit. on pp. 142, 146).

[98] Uschmann I. et al. “X-ray reflection properties of elastically bent perfect crystals in Bragg geometry”. In: *Journal Of Applied Crystallography* 26.3 (1993), pp. 405–412. ISSN: 0021-8898. DOI: 10.1107/S0021889892013025 (cit. on p. 143).

[99] Sánchez del Río M. and Dejus R.J. “XOP v2.4: recent developments of the x-ray optics software toolkit”. In: *Advances in Computational Methods for X-Ray Optics II*. Ed. by Manuel Sanchez del Rio and Oleg Chubar. Vol. 8141. International Society for Optics and Photonics. SPIE, 2011, pp. 368–372. DOI: 10.1117/12.893911. URL: https://doi.org/10.1117/12.893911 (cit. on p. 143).

[100] Marmar E.S. et al. “Alcator C-Mod: research in support of ITER and steps beyond”. In: *Nuclear Fusion* 55.10 (2015), p. 104020. DOI: 10.1088/0029-5515/55/10/104020. URL: https://dx.doi.org/10.1088/0029-5515/55/10/104020 (cit. on p. 146).

[101] Schroeder D.V. *An Introduction to Thermal Physics*. OUP Oxford, 2020. ISBN: 9780192648105. URL: https://books.google.fr/books?id=gqkPEAAAQBAJ (cit. on p. 147).

[102] Bombarda F. PhD dissertation (private communication). Università La Sapienza, Rome (Italy), 1981 (cit. on p. 147).

[103] Verma H. et al. “Study of buried interfaces in Fe/Si multilayer by hard x-ray emission spectroscopy”. In: *Surface and Interface Analysis* 53.12 (2021), pp. 1043–1047. DOI: https://doi.org/10.1002/sia.7005. URL: https://analyticalsciencejournals.onlinelibrary.wiley.com/doi/abs/10.1002/sia.7005 (cit. on p. 155).

[104] Manas P. et al. “Maximizing the ion temperature in an electron heated plasma: from WEST towards larger devices”. In: *Nuclear Fusion* 64.3 (2024), p. 036011. DOI: 10.1088/1741-4326/ad171e. URL: https://dx.doi.org/10.1088/1741-4326/ad171e (cit. on p. 160).

[105] Artaud J.F. et al. “Metis: a fast integrated tokamak modelling tool for scenario design”. In: *Nuclear Fusion* 58.10 (2018), p. 105001. DOI: 10.1088/1741-4326/aad5b1. URL: https://dx.doi.org/10.1088/1741-4326/aad5b1 (cit. on p. 160).

[106] Rice J.E. et al. “X-ray observations of medium Z H- and He-like ions with satellites from C-Mod tokamak plasmas”. In: *Journal of Physics B: Atomic, Molecular and Optical Physics* 48.14 (2015), p. 144013. DOI: 10.1088/0953-4075/48/14/144013. URL: https://dx.doi.org/10.1088/0953-4075/48/14/144013 (cit. on p. 162).

[107] Rice J.E. et al. “Radial profiles of ground-state transitions of heliumlike argon from the Alcator-C tokamak”. In: *Phys. Rev. A* 35 (7 Apr. 1987), pp. 3033–3045. DOI: 10.1103/PhysRevA.35.3033. URL: https://link.aps.org/doi/10.1103/PhysRevA.35.3033 (cit. on p. 163).

[108] Rosmej F.B. et al. “Influence of charge-exchange processes on x-ray spectra in TEXTOR tokamak plasmas: experimental and theoretical investigation”. In: *Plasma Physics and Controlled Fusion* 41.2 (1999), p. 191. DOI: 10.1088/0741-3335/41/2/004. URL: https://dx.doi.org/10.1088/0741-3335/41/2/004 (cit. on p. 164).

[109] Rosmej F.B., Astapenko V.A., and Lisitsa V.S. “Applications to Plasma Spectroscopy”. In: *Plasma Atomic Physics*. Cham: Springer International Publishing, 2021, pp. 459–592. ISBN: 978-3-030-05968-2. DOI: 10.1007/978-3-030-05968-2_10. URL: https://doi.org/10.1007/978-3-030-05968-2_10 (cit. on p. 164).

[110] Bartiromo R. et al. “Spectroscopic study of nonthermal plasmas”. In: *Phys. Rev. A* 32 (1 1985), pp. 531–537. DOI: 10.1103/PhysRevA.32.531. URL: https://link.aps.org/doi/10.1103/PhysRevA.32.531 (cit. on p. 165).

[111] Lee S.G. et al. “The first experimental results from W divertor utilizing x-ray imaging crystal spectrometer on KSTAR”. In: *Review of Scientific Instruments* 95.7 (July 2024), p. 073515. ISSN: 0034-6748. DOI: 10.1063/5.0210736. eprint: https://pubs.aip.org/aip/rsi/article-pdf/doi/10.1063/5.0210736/20050186/073515_1_5.0210736.pdf. URL: https://doi.org/10.1063/5.0210736 (cit. on p. 170).

[112] Peyrusse O. Bauche J. Bauche-Arnoult C. “Atomic Properties in Hot Plasmas”. In: Springer Cham, 2015. ISBN: 978-3-319-18147-9. DOI: https://doi.org/10.1007/978-3-319-18147-9. URL: https://doi.org/10.1007/978-3-642-02233-3_7 (cit. on p. 175).

[113] Summers H.P. et al. “Ionization state, excited populations and emission of impurities in dynamic finite density plasmas: I. The generalized collisional–radiative model for light elements”. In: *Plasma Physics and Controlled Fusion* 48.2 (Jan. 2006), p. 263. DOI: 10.1088/0741-3335/48/2/007. URL: https://dx.doi.org/10.1088/0741-3335/48/2/007 (cit. on p. 175).

[114] Griffin D.C. et al. “R-matrix electron-impact excitation cross sections in intermediate coupling: an MQDT transformation approach”. In: *Journal of Physics B: Atomic, Molecular and Optical Physics* 31.16 (Aug. 1998), p. 3713. DOI: 10.1088/0953-4075/31/16/022. URL: https://dx.doi.org/10.1088/0953-4075/31/16/022 (cit. on p. 176).

[115] Shevelko V.P. and Vainshtein L.A. *Atomic physics for hot plasmas*. eng. Institute of Physics Pub., 1993. ISBN: 0750302313 (cit. on p. 176).

[116] Mao J. et al. “The electron energy loss rate due to radiative recombination ”. In: *AA* 599 (2017), A10. DOI: 10.1051/0004-6361/201629708. URL: https://doi.org/10.1051/0004-6361/201629708 (cit. on p. 176).

[117] Bulbul E. et al. "Laboratory Measurements of X-Ray Emission from Highly Charged Argon Ions". In: *The Astrophysical Journal* 870.1 (Dec. 2018), p. 21. DOI: 10.3847/1538-4357/aaee7d. URL: https://dx.doi.org/10.3847/1538-4357/aaee7d (cit. on p. 176).

[118] Badnell N.R. "On the effects of the two-body non-fine-structure operators of the Breit - Pauli Hamiltonian". In: *Journal of Physics B: Atomic, Molecular and Optical Physics* 30.1 (Jan. 1997), p. 1. DOI: 10.1088/0953-4075/30/1/005. URL: https://dx.doi.org/10.1088/0953-4075/30/1/005 (cit. on p. 176).

[119] Langenberg A. et al. "Inference of temperature and density profiles via forward modeling of an x-ray imaging crystal spectrometer within the Minerva Bayesian analysis framework". In: *Review of Scientific Instruments* 90.6 (June 2019), p. 063505. ISSN: 0034-6748. DOI: 10.1063/1.5086283. eprint: https://pubs.aip.org/aip/rsi/article-pdf/doi/10.1063/1.5086283/13610185/063505_1_online.pdf. URL: https://doi.org/10.1063/1.5086283 (cit. on p. 177).

[120] Schwob J.L. et al. "High-resolution duo-multichannel soft x-ray spectrometer for tokamak plasma diagnostics". In: *Review of Scientific Instruments* 58.9 (1987), pp. 1601–1615. ISSN: 0034-6748. DOI: 10.1063/1.1139408. eprint: https://pubs.aip.org/aip/rsi/article-pdf/58/9/1601/19097902/1601_1_online.pdf. URL: https://doi.org/10.1063/1.1139408 (cit. on p. 177).

[121] Manson J.E. *Manson Model 5 Ultrasoft-X-Ray Calibration Source (Austin Instruments Inc.)* 1985 (cit. on p. 178).

[122] Guirlet R. et al. "Extreme UV spectroscopy measurements and analysis for tungsten density studies in the WEST tokamak". In: *Plasma Physics and Controlled Fusion* 64.10 (2022), p. 105024. DOI: 10.1088/1361-6587/ac8d2c. URL: https://dx.doi.org/10.1088/1361-6587/ac8d2c (cit. on pp. 179, 193).

[123] Gil C. et al. "Renewal of the interfero-polarimeter diagnostic for WEST". In: *Fusion Engineering and Design* 140 (2019), pp. 81–91. ISSN: 0920-3796. DOI: https://doi.org/10.1016/j.fusengdes.2019.02.003. URL: https://www.sciencedirect.com/science/article/pii/S0920379619301759 (cit. on p. 188).

[124] Langenberg A. et al. "Prospects of X-ray imaging spectrometers for impurity transport: Recent results from the stellarator Wendelstein 7-X (invited)". In: *Review of Scientific Instruments* 89.10 (July 2018), 10G101. ISSN: 0034-6748. DOI: 10.1063/1.5036536. eprint: https://pubs.aip.org/aip/rsi/article-pdf/doi/10.1063/1.5036536/16726435/10g101_1_online.pdf. URL: https://doi.org/10.1063/1.5036536 (cit. on p. 199).

[125] Moss D.S. et al. “International tables for X-ray crystallography. Vol. IV edited by J. A. Ibers and W. C. Hamilton”. In: *Acta Crystallographica Section B Structural Crystallography and Crystal Chemistry* 31 (1975), pp. 2558–2558. URL: https://api.semanticscholar.org/CorpusID:93503470 (cit. on p. 204).

[126] Hönl H. et al. “Zur Dispersionstheorie der Röntgenstrahlen”. In: *Zeitschrift für Physik* 84.1 (Jan. 1, 1933), pp. 1–16. ISSN: 0044-3328. DOI: 10.1007/BF01330269. URL: https://doi.org/10.1007/BF01330269 (cit. on p. 204).